

# **Silicon and oxygen self-diffusion in forsterite and implications to upper-mantle rheology**

eingereicht an der Fakultät für Biologie, Chemie and Geowissenschaften

der Universität Bayreuth

zur Erlangung der Würde eines

Doktors der Naturwissenschaften

- Dr. rer. nat. –

**Dissertation**

vorgelegt von

**Hongzhan Fei**

aus Zhejiang (China)

Bayreuth, 2013

# Silicon and oxygen self-diffusion in forsterite and implications to upper-mantle rheology



**Hongzhan Fei**

费宏展

Supervisor: Tomoo Katsura

Universität Bayreuth

Bayreuth, 2013

This doctoral thesis was prepared at the Department of Bayerisches Geoinstitut, University of Bayreuth from April 2010 until October 2013 supervised by Prof. Dr. Tomoo Katsura.

This is a full reprint of the dissertation submitted to obtain the academic degree of Doctor of Natural Sciences (Dr. rer. nat.) and approved by the Faculty of Biology, Chemistry and Geosciences of the University of Bayreuth.

Acting dean: Prof. Dr. Rhett Kempe

Date of submission: 07th August, 2013

Date of defence (disputation): 30th October, 2013

Doctoral Committee:

Prof. Dr. Tomoo Katsura, University of Bayreuth (1<sup>st</sup> reviewer)

Prof. Dr. David Dobson, University College London (2<sup>nd</sup> reviewer)

Prof. Dr. Dan Frost, University of Bayreuth (3<sup>rd</sup> reviewer)

Prof. Dr. Leonid Dubrovinsky, University of Bayreuth (Chairman)

Prof. Dr. Hans Keppler, University of Bayreuth

Prof. Dr. Jürgen Senker, University of Bayreuth



# Contents

<b>Summary.....</b>	<b>1</b>
(1) Silicon lattice diffusion coefficient in dry forsterite.....	1
(2) Effect of water on silicon self-diffusion coefficient in forsterite .....	2
(3) Effect of water on oxygen self-diffusion coefficient in forsterite .....	2
(4) Silicon grain boundary diffusion coefficient in forstetrite .....	3
<b>Zusammenfassung.....</b>	<b>4</b>
(1) Gitterdiffusionskoeffizient von Silizium in wasserfreiem Forsterit .....	4
(2) Der Einfluss von Wasser auf den Silizium-Eigendiffusionskoeffizienten in Forsterit .....	5
(3) Der Einfluss von Wasser auf den Sauerstoff-Eigendiffusionskoeffizienten in Forsterit .....	6
(4) Korngrenzen-Diffusionskoeffizient für Silizium in Forsterit .....	6
<b>1. Introduction to Si and O diffusion in minerals and mantle rheology.....</b>	<b>8</b>
1.1 Theory of diffusion .....	8
1.1.1 Fick's law .....	9
1.1.2 Point defects in a crystal .....	10
1.1.3 Diffusion mechanisms.....	11
1.1.4 Atomic diffusion-coefficient in a crystal .....	13
1.1.5 Various types of diffusion .....	13
1.1.6 Temperature and pressure dependences of diffusion coefficients .....	15
1.2 Mineralogical model of the Earth's mantle.....	18
1.3 General information about olivine/forsterite.....	19
1.3.1 Crystal structure .....	19
1.3.2 Defect chemistry in olivine .....	21
1.3.3 Water in olivine .....	25
1.4 Deformation mechanisms of olivine and upper mantle rheology .....	30

1.4.1 Diffusion creep.....	31
1.4.2 Dislocation creep.....	32
1.4.3 Grain boundary sliding.....	34
1.4.4 Rheology in Earth's upper mantle.....	34
1.5 Experimental approaching to mantle rheology .....	42
1.5.1 Deformation experiments.....	42
1.5.2 Diffusion experiments.....	44
1.6 Previous studies of silicon and oxygen diffusion in mantle minerals .....	47
1.6.1 Silicon diffusion .....	47
1.6.2 Oxygen diffusion.....	59
1.7 Aim of this study .....	63
1.7.1 Discrepancy between silicon diffusion and deformation in olivine .....	64
1.7.2 Pressure dependence of silicon diffusion and creep rate .....	65
1.7.3 Effect of water on silicon diffusion and creep rate in olivine .....	66
1.7.4 Grain-boundary diffusion in olivine under upper mantle conditions.....	68
1.7.5 This study .....	68
1.8 General experimental methods in this study .....	69
1.8.1 Sample preparation.....	69
1.8.2 Thin film deposition .....	71
1.8.3 Diffusion annealing.....	71
1.8.4 Diffusion profile analysis .....	73
1.8.5 Obtain diffusion coefficients and other parameters .....	75
<b>2. Silicon self-diffusion in dry forsterite .....</b>	<b>76</b>
2.1 Abstract .....	76
2.2 Introduction.....	76
2.3 Experimental and analytical methods .....	78

2.3.1 Starting material and sample preparing.....	78
2.3.2 Annealing experiments.....	80
2.3.3 FT-IR analysis.....	82
2.3.4 SIMS analysis.....	83
2.3.5 Surface roughness .....	84
2.4 Results.....	88
2.4.1 Water content .....	88
2.4.2 Silicon diffusion coefficients .....	90
2.5 Discussion .....	93
2.5.1 “Dry” experimental conditions at high pressures.....	93
2.5.2 Comparison with previous studies of $D_{Si}$ in forsterite .....	93
2.5.3 Comparison with dislocation climb rate .....	97
2.5.4 Activation energy and activation volume in forsterite and in natural olivine .....	98
2.5.5 Comparison with wadsleyite and ringwoodite.....	100
2.5.6 $D_{Si}$ in the upper mantle and mantle transition zone .....	101
2.6 Acknowledgments.....	103
<b>3. Silicon self-diffusion in wet forsterite .....</b>	<b>104</b>
3.1 Abstract.....	104
3.2 Introduction.....	104
3.3 Experimental methods.....	106
3.3.1 Starting material .....	106
3.3.2 Water-doping experiments .....	106
3.3.3 Deposition .....	108
3.3.4 Diffusion annealing.....	108
3.3.5 FT-IR analysis.....	110
3.3.6 SIMS analysis.....	110

3.4 Results .....	111
3.5 Discussion .....	112
3.5.1 Well-controlled $C_{H_2O}$ during diffusion annealing experiments.....	112
3.5.2 Activation energy for Si diffusion and deformation of olivine .....	116
3.5.3 Defect chemistry .....	117
3.5.4 Comparing with deformation experiments.....	120
3.5.5 Implications to upper mantle rheology .....	126
3.6 Acknowledgments.....	128
<b>4. Oxygen self-diffusion in forsterite .....</b>	<b>129</b>
4.1 Abstract .....	129
4.2 Introduction.....	129
4.3 Experimental and analytical methods .....	130
4.4 Results .....	134
4.5 Discussion .....	135
4.5.1 Activation energy and activation volume .....	135
4.5.2 Defect chemistry .....	137
4.5.3 Geophysical implications .....	139
4.6 Acknowledgments.....	140
<b>5. Silicon grain boundary diffusion in forsterite.....</b>	<b>141</b>
5.1 Abstract .....	141
5.2 Introduction.....	141
5.3 Experimental and analytical procedures .....	143
5.3.1 Starting material .....	143
5.3.2 Pre-annealing experiments .....	144
5.3.3 Deposition .....	146
5.3.4 Diffusion annealing .....	147

5.3.5 FT-IR analysis .....	150
5.3.6 SIMS analysis.....	154
5.3.7 Calculations of creep rates from silicon diffusion coefficients.....	158
5.4 Results .....	160
5.5 Discussion .....	162
5.5.1 Examine the validity of results.....	162
5.5.2 $P$ , $T$ , $C_{\text{H}_2\text{O}}$ , and grain size dependences of $D_{\text{Si}^{\text{gb}}}$ , $D_{\text{Si}^{\text{lat}}}$ , and creep rates.....	166
5.5.3 Defect chemistry .....	168
5.5.4 Comparison with previous diffusion and deformation studies .....	169
5.5.5 Stress and strain rate in the upper mantle.....	172
5.5.6 Deformation mechanisms in Earth's upper mantle.....	175
5.5.7 Geophysical implications .....	180
5.6 Acknowledgments.....	182
<b>6. Conclusions.....</b>	<b>183</b>
<b>Appendix I:</b> Kröger-Vink notation.....	184
<b>Appendix II:</b> water content exponents for defect species in olivine .....	186
<b>Appendix III:</b> Linkages between self-diffusion, creep rate, and viscosity .....	190
<b>References .....</b>	<b>196</b>
<b>Publications related to this work.....</b>	<b>213</b>
Acknowledgments.....	215
Erklärung.....	216



# SUMMARY

---

## Summary

Most of geodynamic processes in Earth's upper mantle are believed to be controlled by the plastic deformation of olivine, which is the main constituent in the lithosphere and asthenosphere. Determination of olivine rheological properties could thus give the basic understanding of upper mantle dynamics. There are mainly two ways to study the olivine rheology: (a) Deformation experiments. However, the deformation studies usually have serious limitations due to the experimental difficulties, for example, extremely high stress applied to the samples; limited pressure and water content conditions; both of which could lead to misunderstanding to the Earth's interior. (b) Silicon self-diffusion experiments. The high-temperature deformation of minerals is controlled by dislocation creep and diffusion creep, both of which are limited by self-diffusion of the slowest species, i.e., silicon in olivine. Oxygen is second slowest diffusion species with similar rate as silicon. Thus, measurement of silicon and oxygen self-diffusion coefficients in olivine is an independent way in comparison with deformation experiments to study the upper mantle rheology. In this project, I focused on measuring the lattice and grain-boundary diffusion coefficients of silicon and oxygen in olivine as a function of pressure, temperature, and water content, and investigated the upper mantle rheology based on silicon and oxygen diffusion rates.

### *(1) Silicon lattice diffusion coefficient in dry forsterite*

The high temperature creep of olivine is believed to be controlled by self-diffusion of olivine. However, the experimentally measured silicon diffusion coefficients ( $D_{Si}$ ) [Dohmen *et al.*, 2002; Jaoul *et al.*, 1981] were about 2-3 orders of magnitude lower than those estimated from dislocation creep rates by deformation experiments [Durham and Goetze, 1977a; Goetze and Kohlstedt, 1973]. In order to resolve this discrepancy, we measured  $D_{Si}$  in a dry forsterite single crystal at 1600-1800 K, 1 atm -13 GPa using an ambient pressure furnace and Kawai-type multi-anvil apparatus. The water contents in the samples were carefully controlled at <1 wt. ppm. The results of  $D_{Si}$  showed small negative pressure dependence with an activation volume of  $1.7 \pm 0.4$  cm<sup>3</sup>/mol. The activation energy is found to be  $410 \pm 30$  kJ/mol.  $\text{Log}D_{Si}$  at 1600 and 1800 K at

ambient pressure are  $-19.7 \pm 0.4$  and  $-18.1 \pm 0.3$  ( $D_{Si}$  in  $m^2/s$ ), respectively, which are  $\sim 2.4$  orders of magnitude higher than those reported by Jaoul et al. [1981]. Their low  $D_{Si}$  might reflect the effects of a horizontal migration of the isotopically enriched thin films applied on the sample surfaces, which may inhibit diffusion into the substrate during annealing. Our results resolved the discrepancy of  $D_{Si}$  measured in diffusion experiments with those deduced from creep rates measured in deformation experiments.

### ***(2) Effect of water on silicon self-diffusion coefficient in forsterite***

Water has been considered to largely affect geodynamical processes in the Earth's interior. In particular, experimental deformation studies suggested that even several tens wt. ppm of water can enhanced creep in olivine by several orders of magnitude. However, those deformation results are doubtful because of the experimental limitations, e.g., considering only a limited range of water content and very high stresses applied to the samples. Because the high temperature creep of silicate minerals is controlled by silicon self-diffusion, we systematically measured  $D_{Si}$  in iron-free forsterite at 8 GPa, 1600 - 1800 K, and water content ( $C_{H_2O}$ ) from  $<1$  up to  $\sim 800$  wt. ppm, showing a relationship,  $D_{Si} \propto (C_{H_2O})^{0.32 \pm 0.07}$ . This  $C_{H_2O}$  exponent is strikingly lower than 1.2, which has been obtained by deformation experiments [Hirth and Kohlstedt, 2003]. The high nominal creep rates in the deformation studies under wet conditions may be caused by excess grain boundary water. Thus, the effect of water on olivine rheology is much smaller than that it has been considered before and many geodynamic problems should be reconsidered. The viscosity in the upper mantle calculated from  $D_{Si}$  continuously decreases with increasing depth without appearing a minimum zone by mineral hydration, and therefore, the asthenosphere softening cannot be caused by water effect. The  $C_{H_2O}$  differences between the source of hotspots and their surrounding regions only causes a viscosity contrast by a factor of two, which is rather small in comparison with that caused by temperature differences. Therefore,  $C_{H_2O}$  differences cannot be the major reason that leads to the immobility of hotspots.

### ***(3) Effect of water on oxygen self-diffusion coefficient in forsterite***

Oxygen is the second slowest diffusion species in olivine with similar diffusion coefficients as silicon. Therefore, oxygen diffusion also plays essential role in rock deformation as well as silicon diffusion. In order to examine the effects of water on creep reported by rock deformation

experiments, we also measured oxygen self-diffusion coefficient ( $D_O$ ) in forsterite at a pressure of 8 GPa and temperatures of 1600 - 1800 K as a function of  $C_{H_2O}$  from <1 up to ~800 wt. ppm. The experimental results showed  $D_O \propto (C_{H_2O})^{0.06 \pm 0.1} \approx (C_{H_2O})^0$ . Namely, water has no effect on  $D_O$ . Together with the small effect of water on silicon self-diffusion coefficient, we conclude that the role of water on upper mantle rheology is insignificant.

#### ***(4) Silicon grain boundary diffusion coefficient in forsterite***

Dislocation creep causes non-Newtonian viscosity and seismic anisotropy whereas diffusion creep doesn't. Determination of deformation mechanism in Earth's interior is thus essential to understand mantle dynamics. We have measured silicon grain-boundary diffusion coefficient in forsterite as a function of pressure, temperature, and water content. The activation volume, activation energy, and water exponent are found to be  $1.8 \pm 0.2$  cm<sup>3</sup>/mol,  $245 \pm 12$  kJ/mol, and  $0.22 \pm 0.05$ , respectively. The rates of dislocation creep, Coble diffusion creep, and Nabarro-Herring diffusion creep calculated from silicon lattice and grain-boundary diffusion coefficients suggest dominant diffusion creep in cold mantles and mantle wedges. In the asthenosphere, dislocation creep always dominates because of the high temperature. The deformation mechanism transition does not occur in the asthenosphere. In the lithosphere, diffusion creep dominates in shallow regions and dislocation creep dominates in lower regions. In mantle wedges, diffusion creep dominates and therefore olivine does not form lattice-preferred orientation: their strong anisotropy is caused not by olivine but by serpentine. The Newtonian rheology suggested by postglacial rebound and the seismically observed mid-lithospheric discontinuity should be attributed to the diffusion creep dominated cold continental lithosphere.

# Zusammenfassung

---

## Zusammenfassung

Es wird angenommen, dass der größte Teil der im oberen Erdmantel ablaufenden geodynamischen Prozesse durch die plastische Verformung von Olivin bestimmt wird, dem wichtigsten Mineral in der Litho- und Asthenosphäre. Bestimmungen seiner rheologischen Eigenschaften könnten daher Grundkenntnisse über dynamische Prozesse im oberen Erdmantel liefern. Es gibt im wesentlichen zwei Ansätze zur Untersuchung der Olivin-Rheologie: a) Verformungsexperimente. Deformationsuntersuchungen aufgrund der experimentellen Einschränkungen sind jedoch sehr eng limitiert; zum Beispiel durch extrem hohe Spannungen, die auf das Probenmaterial einwirken, oder begrenzte Bedingungen hinsichtlich Druck und Wassergehalt. Diese Einschränkungen könnten zu einer Fehlinterpretation der gewonnenen Informationen über das Erdinnere führen. - b) Experimente zur Eigendiffusion von Silizium. Die Mineralverformung unter hohen Temperaturen wird durch Versetzungs- und Diffusionskriechen bestimmt; diese beiden Prozesse werden wiederum durch die Eigendiffusion der langsamsten Spezies kontrolliert, d.h. durch Silizium in Olivin. An zweiter Stelle in der Langsamkeit bei der Diffusion steht Sauerstoff. Für Rheologieuntersuchungen des oberen Erdmantels gibt daher die Bestimmung der Eigendiffusionskoeffizienten von Silizium und Sauerstoff eine unabhängige Methode zusätzlich zu Verformungsexperimenten. Die vorliegende Arbeit konzentriert sich auf die Gitter- und Korngrenzen-Diffusionskoeffizienten von Silizium und Sauerstoff als Funktion von Druck, Temperatur und Wassergehalt; dabei wurden rheologische Prozesse im oberen Mantel auf der Basis von Silizium- und Sauerstoff-Diffusionsraten untersucht.

### ***(1) Gitterdiffusionskoeffizient von Silizium in wasserfreiem Forsterit***

Die Eigendiffusion gilt als kontrollierender Faktor des Hochtemperatur-Kriechens von Olivin. Jedoch liegen die experimentell bestimmten Silizium-Diffusionskoeffizienten ( $D_{Si}$ ) [Dohmen et al., 2002; Jaoul et al., 1981] um ca. 2-3 Größenordnungen niedriger als jene, die auf Abschätzungen auf der Basis von Versetzungskriechraten aus Verformungsexperimenten beruhen (Durham and Goetze, 1977a; Goetze and Kohlstedt, 1973). Zur Klärung dieser Diskrepanz wurde von uns  $D_{Si}$  in einem wasserfreiem Forsterit-Einkristall bei 1600-1800 K und

bei Drücken von 1 atm – 13 GPa bestimmt. Dafür wurden ein Hochtemperaturofen (Umgebungsdruck) und eine Multianvil-Pressen (Kawai-Typ) eingesetzt. Der Wassergehalt der Proben wurde sehr sorgfältig auf weniger als 1 ppm (Gewicht) eingestellt. Die Ergebnisse für  $D_{Si}$  zeigen eine kleine negative Abhängigkeit vom Druck, mit einem Aktivierungsvolumen von  $1,7 \pm 0,4 \text{ cm}^3/\text{mol}$ . Für die Aktivierungsenergie wurde ein Wert von  $410 \pm 30 \text{ kJ/mol}$  ermittelt. Die  $\log D_{Si}$ -Werte bei 1600 und 1800 K unter Umgebungsdruck sind damit  $-19,7 \pm 0,4$  beziehungsweise  $-18,1 \pm 0,3$  ( $D_{Si}$  in  $\text{m}^2/\text{s}$ ); sie liegen damit um  $\sim 2,4$  Größenordnungen über denen, die von Jaoul et al. (1981) bestimmt wurden. Deren niedriger  $D_{Si}$ -Wert könnte den Einfluss einer horizontalen Migration der auf der Probe aufgetragenen dünnen, mit Isotopen angereicherten Oberflächenfilme widerspiegeln, wodurch eine Diffusion in das Substrat bei der Abkühlung verhindert wird. Mit unseren Ergebnissen konnte die Diskrepanz der  $D_{Si}$ -Werte aus Diffusionsexperimenten und der daraus abgeleiteten Kriechraten mit Messungen aus Verformungsexperimenten, geklärt werden.

## ***(2) Der Einfluss von Wasser auf den Silizium-Eigendiffusionskoeffizienten in Forsterit***

Geodynamische Prozesse im Erdinneren werden in großem Umfang durch Wasser beeinflusst. Insbesondere haben Verformungsexperimente darauf hingewiesen, dass Wasser bereits im ppm-Bereich Kriechprozesse in Olivin um einige Größenordnungen verstärkt. Diese Ergebnisse zur Kristallverformung sind jedoch aufgrund der experimentellen Gegebenheiten nicht gesichert; zum Beispiel wird hier bezüglich des Wassergehalts ein enger Bereich betrachtet und die Proben unterlagen sehr hohen Spannungen. Da das Hochtemperatur-Kriechverhalten von Silikatmineralen durch die Eigendiffusion von Silizium bestimmt wird, haben wir systematisch  $D_{Si}$  in eisenfreiem Forsterit bei 8 GPa, 1600 - 1800 K und einem Wassergehalt ( $C_{H_2O}$ ) von  $<1$  bis  $\sim 800$  ppm, gemessen. Es ergab sich folgende Beziehung:  $D_{Si} \propto (C_{H_2O})^{0,32 \pm 0,07}$ . Dieser  $C_{H_2O}$ -Exponent ist signifikant niedriger als in Verformungsexperimenten, mit einem Wert von 1,2 (Hirth and Kohlstedt, 2003). Die hohen nominalen Kriechraten in den Verformungsexperimenten unter wasserhaltigen Bedingungen könnten ihre Ursache in einem Überschuss an Wasser an Korngrenzen haben. Somit ist der Einfluss von Wasser auf die Olivinrheologie viel geringer als bisher angenommen; zahlreiche geodynamische Fragestellungen sollten im Licht dieser Erkenntnisse neu überdacht werden. Die mit Hilfe von  $D_{Si}$  berechneten Viskositäten im oberen Erdmantel nehmen mit zunehmender Tiefe kontinuierlich ab, ohne dass eine Zone mit einem

Minimum aufgrund von Wasser erkennbar wird. Daher spielt Wasser für die Aufweichung der Asthenosphäre sicherlich keine Rolle. Die  $C_{H_2O}$ -Differenz zwischen der Ursprungsregion von *Hotspots* und dem normalen Mantel verursacht lediglich einen Kontrast in den Viskositäten mit einem Faktor 2, der relativ klein ist im Vergleich zu dem, der durch Temperaturunterschiede hervorgerufen wird. Daher können  $C_{H_2O}$ -Differenzen nicht als Hauptgrund für das Verharren von *Hotspots* auf ihrer Position herangezogen werden.

### ***(3) Der Einfluss von Wasser auf den Sauerstoff-Eigendiffusionskoeffizienten in Forsterit***

Sauerstoff ist die zweitlangsamste Diffusionsspezies in Olivin mit ähnlichen Diffusionskoeffizienten wie Silizium. Daher spielt die Sauerstoffdiffusion neben der Siliziumdiffusion eine wesentliche Rolle in der Gesteinsverformung. Zur Untersuchung der Auswirkung von Wasser auf das Kriechen, das nach Experimenten zur Gesteinsverformung beschrieben wurde, haben wir auch den Eigendiffusionskoeffizienten für Sauerstoff ( $D_O$ ) in Forsterit bei einem Druck von 8 GPa und Temperaturen von 1600 – 1800 K als Funktion von  $C_{H_2O}$  von <1 bis ~800 ppm (Gewicht) untersucht. Das experimentell ermittelte Ergebnis lautet  $D_O \propto (C_{H_2O})^{0,06 \pm 0,1} \approx (C_{H_2O})^0$ . Wasser hat damit keinen Einfluss auf  $D_O$ . Im Zusammenhang mit der geringen Auswirkung von Wasser auf den Eigendiffusions-Koeffizienten von Silizium lässt sich daraus schließen, dass Wasser für die Rheologie des oberen Erdmantels eine unbedeutende Rolle spielt.

### ***(4) Korngrenzen-Diffusionskoeffizient für Silizium in Forsterit***

Versetzungskriechen bewirkt nicht-Newton'sche Viskosität und seismische Anisotropien, was dagegen bei Diffusionskriechen nicht der Fall ist. Die Bestimmung von Verformungsmechanismen im Erdinneren ist daher für das Verständnis der Dynamik im Erdmantel sehr wichtig. Von uns wurde der Korngrenzen-Diffusionskoeffizient für Silizium in Forsterit in Abhängigkeit von Druck, Temperatur und Wassergehalt bestimmt. Als Werte für Aktivierungsvolumen, Aktivierungsenergie sowie des Exponenten für die Abhängigkeit vom Wassergehalt ergaben sich  $1,8 \pm 0,2$  cm<sup>3</sup>/mol,  $245 \pm 12$  kJ/mol sowie  $0,22 \pm 0,05$ . Wir haben die Kriechgeschwindigkeiten dreier verschiedener Arten von Kriechen verglichen: Versetzungskriechen, Coble-Diffusionskriechen und Nabarro-Herring-Diffusionskriechen; in

allen Fällen wurde die Geschwindigkeit aus Gitter- und Korngrenzen-Diffusionskoeffizienten für Silizium berechnet. Die Ergebnisse deuten auf eine Dominanz des Diffusionskriechen in kühlen Mantelregionen und Mantelkeilen hin. In der Asthenosphäre dominiert aufgrund hoher Temperaturen stets Versetzungskriechen; es treten keine Übergänge in den Verformungsmechanismen auf. In der Lithosphäre dominiert in geringer Tiefe das Diffusionskriechen, in tieferen Bereichen überwiegt Dislokationskriechen. Da in Mantelkeilen Olivin keine Vorzugsrichtung im Kristallgitter ausbildet, wird die starke elastische Anisotropie in diesen Zonen wohl nicht durch Olivin sondern durch Serpentin verursacht. Eine Newton'sche Rheologie, die aufgrund der postglazialen Hebung angenommen wird, sowie die beobachtete seismische Diskontinuität im Zentrum der Lithosphäre sollte der kühlen kontinentalen Lithosphäre mit dominierendem Diffusionskriechen zugeschrieben werden.

# Chapter 1

## Introduction to Si and O diffusion in minerals and mantle rheology

### 1.1 Theory of diffusion

Diffusion is a process by which thermally activated atoms, ions, and molecules in materials are transported from one part of a system to another as a result of random molecular motions [Crank, 1975; Zhang and Cherniak, 2010]. The random motion leads to a net flux when the concentration (chemical potential) of a component is not uniform. The initially concentrated atomic species will “diffuse out” as time goes on. Therefore, in a diffusion process, the species tend to diffuse from a highly concentrated region to a less concentrated region, and leads to homogenize the material (**Fig. 1.1**).

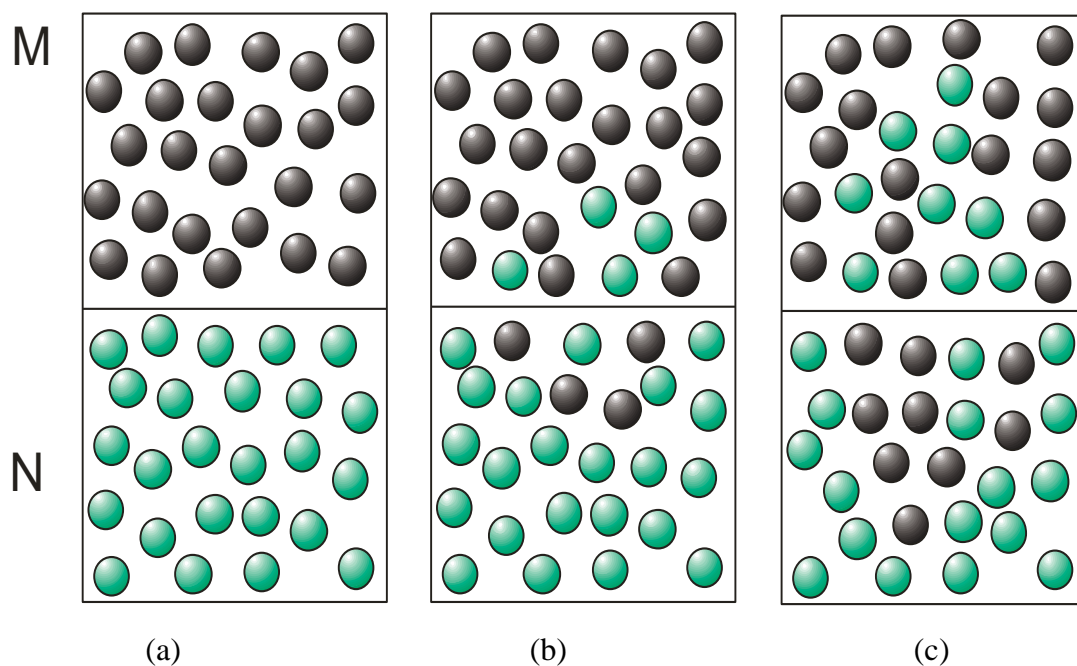


**Fig. 1.1.** An example of random motion of particles. (a) Initially, all M particles are in the upper side and N in the lower side. (b) Due to the random motion, there is a net flux of M from the upper to lower side, and a net flux of N from lower to upper side. (c) As time increases, M and N become randomly and uniformly distributed in the system (figure modified from Zhang and Cherniak [2010]).

### 1.1.1 Fick's law

An empirical law to describe the process of diffusion is called Fick's First Law, which states that the atomic flux is linearly proportional to the concentration gradient, namely,

$$J = -D \frac{\partial c}{\partial x} \quad (1.1)$$

where  $J$  is the flux of a given species,  $c$  is the number of atoms per unit volume (concentration),  $D$  is the diffusion coefficient, and  $x$  is the position. Therefore, the diffusion coefficient,  $D$ , has a dimension of  $\text{m}^2/\text{s}$  in SI units.

If we combine Fick's first law with the equation of mass conservation:

$$\frac{\partial c}{\partial t} = -\frac{\partial J}{\partial x} \quad (1.2)$$

we obtain Fick's second law of diffusion:

$$\frac{\partial c}{\partial t} = D \frac{\partial^2 c}{\partial x^2} \quad (1.3)$$

which predicts how diffusion causes concentration change with time  $t$ .

If two materials, M and N, each is initially uniform, but the two have different compositions, are jointed together at a surface ( $x = 0$ ), the initial concentration of a given species is  $c = c_1$  for  $x < 0$  and  $c = c_0$  for  $x > 0$  (**Fig. 1.2a**). After heated up, diffusive flux across the interface and tries to homogenize the couple (**Fig. 1.2b**). Therefore, the concentration of the given species is a function of two independent variables, duration and position,  $c = c(x, t)$  (**Fig. 1.2b**), which is one solution of **Eqs. 1.3**, as,

$$c(x, t) = \frac{c_1 + c_0}{2} - \frac{c_1 - c_0}{2} \operatorname{erf}\left(\frac{x}{\sqrt{4Dt}}\right) \quad (1.4)$$

where  $\operatorname{erf}(y)$  is the error function defined by

$$\operatorname{erf}(y) = \frac{2}{\sqrt{\pi}} \int_0^y \exp(-z^2) dz \quad (1.5)$$

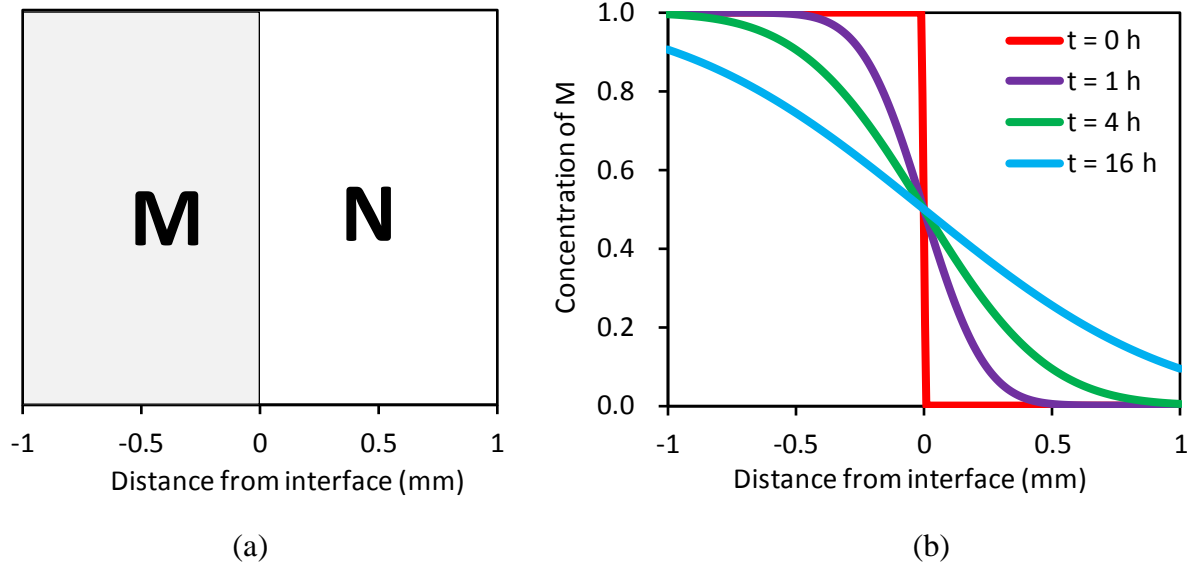


**Fig. 1.2.** (a) Material M and N contact with each other. (b) The material M diffuses into N, and N diffuses into M. The concentration of M in the object is a function of time and distance from the interface.

**Equation 1.4** indicates that the concentration profile  $c(x, t)$  controlled by diffusion is characterized by a non-dimensional parameter:  $\xi \equiv x/\sqrt{4Dt}$ , named diffusion depth.

### 1.1.2 Point defects in a crystal

Point defects are atomistic in nature defined as deviations from the perfect atomic arrangement: missing ions, substituted ions, interstitial ions, and their associated valence electrons, occur (to greater or smaller degrees) in all crystalline materials. They are defects those occur only at or around a single lattice point site and are not extended in space in any dimension. The point defects occur thermally in many materials including metal, ionic and molecular crystals [Chadwick and Terenzi, 1985].

#### (1) Vacancy defects

Vacancy defects are lattice sites in a crystal which should be occupied by a regular atom or ion, but actually are vacant (**Fig. 1.3**). The neighboring atoms or ions could jump into the vacant site and the vacancy moves in the opposite direction due to thermal vibration. A group of anion and cation vacancies (follow the stoichiometric ratio in order to preserve the electrical neutrality

of the crystal) is called a Schottky defect, which is caused when cations and anions move to the crystal surface and leave vacancies in their original sites [Chiang *et al.*, 1997].

## (2) *Interstitial defects*

Interstitial defects are atoms that occupy a site in the crystal structure at which no atom or ion usually occupies (Fig. 1.3). They are generally high energy configurations. A nearby pair of a vacancy and an interstitial is called a Frenkel defect. This is caused when an ion moves into an interstitial site forming a defect pair: a vacancy on the regular site and an interstitial defect. In ionic materials, both the cations and anions can undergo this kind of displacement [Chiang *et al.*, 1997].

## (3) *Substitutional defects*

Materials in the nature are never 100 % pure. Impurity atoms or ions are often incorporated into a crystal. This is neither a vacant site nor a regular atom on an interstitial site and it is called a substitutional defect (Fig. 1.3). The substitutional defects could locate in a regular atomic site or in an interstitial site.

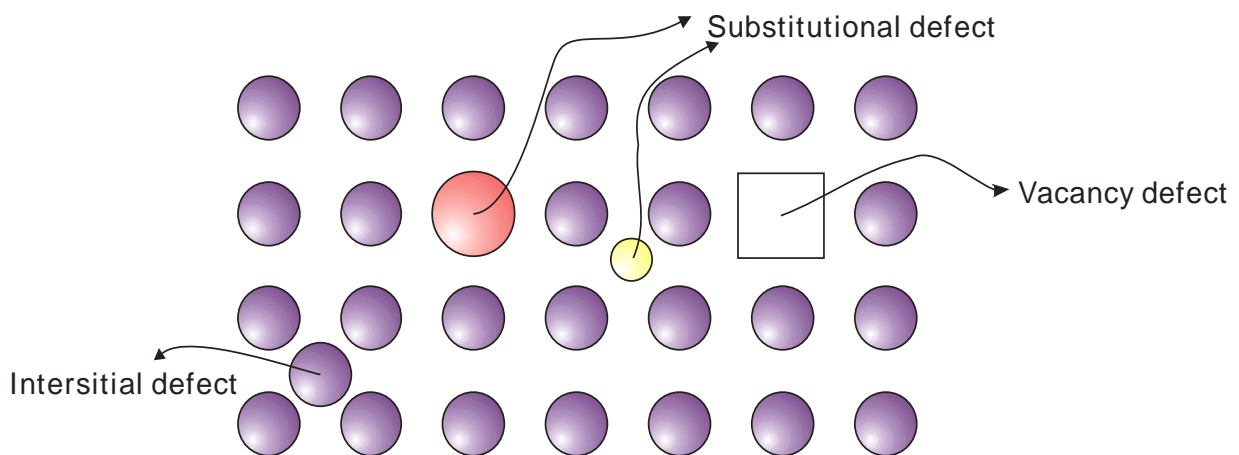


**Fig. 1.3.** Vacancy, interstitial, and substitutional defects in a crystal. Different colors of spheres indicate different types of atoms.

### 1.1.3 Diffusion mechanisms

There are several mechanisms that lead to atomic diffusions in a crystal. By far the most prominent is the vacancy mechanism and the interstitial mechanism.

### (1) Vacancy mechanism

In thermal equilibrium, any crystal at a given temperature above absolute zero contains a certain number of vacant lattice sites. These vacancies provide an easy path for diffusion. The elementary atom jump in a vacancy mechanism is the jump of an atom into a neighboring vacancy shown in **Fig. 1.4a**. The site of previously occupied by the atom then is vacant, so that in effect the atom and vacancy merely exchange positions. Each atom moves through the crystal by making a series of exchanges with the various vacancies which from time to time and in its vicinity [Manning, 1990; Borg and Dienes, 1988].

### (2) Interstitial mechanism

Interstitial mechanism is also called direct interstitial mechanism, in which an atom moves through the crystal by jumping directly from one interstitial site to another (**Fig. 1.4b**). This mechanism is particularly likely for diffusion of small impurity atoms, which easily fit into interstitial sites and do not greatly displace the solvent atoms from their normal lattice sites in jumping [Manning, 1990; Borg and Dienes, 1988].

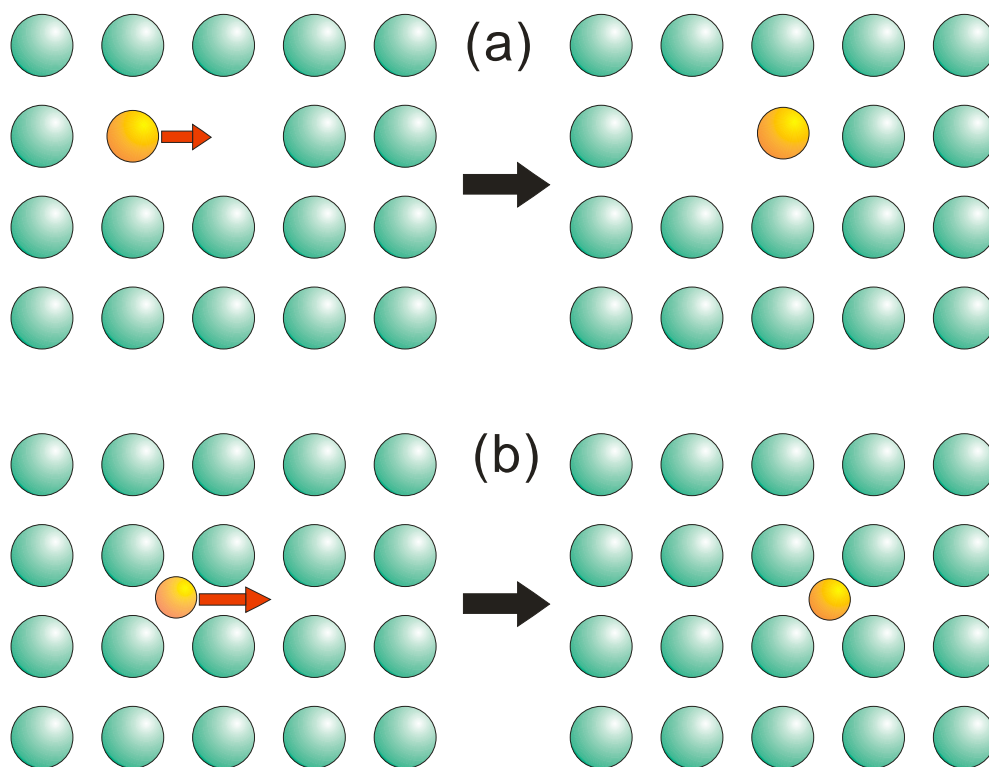


**Fig. 1.4.** Diffusion mechanisms. (a) Vacancy mechanism. (b) Interstitial mechanism.

#### 1.1.4 Atomic diffusion-coefficient in a crystal

Atoms are generally mobile due to thermal vibration. They are the vehicles that make the atoms of the crystal mobile and enhance the solid state diffusion. An atomic jump in a crystal to the next site occurs at an appreciable rate only when the neighboring site is vacant or only when the jump of an interstitial atom is considered. Thus, the jump frequency (probability) of an atom in a crystal is proportional to the probability of finding a defect multiplied by the probability of atomic jump when a defect is present. Therefore, the diffusion coefficient of species A ( $D_A$ ) is proportional the mobility and number of point defect on the A site, as the equation:

$$D_A = [V_A] \times D_V \quad (1.6)$$

where  $[V_A]$  includes all defect types on A sites and  $D_V$  is the diffusion rate of  $V_A$ , which reflects the mobility of  $V_A$ .

#### 1.1.5 Various types of diffusion

There are many types of diffusion in nature. Because diffusion involves a diffusing species in diffusion medium, it can be classified based on either the diffusion medium or the diffusing species. For example, when considering the diffusion medium, thermally activated diffusion can be classified as volume diffusion and grain boundary diffusion. When considering differences in diffusing species, the diffusion can be classified as self-diffusion, tracer diffusion, or chemical diffusion [Zhang and Cherniak, 2010].

##### *(1) Volume diffusion*

Volume diffusion (also called lattice diffusion) refers to atomic diffusion within a crystalline lattice. An example of volume diffusion is the diffusion of silicon and oxygen in olivine single crystal [Costa and Chakraborty, 2008]. The volume diffusion can be either isotropic or anisotropic depending on the diffusion medium. For example isotropic melts or glasses, the diffusion properties do not depend on direction [Zhang and Cherniak, 2010]. Non-isometric minerals are in general anisotropic media. For example, the oxygen diffusivity in quartz along  $c$ -axis is about two orders of magnitude greater than that along  $a$  or  $b$  axis [Giletti and Yund, 1984].

However, in some minerals like olivine, the dependence of diffusivities on the directions is weak though the lattice is anisotropic [*Costa and Chakraborty, 2008; Jaoul et al., 1981*].

## **(2) Grain-boundary diffusion**

Grain-boundary diffusion is a diffusion process along interphase interfaces, including mineral-fluid interfaces, boundaries of grains between the same minerals, and those between different minerals. Because the crystal structures on the interfaces are generally highly disordered, leading to very high concentrations of defects, the grain-boundary diffusion coefficients are usually much higher than volume diffusivities [*Zhang and Cherniak, 2010*]. For example in forsterite, wadsleyite aggregates, the silicon grain-boundary diffusion coefficient is about nine orders of magnitude higher than the volume diffusion coefficients [*Farver and Yund, 2000*].

## **(3) Self-diffusion**

Self-diffusion is a process happens in a system with difference in the isotopic ratio of the same element, but no chemical potential gradient in terms of elemental composition. Therefore, the external driving forces like gradient of chemical potential, electrical potential are equal to zero in a self-diffusion process. Atoms jump at random with no preferred directions, and each atom follows a random walk. The diffusion coefficient of an isotope of a given atomic species is often referred to as the self-diffusion coefficient of the atom. Because the isotopes of a given species (e.g.  $^{16}\text{O}$  and  $^{18}\text{O}$ ) have exactly the same electron distribution, their chemical bondings are identical. Consequently, when a gradient in the concentration of one isotope is present, the motion of the isotope through the matrix does not cause any changes in energy, and there is no interaction between isotopes [*Zhang and Cherniak, 2010; Karato, 2008*].

## **(4) Tracer diffusion**

If one the component has the concentration of at a trace level (e.g., from 1 to 10 wt. ppb) but with variable concentrations in different area, and the other components have uniform concentration, the diffusion process of that component is called tracer diffusion [*Zhang, 2008*], for example, the trace elements, Li, Be, V, Cr, and so on, diffusion in San Carlos olivine

[Spandler and O'Neill, 2010], and Ce, Sm, Dy, and Yb as trace elements diffusion in garnet [Van Orman *et al.*, 2002].

When the concentration levels of the diffusing species are higher (e.g., at the levels of ppm or higher), the process is referred to chemical diffusion. The trace element diffusivity is usually constant across the whole profile because the only variation along the profile is the concentration of the trace element that is not expected to affect the diffusion coefficient [Zhang, 2008]. Other general cases of chemical diffusion are referred to as inter-diffusion. For example, Fe-Mg diffusion between two crystals of different Mg/Fe ratios called Fe-Mg inter-diffusion [Dohmen *et al.*, 2007; Holzappel *et al.*, 2005]. In the inter-diffusion process, the diffusivity often varies across the profile because there are major concentration changes, and diffusivity usually depends on the major composition [Zhang, 2008].

### 1.1.6 Temperature and pressure dependences of diffusion coefficients

#### (1) Temperature dependence

The atomic jump process is referred to a thermally activated process and the rate of atomic jumps increases significantly with temperature. Therefore, the diffusion coefficient,  $D$ , depends strongly on temperature. Since the diffusion coefficient is a function of the concentration of point defects (**Section 1.1.4**), the temperature dependence of diffusion coefficient can be understood by the concentration of defects various with temperature in the view of statistical thermodynamics [Schmalzried, 1995].

In the view of thermodynamics, at a given temperature,  $T$  ( $T > 0$  K), the Gibbs free energy,  $G$ , of a crystal,  $G(T)$ , is,

$$G(T) = G^0(T) + N_V \Delta E_f - T \Delta S_{\text{conf}} \quad (1.7)$$

where  $G_0(T)$  is the Gibbs free energy of a perfect crystal at temperature  $T$ ,  $\Delta E_f$  is the energy required to form a single defect,  $N_V$  is the number of defects, and  $\Delta S_{\text{conf}}$  is configuration of the crystal entropy [Borg and Dienes, 1988; Schmalzried, 1995].

The configuration entropy of the defects in the lattice is,

$$\Delta S_{\text{conf}} = k \ln \Omega = k \ln \frac{N!}{N_V!(N-N_V)!} \approx -k N_V \ln \frac{N_V}{N} \quad (1.8)$$

where  $k$  is the Boltzmann constant,  $N$  is the total number of site, and  $\Omega$  is the number of possible configurations related to the total number of possible random distributions of the  $N_V$  defects in  $N$  sites [*Chiang et al.*, 1997; *Borg and Dienes*, 1988; *Schmalzried*, 1995].

Under the equilibrium condition, the  $N_V$  and  $G(T)$  are constant. Therefore,

$$\frac{\partial G(T)}{\partial (N_V)} = \frac{\partial G^0(T)}{\partial (N_V)} + \frac{\partial N_V \Delta E_f}{\partial (N_V)} + \frac{\partial k T N_V \ln \frac{N_V}{N}}{\partial (N_V)} = 0 \quad (1.9)$$

From **Eqs. 1.8** and **1.9**, we obtain [*Borg and Dienes*, 1988; *Schmalzried*, 1995],

$$N_V = A_0 N \exp\left(-\frac{\Delta E_f}{kT}\right) \quad C_V = \frac{N_V}{N} = A_0 \exp\left(-\frac{\Delta E_f}{kT}\right) \quad (1.10)$$

where  $A_0$  is a constant and  $C_V$  is the concentration of defects. **Eqs. 1.10** is also called Arrhenius relationship. If convert the Boltzmann constant to ideal gas constant,  $R$ , and  $\Delta E_f$  to the energy required to form 1 mol of defects,  $\Delta E_{\text{mol}}$ , **Eqs. 1.10** becomes [*Borg and Dienes*, 1988; *Schmalzried*, 1995],

$$\frac{N_V}{N} = A_0 \exp\left(-\frac{\Delta E_{\text{mol}}}{RT}\right) \quad (1.11)$$

Therefore, the concentration of defects is a function of temperature linearly proportional to  $\exp(-\Delta E_{\text{mol}}/RT)$ .

On the other hand, not only the defects but also the diffusion species are thermally activated, which give additional activation energy ( $\Delta E_i$ ) for the exchange between regular ions and defects. As a result, the diffusion coefficient follows the Arrhenius equation,

$$D = D_0 \exp\left(-\frac{\Delta E_{\text{mol}} + \Delta E_i}{RT}\right) = D_0 \exp\left(-\frac{\Delta E}{RT}\right) \quad (1.12)$$

where  $D_0$  is the pre-exponential factor.  $\Delta E$  is so called activation energy here. **Equation 1.12** implies a linear relationship of  $\ln D$  versus inverse temperature and the slope of the linear

relationship gives the activation energy. The Arrhenius relationship for diffusion is also confirmed experimentally in a series diffusion studies (e.g., diffusion in minerals reviewed in Zhang and Cherniak, [2010]).

In above discussion, we assume that the diffusion is controlled by thermally activated intrinsic vacancies or interstitials (so called intrinsic diffusion) whose concentrations increase with increasing temperature following the Arrhenius relationship (**Eqs. 1.10**) and therefore the diffusion coefficient also follows the Arrhenius equation (**Eqs. 1.12**). The other case is extrinsic diffusion, in which the defect concentrations are controlled by impurities, for example, ferric iron occupy the magnesium site in olivine and controls the concentration of magnesium defects. In this case, the temperature dependence of the magnesium defects concentration does not follow the Arrhenius form. When the temperature increases, the concentration of defects remains the same because the concentration of substitutional defects does not change with temperature. Therefore, the diffusion rate increases with increasing temperature following the Arrhenius equation  $D = D_0 \exp(-\Delta E/RT)$  where  $\Delta E = \Delta E_i$  only because of the enhanced thermal motion (the mobility of defects and diffusion species). Since the activation energy for extrinsic diffusion ( $\Delta E_i$ ) is smaller than that for intrinsic diffusion ( $\Delta E_{mol} + \Delta E_i$  as shown in **Eqs.1.12**), the temperature dependence for extrinsic diffusion is usually weaker than that for intrinsic diffusion [Chakraborty 1997].

## (2) *Pressure dependence*

In **Eqs. 1.12**, we only considered the temperature dependence of the equilibrium state. In the view of thermodynamics, pressure could also affect the equilibrium state by influence on the Gibbs free energy and therefore affect the concentration of defects, sequentially affect the diffusion coefficients. From first and second law of thermodynamics, we have,

$$\Delta G = \Delta H - T\Delta S, \Delta H = \Delta E + P\Delta V \quad (1.13)$$

Namely,

$$\Delta V = \left( \frac{\partial \Delta G}{\partial P} \right)_T \quad (1.14)$$

where  $\Delta H$  is the activation enthalpy,  $\Delta E$  is the activation energy,  $\Delta V$  is the activation volume. Therefore The diffusion coefficient at variable pressure  $P$  and temperature  $T$ ,  $D(P, T)$ , is then given by:

$$D(P, T) = D_0 \exp\left(\frac{-\Delta G}{RT}\right) \quad (1.15)$$

$$D(P, T) = \left[ D_0 \exp\left(-\frac{\Delta S}{R}\right) \right] \exp\left(-\frac{\Delta E + P\Delta V}{RT}\right) = D'_0 \exp\left(-\frac{\Delta E + P\Delta V}{RT}\right) \quad (1.16)$$

**Equation 1.16** indicates that, at a given temperature condition,  $\ln D$  is proportional to pressure with either positive or negative dependence and the slope gives the activation volume. The effect of pressure on atomic diffusion coefficient is small compare to the temperature dependency, but could become significant under the enormous pressure conditions as that in the Earth's interior.

## 1.2 Mineralogical model of the Earth's mantle

The widely accepted mineralogical model in the earth mantle is given by Ringwood [1962]. In the Earth's upper mantle, i.e. from 0 to ~410 km depth, olivine, garnet, and pyroxenes (OPX and CPX, i.e., orthopyroxene and clinopyroxene, respectively) are the dominant phases. Olivine is the main upper mantle constituent, which contributes ~60 % in volume. The volume fraction of garnet increases with increasing depth, while those for both OPX and CPX decrease with increasing depth (**Fig. 1.5**).

At the 410-km depth seismic discontinuity, with a pressure of ~14 GPa, and temperature of ~1800 K, the  $(\text{Mg,Fe})_2\text{SiO}_4$  olivine transits to its  $\beta$  phase, i.e. wadsleyite, furthermore, to  $\gamma$  phase (ringwoodite) at 520 km depth (~17.5 GPa, 1900 K). The wadsleyite and ringwoodite, with ~40 % of garnet, constitute the mantle transition zone (410-670 km depth) (**Fig. 1.5**). In the lower mantle with depth >670 km,  $(\text{Mg,Fe})\text{SiO}_3$  perovskite and  $(\text{Mg,Fe})\text{O}$  ferropericlaase are stable and constitute the main part of low mantle.

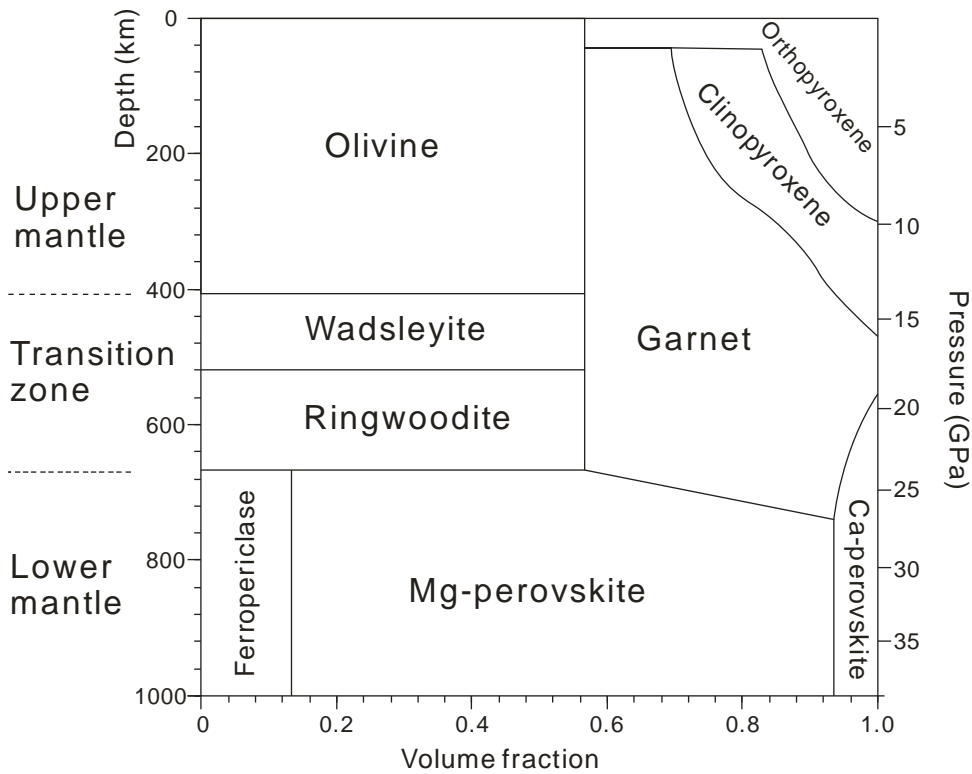


**Fig. 1.5.** Mineralogical model of the Earth's mantle (modified from Shekhar [2012]).

### 1.3 General information about olivine/forsterite

Olivine, which is the major mineral in upper mantle with a chemical formula of  $(\text{Mg,Fe})_2\text{SiO}_4$ , is usually considered as the weakest phase [Durham and Goetze, 1977a; Kohlstedt and Goetze, 1974; Mackwell, 1991] and therefore it dominates the plastic flow in upper mantle [Karato and Wu, 1993]. The Mg and Fe rich end member of olivine are forsterite ( $\text{Mg}_2\text{SiO}_4$ ) and fayalite ( $\text{Fe}_2\text{SiO}_4$ ), respectively. The natural olivine usually contains ~10 % of fayalite constituent, namely,  $(\text{Mg}_{0.9}\text{Fe}_{0.1})_2\text{SiO}_4$ .

#### 1.3.1 Crystal structure

Because iron-bearing olivine has the same crystal structure as forsterite, here we use forsterite as an example. The ideal forsterite crystal structure comprises a hexagonal-close-packed arrangement of O ions (**Fig. 1.6**), with M(1) (has  $\bar{1}$  symmetry) and M(2) (has mirror symmetry) metal cations in the octahedral interstices, and Si in the tetrahedral interstices (**Fig. 1.7**). The Mg-O distances in M(1) and M(2) octahedrons are ~2.16 and 2.19 Å, and are cross-

linked by edge-shared  $\text{SiO}_4$  tetrahedrons. The cell parameters at ambient pressure and room temperature are determined to be  $a = 4.7535$ ,  $b = 10.1943$ ,  $c = 5.9807 \text{ \AA}$ , and unit cell volume of  $289.80 \text{ \AA}^3$  [Hazen, 1976].

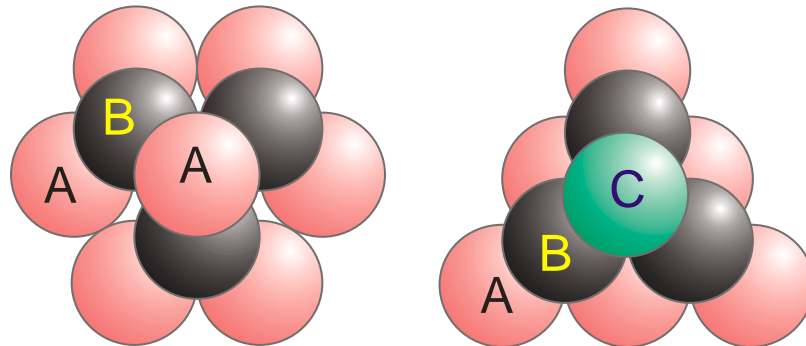


**Fig. 1.6.** hexagonal-close-packed (HCP) and face-center-cubic (FCC) structures. Spherical atoms in the crystal are close packed in layers. The A and B layers (first and second layers, respectively) are packed as shown in the figure. The HCP and FCC structures are formed by stacking the third layer. In a HCP structure (left), the atoms in the third layer are directly above those in the first layer and the lattice is formed by stacking of ABABAB..... This is different from FCC structure (right), in which atoms in the third layer (C layer) are not directly over atoms in either the A or B layer and the lattice is formed by stacking of ABCABCABC.....

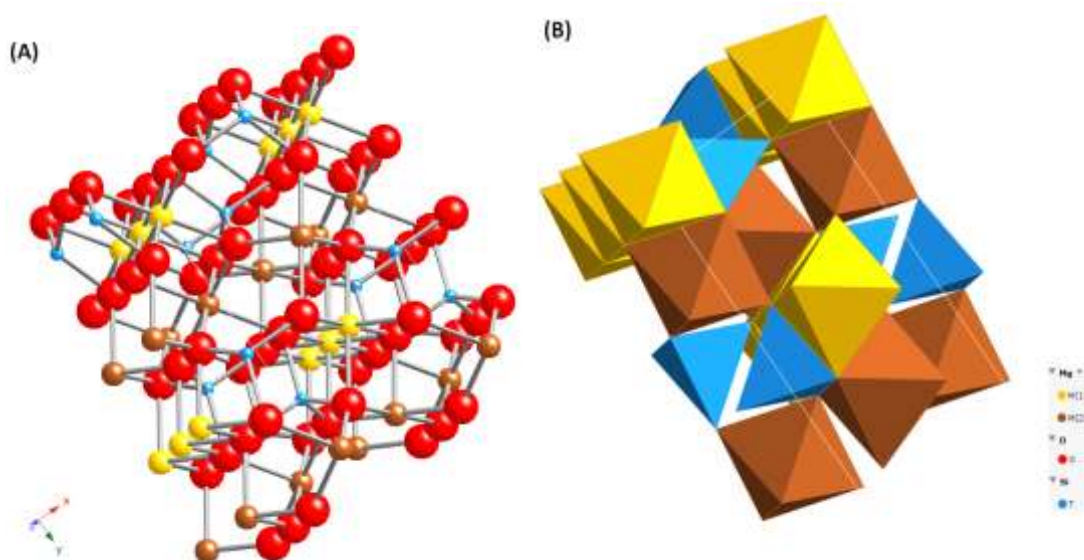
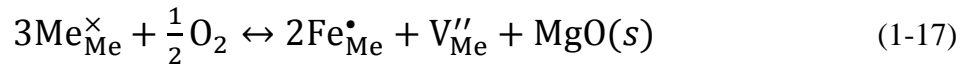


**Fig. 1.7.** Crystal structure of ideal forsterite. (a) Ball-stick model. (b) Polyhedral model. The polyhedral representation consists of kinked chains of M(1) and M(2) octahedral, cross-linked by edge-shared  $\text{SiO}_4$  tetrahedral.

Nature olivine in the Earth's interior contains ~10 % of fayalite constituent, iron ions occupy both M(1) and M(2) sites in a ferrous state, which induces the same crystal structure of forsterite and iron-bearing olivine.

### 1.3.2 Defect chemistry in olivine

As discussed in **1.3.1**, the structure elements in olivine crystal are Me (Mg or Fe metal ions), Si, and O. Thus, the major species, vacancy defects, and interstitial defects are  $\text{Me}_{\text{Me}}^{\times}$ ,  $\text{Si}_{\text{Si}}^{\times}$ ,  $\text{O}_{\text{O}}^{\times}$ ;  $\text{V}_{\text{Me}}^{\prime\prime}$ ,  $\text{V}_{\text{Si}}^{\prime\prime\prime}$ ,  $\text{V}_{\text{O}}^{\prime\prime}$ ; and  $\text{Me}_i^{\bullet}$ ,  $\text{Si}_i^{\bullet\bullet}$ ,  $\text{O}_i^{\prime\prime}$ ; respectively (Kröger-Vink [1956] notation is used in this thesis for defect chemistry, see **Appendix I**). Besides, small variable amount of ferric iron can exist in olivine as point defects ( $\text{Fe}_{\text{Me}}^{\bullet}$ ) under relatively oxidizing conditions due to the reaction:



In addition, water could also change the charge the charge neutrality conditions in olivine by incorporation of hydroxyl as defects (**Section 1.3.3**). Therefore, the defect chemistry should be considered under anhydrous and hydrous conditions, separately.

#### (1) Anhydrous condition

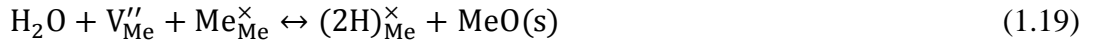
Though  $[\text{Fe}_{\text{Me}}^{\bullet}]$  is very small in natural olivine ( $[\text{Fe}_{\text{Me}}^{\bullet}]/[\text{Me}_{\text{Me}}^{\times}]$  is at the level of  $10^{-5}$ - $10^{-6}$ ) as point defects [Karato, 2008], it is still the major positive charged defect species under anhydrous conditions based on a series of thermogravimetry, diffusion, and electrical conductivity measurements. On the other hand, the Mg-Fe diffusion coefficient,  $D_{\text{Me}}$ , is almost five orders of magnitude larger than silicon diffusion coefficient,  $D_{\text{Si}}$ , [Costa and Chakraborty, 2008; Dohmen *et al.*, 2002; Dohmen *et al.*, 2007; Dohmen and Chakraborty, 2007]. Since the diffusivities of metal vacancies and silicon vacancies are of the same order of magnitude [Mackwell *et al.*, 1988; Wanamaker, 1994], the relation  $[\text{V}_{\text{Me}}^{\prime\prime}] \gg [\text{V}_{\text{Si}}^{\prime\prime\prime}]$  must hold because  $D_{\text{A}} = [\text{V}_{\text{A}}] \times D_{\text{V}}$ . Therefore, the major negative charged defect in dry olivine is  $\text{V}_{\text{Me}}^{\prime\prime}$ , and the charge neutrality condition is generally taken to be:  $[\text{Fe}_{\text{Me}}^{\bullet}] = 2[\text{V}_{\text{Me}}^{\prime\prime}]$  in dry olivine [Kohlstedt and Mackwell, 1998; Kohlstedt, 2006].

## (2) Hydrous condition

Water could change the charge neutrality conditions in olivine by H<sup>+</sup> entering the crystal structure and forming OH bond. There are mainly four possible types of hydroxyl in olivine:

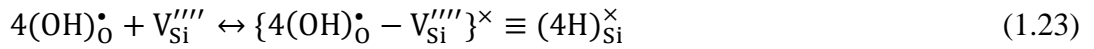
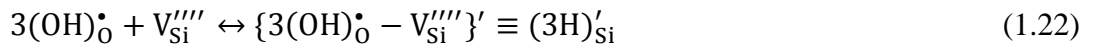
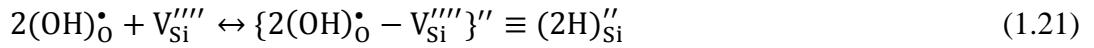
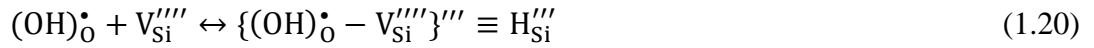
(i). One or two protons at Me-site vacancies and oxygen at O-site (**Fig. 1.8a**).

- i.e., ((OH)<sub>O</sub><sup>•</sup>-V<sub>Me</sub><sup>''</sup>)' and ((OH)<sub>O</sub><sup>•</sup>-V<sub>Me</sub><sup>''</sup>-((OH)<sub>O</sub><sup>•</sup>)<sup>×</sup>, which are simplified as H<sub>Me</sub>' and (2H)<sub>Me</sub><sup>×</sup>, formed by the reactions:



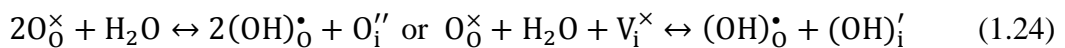
(ii). Up to four protons at Si-site vacancies and oxygen at O-site (**Fig. 1.8b**).

- i.e., ((OH)<sub>O</sub><sup>•</sup>-V<sub>Si</sub><sup>''''</sup>)''', (2(OH)<sub>O</sub><sup>•</sup>-V<sub>Si</sub><sup>''''</sup>)'', (3(OH)<sub>O</sub><sup>•</sup>-V<sub>Si</sub><sup>''''</sup>)', and (4(OH)<sub>O</sub><sup>•</sup>-V<sub>Si</sub><sup>''''</sup>)<sup>×</sup>, which are simplified as H<sub>Si</sub>''', (2H)<sub>Si</sub>'', (3H)<sub>Si</sub>', and (4H)<sub>Si</sub><sup>×</sup>, formed by the reactions:



(iii). Proton at interstitial and oxygen at O site (**Fig. 1.8c**).

- i.e., (OH)<sub>O</sub><sup>•</sup>, formed by the reaction:



(iv). Proton at interstitial site and O at interstitial site (**Fig. 1.8d**).

- i.e., (OH)<sub>i</sub><sup>•</sup>, formed by the reaction:

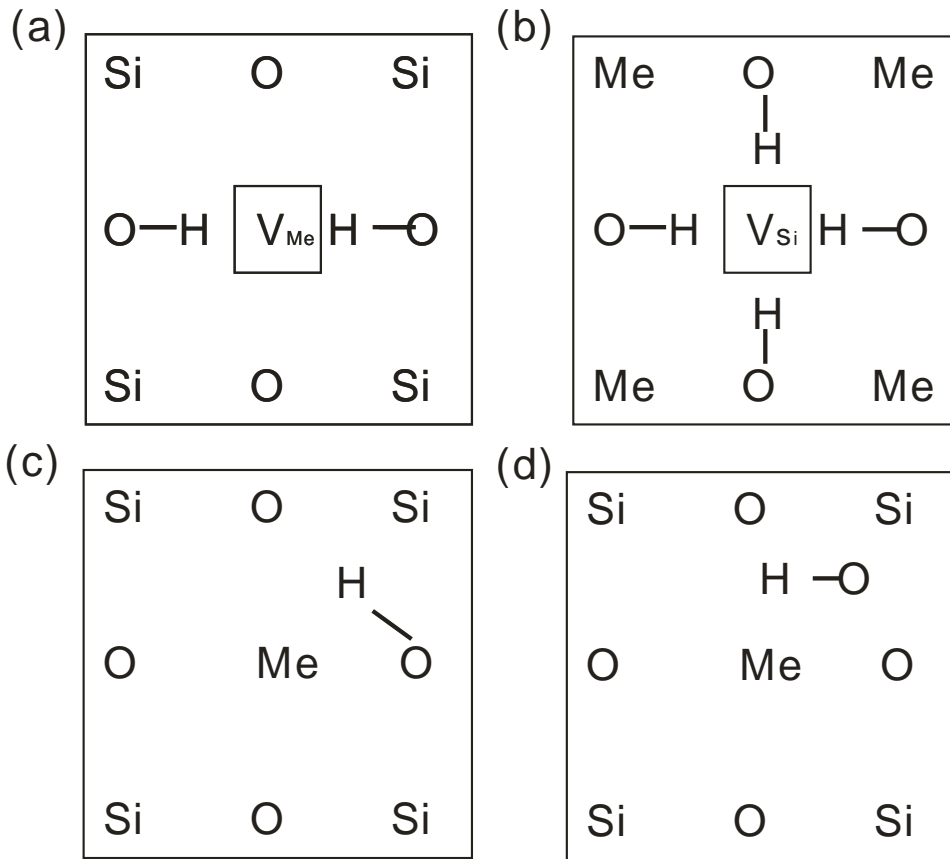


**Fig. 1.8.** Hydroxyl in olivine (Modified from Karato [2008]). **(a)**  $H^+$  on  $V_{Mg}''$  site. **(b)**  $H^+$  on  $V_{Si}''''$ . **(c)**  $H^+$  on interstitial site. **(d)**  $H^+$  and  $O^{2-}$  on interstitial site.

Formation of an Mg vacancy,  $V_{Mg}''$ , requires less energy than a Si vacancy,  $V_{Si}''''$  [Brodholt and Refson, 2000]. Besides, the concentration of  $V_{Mg}''$  is much higher than that of  $V_{Si}''''$ ;  $[V_{Mg}''] \gg [V_{Si}'''']$  in olivine [Kohlstedt, 2006]. Therefore, most of  $H^+$  should be incorporated with  $V_{Mg}''$  and form  $H_{Me}'$  or  $(2H)_{Me}^{\times}$  [Kohlstedt et al., 1996] under hydrous conditions. This idea is supported by the experimental results of the linear relationship between water solubility and fugacity,  $C_{OH} \propto f_{H_2O}$  [Kohlstedt et al., 1996; Zhao et al., 2004]. Because  $[(2H)_{Me}^{\times}] \propto f_{H_2O}$  [Kohlstedt, 2006], we have  $C_{OH} \propto [(2H)_{Me}^{\times}]$ .

As discussed above, the charge neutrality condition is generally taken to be:  $[Fe_{Me}^{\bullet}] = 2[V_{Mg}'']$  in dry olivine. With increasing water content, namely, with increasing  $[(OH)_0^{\bullet}]$ , there are two possible charge neutrality conditions: (a) if  $[Fe_{Me}^{\bullet}]$  is relatively high, namely, under relatively oxidizing condition,  $[H_{Me}']$  becomes higher than  $[V_{Mg}'']$  and the major negatively

charged species would be  $[H_{Me}']$ . In this case, the charge neutrality conditions would change to  $[Fe_{Me}'] = [H_{Me}']$ ; (b) if  $[Fe_{Me}']$  is relatively low, namely, under reducing conditions,  $[(OH)']$  is higher than  $[Fe_{Me}']$  due to the increasing of water content and becomes the major positively charged defect species. Therefore, the charge neutrality condition would be  $[(OH)_O'] = 2[V_{Me}']$ .

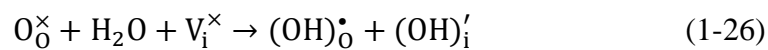
Under the charge neutrality conditions of  $[(OH)_O'] = 2[V_{Me}']$ ,  $[Fe_{Me}']$  decreases with increasing water content (**Table 1.1**). In the case of  $[Fe_{Me}'] = [H_{Me}']$ ,  $[Fe_{Me}']$  increases with increasing water content at an exponent of 1/4, meanwhile  $[(OH)_O']$  has a water content exponent of 3/4. Therefore, under both  $[(OH)_O'] = 2[V_{Me}']$  and  $[Fe_{Me}'] = [H_{Me}']$  neutrality conditions,  $[(OH)_O']$  could be higher than  $[Fe_{Me}']$  if water content is high enough. As a result, the charge neutrality condition would be replaced by  $[(OH)_O'] = [H_{Me}']$  with sufficiently high water content.

If water content is extremely high in the olivine crystal structure,  $H^+$  would also occupy silicon sites and form  $H_{Si}'$ ,  $(2H)_{Si}''$ ,  $(3H)_{Si}'$ , or  $(4H)_{Si}^\times$ . In that case, the charge neutrality condition would be  $[(OH)_O'] = 3[H_{Si}''']$ ,  $[(OH)_O'] = 2[(2H)_{Si}''']$ , or  $[(OH)_O'] = [(3H)_{Si}']$ .

In summary, the charge neutrality conditions in dry olivine is  $[Fe_{Me}'] = 2[V_{Me}']$ . With increasing water content, it is replaced by either  $[(OH)_O'] = 2[V_{Me}']$  under relatively reducing conditions, or  $[Fe_{Me}'] = [H_{Me}']$  under relatively oxidizing conditions. Then change to  $[(OH)_O'] = [H_{Me}']$ ,  $[(OH)_O'] = 3[H_{Si}''']$ ,  $[(OH)_O'] = 2[(2H)_{Si}''']$ , or  $[(OH)_O'] = [(3H)_{Si}']$  if water content is sufficiently high.

Under different charge neutrality conditions, each species in the crystal varies with water content with different relationships. The water content dependencies of defect concentrations under each four charge neutrality conditions are summarized in **Table 1.1**.

In addition, the interstitial defect  $(OH)_i'$  may also be an important site for the incorporation of  $OH^-$  into the olivine structure based on measurements of the  $OH^-$  solubility in olivine as a function of water fugacity [Bai and Kohlstedt, 1992; 1993] through the reaction:



In this case, the charge neutrality conditions could be  $[(OH)_O^\bullet] = [(OH)_i']$  for hydrous olivine if water content is extremely high [Kohlstedt et al., 1996].

**Table 1.1.** Water content exponents of defect concentrations for each charge neutrality conditions, expressed as the exponent  $r$  in the relationship  $[x] \propto (C_{H_2O})^r$ . Data in the table were derived by a series of reactions between different species described in Kohlstedt [2006] and the derivations are described in detail in **Appendix II**.

Charge neutrality	$Fe_{Me}^{\bullet}$	$V_{Me}^{\prime\prime}$	$H_{Me}^{\prime}$	$(2H)_{Me}^{\times}$	$(OH)_O^{\bullet}$	$V_O^{\prime\prime}$	$V_{Si}^{\prime\prime\prime}$	$H_{Si}^{\prime\prime\prime}$	$(2H)_{Si}^{\prime\prime}$	$(3H)_{Si}^{\prime}$	$(4H)_{Si}^{\times}$
$[Fe_{Me}^{\bullet}] = 2[V_{Me}^{\prime\prime}]$	0	0	1/2	1	1/2	0	0	1/2	1	3/2	2
$[(OH)_O^{\bullet}] = 2[V_{Me}^{\prime\prime}]$	-1/6	1/3	2/3	1	1/3	-1/3	2/3	1	4/3	5/3	2
$[Fe_{Me}^{\bullet}] = [H_{Me}^{\prime}]$	1/4	-1/2	1/4	1	3/4	1/2	-1	-1/4	1/2	5/4	2
$[(OH)_O^{\bullet}] = [H_{Me}^{\prime}]$	0	0	1/2	1	1/2	0	0	1/2	1	3/2	2

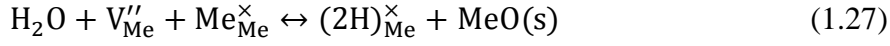
### 1.3.3 Water in olivine

Water has been considered to have large effect on the processes that occur in the Earth's interior through affecting the physical properties of rocks and minerals, e.g., electrical conductivity [Karato, 1990; Manthilake et al., 2009; Wang et al., 2006; Wang et al., 2008; Yoshino et al., 2008; Yoshino et al., 2009], elastic properties [Inoue et al., 1998; Jacobsen et al., 2008; Mao et al., 2008; Wang et al., 2006], atomic diffusivity [Costa and Chakraborty, 2008; Demouchy et al., 2005; Hier-Majumder et al., 2005; Shimojuku et al., 2010; Wang et al., 2004], and plastic deformation. Olivine, which is considered as nominally anhydrous minerals, can contain small amount of water (at the level of  $10^2$ - $10^3$  wt. ppm under upper mantle conditions structurally bound as hydroxyl [Bell and Rossman, 1992]), and acts as water reservoir of Earth's upper mantle. Therefore, it is important to understand the water behavior in olivine.

#### (1) Water solubility in olivine

Kohlstedt et al. [1996] measured the water solubility in natural olivine at 1373 K and found that the water solubility significantly increases with increasing pressure approximately with a linear relationship (**Fig. 1.9**).

In the view of defect chemistry and thermodynamics, most of hydrogen incorporates into olivine structure by the reaction,



and the water solubility is,

$$C_{\text{OH}} \approx [(2\text{H})_{\text{Me}}^{\times}] = f_{\text{H}_2\text{O}} \frac{a_{\text{MeO}}}{[\text{V}_{\text{Me}}'']} K \quad (1.28)$$

where  $f_{\text{H}_2\text{O}}$  is the water partial pressure,  $a_{\text{MeO}}$  is the MeO activity, and  $K$  is the equilibrium constant [Bali *et al.*, 2008; Zhao *et al.*, 2004]. Since  $f_{\text{H}_2\text{O}}$  linearly increases with increasing confining pressure, the water solubility in olivine increases with pressure as shown in **Fig. 1.9** determined by Kohlstedt *et al.* [1996].

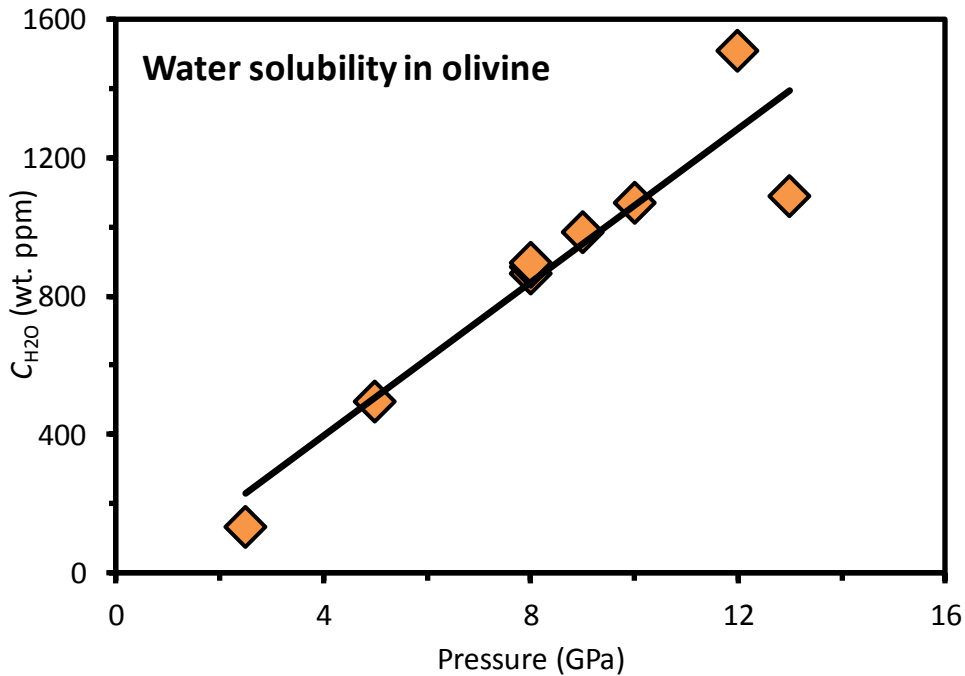


**Fig. 1.9.** Water solubility in olivine at 1373 K determined by Kohlstedt *et al.* [1996]. It linearly increases with increasing pressure from 2.5 up to 13 GPa.

Smyth *et al.* [2006] investigated the temperature dependence of water solubility in iron-free forsterite at 12 GPa, and found that the water solubility increases with increasing temperature at below 1250 °C, and decreases at higher temperature. The maximum  $C_{\text{H}_2\text{O}}$  determined at 1250 °C is determined to be ~ 8900 wt. ppm (**Fig. 1.10**). This value is significantly higher than that measured in natural olivine by Kohlstedt *et al.* [1996]. Because the  $\text{SiO}_2$  activity could affect the concentration of Si and Mg vacancies which relate to the incorporations of hydrogen in the

crystal structure, Smyth et al. [2006] also compared the water solubility between Si excess and Mg excess samples. However, no significantly difference was found.

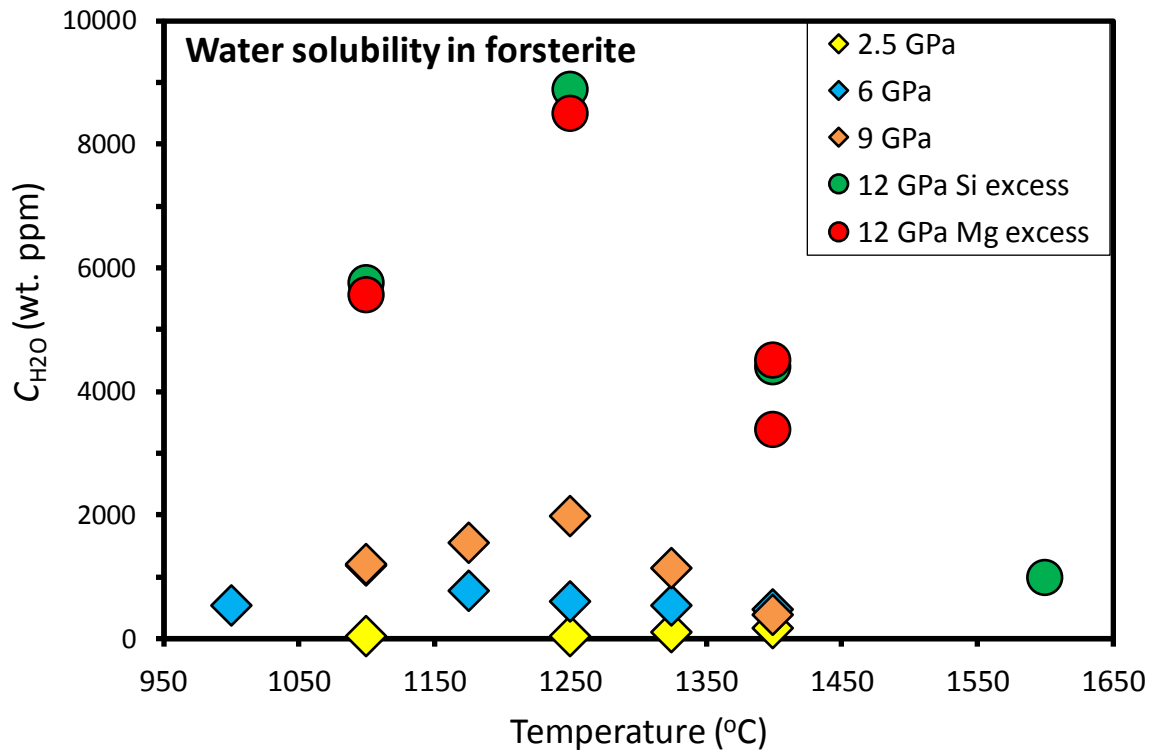


**Fig. 1.10.** Water solubility in pure forsterite. The data points at 12 GPa are taken from Smyth et al. [2006], and those at 2.5, 6, and 9 GPa are from Bali et al. [2008].

Bali et al. [2008] measured the pressure and temperature dependence of water solubility in forsterite at 2.5, 6, and 9 GPa. They found the maximum water content (~2000 wt. ppm at 9 GPa) at ~1250 °C, and that it increases with increasing pressure (**Fig. 1.10**). This value is lower than that determined at 12 GPa by Smyth et al. [2006] by factor ~4.5, and higher than that by Kohlstedt et al. [1996] by factor two. The difference of water solubility determined in these studies could be the different calibrations to calculate the water content from infrared spectrum (See next section), the uncertainty in calculating water content, the different experimental conditions, the difference in iron concentration, and so on.

## (2) Infrared spectroscopy of olivine

Fourier transform infrared (FTIR) spectroscopy is the most sensitive and convenient technique to determine the water in rocks and minerals. It could not only quantify the water

content, but also specify the site information of hydroxyl [Bell *et al.*, 2003] by determining the –OH absorptions in the crystal structure.

### a. Infrared spectrum

**Figure 1.11** shows a typical infrared spectrum measured in an iron-free forsterite single crystal. There are mainly two groups of –OH absorptions: (1) group II located at wavenumber of  $\sim 3500\text{--}3600\text{ cm}^{-1}$ , with the major –OH peaks are at 3612, 3571, 3565, 3540, 3531, 3471  $\text{cm}^{-1}$ ; (2) group I at wavenumber of  $\sim 3150\text{--}3250\text{ cm}^{-1}$  with the major –OH peaks at 3150  $\text{cm}^{-1}$ . Based on first principle calculation, it is usually considered that the group II absorptions are due to the H incorporating into silicon vacancies, whereas group I absorptions are due to that incorporating into metal vacancies [Balan *et al.*, 2011; Baxter, 2010]. However, this idea is not supported by experimental results which suggest a linear relationship between water solubility and fugacity [Kohlstedt *et al.*, 1996; Zhao *et al.*, 2004], indicating that a defect formed from two  $\text{H}^+$  ions associated with a Mg vacancy as the dominant defect facilitating hydrogen incorporation in olivine. Besides, in contrast with Smyth *et al.* [2006], Kohlstedt [2012] found that the hydrogen solubility increases with increasing silica activity, which further supports that most of hydrogen in olivine should be incorporated with metal vacancies.

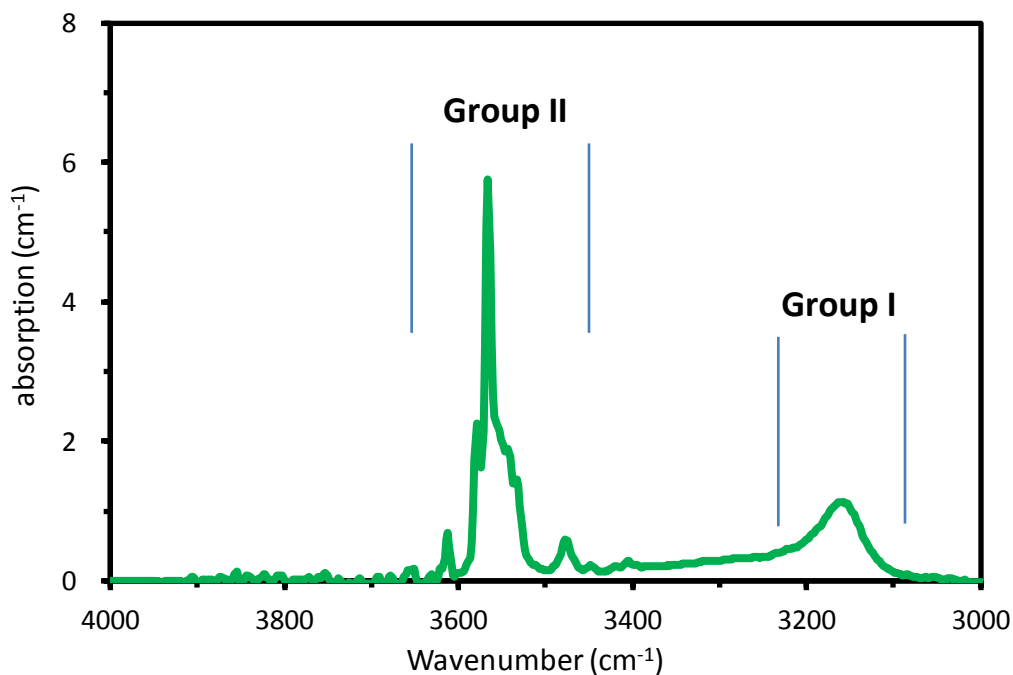


**Fig. 1.11.** A typical infrared spectrum measured in a forsterite single crystal.

## b. Infrared calibrations

Using the absolute values of hydrogen content measured by ion probe, a number of calibrations have been reported to determine the water content from infrared spectrum (e.g., [Aubaud *et al.*, 2005; Aubaud *et al.*, 2007; Aubaud *et al.*, 2009; Bell *et al.*, 2003; Koch-Muller and Rhede, 2010; Libowitzky and Rossman, 1997; Paterson, 1982]).

*Paterson's* [1982] *calibration*: Paterson's calibration is commonly used to determine the water content in olivine from un-polarized infrared spectrum. The general equation is,

$$C_{OH} = \frac{B_i}{150\zeta} \int \frac{H(\nu)}{3780-\nu} d\nu \quad (1.29)$$

where  $C_{OH}$  is the concentration of hydroxyl in wt. ppm,  $\zeta$  is an orientation factor ( $\zeta = 1/2$  for spectra obtained from randomly oriented grains), and  $H(\nu)$  is the absorption coefficient at wavenumber  $\nu$  in  $\text{cm}^{-1}$ , and  $B_i$  is the volume of unit cell ( $B_i \approx 2790$  wt. ppm). The integration is usually performed from 2950-3780  $\text{cm}^{-1}$ .

*Bell et al.'s* [2003] *calibration*: Based on the Beer-Lambert Law,  $A_\nu = C_{H_2O} d \epsilon$ , where  $A_\nu$  ( $\text{cm}^{-1}$ ) is the infrared absorption at wavenumber of  $\nu$ ,  $C_{H_2O}$  is the water concentration (mol/L),  $\epsilon$  is the molar absorption coefficient with a unit of  $\text{L}/(\text{mol}\cdot\text{cm}^3)$ , and  $d$  is the thickness of the sample. Therefore,  $C_{H_2O}$  (mol/L) =  $A_\nu/(\epsilon d)$ . Namely,  $C_{H_2O}$  (wt. ppm) =  $k A_\nu$  where  $k$  is a constant related to the density of mineral and absorption coefficient and  $A_\nu$  is the absorption area corrected to a certain thickness (1 cm). By comparing the value of  $A_\nu$  determined from polarized infrared spectrum and  $C_{H_2O}$  from  $^{15}\text{N}$  nuclear reaction analysis, Bell *et al.* [2003] found a value of  $k \approx 0.188$ . Therefore,  $C_{H_2O}$  (wt. ppm) =  $0.188 A_\nu$ . The total  $C_{H_2O}$  in the crystal is the integration of  $0.188 A_\nu$ , namely,

$$C_{H_2O} = \int 0.188 A_\nu d\nu \quad (1.30)$$

The integration is usually performed from wavenumber 3000 to 4000  $\text{cm}^{-1}$ .

By comparing the  $C_{H_2O}$  values obtained using Paterson's calibration [Paterson, 1982], Bell *et al.* [2003] suggested that Paterson's calibration [Paterson, 1982] have underestimated the water content by a factor of  $\sim 3.5$ .

*Thomas et al.*'s [2009] calibration: Similar calibrations as Bell et al. [2003] have also been reported for olivine infrared calibration [Aubaud et al., 2007; Thomas et al., 2009]. For example in Thomas et al. [2009], the water content is expressed as,

$$C_{\text{H}_2\text{O}} = \int \frac{M_{\text{H}_2\text{O}} A_{\nu}}{\rho \epsilon d} d\nu \quad (1.31)$$

where  $M_{\text{H}_2\text{O}}$  is the molecular weight of water (18.02 g/mol) and the absorption coefficient  $\epsilon$  is experimentally determined ( $\sim 28000\text{-}38000 \text{ L mol}^{-1}\text{cm}^{-2}$ , [Thomas et al., 2009]).

### (3) Water content in olivine in the Earth's upper mantle

Water in the depleted mantle is estimated to be  $\sim 70\text{-}160$  wt. ppm [Workman and Hart, 2005], and 4-5 times higher in enriched mantle [Hirschmann, 2006]. These values are much lower than the water solubility in olivine. In the mantle wedge, the water content could be higher,  $10^3\text{-}10^4$  wt. ppm [Bell and Rossman, 1992; Dixon et al., 2002; Hirschmann et al., 2005; Hirschmann, 2006; Iwamori and Nakakuki, 2013; Nakamura and Iwamori, 2009; Workman and Hart, 2005]. Therefore, most part of Earth's upper mantle is wet but unsaturated with water except some regions like mantle wedge or subducting slabs.

## 1.4 Deformation mechanisms of olivine and upper mantle rheology

Rheological properties of the Earth's mantle play an important role in the dynamics of the lithosphere and asthenosphere [Karato and Wu, 1993], as well as the mantle transition zone and lower mantle. It controls most of the important geological processes such as the style of mantle convection (e.g., stagnant lid versus plate tectonics) and the nature of thermal evolution [Karato, 2010]. However, inferring the mantle rheology is always challenging because of the presence of multiple mechanisms and different mechanisms have different dependences on stress, grain size, temperature, pressure, and chemical composition [Karato, 2010].

There are generally two types of rock deformation mechanisms that occur in the Earth's interior: i.e., (1) diffusion creep including Coble diffusion creep and Nabarro-Herring diffusion creep, which dominate the deformation mechanism under low stress and small grain size conditions; (2) dislocation creep (climb and glide) which dominate the deformation mechanism at high stress and large grain size. Recently, another mechanism, grain boundary sliding, is also

proposed as an important deformation mechanism that affects mantle rheology at the conditions near the transition between diffusion creep and dislocation creep [*Hansen et al.*, 2011; *Hirth and Kohlstedt*, 2003].

A general equation to describe the dependence of creep on temperature, grain size, and stress based on experimental results is,

$$\dot{\varepsilon} = \frac{d\varepsilon}{dt} = A \frac{\sigma^m}{d^b} \exp\left(-\frac{Q}{RT}\right) \quad (1.32)$$

where  $\dot{\varepsilon}$  is the creep rate (or strain rate),  $\varepsilon$  is the strain,  $t$  is time,  $A$  is a constant dependent on the material and the particular creep mechanism,  $\sigma$  is the stress,  $d$  is the grain size,  $m$  and  $b$  are the stress and grain size exponents dependent on the creep mechanism,  $Q$  is the activation energy,  $R$  is the ideal gas constant, and  $T$  is the absolute temperature.

#### 1.4.1 Diffusion creep

##### (1) Nabarro-Herring diffusion creep

Nabarro-Herring creep [*Herring*, 1950; *Nabarro*, 1948] is a form of diffusion creep. When a compressive stress of  $\sigma$  is applied to a grain, the energy for the vacancy formation near the boundary is reduced or increased (depends on the direction of compressive stress), leading to a vacancy concentration gradient in the grain interior which causes atoms diffuse in the lattice by atoms-vacancies exchange and therefore the grain is elongated along the stress axis (**Fig. 1.12**, see **Appendix III**). The Nabarro-Herring creep is thus controlled by self-diffusion of atoms and vacancies in the lattices. The activation energy,  $Q$ , in **Eqs. 1.32** should be the same as the activation energy for the self-diffusion of atoms through the lattice. The values of  $m$  and  $b$  for Nabarro-Herring creep are 1 and 2, respectively.

Since the self-diffusion coefficient of ions significantly increases with increasing the temperature following the Arrhenius equation (both intrinsic diffusion and extrinsic diffusion as discussed in **Section 1.1.6**), the Nabarro-Herring creep is also strongly temperature dependent.

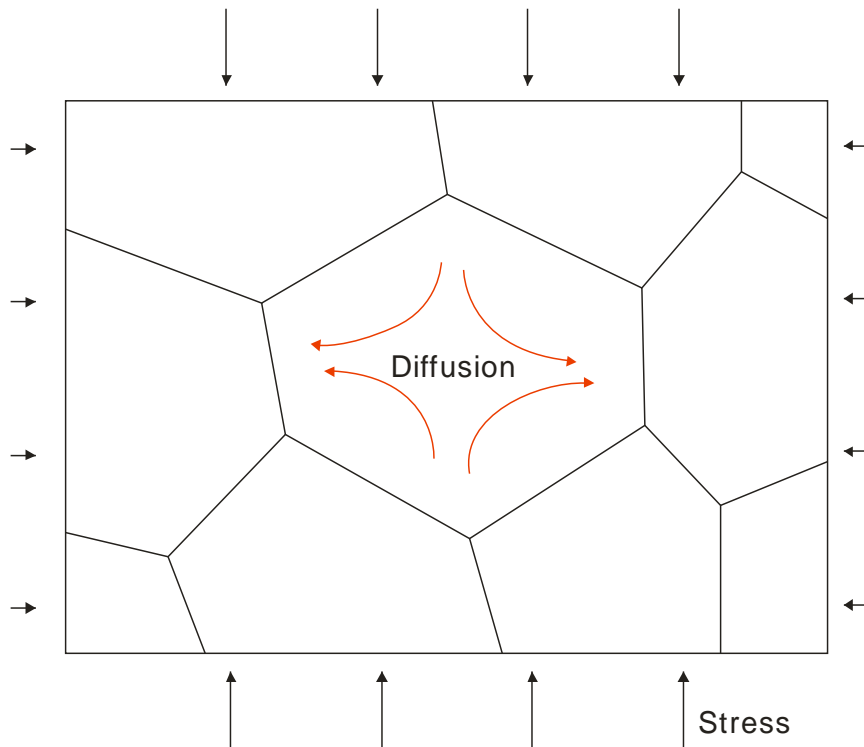


**Fig. 1.12.** Nabarro-Herring diffusion creep. Atoms diffuse within grain interior.

### (2) Coble diffusion creep

Vacancies and atoms can diffuse not only within the grain interior, but also along the grain boundaries. Coble diffusion creep [Coble, 1963] is a process that elongates the grains under an applied stress by diffusion along the grain boundaries (Fig. 1.13, also see Appendix III). This causes Coble creep to have stronger grain size dependence than Nabarro-Herring creep. The  $b$  and  $m$  in Eqs. 1.32 for Coble creep is 3 and 1, respectively, and  $Q$  should be the same as the activation energy for grain boundary diffusion. Because the crystal structure on the grain boundaries is already highly disordered, the concentration of vacancies does not significantly change with increasing temperature. Therefore, the temperature dependence of Coble creep is usually smaller than that for Nabarro-Herring creep.

### 1.4.2 Dislocation creep

Dislocation creep takes place due to the movement of dislocations through a crystal lattice under high stress conditions (Fig. 1.14) with  $m = \sim 3-6$  and  $b = 0$  in Eqs. 1.32. Namely, dislocation creep has strong dependence on the applied stress, but no grain size dependence.

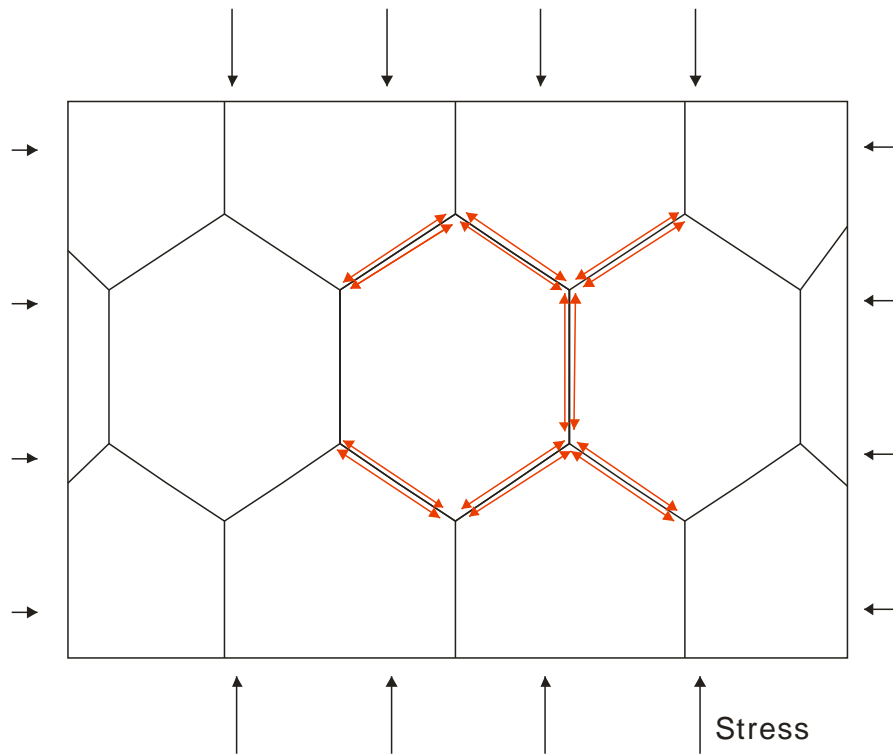


**Fig. 1.13.** Coble diffusion creep. Atoms diffuse along grain boundaries.

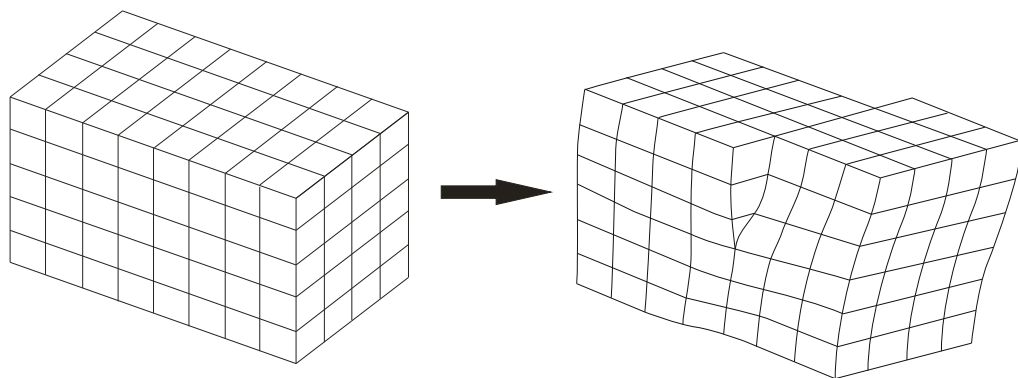
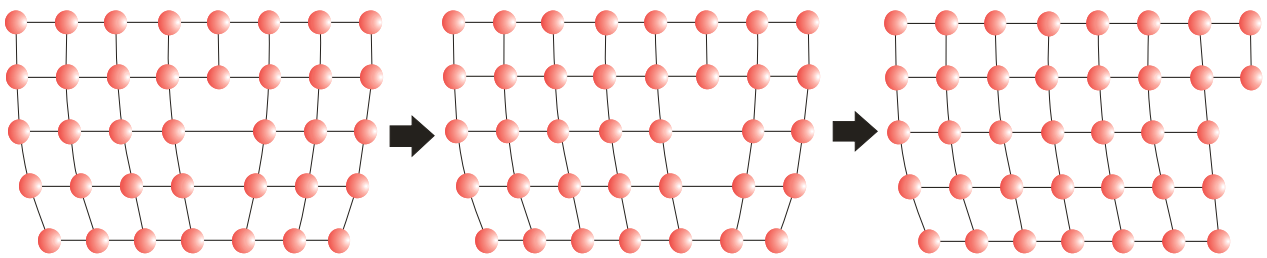


**Fig. 1.14.** Dislocation creep controlled by the movement of dislocations in the lattice, which is limited by the absorbing and emitting of point defects into or from dislocations (controlled by diffusion of atoms or vacancies). Top: Edge dislocation. Bottom: Screw dislocation.

As we know, the movement of dislocations at high temperature occurs by absorbing or emitting point defects into or from dislocations [Hirth and Lothe, 1982; Hull and Bacon, 2011; Mordehai et al., 2008]. Thus, the dislocation creep rate is also believed to be controlled by self-diffusion of atoms in the lattice, and therefore the activation energy for dislocation is identical to that for lattice diffusion.

### 1.4.3 Grain boundary sliding

As discussed above, the diffusion creep has small stress dependence and large grain size dependence, and dislocation creep has large stress dependence and no grain size dependence. However, at the condition near the transition between diffusion creep and dislocation creep (**Fig. 1.15**), there is a region that creep rate has a large stress dependence ( $m \approx 3$ ), and also significant grain size dependence ( $b \approx 1-2$ ). This deformation mechanism is proposed as grain boundary sliding [Hansen et al., 2011; Hirth and Kohlstedt, 1995a; Hirth and Kohlstedt, 2003].

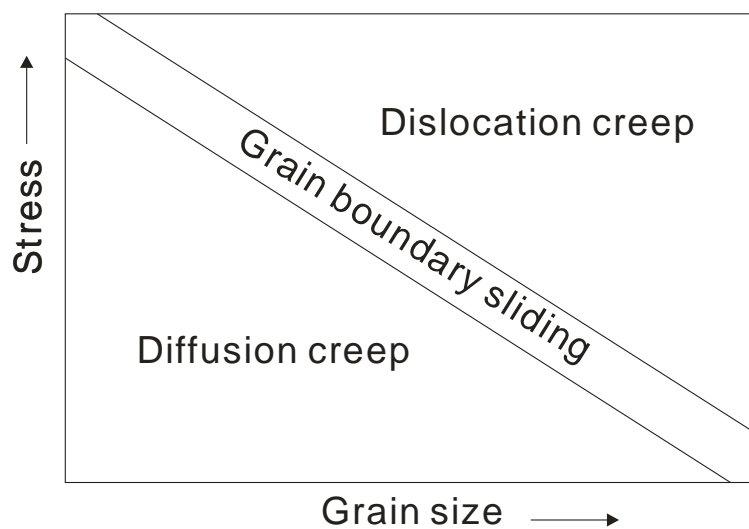


**Fig. 1.15.** Deformation mechanism map. Diffusion creep dominate the plastic deformation at low stress and small grain size, dislocation creep dominate at high stress and large grain size, and grain boundary sliding dominate the deformation at the condition near the transition between diffusion creep and dislocation creep (This figure is modified from Hansen et al. [2011]).

### 1.4.4 Rheology in Earth's upper mantle

Because the upper mantle rheology is dominated by the deformation of olivine, many studies have been carried out on olivine to investigate the effect of pressure, temperature, stress,

grain size, water content, and other factors on diffusion and dislocation creep rates, e.g., [Durham and Goetze, 1977a; b; Goetze and Kohlstedt, 1973; Hansen et al., 2011; Hirth and Kohlstedt, 1995a; b; Jung and Karato, 2001; Karato and Ogawa, 1982; Karato and Sato, 1982; Karato et al., 1993; Karato et al., 1986; Kohlstedt and Goetze, 1974; Mackwell and Kohlstedt, 1986; Mei and Kohlstedt, 2000a; b].

### (1) *Temperature dependence of creep rate*

The temperature dependence on creep rate is related to the activation energy,  $Q$ , in **Eqs. 1.13**. Higher activation energy indicates larger temperature dependence. The activation energy for both diffusion creep and dislocation creep in olivine is experimentally investigated shown in **Table 1.2** under dry and wet conditions. We can see the activation energy for diffusion creep (300-400 kJ/mol) is typically lower than that for dislocation creep (400-600 kJ/mol). This is reasonable because the Coble diffusion creep is controlled by grain boundary diffusion, which has lower activation energy in comparison with lattice diffusion which controls the dislocation creep. We also find that water slightly decreases the activation energy for creep by comparing the results obtained under dry and wet conditions (effect of water on creep rate is discussed in the following). The difference of activation energy between iron-bearing olivine and pure forsterite is very small, i.e., within experimental uncertainty [Durham and Goetze, 1977b; Ricoult and Kohlstedt, 1985].

### (2) *Pressure dependence of creep rate*

The pressure dependence of creep is derived by considering the free energy of the activation process. The activation enthalpy  $\Delta H$ , at variable pressure  $P$  is then given by,

$$\Delta H = Q + P\Delta V \quad (1.33)$$

where  $Q$  is the activation energy at room pressure and  $\Delta V$  is the activation volume. By replace the  $Q$  in **Eqs. 1.13** by  $\Delta H$ , we obtain,

$$\dot{\epsilon} = \frac{d\epsilon}{dt} = A \frac{\sigma^m}{d^b} \exp\left(-\frac{Q+P\Delta V}{RT}\right) \quad (1.34)$$

Therefore, the logarithm term of creep rate,  $\ln\dot{\epsilon}$ , has a linear relationship with pressure and the slope reflects the activation volume.

The activation volume for olivine creep is experimentally determined directly in deformation and dislocation recovery studies [For example *Borch and Green II*, 1989; *Karato and Ogawa*, 1982; *Karato and Jung*, 2003; *Li et al.*, 2006; *Raterron et al.*, 2009]. However, because of the difficulties of rock deformation experiments at high pressures, the uncertainty of determined activation volume is usually very large. As a result, the reported activation volume varies from ~5 up to 27 cm<sup>3</sup>/mol [*Borch and Green II*, 1989; *Li et al.*, 2006], results in several orders of magnitude uncertainty in the viscosity in the upper mantle. Besides, it is also considered that the activation volume decreases with increasing pressure based on experimental observation [*Hirth and Kohlstedt*, 2003]. For example, the activation volumes determined in low pressure studies are usually higher than those determined in higher pressure experiments as shown in **Table 1.3**.

**Table 1.2.** Activation energy for diffusion creep, dislocation creep, and grain boundary sliding in forsterite and iron-bearing olivine under dry and wet conditions.

Deformation mechanism	Sample	water	$\Delta E$ (kJ/mol)	Reference
Diffusion creep	Olivine	wet	295	[ <i>Mei and Kohlstedt</i> , 2000a]
Diffusion creep	Olivine	dry	375±50	[ <i>Hirth and Kohlstedt</i> , 2003]
Diffusion creep	Olivine	dry	380±105	[ <i>Cooper and Kohlstedt</i> , 1984]
Diffusion creep	Olivine	Dry	360±120	[ <i>Schwenn and Goetze</i> , 1978]
Diffusion creep	Olivine	Dry	484±30	[ <i>Faul and Jackson</i> , 2007]
Diffusion creep	Dunite	Dry	310-440	[ <i>Hirth and Kohlstedt</i> , 1995b]
Dislocation creep	Olivine	Dry	510±30	[ <i>Mei and Kohlstedt</i> , 2000b]
Dislocation creep	Olivine	wet	470±40	[ <i>Mei and Kohlstedt</i> , 2000b]
Dislocation creep	Olivine	wet	410±40	[ <i>Karato and Jung</i> , 2003]
Dislocation creep	Olivine	dry	523±21	[ <i>Durham and Goetze</i> , 1977a]
Grain boundary sliding	Olivine	dry	445±20	[ <i>Hansen et al.</i> , 2011]
Dislocation creep	Forsterite	dry	550±100	[ <i>Ricoult and Kohlstedt</i> , 1986]
Dislocation creep	Forsterite	dry	564±63	[ <i>Durham and Goetze</i> , 1977b]
Dislocation creep	Dunite	wet	530±30	[ <i>Hirth and Kohlstedt</i> , 1996]

**Table 1.3.** Activation volume determined in olivine deformation and dislocation recovery experiments.

Method	$\Delta V$ (kJ/mol)	$P$ range (GPa)	Reference
Deformation (dry)	14 (18*)	1-2	[Karato and Jung, 2003]
Deformation (wet)	24	1-2	[Karato and Jung, 2003]
Deformation (dry)	27	0.6-2.0	[Borch and Green II, 1989]
Deformation (dry)	13.4 (18*)	0.5-1.5	[Ross et al., 1979]
Deformation (dry)	14	0.3-15	[Karato and Rubie, 1997]
Deformation (dry)	0±5	3.5-7.5	[Li et al., 2006]
Deformation (dry)	1-3	2.1-7.5	[Raterron et al., 2007]
Recovery (dry)	19	10 <sup>-4</sup> -0.5	[Kohlstedt et al., 1980]
Recovery (dry)	14	10 <sup>-4</sup> -2.0	[Karato and Ogawa, 1982]
Recovery (dry)	6	10 <sup>-4</sup> -10	[Karato et al., 1993]

\*Corrected for effect of pressure on thermocouple emf. [Hirth and Kohlstedt, 2003].

### (3) Water dependence of olivine creep rate

As discussed in **section 1.3.3**, incorporation of water in olivine crystal could affect the defect chemistry of olivine. By increasing the water content, the concentration of point defects largely increases and therefore the atomic diffusion, which dominates both diffusion and dislocation creep, is enhanced.

Hirth and Kohlstedt [2003] summarized the effect of water on creep rate of olivine based on a series of deformation experiments [Borch and Green II, 1989; Jung and Karato, 2001; Karato et al., 1986; Karato and Jung, 2003; Mei and Kohlstedt, 2000a; b], and found that the creep rate largely increases with increasing water content/fugacity by an exponent power of ~1.2 (**Fig. 1.16**),

$$\dot{\epsilon} \propto (C_{H_2O})^{1.2} \propto (f_{H_2O})^{1.2} \quad (1.35)$$

where  $C_{H_2O}$  and  $f_{H_2O}$  are the content and fugacity of water, respectively. Based on the water content dependence shown in **Eqs. 1.16**, if the water content in olivine increases from 1 to 1000 wt. ppm, the creep rate would be enhanced by a factor of 4000.

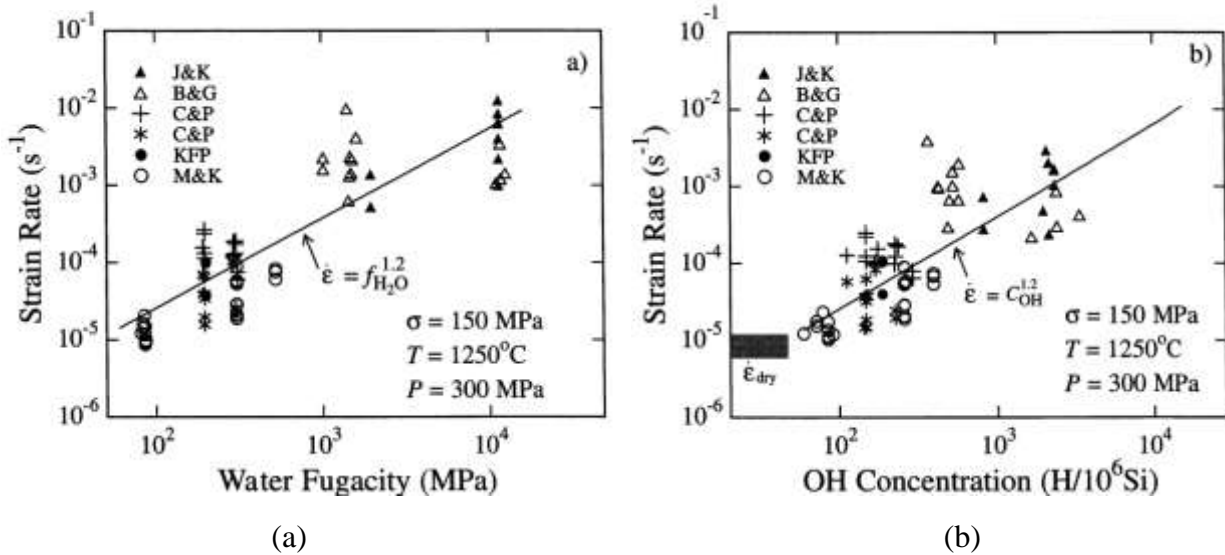


**Fig. 1.16.** Effect of water on strain rate of olivine (A) against water fugacity,  $f_{H_2O}$ ; (B) against water (hydroxyl) concentration,  $C_{OH}$ . This figure is taken from Hirth and Kohlstedt [2003]. J&K: Jung and Karato [2001]; B&G: Borch and Green [1989]; C&P: Chopra and Paterson [1984]; KFP: Karato et al. [1986]; M&K: Mei and Kohlstedt [2000].

As we know, the water content in the Earth's interior largely varies in different regions, e.g., it is less than 30 wt. ppm in the lithosphere,  $10^2$ - $10^3$  in the asthenosphere, and  $10^3$ - $10^4$  in the mantle wedge or subducting zone [Bell and Rossman, 1992; Dixon et al., 2002; Hirschmann et al., 2005; Hirschmann, 2006; Workman and Hart, 2005], and therefore the effect of water on mantle rheology has been considered to be significant.

#### (4) Effect of iron content on creep rate of olivine

As we know, the natural olivine could contain ~10 % of fayalite component. The common formula for olivine is  $(Mg_xFe_{1-x})_2SiO_4$ , and  $x$  is typically 0.9. However, the value of  $x$  could be slightly varied due to environmental conditions for example the existence of second phase, the oxygen fugacity, and the chemical environments in different regions. Additionally, small amount of ferric iron could exist in olivine crystal structure which could change the charge neutrality condition and therefore affect the defect chemistry under some given conditions (Section 1.3.3). Thus, in order to understand the rheological properties of olivine under mantle conditions, it is necessary to know the effect of iron on creep rates.

Durham and Goetze [1977b] compared dislocation creep rates along [101] orientation in pure forsterite ( $\text{Fo}_{100}$ ) and natural olivine ( $\text{Fo}_{92}$ ) and found that the activation energy ( $Q$ ) and stress exponent ( $n$ ) are almost the same ( $Q = 523 \text{ kJ/mol}$ ,  $n = 3.6$  for  $\text{Fo}_{92}$ , and  $Q = 564 \text{ kJ/mol}$ ,  $n = 3.5$  for  $\text{Fo}_{100}$  [Durham and Goetze, 1977a]). Under upper mantle conditions, the difference of creep rates between  $\text{Fo}_{100}$  and  $\text{Fo}_{92}$  is only about 14 % ( $\text{Fo}_{100}$  is ~14 % harder) ascribed to an 8 % change in iron content. Since the range of iron content of natural olivine is not large ( $\text{Fo}_{80}$ - $\text{Fo}_{93}$ ), they concluded that iron is not an important creep variable in the Earth's mantle [Durham and Goetze, 1977b].

Ricoult and Kohlstedt [1985] also compared the dislocation creep rates of natural olivine ( $\text{Fo}_{90}$ ) and synthesized pure forsterite. They found that under the conditions of the Earth's upper mantle [ $\text{SiO}_2$  rich, means lowest concentration of  $\text{V}_{\text{Si}}$  condition], the difference of creep rates between natural olivine and pure forsterite is almost negligible (Fig. 1.17). Therefore, the existence of iron in olivine does not significantly affect the creep properties under upper mantle conditions.

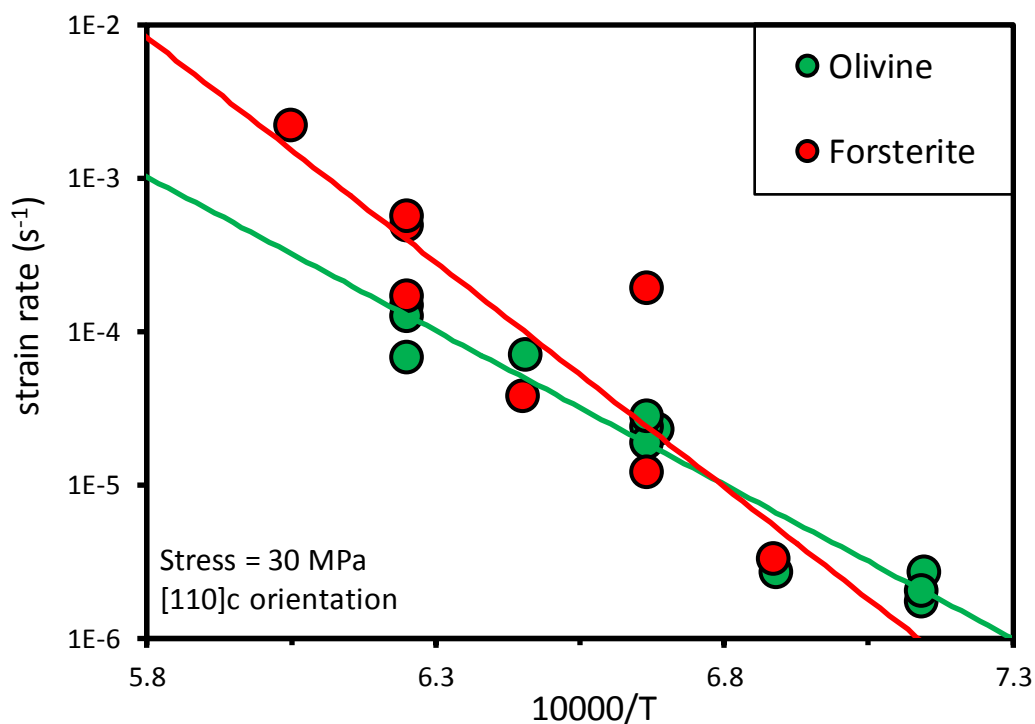


**Fig. 1.17.** Difference of creep rate between  $(\text{Mg,Fe})\text{SiO}_3$  buffered natural olivine and  $\text{MgSiO}_3$  buffered iron-free forsterite. The data points are taken from Ricoult and Kohlstedt [1985] corrected to a stress of 30 MPa using a stress exponent of 3.7 they suggested.

### (5) Effect of SiO<sub>2</sub> and f<sub>O2</sub> on creep rate of olivine

The Gibbs phase rule states that four independent state variables must be fixed to thermodynamically define a ternary system: pressure, temperature, partial pressure of oxygen (or oxygen fugacity,  $f_{O_2}$ ), and activity of one of the constituent oxides [Ricoult and Kohlstedt, 1985]. In the case of olivine deformation, both  $f_{O_2}$  and SiO<sub>2</sub> activity ( $a_{SiO_2}$ ) could change the charge neutrality condition in the crystal [Smyth and Stocker, 1975; Stocker and Smyth, 1978] and sequentially change the creep properties [Ricoult and Kohlstedt, 1985]. Under the charge neutrality condition of  $[Fe_{Mg}^*] = 2[V_{Mg}^{''}]$  in dry olivine, the concentration of silicon vacancy has an  $f_{O_2}$  and SiO<sub>2</sub> dependences,  $[V_{Si}^{''''}] \propto (f_{O_2})^{1/3} \times (a_{SiO_2})^{-10/3}$  [Smyth and Stocker, 1975; Stocker and Smyth, 1978]. If considering a silicon diffusion controlled creep, the creep rate should have  $f_{O_2}$  and SiO<sub>2</sub> exponents of 1/3 and -10/3, respectively.

Ricoult and Kohlstedt [1985] measured the dislocation creep rate in iron-bearing olivine single crystal and found a relationship,  $\dot{\epsilon} \propto f_{O_2}^{1/6}$  for un-buffered samples and  $\dot{\epsilon} \propto f_{O_2}^0$  for (Mg,Fe)O or (Mg,Fe)SiO<sub>3</sub> buffered samples. The non- $f_{O_2}$  dependence for buffered olivine is reasonable because the  $[V_{Si}^{''''}]$  is maximized or minimized by the buffer and therefore  $[V_{Si}^{''''}]$  does not change with  $f_{O_2}$ . For the un-buffered sample, they proposed an oxygen self-diffusion via a vacancy mechanism to explain the experimentally determined  $f_{O_2}$  exponents. However, it is already demonstrated that silicon is the slowest diffusion species in olivine [Dohmen et al., 2002; Jaoul et al., 1981]. The creep rate should be limited by silicon rather than oxygen diffusion. Therefore, their model is inadequate. Since the silicon ions are surrounded by oxygen in tetrahedrons, we can expect that silicon diffusion is controlled by both  $V_{Si}^{''''}$  and  $V_{O}^{''}$ , namely,  $D_{Si} \propto [V_{Si}^{''''}][V_{O}^{''}] \propto f_{O_2}^{1/3} \times f_{O_2}^{-1/6} \propto f_{O_2}^{1/6}$ . Thus, the  $f_{O_2}$  exponent of creep rate can be explained by  $V_{Si}^{''''}$  and  $V_{O}^{''}$  controlled silicon self-diffusion.

For  $a_{SiO_2}$  dependence of creep rate, Ricoult and Kohlstedt [1985] found that the creep rate in (Mg,Fe)SiO<sub>3</sub> buffered olivine is about 1.2 orders of magnitude higher than that in (Mg,Fe)O buffered samples and suggested a relationship  $\dot{\epsilon} \propto a_{SiO_2}^{1.2}$ . However, this relationship is too simplistic because the  $a_{SiO_2}$  value in (Mg,Fe)SiO<sub>3</sub> buffered sample is simply not 1.2 orders of magnitude higher than that in (Mg,Fe)O buffered sample. Therefore, the  $a_{SiO_2}$  exponent for creep rate is still unknown.

## ***(6) Deformation mechanisms in the upper mantle***

Based on the experimentally determined pressure, temperature, and water content dependence of olivine creep rate, the rheological properties of olivine are investigated under different conditions corresponding to different regions of the of Earth's upper mantle.

Karato and Wu [1993] calculated the diffusion and dislocation creep rates in the Earth's upper mantle as a function of depth based on the pressure and temperature dependences of olivine creep rates. Since they used a very large value of activation volume for dislocation creep (10-25 cm<sup>3</sup>/mol), they found that the dislocation creep rate significantly decreases with increasing depth and a deformation mechanism transition from dislocation creep in the shallow regions to diffusion creep in the deep regions with an interface at around 200-250 km depth. Sequentially, this mechanism transition is used to explain the Lehmann discontinuity [Lehmann, 1959] in which the seismic velocity increases and anisotropy decreases [Karato, 1992] because olivine deformed by dislocation creep has lattice preferred orientation (LPO) and therefore has anisotropic distribution while that deformed by diffusion creep does not [Karato and Wu, 1993].

Hirth and Kohlstedt [2003] also calculated the deformation mechanism in the upper mantle by considering the water dependence of diffusion and dislocation creep rates [Mei and Kohlstedt, 2000a; b]. They pointed out that the grain size has to be less than 10 μm for diffusion creep to dominate at 100 km depth, which is not realistic for the real mantle. Using a grain size condition of ~1 cm, they obtained a similar dislocation to diffusion creep transition depth (~200-250 km) as that by Karato and Wu [1993].

Therefore, both Karato and Wu [1993] and Hirth and Kohlstedt [2003] suggested a dislocation creep dominated shallow upper mantle and diffusion creep dominated deeper upper mantle with an interface at ~200-250 km depth, similar depth as the Lehmann discontinuity. However, we found that their calculations were based on very large activation volumes (typically >10 cm<sup>3</sup>/mol) for dislocation creep. As shown in **Table 1.3**, the values of activation volumes vary largely in different studies. If we use a value of <5 cm<sup>3</sup>/mol, there would be no such a transitions between diffusion creep and dislocation creep [Karato and Wu, 1993].

Besides, as discussed above, the Coble creep is rate limited by silicon grain boundary diffusion and the dislocation creep by silicon lattice diffusion in olivine [Frost and Ashby, 1982; Weertman, 1999]. Experimental results based on silicon diffusion suggest that the activation energy for silicon grain boundary diffusion ( $203 \pm 36$  kJ/mol [Farver and Yund, 2000]) is much lower than that for lattice diffusion ( $529 \pm 41$  kJ/mol [Dohmen et al., 2002]), which means that Coble diffusion creep should dominant at low temperature condition corresponding to shallow regions of the Earth's upper mantle, while dislocation creep should dominant at high temperature corresponding to deeper regions. This is also against the dislocation to diffusion creep transition model supposed by Karato and Wu [1993] and Hirth and Kohlstedt [2003]. Since, the activation energy difference between lattice diffusion and grain boundary diffusion is not taken into account in Karato and Wu [1993] and Hirth and Kohlstedt [2003], the deformation mechanism in Earth's upper mantle is still not specified.

## **1.5 Experimental approaching to mantle rheology**

### **1.5.1 Deformation experiments**

Measurement of creep rate in rocks is a direct way to study the rock deformation properties in which a sample is deformed by applying deviatoric stresses. By measuring the strain rate and stress, a constitutive mechanical equation is obtained [Karato, 2008]. The strain rate can be determined by measuring the sample dimension before and after experiment and the deformation duration. The most difficult thing in deformation experiments is to precisely determine the deviatoric stress.

One simple way to generate a deviatoric stress is dead weight loading in which load is applied by a mass being placed on top of the sample [Kohlstedt and Goetze, 1974]. The stress can be precisely determined by measuring the weight of load and the sample area by,  $\sigma=mg/A$  ( $\sigma$ , stress;  $m$ , mass;  $g$ , gravity acceleration;  $A$ , area) [Karato, 2008]. However, the pressure condition of dead weight loading apparatus is limited at ambient pressure. In order to understand the rock deformation under pressure and temperature conditions corresponding to the Earth's mantle, high-pressure deformation apparatus is required.

Paterson [1970] developed a gas-medium apparatus (so called Paterson deformation apparatus) for rock deformation experiments at high pressures, in which noble gas (usually argon) is used for generating confining pressures. Because the gas pressure medium provides a friction free stress field, there is no shear tractions along the sides of the samples. The stress can be measured by the external load supported by the sample and therefore the resolution of stress measurement is almost the same as that at room pressure. Stress at the level near the Earth's interior can be obtained and slow strain rate can be fulfillment. Unfortunately, the confining pressure achieved by the gas medium is limited at ~0.5 GPa, which is too low in comparing with that in the Earth's interior.

In order to conduct deformation experiments under higher confining pressures, the Griggs apparatus is developed based on a piston cylinder apparatus. It uses a hydraulic ram to compress the sample surrounded by soft material (e.g., NaCl), and a second piston is applied onto the sample through the hole at the center of the hydraulic ram to generate a deviatoric stress. However, the confining pressure of the Griggs apparatus is limited at ~3 GPa, which is still too low to investigate the rheological properties in the Earth's interior, e.g., the pressure at the top of the continental asthenosphere is already under higher pressure than this limit.

The D-DIA apparatus [Wang et al. 2003] is invented based on multi-anvil apparatus for rock deformation experiments. Six tungsten carbide anvils are used to compress the cubic cell assembly with sample inside it. The top and bottom anvils could move independently and therefore a deviatoric stress could be applied by moving two anvils forward or backward at a designed rate. Using the D-DIA apparatus, the experimental conditions can reach to pressure of 20 GPa and temperature of 2000 K [Kawazoe et al., 2010; Kawazoe et al., 2011] corresponding the pressure and temperature conditions at the lower part of mantle transition zone. However, in order to obtain laboratorially determinable stress and strain, the deformation experiments by a D-DIA apparatus are usually performed under very high stress conditions, typically  $10^2$ - $10^3$  MPa. It is at least is 2-4 orders of magnitude higher than that in the Earth's interior (~0.1-1.0 MPa in the converting mantle [Jackson, 2000]). The very-high stress could cause extremely high density defects, e.g., sub-grain boundaries, high-density dislocations, stacking faults, and therefore make artificial results which could lead to misunderstanding to the deformation properties in the Earth's interior.

Besides, some other techniques, e.g., rotational drickamer apparatus (RDA), diamond anvil cell (DAC), dislocation recovery in 6-8 multi-anvil apparatus, are developed for deformation experiments. But all of them have limitations (**Table 1.4**). For example the RDA has very poor resolution of stress measurement due to the poor X-ray diffraction, and impractical temperature measurement; the DAC method has very high stress and highly-inhomogeneous temperature distribution; the dislocation recovery experiments could only estimate the stress-strain rate relationship by dislocation density changes during annealing and stress/strain rate cannot be measured directly. Therefore, in order to confirm the rheological properties of rocks and minerals in the Earth's interior, the experimental results obtained from deformation apparatus should be examined by independent ways.

**Table 1.4.** A comparison of different deformation apparatus (modified from Karato [2008]).

Apparatus	Pressure (GPa)	Temperature (K)	Comments
Dead weight loading	<10 <sup>-4</sup>	<2000	Limited pressure
Gas medium	<0.5	<1600	Limited pressure
Griigs type	<3	<1600	Limited strain, pressure
D-DIA	<20	<2000	Very high stress, limited strain
Rotational Drickamer	<18	<2000	Limited resolution of stress and temperature measurements
Diamond anvil cell	<200	<1000	Very high stress
6-8 multi-anvil (Dislocation recovery)	<25	<2500	Relaxation experiments only

### 1.5.2 Diffusion experiments

Because of the limitations of deformation experiments (**section 1.5.1**), an independent way to study the mantle rheology is necessary. As discussed in **section 1.4**, the dislocation creep and Nabarro-Herring diffusion creep is controlled by atomic self-diffusion in the lattice (lattice diffusion), whereas the Coble diffusion creep is controlled by the self-diffusion on the grain boundaries (grain boundary diffusion), both of which are limited by the slowest diffusion species under upper mantle conditions [*Coble, 1963; Frost and Ashby, 1982; Herring, 1950; Weertman, 1999*], which are silicon and oxygen in most of mantle minerals [*Bejina and Jaoul, 1997; Costa and Chakraborty, 2008; Dobson et al., 2008; Dohmen et al., 2002; Jaoul et al., 1981; Ryerson et al., 1989; Shimojuku et al., 2009; Yamazaki et al., 2000*]. The following equations are the Frost

and Ashby [1982] and Weertman [1999] models to describe the linkages between diffusion coefficients and creep rates (the logics to reach these equations are given in **Appendix III**):

$$\dot{\varepsilon}(\text{dislocation}) = 2\pi \frac{GV_m}{RT} \left( \frac{\sigma}{G} \right)^3 \frac{D_{Si}^{lat}}{b^2} \frac{1}{\ln(G/\sigma)} \frac{l_g}{l_c} \quad (1.36)$$

$$\dot{\varepsilon}(\text{Nabarro - Herring - creep}) = A\sigma \frac{D^{lat}}{d^2} \frac{V_m}{RT} \quad (1.37)$$

$$\dot{\varepsilon}(\text{Coble - creep}) = A\sigma\pi \frac{\delta D^{gb}}{d^3} \frac{V_m}{RT} \quad (1.38)$$

where  $D^{gb}$  and  $D^{lat}$  are the grain boundary diffusion coefficient and lattice diffusion coefficients of the slowest species, respectively,  $\dot{\varepsilon}$  is the creep rate,  $A$  is a constant,  $\sigma$  is the stress,  $\delta$  is the grain boundary width,  $d$  is the grain size,  $G$  is the shear modulus,  $V_m$  is the molar volume,  $b$  is the magnitude of the Burgers vector, and  $l_g/l_c$  is the ratio of dislocation glide distance to the climb distance.

Using above equations, if the diffusion coefficients of the slowest diffusion species are measured, the creep rates of dislocation and diffusion, which dominate the plastic deformation of mantle minerals, can be estimated.

Besides, the viscosity of materials is a measure of the resistance of a fluid which is being deformed by either shear stress or tensile stress. In the Earth's mantle, it defines the mobility of mantle flow. If the diffusion coefficient of the slowest species in minerals is determined, the viscosity in the mantle is inversely proportional to it described by the Stock-Einstein Equation (**Appendix III**):

$$\eta = \frac{10kTR^2}{D_s m_a} \quad (1.39)$$

where  $\eta$  is the viscosity,  $k$  is the Boltzmann constant,  $T$  is the absolute temperature,  $R$  is the radius of crystal,  $D_s$  is the self-diffusion coefficient of the slowest diffusion species, and  $m_a$  is the ionic mass of the slowest diffusion species.

The experiments for measuring self-diffusion coefficients could be performed over a much wider range of experimental conditions (e.g., pressure could reach 25 GPa if using a 6-8 tungsten carbide multi-anvil apparatus, ~100 GPa using diamond-cube multi anvil) than rock deformation experiments as discussed in **Section 1.5.1**. Additionally, the diffusion experiments are performed under nearly hydrostatic pressure and therefore do not cause anomalously high-density defects. Thus, measurements of grain boundary and lattice self-diffusion coefficients of the slowest species in minerals are independent way in comparison with deformation experiments to study the mantle rheology.

One problem of the experimental studies (both deformation and diffusion experiments) on mantle rheology is that most studies used a single phase, i.e. pure olivine or pure forsterite. On the other hand, the Earth's upper mantle is a complex system which has several phases, for example olivine, orthopyroxene, and clinopyroxene (**Section 1.2**) though olivine is the weakest and dominant which contributed 60 % of the Earth's upper mantle in volume.

Experimental results demonstrate that the rheological properties of olivine could be influenced by the second phase. For example, reaction may occur between two phases on the boundaries, which could weaken the aggregates. Using the weakest component to represent the strength of the aggregates may overestimate the strength of a polyphase rock [Bruhn *et al.*, 1999]. Sundberg and Cooper [2008] and Wheeler [1992] also pointed out that diffusion creep in a two-phase system is controlled by the interface reaction, rate limited by self-diffusion of the faster species (e.g., magnesium or oxygen in olivine) rather than silicon which is the slowest species. Modeling the polyphase mantle is beyond the scope of the present thesis. The upper mantle rheology is assumed to be dominated by a single phase (olivine) in this study. One should be aware that it is necessary to consider the second phase influence when applying the results obtained in a single phase to the real Earth's upper mantle. Recent study [Tasaka *et al.*, 2013] found that the strength of forsterite+enstatite aggregates decreases with increasing enstatite volume fraction ( $f_{En}$ ) for samples with  $0 < f_{En} < 0.5$  and increases with increasing  $f_{En}$  for samples with  $0.5 < f_{En} < 1$ . Based on their experimental results, the strength of aggregates with 60 % forsterite and 40 % ( $f_{En} = 0.4$ ) is about one order of magnitude lower than that of pure forsterite in the diffusion creep regime.

## 1.6 Previous studies of silicon and oxygen diffusion in mantle minerals

In Mg-Fe silicate minerals (e.g., olivine, wadsleyite, ringwoodite, perovskite, etc., which are the main constituent of earth mantle [Ringwood, 1991]), the silicon ions are +4 charged, oxygen are -2 charged, and Mg or Fe are +2 charged. Therefore, the silicon ions should support the largest Coulomb force in the crystal structure and thus should have the slowest diffusion rate. On the other hand, oxygen has the largest ionic radius. As a result, the diffusion rate of oxygen should also be slow. Besides, silicon ions are surrounded by oxygen in tetrahedrons, and it should diffuse through oxygen vacancies or space between oxygen ions, which means silicon diffusion rate should be slower than oxygen. On the other hand, Formation of Mg and Fe vacancies,  $V_{Mg}''$  and  $V_{Fe}''$ , requires less energy than that for Si vacancy,  $V_{Si}''''$  [Brodholt and Refson, 2000]. Hence, the concentration of  $V_{Mg-Fe}''$  is much higher than that of  $V_{Si}''''$ , namely  $[V_{Mg-Fe}''] \gg [V_{Si}''']$  [Mackwell et al., 1988; Wanamaker, 1994]. As a result, Fe and Mg are the fastest diffusion species. All of above indicate that  $D_{Fe-Mg} \gg D_O \approx D_{Si}$  in most of Fe-Mg silicate minerals. This relationship is also demonstrated by experimental results [Chakraborty et al., 1994; Costa and Chakraborty, 2008; Dobson et al., 2008; Dohmen et al., 2007; Dohmen and Chakraborty, 2007; Houlier et al., 1990; Shimojuku et al., 2009; Chakraborty, 2010].

Since silicon is the slowest diffusion species in most mantle minerals. Therefore, the rates of diffusion and dislocation creep under mantle conditions are believed to be controlled by silicon. Oxygen is the second slowest diffusion species with similar diffusion coefficient as silicon [Costa and Chakraborty, 2008; Dobson et al., 2008; Shimojuku et al., 2009]. Thus, the oxygen diffusion coefficient may also play an essential role in upper mantle rheology.

### 1.6.1 Silicon diffusion

Silicon self-diffusion coefficients are experimentally measured in olivine, wadsleyite, ringwoodite, perovskite, and diopside, which are the main constituent of the Earth's mantle. Their results are listed in **Table 1.5** for the Arrhenius equation,

$$D_{Si} = A_0 \exp\left(-\frac{\Delta H}{RT}\right) \quad (1.40)$$

Here we discuss the results of silicon diffusion in olivine, wadsleyite, and ringwoodite, and perovskite, which are the most important minerals in the Earth's upper mantle, mantle transition zone, and top part of lower mantle.

**Table 1.5.** Experimental results of silicon lattice diffusion coefficients in mantle minerals (*Fo*: forsterite, namely, iron-free olivine. *Ol*: iron-bearing natural olivine. *Wd*: wadsleyite. *Rw*: ringwoodite. *Pv*: MgSiO<sub>3</sub> perovskite. *Qz*: quartz. *Di*: diopside).

Sample	Type	<i>T</i> (K)	<i>P</i> (GPa)	$\Delta H$ (kJ/mol)	<i>A</i> <sub>0</sub> (m <sup>2</sup> /s)	Reference
<i>Fo</i> <sup>dry</sup>	Lattice	1600-2000	10 <sup>-4</sup>	368±38	1.5×10 <sup>-10</sup>	[Jaoul et al., 1981]
<i>Fo</i> <sup>dry</sup>	Lattice	1523-1793	10 <sup>-4</sup>	150-600	—	[Andersson et al., 1989]
<i>Ol</i> <sup>dry</sup>	Lattice	1400-1800	10 <sup>-4</sup>	291±15	1.8×10 <sup>-13</sup>	[Houlier et al., 1990]
<i>Ol</i> <sup>dry</sup>	Lattice	1373-1773	10 <sup>-4</sup>	529±41	6.3×10 <sup>-5</sup>	[Dohmen et al., 2002]
<i>Ol</i> <sup>wet</sup>	Lattice	1473-1623	2	358±28	1.7×10 <sup>-7</sup>	[Costa and Chakraborty, 2008]
<i>Wd</i> <sup>wet</sup>	Lattice	1700-1900	18	299±112	3.4×10 <sup>-11</sup>	[Shimojuku et al., 2004]
<i>Wd</i> <sup>wet</sup>	Lattice	1700-1900	18	342±143	1.3×10 <sup>-10</sup>	[Shimojuku et al., 2010]
<i>Wd</i> <sup>wet</sup>	Lattice	1673-1873	16	409±103	2.5×10 <sup>-8</sup>	[Shimojuku et al., 2009]
<i>Rw</i> <sup>wet</sup>	Lattice	1673-1873	22	483±94	3.2×10 <sup>-6</sup>	[Shimojuku et al., 2009]
<i>Pv</i> <sup>dry</sup>	Lattice	1673-2073	25	336±36	2.7×10 <sup>-10</sup>	[Yamazaki et al., 2000]
<i>Pv</i> <sup>dry</sup>	Lattice	1673-2073	25	347±73	8.3×10 <sup>-10</sup>	[Dobson et al., 2008]
<i>Pv</i> <sup>dry</sup>	Lattice	1673-2073	25	308±58	5.1×10 <sup>-11</sup>	[Xu et al., 2011]
<i>Qz</i> <sup>dry</sup>	Lattice	1623-1873	10 <sup>-4</sup>	746±125	2.9×10 <sup>+3</sup>	[Bejina and Jaoul, 1996]
<i>Qz</i> <sup>dry</sup>	Lattice	1673-1873	10 <sup>-4</sup>	733±97	1.3×10 <sup>+2</sup>	[Jaoul et al., 1995]
<i>Qz</i> <sup>dry</sup>	Lattice	1673-2073	14	322-334	10 <sup>-11.3</sup>	[Shatskiy et al., 2010]
<i>Di</i> <sup>dry</sup>	Lattice	1623-1873	10 <sup>-4</sup>	211±110	2.3×10 <sup>-6</sup>	[Bejina and Jaoul, 1996]
<i>Fo</i> <sup>dry</sup>	Boundary	1173-1473	10 <sup>-4</sup>	203±36	5.4×10 <sup>-9</sup>	[Farver and Yund, 2000]
<i>Wd</i> <sup>wet</sup>	Boundary	1700-1900	18	248±135	1.1×10 <sup>-17</sup>	[Shimojuku et al., 2004]
<i>Wd</i> <sup>wet</sup>	Boundary	1673-1873	16	327±101	1.3×10 <sup>-15</sup>	[Shimojuku et al., 2009]
<i>Rw</i> <sup>wet</sup>	Boundary	1673-1873	22	402±88	6.3×10 <sup>-14</sup>	[Shimojuku et al., 2009]
<i>Pv</i> <sup>dry</sup>	Boundary	1673-2073	25	311±48	7.1×10 <sup>-17</sup>	[Yamazaki et al., 2000]
<i>Qz</i> <sup>dry</sup>	Boundary	873-1073	0.15	178±38	6.2×10 <sup>-9</sup>	[Farver and Yund, 2000]
<i>Qz</i> <sup>wet</sup>	Boundary	873-1073	0.15	137±18	3.7×10 <sup>-10</sup>	[Farver and Yund, 2000]

### (1) Silicon lattice diffusion in forsterite/olivine

The lattice diffusion coefficient of silicon ( $D_{Si^{lat}}$ ) in olivine is firstly determined experimentally by Jaoul et al. [1981] from 1600 – 2000 K at ambient pressure using an iron-free forsterite single crystal sample. By comparing with the oxygen diffusion data [Jaoul et al., 1980], they firstly found that silicon has the slowest diffusion rate in forsterite (**Fig. 1.18**) though it has the smallest ionic radius (the ionic radiuses of silicon, oxygen, and magnesium are 42, 140, and 65 pm, respectively), and therefore people started to consider that the plastic deformation of olivine should be dominated by self-diffusion of silicon rather than oxygen which has the largest ionic radius. Besides, it was found that silicon diffusion rate is also the slowest in San Carlos olivine (**Fig. 1.18**) [Dohmen et al., 2002].

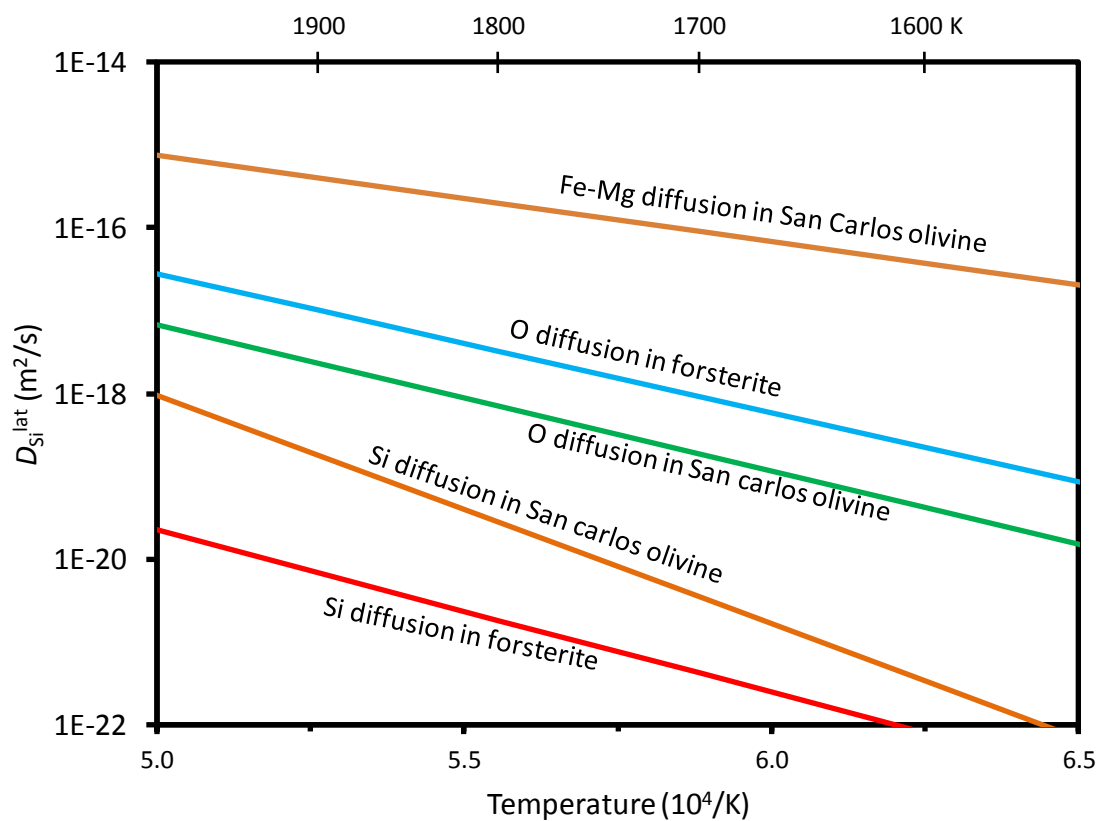


**Fig. 1.18.** A comparison of silicon [Dohmen et al., 2002; Jaoul et al., 1981], oxygen [Dohmen et al., 2002; Jaoul et al., 1980], and Fe-Mg diffusion [Dohmen et al., 2007] in forsterite and San Carlos olivine. The diffusion coefficient of silicon is about 2-4 orders of magnitude lower than oxygen diffusion, and 5-6 orders of magnitude lower than Fe-Mg diffusion.

The  $D_{Si^{lat}}$  in pyroxene buffered natural San Carlos olivine was determined at ambient pressure by Houlier et al. [1988; 1990] as a function of temperature and oxygen fugacity. The

activation energy for silicon diffusion was determined to be  $\sim 290 \pm 15$  kJ/mol [Houlier et al., 1990], which is significantly lower than that in pure forsterite ( $\sim 375$  kJ/mol [Jaoul et al., 1981]), and lower than that for olivine dislocation creep ( $\sim 400$ - $600$  kJ/mol) [Darot and Gueguen, 1981; Durham and Goetze, 1977a; b; Karato and Ogawa, 1982]. Besides, the oxygen fugacity ( $f_{O_2}$ ) dependence of  $D_{Si^{lat}}$  in natural olivine was found to be  $D_{Si^{lat}} \propto f_{O_2}^{-0.19} \approx f_{O_2}^{-1/6}$  [Houlier et al., 1990], while it has no  $f_{O_2}$  dependence in pure forsterite [Jaoul et al., 1981]. The  $f_{O_2}$  exponent for  $D_{Si^{lat}}$  was explained by an interstitial mechanism for silicon diffusion because the concentration of silicon interstitials decreases with increasing  $f_{O_2}$  by oxidization of ferrous iron to ferric state in natural olivine [Houlier et al., 1990; Stocker and Smyth, 1978]. This  $f_{O_2}$  exponent for  $D_{Si^{lat}}$  in natural olivine slightly differs from that determined in deformation experiments [Ricoult and Kohlstedt, 1985] in which an  $f_{O_2}$  exponent of 0 was suggested for (Mg,Fe)SiO<sub>3</sub> buffered samples. However, Houlier et al. [1990] also pointed out that the dependence of  $f_{O_2}$  is not statistically significant. Therefore, the  $D_{Si^{lat}}$  and creep rate have probably no  $f_{O_2}$  dependence in (Mg,Fe)SiO<sub>3</sub> buffered olivine. Since the Earth's upper mantle is  $\sim 60$  % olivine with pyroxene (**Section 1.2**),  $f_{O_2}$  is not an essential factor that affects mantle rheology.

Because the activation energy for  $D_{Si^{lat}}$  determined by Houlier et al. [1990] ( $\sim 290$  kJ/mol) is not consistent with that determined in olivine deformation experiments [Darot and Gueguen, 1981; Durham and Goetze, 1977a; b], Dohmen et al. [2002] also measured  $D_{Si^{lat}}$  in San Carlos olivine at ambient pressure, who obtained a much higher activation energy,  $529 \pm 41$  kJ/mol, and the discrepancy of activation energy between silicon diffusion experiments and deformation experiments was resolved. Dohmen et al. [2002] suggested most of the silicon diffusion profiles obtained by Houlier et al. [1990] were largely affected by convolution, i.e., the experimental durations were not long enough and the diffusion profiles were too short, within the depth resolution of the Rutherford backscattering spectrometry used in Houlier et al. [1990], and therefore the activation energy determined in Houlier et al. [1990] were not believable. However, using the data listed in Dohmen et al. [2002], we found that the lengths of their diffusion profiles were also very short (typically  $\sim 30$ - $50$  nm length) which should also be largely affected by the convolution (for example, the length of profile measured in the sample without annealing is about  $30$ - $40$  nm shown in Dohmen et al. [2002], which is comparable with the long-duration annealed samples).

Bejina et al. [1997; 1999] measured  $D_{\text{Si}^{\text{lat}}}$  in natural olivine at 1763 K as a function of pressure from 4 to 9 GPa and the activation volume for  $D_{\text{Si}^{\text{lat}}}$  was determined to be  $-1.9 \pm 2.4$   $\text{cm}^3/\text{mol}$  [Bejina et al., 1997] and  $0.7 \pm 2.3$   $\text{cm}^3/\text{mol}$  after a correction for oxygen fugacity [Bejina et al., 1999], which is very close to zero. Their results demonstrate that pressure has practically no effect upon silicon diffusion, which is against the olivine deformation experiments which suggested a very large activation volume (typically higher than 10  $\text{cm}^3/\text{mol}$ , for example, Broch and Green II [1989], Ross et al. [1979], and Karato and Rubie [1997]). However, the data points in Bejina et al. [1997; 1999] are largely scattered (Fig. 1.19) in which the pressure dependence of  $D_{\text{Si}^{\text{lat}}}$  could be hidden.

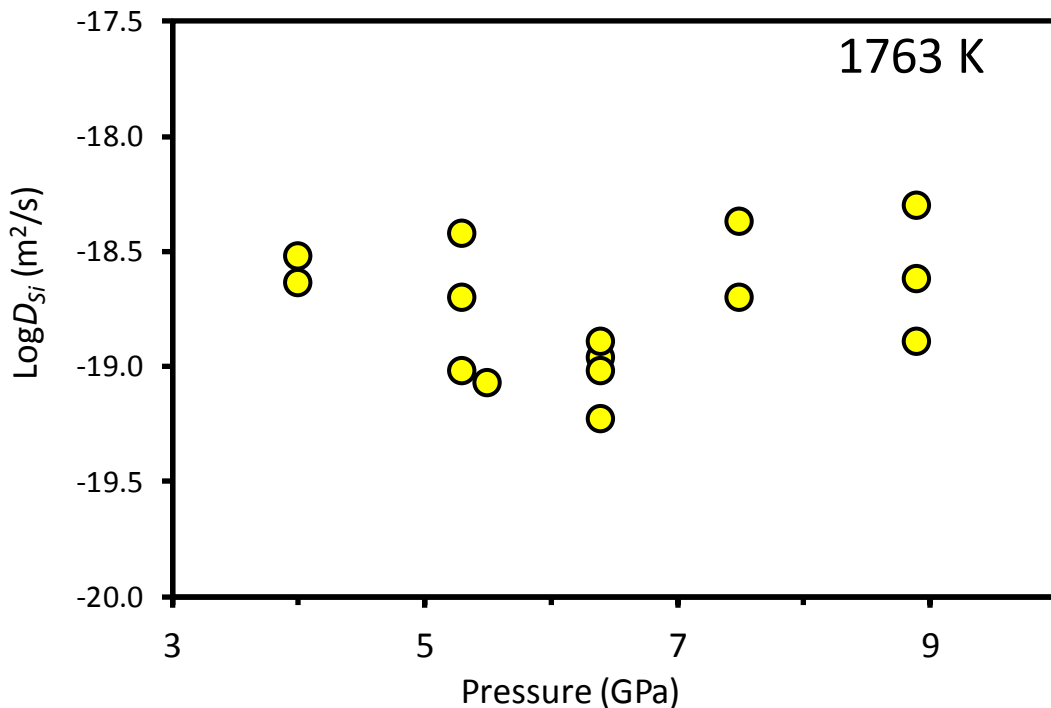


**Fig. 1.19.** Almost no pressure dependence of  $D_{\text{Si}^{\text{lat}}}$  in olivine determined by Bejina et al. [1999].

Recently, Costa and Chakraborty [2008] measured  $D_{\text{Si}^{\text{lat}}}$  in olivine at 2 GPa, 1470 – 1620 K with water contents from 30 – 50 to ~370 wt. ppm. By comparing with the results determined at ambient pressure and dry condition by Dohmen et al. [2002], they concluded that water has significant effect on silicon diffusion rate in olivine. Even ~45 wt. ppm of water could enhance  $D_{\text{Si}^{\text{lat}}}$  by three orders of magnitude, and 10 wt. ppm of water is enough to make the transition from rheologically dry to water-bearing condition (Fig. 1.20). Therefore, though the mantle is far

from water saturated, the influence of water on need to be considered for understanding the physical and chemical behavior and evolution of the upper mantle and a rheologically “wet” mantle model should be used. Besides, the activation energy for silicon diffusion was determined to be ~450 kJ/mol (or ~360 kJ/mol without oxygen fugacity correction), which is slightly lower than that for dry olivine determined by Dohmen et al. [2002].

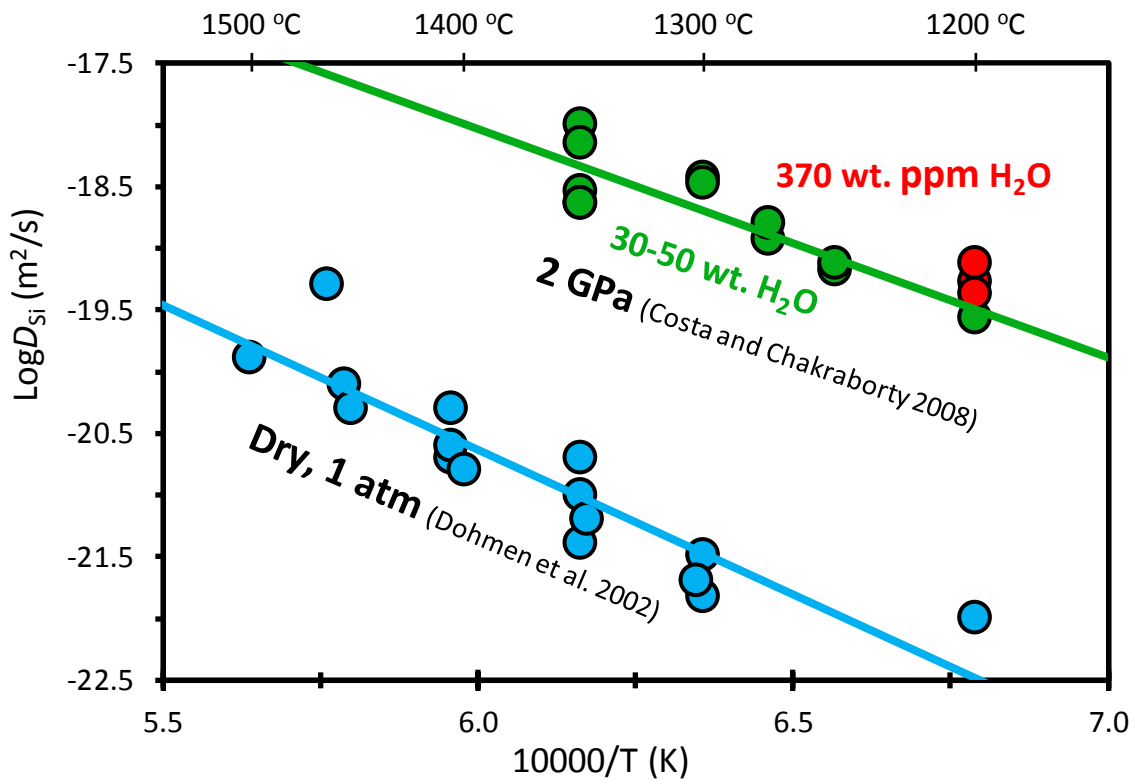


**Fig. 1.20.** Silicon diffusion coefficients at dry and wet conditions measured by Dohmen et al. [2002] and Costa and Chakraborty [2008], respectively.

## (2) Silicon grain-boundary diffusion in forsterite

Farver and Yund [2000] measured silicon diffusion coefficients along grain boundaries ( $D_{Si}^{gb}$ ) in forsterite aggregates with grain sizes of ~4.5  $\mu\text{m}$  at ambient pressure under dry conditions from 1270 – 1470 K. The silicon grain-boundary diffusion rate was determined to be about nine orders of magnitude greater than the volume diffusion rate and therefore Farver and Yund [2000] concluded that the diffusional transport of silicon in forsterite should be dominated by grain boundaries.

The comparison of diffusion creep rate calculated from  $D_{Si^{gb}}$  [Farver and Yund, 2000] with that measured in deformation experiments [Faul and Jackson, 2007; Mei and Kohlstedt, 2000a] is shown in **Fig. 1.21**. After corrected to the same pressure, temperature, stress, and grain size condition, the creep rate calculated from  $D_{Si^{gb}}$  is about 1.5-3.5 orders of magnitude higher than that measured directly in deformation experiments. One possible explanation for this discrepancy could be the porosities in the samples which could make nominally long diffusion profiles and lead to an overestimation of  $D_{Si^{gb}}$ .

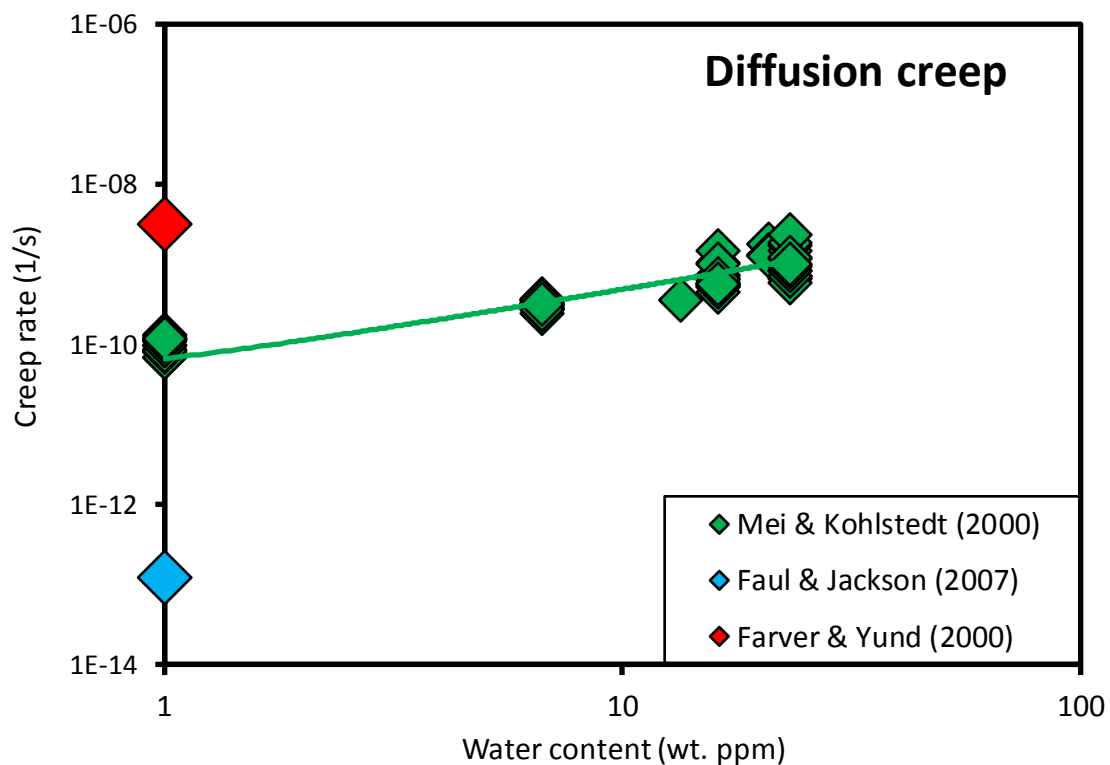


**Fig. 1.21.** A comparison of diffusion creep rate calculated from  $D_{Si^{gb}}$  [Farver and Yund, 2000] with that measured in deformation experiments [Faul and Jackson, 2007; Mei and Kohlstedt, 2000a] at 8 GPa, 1300 K, stress of 1 MPa, and grain size of 10  $\mu\text{m}$ .

The activation energy for  $D_{Si^{gb}}$  is determined to be  $\sim 200$  kJ/mol, much lower than that for lattice diffusion [Dohmen *et al.*, 2002; Jaoul *et al.*, 1981], which means temperature has a very small effect on  $D_{Si^{gb}}$  than that on  $D_{Si^{lat}}$ . Since the Coble diffusion creep is controlled by  $D_{Si^{gb}}$  and dislocation creep is controlled by  $D_{Si^{lat}}$  [Frost and Ashby, 1982; Weertman, 1999], the Coble diffusion creep should dominate olivine deformation mechanism at low temperature corresponding to low temperature regions in the Earth's interior, which is inconsistent with the

diffusion creep dominated lower asthenosphere and dislocation creep dominated upper asthenosphere.

Besides, Farver and Yund [2000] only measured  $D_{\text{Si}^{\text{gb}}}$  in forsterite at ambient pressure under dry conditions, which cannot be applied to the wet and high-pressure Earth's mantle. The effects of water and pressure on  $D_{\text{Si}^{\text{gb}}}$  are still unknown.

### (3) *Silicon lattice diffusion in wadsleyite and ringwoodite*

The silicon lattice diffusion coefficients in iron-free wadsleyite, iron bearing wadsleyite and ringwoodite polycrystalline samples were systematically measured by Shimojuku et al. [2004; 2009; 2010]. In iron-free wadsleyite, the activation energy for  $D_{\text{Si}^{\text{lat}}}$  is about 300 kJ/mol [Shimojuku et al., 2004]. It is lower than the value of ~410 kJ/mol determined in iron-bearing wadsleyite [Shimojuku et al., 2009], and also much lower than 530 or 450 kJ/mol determined olivine [Costa and Chakraborty, 2008; Dohmen et al., 2002]. If we consider a pressure correction using an activation volume, this difference could be even larger. Because the activation energy for silicon diffusion reflects the energy required to form a silicon vacancy, the concentration of silicon vacancies in wadsleyite is probably much higher than that in olivine. In ringwoodite, higher pressure phase of olivine and wadsleyite, the activation energy is similar as olivine, i.e., ~480 kJ/mol [Shimojuku et al., 2009].

Shimojuku et al. [2010] also investigated the effects of water and iron content on  $D_{\text{Si}^{\text{lat}}}$  in wadsleyite. They found that  $D_{\text{Si}^{\text{lat}}}$  in  $\text{Mg}_2\text{SiO}_4$ -wadsleyite and in  $(\text{Mg}_{0.9}\text{Fe}_{0.1})_2\text{SiO}_4$ -wadsleyite [Shimojuku et al., 2009] are comparable under upper mantle conditions (**Fig. 1.22a**) though the activation energies are largely different. Besides,  $D_{\text{Si}^{\text{lat}}}$  in  $\text{Mg}_2\text{SiO}_4$  wadsleyite containing 14-507 wt. ppm of water [Shimojuku et al., 2004] is about half an order of magnitude higher than that under nominally dry conditions with about ~20-60 wt. ppm of water [Shimojuku et al., 2010] (**Fig. 1.22b**). However, we noted that the water contents in their samples were not well controlled. In their experiments, almost 70 % of water was lost in their high water content samples during diffusion annealing, meanwhile, in some samples the water content increased. Therefore, the silicon diffusion occurred under various rate in each experiment. The real effect of water on silicon diffusion in wadsleyite is still unknown.

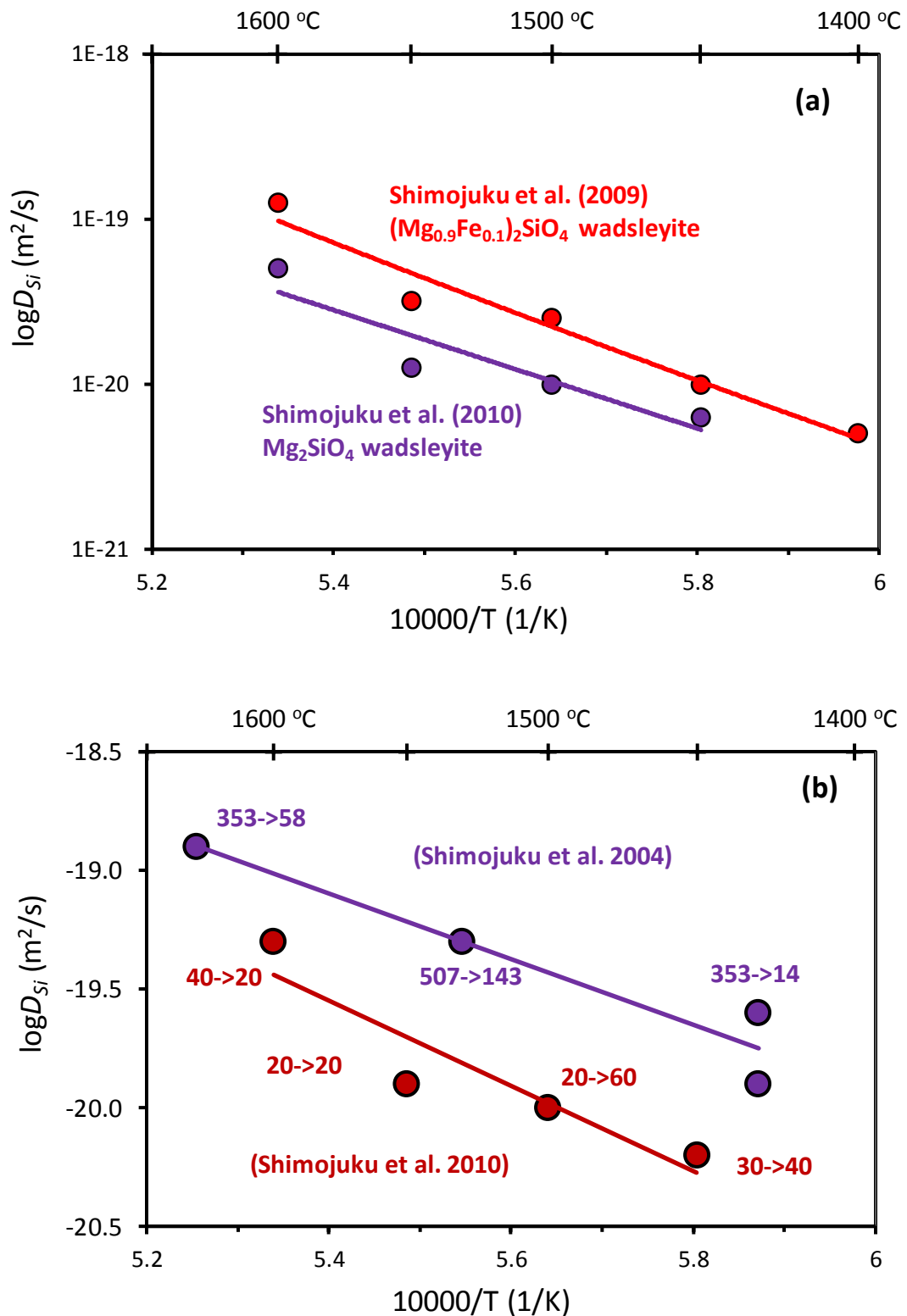


**Fig. 1.22.** Effects of (a) iron and (b) water content on silicon lattice diffusion in  $Mg_2SiO_4$ -wadsleyite determined by Shimojuku et al. [2004] and in  $(Mg_{0.9}Fe_{0.1})_2SiO_4$ -wadsleyite by Shimojuku et al. [2009]. The numbers in the figure with arrows mean the water contents (wt. ppm) in the samples before and after diffusion annealing.

#### (4) Silicon grain-boundary diffusion in wadsleyite and ringwoodite

The silicon grain-boundary diffusion coefficients in wadsleyite and ringwoodite were simultaneously measured with the lattice diffusion [Shimojuku *et al.*, 2004; 2009; 2010]. The activation energies for  $D_{\text{Si}^{\text{gb}}}$  in iron-free and iron-bearing wadsleyite are  $\sim 250$  and  $327$  kJ/mol, respectively. Shimojuku *et al.* [2004; 2009]’s results showed that the activation energy in iron-free wadsleyite is lower than that for iron-bearing wadsleyite for both lattice and grain-boundary diffusion. However, similar as lattice diffusion, the absolute values of  $D_{\text{Si}^{\text{gb}}}$  in iron-free and iron-bearing wadsleyite are comparable under upper mantle conditions (**Fig. 1.23**). Therefore, the effect of iron content on  $D_{\text{Si}^{\text{lat}}}$  and  $D_{\text{Si}^{\text{gb}}}$  are very small. This is in consistent with the olivine deformation experiments who also suggested a very small iron content effect (**Section 1.4.4**).

Because of the difficulties to obtain well-synthesized ringwoodite samples, Shimojuku *et al.* [2009] is the only study who well determined silicon grain-boundary diffusion coefficients in ringwoodite. They determined an activation energy of  $246 \pm 70$  kJ/mol for  $D_{\text{Si}^{\text{gb}}}$ , i.e. about half of the value for lattice diffusion ( $\sim 480$  kJ/mol, [Shimojuku *et al.*, 2009]).

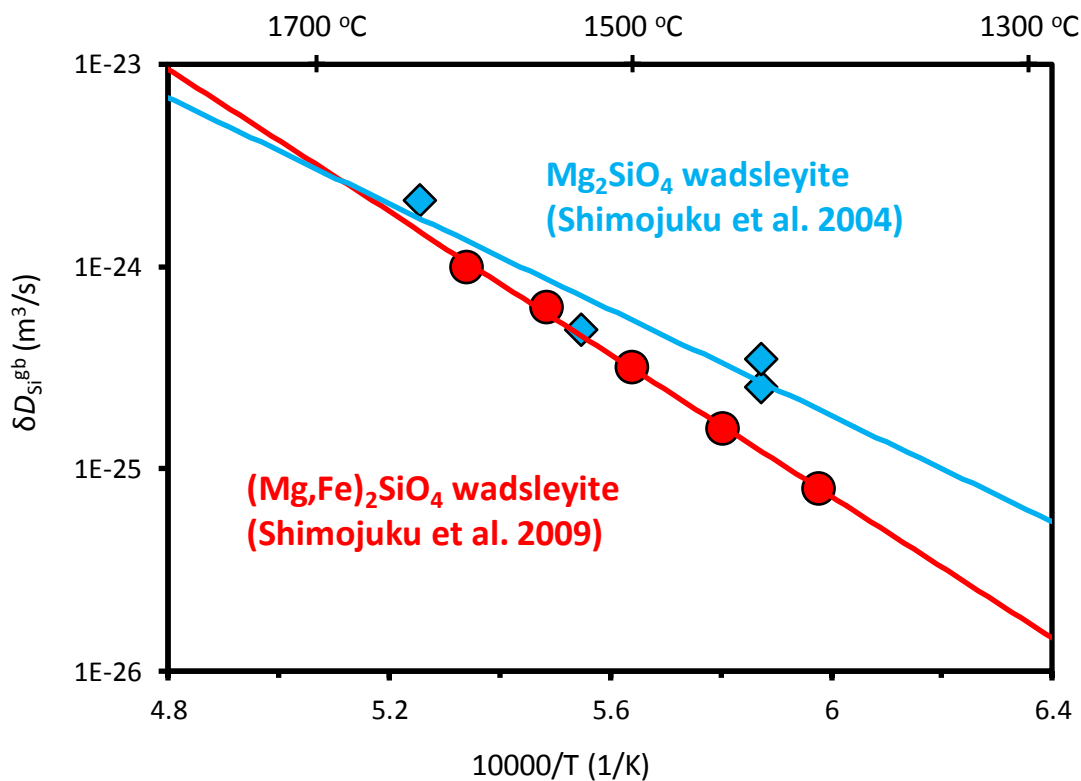


**Fig. 1.23.** Comparable results of  $D_{\text{Si}^{\text{gb}}}$  in iron-bearing and iron-free wadsleyite.

The absolute value of  $\delta D_{\text{Si}^{\text{lat}}}$  is about  $10^{-24}$ - $10^{-26}$  m<sup>3</sup>/s at temperatures of 1670-1870 K. If we consider a grain size of ~1-10 mm, which is the case for upper mantle conditions [Faul and Jackson, 2005; Karato, 1984], the effective silicon diffusion coefficient in wadsleyite and ringwoodite along grain boundaries are about  $10^{-21}$ - $10^{-24}$  m<sup>2</sup>/s, about 1-3 orders of magnitude lower than silicon lattice diffusion coefficient under the same temperature. Therefore, the grain boundary diffusion should be negligible in mass transport of silicon in wadsleyite and ringwoodite under mantle transition zone conditions.

By comparing the values of  $D_{\text{Si}^{\text{gb}}}$  and  $D_{\text{Si}^{\text{lat}}}$  in wadsleyite and ringwoodite and calculating the Coble and Nabarro-Herring creep and dislocation creep rates from  $D_{\text{Si}^{\text{gb}}}$  and  $D_{\text{Si}^{\text{lat}}}$ , Shimojuku et al. [2009] also found that the deformation mechanism of wadsleyite and ringwoodite should be dominated by dislocation creep under the mantle transition zone conditions.

#### **(5) Silicon lattice and grain-boundary diffusion in perovskite**

Because of the difficulty to obtain large single crystal of MgSiO<sub>3</sub>-perovskite samples due to its high-pressure stable field (~25 GPa), it is difficult to measure silicon diffusion rate in perovskite single crystal. Yamazaki et al. [2000] and Dobson et al. [2008] measured  $D_{\text{Si}^{\text{lat}}}$  and  $D_{\text{Si}^{\text{gb}}}$  in MgSiO<sub>3</sub> perovskite using synthetic aggregates, and obtained almost the same results (**Fig. 1.24**). The activation energies for  $D_{\text{Si}^{\text{lat}}}$  and  $D_{\text{Si}^{\text{gb}}}$ ,  $\Delta H_{\text{Si}^{\text{lat}}}$  and  $\Delta H_{\text{Si}^{\text{gb}}}$ , are determined to be ~340-350 and ~310 kJ/mol, respectively. The lattice diffusion and grain boundary diffusion show almost the same temperature dependence. The ratio of  $\Delta H_{\text{Si}^{\text{lat}}}/\Delta H_{\text{Si}^{\text{gb}}}$  is ~1.1, much lower than most of other silicates [Yamazaki et al., 2000]. It could be possibility because of the weaker bond strength of six-coordinated silicon than four-coordinated silicon, which could make it easier to form silicon defects.

Recently, Shatskiy et al. [2007; 2009; 2010] developed a thermal gradient method for crystal growth and large (1 mm) perovskite single crystals were obtained. Base on this method, Xu et al. [2011] measured  $D_{\text{Si}^{\text{lat}}}$  in single crystal of perovskite, and obtained the same results at those reported by Yamazaki et al. [2000] and Dobson et al. [2008] (**Fig. 1.24a**) with an activation energy of ~305 kJ/mol. No significant diffusion anisotropy was found. Besides, Xu et

al. [2011] also found similar rates of silicon and magnesium diffusion with very similar activation energies, which was explained by a Si-Mg coupled diffusion model.

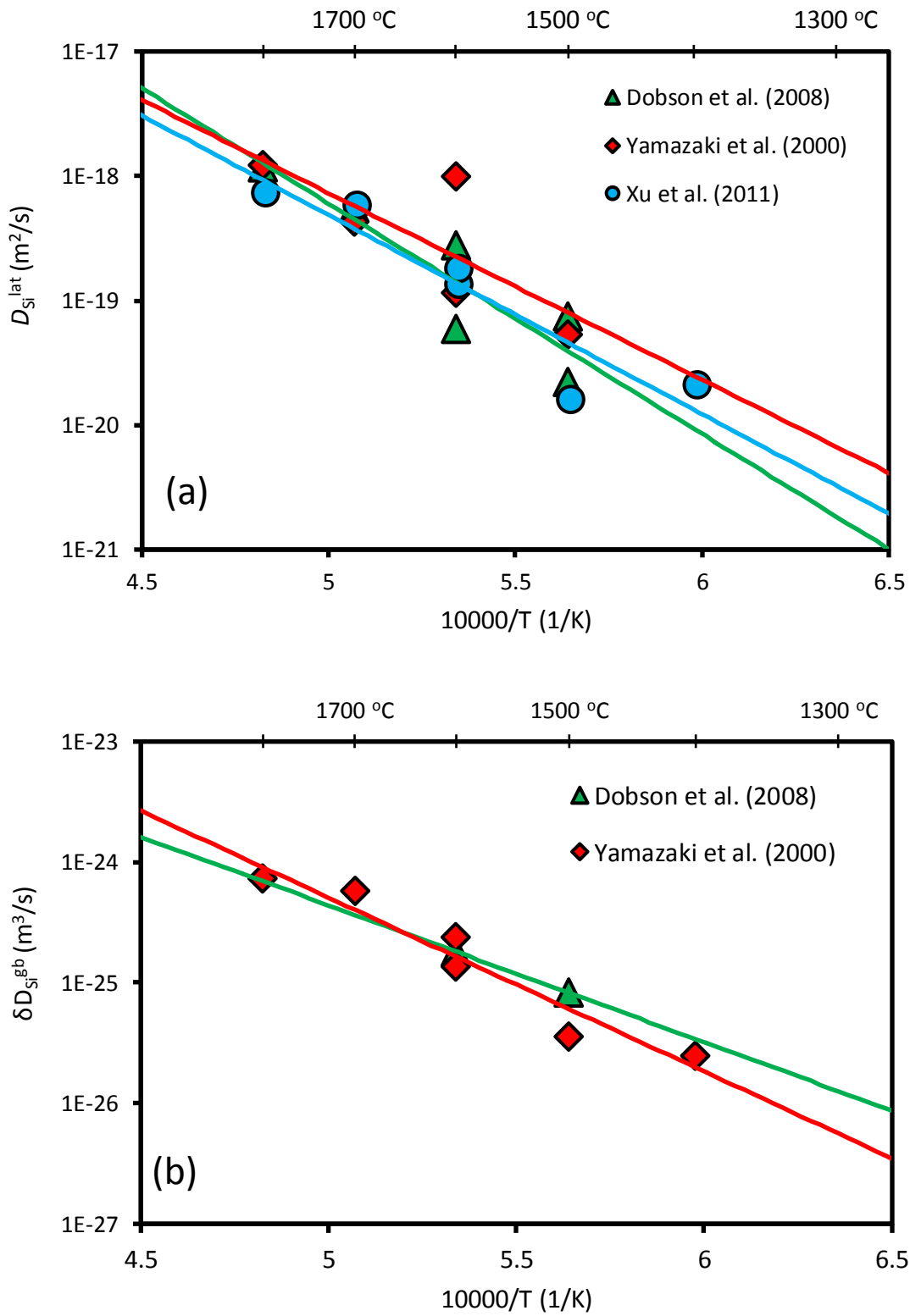


**Fig. 1.24.** (a)  $D_{Si}^{lat}$  and (b)  $D_{Si}^{gb}$  in perovskite from Yamazaki et al. [2000], Dobson et al. [2008], and Xu et al. [2011].

## 1.6.2 Oxygen diffusion

Because oxygen is the second slowest diffusion species in most silicate minerals [Costa and Chakraborty, 2008; Shimojuku et al., 2009] with similar diffusion coefficients as silicon ( $D_{\text{Si}}^{\text{lat}} \approx D_{\text{O}}^{\text{lat}}$  in olivine, wadsleyite, and ringwoodite), measurement of oxygen diffusion is also essential to understand the upper mantle rheology. A summary of reported oxygen lattice and grain-boundary diffusion coefficients are listed in **Table 1.6**.

**Table 1.6.** Experimental results of oxygen lattice and grain-boundary diffusion coefficients in mantle minerals (*For*: forsterite, namely, iron-free olivine. *Oli*: iron-bearing natural olivine. *Wd*: wadsleyite. *Rw*: ringwoodite. *Pv*: MgSiO<sub>3</sub> perovskite).

Min.	Composition	Diffusion type	<i>T</i> (K)	<i>P</i> (GPa)	$\Delta H$ (kJ/mol)	<i>A</i> <sub>0</sub> (m <sup>2</sup> /s)	Reference
<i>For</i> <sup>dry</sup>	Mg <sub>2</sub> SiO <sub>4</sub>	Lattice	1423-1873	10 <sup>-4</sup>	322±42	—	[Jaoul et al., 1980]
<i>For</i> <sup>dry</sup>	Mg <sub>2</sub> SiO <sub>4</sub>	Lattice	1550-1900	10 <sup>-4</sup>	370±13	3.5×10 <sup>-7</sup>	[Reddy et al., 1980]
<i>For</i> <sup>dry</sup>	Mg <sub>2</sub> SiO <sub>4</sub>	Lattice	1523-1793	10 <sup>-4</sup>	302±13	6.9×10 <sup>-10</sup>	[Andersson et al., 1989]
<i>Oli</i> <sup>dry</sup>	(Fe,Mg) <sub>2</sub> SiO <sub>4</sub>	Lattice	1573	10 <sup>-4</sup>	—	—	[Houlier et al., 1988]
<i>Oli</i> <sup>dry</sup>	(Fe,Mg) <sub>2</sub> SiO <sub>4</sub>	Lattice	1473-1673	10 <sup>-4</sup>	266±11	2.6×10 <sup>-10</sup>	[Ryerson et al., 1989]
<i>Oli</i> <sup>dry</sup>	(Fe,Mg) <sub>2</sub> SiO <sub>4</sub>	Lattice	1363-1773	10 <sup>-4</sup>	318±17	6.7×10 <sup>-6</sup>	[Gérard and Jaoul, 1989]
<i>Oli</i> <sup>dry</sup>	(Fe,Mg) <sub>2</sub> SiO <sub>4</sub>	Lattice	1373-1773	10 <sup>-4</sup>	338±14	4.6×10 <sup>-9</sup>	[Dohmen et al., 2002]
<i>Oli</i> <sup>wet</sup>	(Fe,Mg) <sub>2</sub> SiO <sub>4</sub>	Lattice	1473-1623	2	324 <sup>(1)</sup>	1.4×10 <sup>-4</sup>	[Costa and Chakraborty, 2008]
<i>Wd</i> <sup>wet</sup>	(Fe,Mg) <sub>2</sub> SiO <sub>4</sub>	Lattice	1673-1873	16	291±79	3.2×10 <sup>-11</sup>	[Shimojuku et al., 2009]
<i>Rw</i> <sup>wet</sup>	(Fe,Mg) <sub>2</sub> SiO <sub>4</sub>	Lattice	1673-1873	22	367±83	3.2×10 <sup>-9</sup>	[Shimojuku et al., 2009]
<i>Pv</i> <sup>dry</sup>	(Mg,Na)SiO <sub>3</sub>	Lattice	1673-2073	25	501±80	9.2×10 <sup>-4</sup>	[Dobson et al., 2008]
<i>Wd</i> <sup>wet</sup>	(Fe,Mg) <sub>2</sub> SiO <sub>4</sub>	Boundary	1673-1873	16	244±86	1.6×10 <sup>-17</sup>	[Shimojuku et al., 2009]
<i>Rw</i> <sup>wet</sup>	(Fe,Mg) <sub>2</sub> SiO <sub>4</sub>	Boundary	1673-1873	22	246±70	7.9×10 <sup>-18</sup>	[Shimojuku et al., 2009]

\*<sup>(1)</sup> After normalization to a constant oxygen fugacity.

### (1) Oxygen diffusion in olivine/forsterite

The lattice diffusion coefficients of oxygen in forsterite were measured by Reddy et al. [1980], Jaoul et al. [1980] and Andersson et al. [1989] at ambient pressure under dry and controlled oxygen fugacity conditions. In their studies, the activation energy were determined to

be ~300-370 kJ/mol. This value is much smaller than the energy for silicon diffusion in forsterite, indicating that the concentration of oxygen defects is higher than silicon defects. Besides, no  $f_{O_2}$  dependence was found for oxygen diffusion.

Yurimoto et al. [1992] also measured oxygen diffusion rate in forsterite at ambient pressure. They found that oxygen diffuses along grain boundaries or dislocations about four orders of magnitude faster than that in lattice. However, they only conducted experiments within a narrow temperature range (1370 and 1470 K). The activation energy for oxygen grain-boundary diffusion is not determined.

The oxygen diffusion rate were also experimentally measured in natural iron-bearing olivine at ambient pressure and dry conditions [Dohmen et al., 2002; Gérard and Jaoul, 1989; Ryerson et al., 1989]. Slightly lower activation energy (270-340 kJ/mol) was found than pure forsterite. In contrast with forsterite, Gerard and Jaoul [1989] and Ryerson et al. [1989] found a positive  $f_{O_2}$  dependence of  $D_{O}^{lat}$ , supporting an interstitial mechanism for oxygen diffusion because the concentration of oxygen interstitials increases with increasing  $f_{O_2}$  [Smyth and Stocker, 1975; Stocker and Smyth, 1978], which should be an unfavorable diffusion mechanism because oxygen has the largest ionic radius in  $(Mg,Fe)_2SiO_4$  olivine. On the other hand, [Walker et al., 2003] pointed out that a vacancy mechanism should be more favorable. Oxygen interstitials may be formed mediated in natural iron-bearing olivine by oxidation of ferrous iron to ferric iron and induce an interstitial mechanism for oxygen diffusion under high  $f_{O_2}$ .

Costa and Chakraborty [2008] measured oxygen lattice diffusion coefficients in natural olivine at high pressure (2 GPa) with about 30-50 wt. ppm water. By comparing with that obtained at ambient pressure and dry condition by Dohmen et al. [Dohmen et al., 2002], they found a significant effect of water on oxygen diffusion rate. Even 45 wt. ppm water could enhance the  $D_{O}^{lat}$  by about one order of magnitude (**Fig. 1.25**). Costa and Chakraborty [2008] also reported an activation energy of ~324 kJ/mol (~437 kJ/mol before oxygen fugacity correction). This value is identical as that determined in dry olivine (270-340 kJ/mol) [Dohmen et al., 2002; Gérard and Jaoul, 1989; Ryerson et al., 1989].

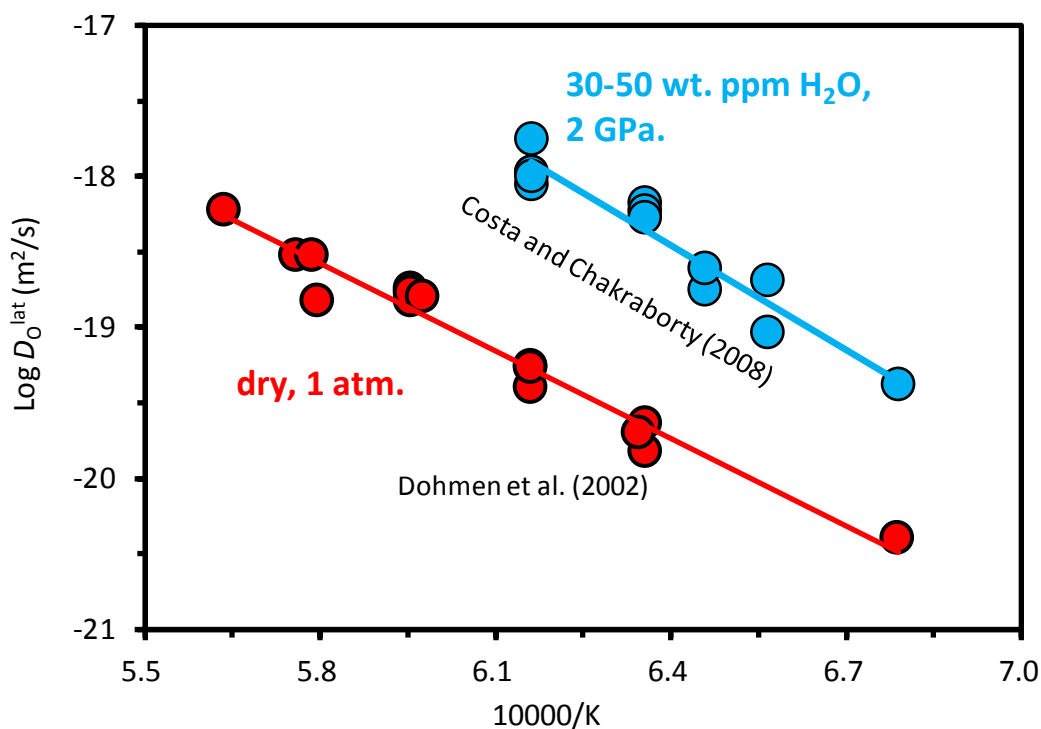


**Fig. 1.25.** Oxygen lattice diffusion coefficient in dry and wet olivine

## (2) Oxygen diffusion in wadsleyite and ringwoodite

Oxygen lattice diffusion coefficients in synthesized iron-bearing wadsleyite and ringwoodite aggregates are shown in **Fig. 1.26**. Both of them are about 0.5 orders of magnitude higher than silicon diffusion, and more than six orders of magnitude slower than Mg/Fe inter-diffusion [Farber *et al.*, 2000]. The activation energies for  $D_{O}^{lat}$  in wadsleyite and ringwoodite are determined to be  $291 \pm 79$  and  $367 \pm 83$  kJ/mol,  $\sim 100$  kJ/mol smaller than that for silicon diffusion.

Oxygen grain-boundary diffusion coefficients in wadsleyite and ringwoodite were simultaneously measured with lattice diffusion by Shimojuku *et al.* [2009], who reported the activation energies of  $244 \pm 86$  and  $246 \pm 70$  kJ/mol, respectively. The  $\delta D_{O}^{lat}$  at 1673-1873 K are about  $10^{-23}$ - $10^{-25}$  m<sup>3</sup>/s (**Fig. 1.27**). If we consider a grain size of  $\sim 1$ -10 mm, the effective oxygen diffusion coefficient in wadsleyite and ringwoodite along grain boundaries are about  $10^{-20}$ - $10^{-23}$  m<sup>2</sup>/s, about 1-2 orders of magnitude lower than oxygen lattice diffusion. Similar as silicon, the mass transport of oxygen in wadsleyite and ringwoodite under mantle transition zone conditions should be dominated by oxygen lattice diffusion.

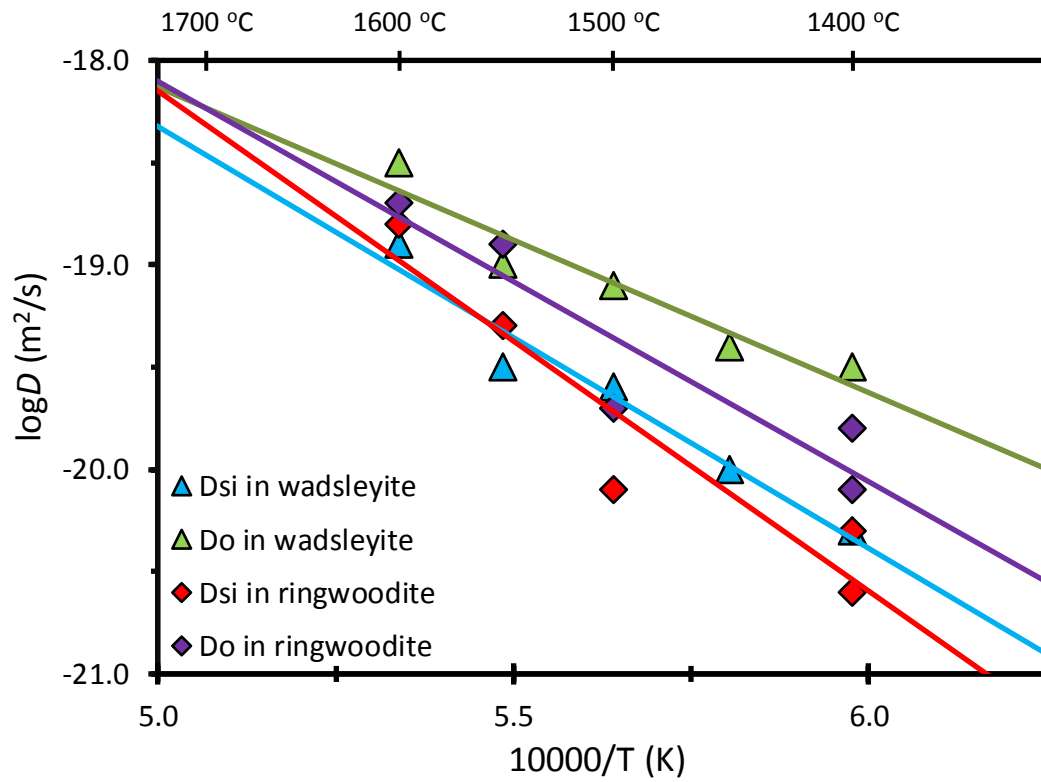


**Fig. 1.26.** Similar  $D_{\text{Si}}^{\text{lat}}$  and  $D_{\text{O}}^{\text{lat}}$  in wadsleyite and ringwoodite [Shimojuku et al., 2009].

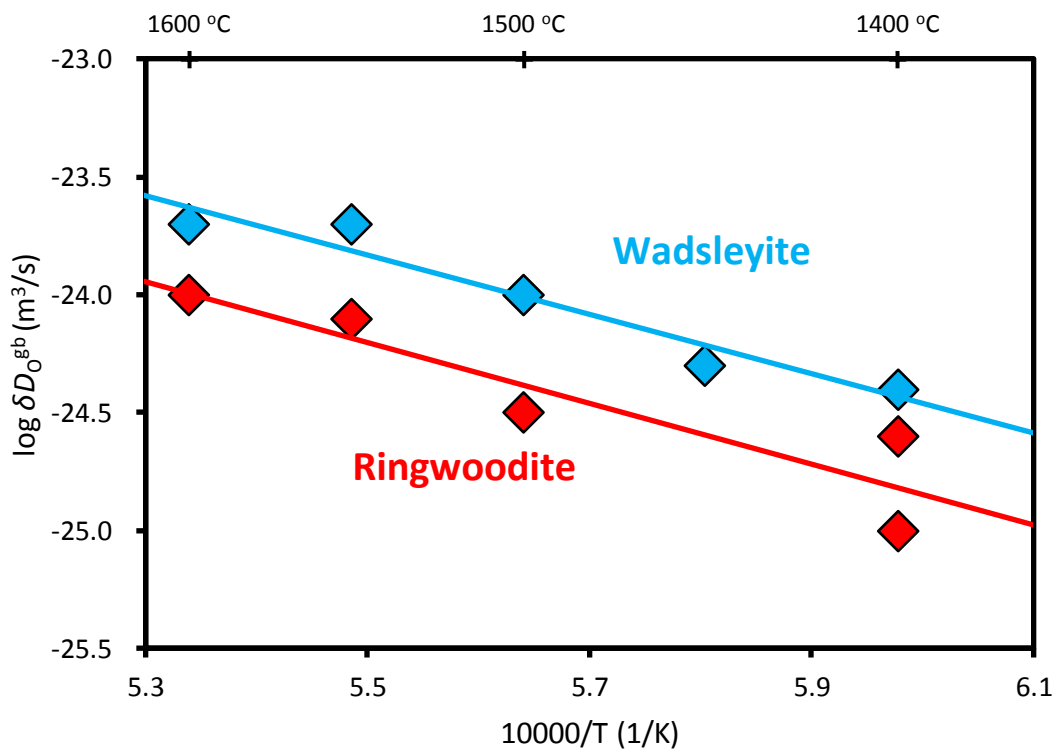


**Fig. 1.27.** Oxygen grain boundary diffusion coefficients in wadsleyite and ringwoodite determined by Shimojuku et al. [2009].

### ***(3) Oxygen diffusion in perovskite***

Dobson et al. [2008] measured oxygen diffusion coefficients in Mg-perovskite, and reported an activation energy of  $\sim 510 \pm 70$  kJ/mol for lattice diffusion. This value is extremely high in comparing with that for silicon diffusion [Dobson et al., 2008], while in olivine, wadsleyite, and ringwoodite, oxygen diffusion usually has lower activation energy than silicon [Costa and Chakraborty, 2008; Shimojuku et al., 2009]. Besides, in olivine, wadsleyite, and ringwoodite, silicon and oxygen have similar diffusion rates, and five to six orders of magnitude slower than Mg/Fe diffusion [Costa and Chakraborty, 2008; Hier-Majumder et al., 2005; Shimojuku et al., 2009]. However, in perovskite, silicon and magnesium diffusion rates are similar, but about 1-2 orders of magnitude slower than oxygen [Dobson et al., 2008; Holzapfel et al., 2005; Xu et al., 2011; Yamazaki et al., 2000]. This is explained by Xu et al. [2011] who supposed a four-step jump defect models, and diffusion of silicon and magnesium are limited by oxygen diffusion.

### ***(4) Activation volume for oxygen diffusion***

There are no reported results about pressure dependence of  $D_O$  in mantle minerals. Zhang et al. [2011] calculated the activation volume for oxygen diffusion in  $Mg_2SiO_4$  polymorphs and  $MgSiO_3$  perovskite using a so called  $cB\Omega$  model ( $g^{act} = c^{act}B\Omega$ , where  $g^{act}$  is the defect Gibbs free energy,  $c^{act}$  is the dimensionless factor which is independent of pressure and temperature,  $B$  is the isothermal bulk modulus, and  $\Omega$  is the volume of atom), and reported values of activation volumes as 17, 11,  $\sim 10$ , and  $\sim 4.5$  cm<sup>3</sup>/mol for olivine, wadsleyite, ringwoodite, and perovskite, respectively.

## **1.7 Aim of this study**

Olivine is the most abundant mineral and also considered to be the weakest phase in the Earth's upper mantle [Durham and Goetze, 1977a; Kohlstedt and Goetze, 1974; Mackwell, 1991]. Therefore, it should dominate the plastic flow in upper mantle [Karato and Wu, 1993]. Because silicon and oxygen are the slowest diffusion species with similar diffusion rates in olivine [Costa and Chakraborty, 2008], the upper mantle rheology should be controlled by self-diffusion of silicon and also oxygen. Many experimental studies about measurements of silicon and oxygen

self-diffusion have been carried out previously as discussed in above section. However, there still remains some questions remain.

### 1.7.1 Discrepancy between silicon diffusion and deformation in olivine

[Goetze and Kohlstedt, 1973] reported a result of  $\sim 100$  nm of prismatic dislocation loops after annealing the olivine sample at 1570 K for 1 hour under dry conditions. The diffusion coefficient of silicon is calculated from deformation rate using **Eqs. 1.36**, which is shown in **Fig. 1.28**. In contrast, Dohmen et al. [2002] measured  $D_{Si}$  in single crystals of natural olivine at ambient pressure under dry conditions, with results by 2-3 orders of magnitude smaller than that deduced from deformation experiments normalized to the same temperature condition.

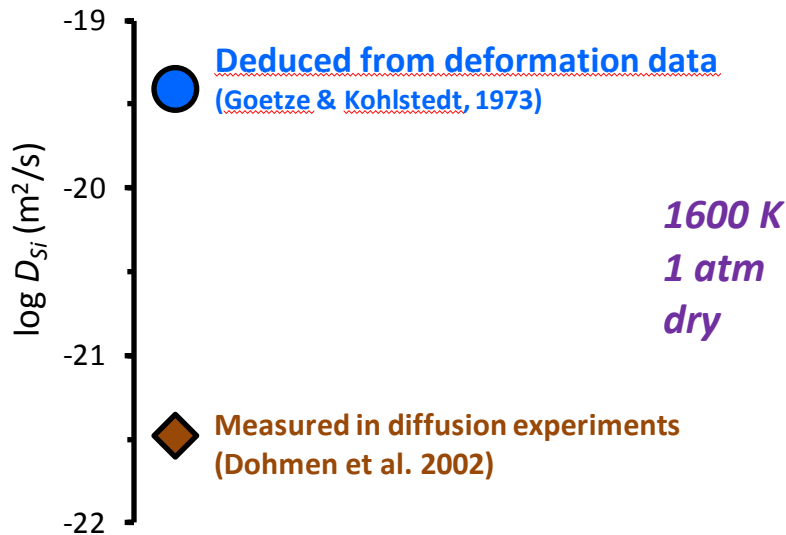


**Fig. 1.28.** Discrepancy between measured silicon diffusion coefficient and that deduced from experimental deformation data in olivine.

Besides, olivine single crystal deformed at ambient pressure and high temperatures require a significant amount of climb, with climb contributing 20 to 30 % of the measured strain [Durham and Goetze, 1977a]. Low-angle tilt boundaries are prominent features in olivine grains deformed under anhydrous, as well as hydrous, conditions (e.g. [Bai and Kohlstedt, 1992; Mackwell et al., 1985]). Formation of such boundaries requires diffusion over distances of at least a few nanometers to a few tens of nanometers at 1600-1700 K in  $\sim 1$ -2 hours, which suggests the silicon diffusion coefficient of  $10^{-19}$ - $10^{-20}$   $m^2/s$  at this temperature. All of these observations

under dry conditions indicate that the measured silicon self-diffusion and the kinetics of dislocation climb are could be underestimated by 2-3 orders of magnitude. Though the high temperature creep of olivine is believed to be controlled by silicon diffusion [Frost and Ashby, 1982; Weertman, 1999], the present experimental results of creep rates in olivine [Durham and Goetze, 1977a; Goetze and Kohlstedt, 1973] cannot be explained by the silicon diffusion coefficients [Dohmen et al., 2002]. This discrepancy remains to be resolved.

### 1.7.2 Pressure dependence of silicon diffusion and creep rate

The results of deformation experiments show very large pressure dependence of creep rate in olivine (the activation volume is usually  $>10 \text{ cm}^3/\text{mol}$ ) [Borch and Green II, 1989; Karato and Ogawa, 1982; Karato and Jung, 2003]. Since the olivine deformation should be controlled by silicon diffusion, the activation volume for creep rate should be the same as that for silicon diffusion. However, Bejina et al. [1997; 1999] reported that pressure has no effect on silicon diffusion rate: the activation volume is nearly zero ( $-1.9 \pm 2.4$  [Bejina et al., 1997] or  $0.7 \pm 2.3 \text{ cm}^3/\text{mol}$  [Bejina et al., 1999])

We note that the high activation volumes in deformation experiments are all obtained at low pressures ( $< 2 \text{ GPa}$ ) [Karato and Ogawa, 1982; Karato and Rubie, 1997; Karato and Jung, 2003; Kohlstedt et al., 1980; Ross et al., 1979]. In order to precisely determine the activation volume, a large pressure range is necessary [Bejina et al., 1999]. The pressure ranges in Bejina et al. [1997; 1999] were relatively wider (4 - 9 GPa). However, their data points were rather scattered (**Fig. 1.29**), in which the pressure dependence could be hidden. Therefore, a more precise measurement of activation for silicon diffusion is necessary.

Besides, the silicon diffusion coefficients in dry olivine at ambient pressure and high pressures were measured by Dohmen et al. [2002] and Bejina et al. [1997; 1999], respectively. If we correct their results to the same temperature using the activation energy they reported, we find that the  $D_{\text{Si}}^{\text{lat}}$  extrapolated from high pressures determined by Bejina et al. [1997; 1999] to ambient pressure is about 1.5 orders of magnitude higher than that measured at ambient pressure by Dohmen et al. [2002].

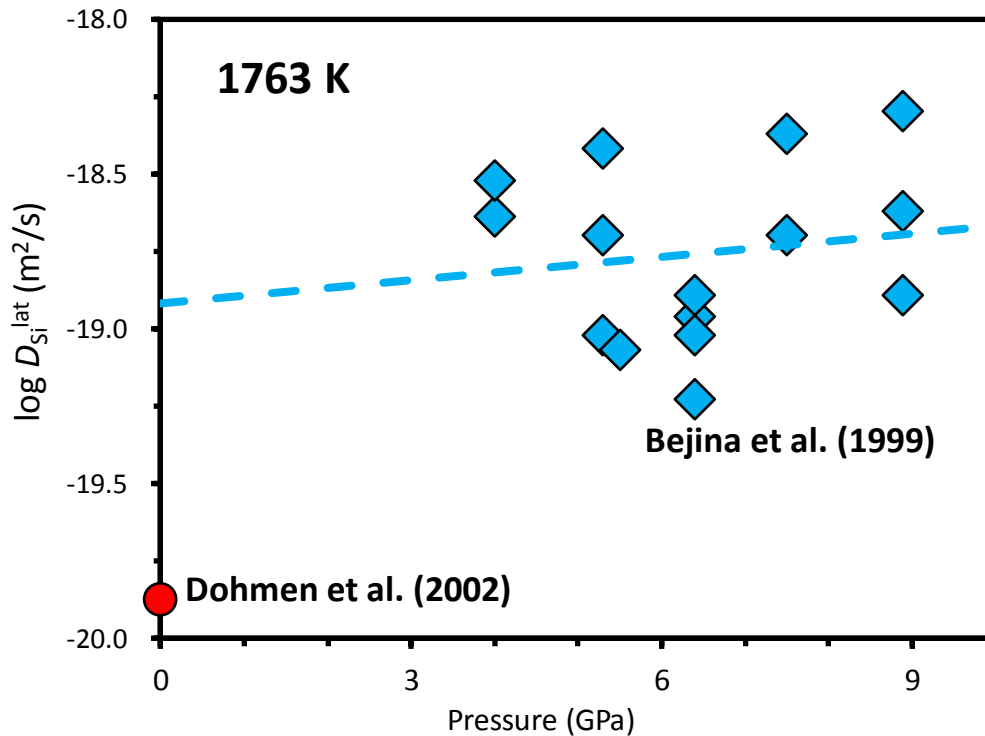


**Fig. 1.29.** Large discrepancy of silicon diffusion rate in olivine between high pressure and ambient pressure experiments.

### 1.7.3 Effect of water on silicon diffusion and creep rate in olivine

Experimental olivine deformation studies have suggested a significant effect of water on both dislocation and diffusion creep rates [Hirth and Kohlstedt, 2003; Jung and Karato, 2001; Karato et al., 1986; Mei and Kohlstedt, 2000a; b]. Even several tens wt. ppm of water could enhance the diffusion and dislocation creep rates by orders of magnitude. However, we note that those studies used polycrystalline olivine samples with over-saturated water. In such setups, free water should have existed on the grain boundaries and have largely enhanced grain boundary sliding and/or pressure solution creep, rather than dislocation or diffusion creeps in grain interior. On the other hand, the majority of the upper mantle is water un-saturated and free water is unlikely to exist, and therefore, the rock deformation in upper mantle should not be enhanced by free water. Hence, it is possible that the effect of water on creep rates in the real mantle is overestimated.

As described in **section 1.6.1**, Costa and Chakraborty [2008] also suggested that even small amount of water (40 wt. ppm) could enhance silicon diffusion in olivine by three of magnitude

by comparing the results of  $D_{Si}^{lat}$  obtained at 2 GPa and wet conditions with that obtained by Dohmen et al. [2002] at ambient pressure and dry conditions. However, the difference of  $D_{Si}$  at 2 GPa between 30-50 and >370 wt. ppm of water is very small: i.e. <0.2 log unit, within experimental error. On the other hand, the difference of  $D_{Si}$  is three orders of magnitude between “dry” at ambient pressure and “wet” at 2 GPa (**Fig. 1.30**). It is not absolutely clear the high  $D_{Si}$  measured at high pressure can be attributed to the effect of water or not.

The effect of water on oxygen diffusion coefficients has also been considered to be significant [Costa and Chakraborty, 2008]. However, similar as the effect of water on silicon diffusion rate, this conclusion is also based on the comparison of data sets obtained at wet and high pressure [Costa and Chakraborty, 2008] with that obtained at ambient pressure and dry conditions [Dohmen et al., 2002]. Therefore, the real effects of water on silicon and oxygen diffusion rates are still unknown.

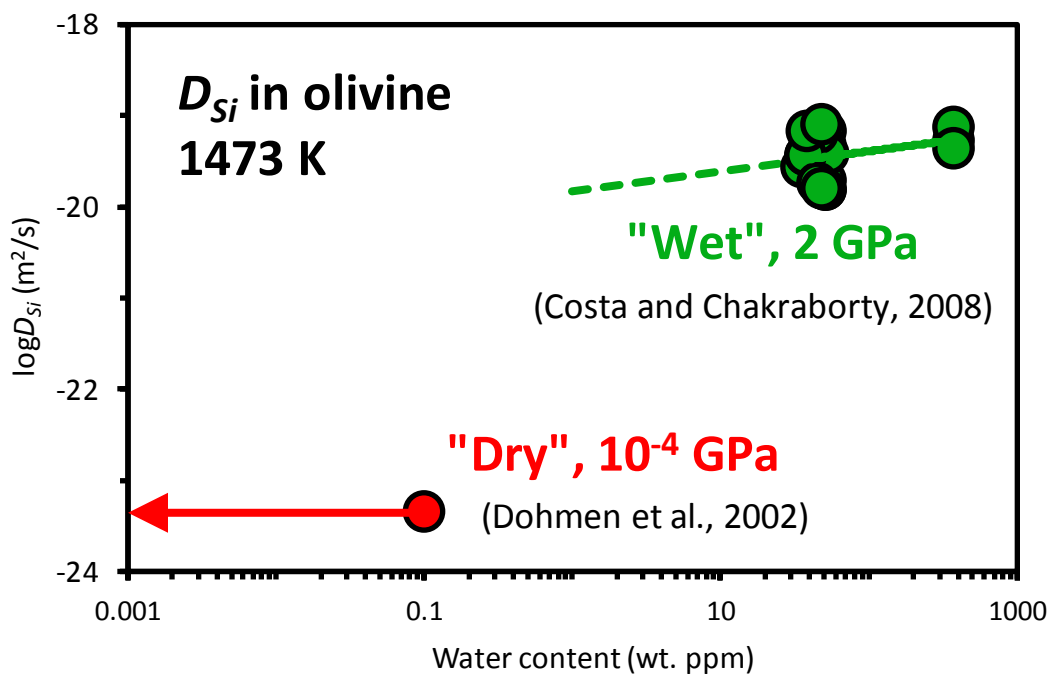


**Fig. 1.30.** Difference of  $D_{Si}$  between 30-50 and >370 wt. ppm of water is 0.2 log unit, while it is three orders of magnitude between 30-50 wt. ppm of water at 2 GPa and dry at ambient pressure. The data points were calibrated to 1473 K using their reported activation energy. The data point at “dry” condition is plotted at water content of 0.1 wt. ppm with an arrow.

#### 1.7.4 Grain-boundary diffusion in olivine under upper mantle conditions

Farver and Yund [2000] reported experimental results of silicon grain-boundary diffusion coefficients in forsterite. The activation energy for grain-boundary diffusion is about 200 kJ/mol, which is extremely lower than lattice diffusion (~400-500 kJ/mol), indicating that Coble-diffusion creep should dominate at low temperature regions while dislocation creep dominate at high temperature regions. As discussed in **Section 1.4.4**, this is inconsistent with rock deformation experiments which suggested a diffusion creep dominated deeper upper mantle and dislocation creep dominated shallow upper mantle [Hirth and Kohlstedt, 2003; Karato, 1992; Karato and Wu, 1993].

Besides, Farver and Yund's [2000] experiments were only conducted at ambient pressure and dry conditions. Based on results of silicon lattice-diffusion and deformation experiments, both pressure and water could affect the silicon diffusion rates in mantle minerals [Costa and Chakraborty, 2008; Karato and Jung, 2003]. Therefore, their results cannot be directly applied to the Earth's mantle because of its hydrous and high-pressure conditions. The effects of pressure, temperature, and water content on silicon grain-boundary diffusion rates are needed to be determined to understand the upper mantle rheology.

#### 1.7.5 This study

The purpose of this study is to resolve the remaining problems discussed above. Because the effects of iron content on silicon and oxygen diffusion rates, as well as on creep rates, are negligible as mentioned in **Section 1.4.4** and **1.6.1**, iron-free pure forsterite samples are used in this study.

To resolve the discrepancy between silicon diffusion and deformation in olivine and to determine the activation volume for silicon diffusion, we have measured silicon self-diffusion coefficients in a forsterite single crystal from ambient pressure to 13 GPa under dry conditions. As discussed below, we made special care to have smooth sample surfaces, which brought us a more precise and accurate determination of diffusion profiles by SIMS (secondary ion mass spectrometry) because the rough sample surface could induce significant error source.

In order to know the role of water on upper mantle rheology, we systematically measured silicon and oxygen diffusion coefficients in a forsterite single crystal as a function of water content ranging from <1 up to ~800 wt. ppm. We used well-controlled water sources the same experimental setups for water-doping and diffusion annealing, which successfully made a constant value of water content during diffusion.

We also measured silicon grain-boundary diffusion rate in a forsterite aggregates sample as a function of pressure, temperature, oxygen fugacity, and water content, and investigated the deformation mechanisms in the Earth's upper mantle by comparing the diffusion and dislocation creep rates calculated from silicon lattice and grain-boundary diffusion coefficients. The experimental details and results are described below and in the following chapters.

## 1.8 General experimental methods in this study

Because of the slow diffusion rates of silicon and oxygen, the silicon and oxygen diffusion profiles are usually very short under the laboratorial conditions. Even the sample is annealed at high temperature (e.g. 1800 K) with long duration (e.g. 50 hours), the lengths diffusion profiles are at the levels of a couple of microns. Some error sources like surface roughness of samples, resolution of analytical instruments, may largely affect the experimental results. Thus, special experimental techniques should be carried out to reduce the experimental uncertainties for silicon and oxygen diffusion experiments.

### 1.8.1 Sample preparation

**Figure 1.31** shows the general method for silicon and oxygen diffusion experiments in olivine. Firstly, the sample should be highly polished (**Fig. 1.31a**). In this study, it is mechanical polished by diamond powder with grain size of 0.25  $\mu\text{m}$  until free of any visible scratches, and then chemically polished using an alkaline colloidal silica solution for a long duration (>1 hours) until any small scratches produced by polishing with the diamond powder are removed. The surface roughness can be reduced to less than 10 nm in following this polishing procedure with an example of sample surface shown in **Fig. 1.32** measured by a 3D-nanofocus microscope with a resolution of 1 nm.

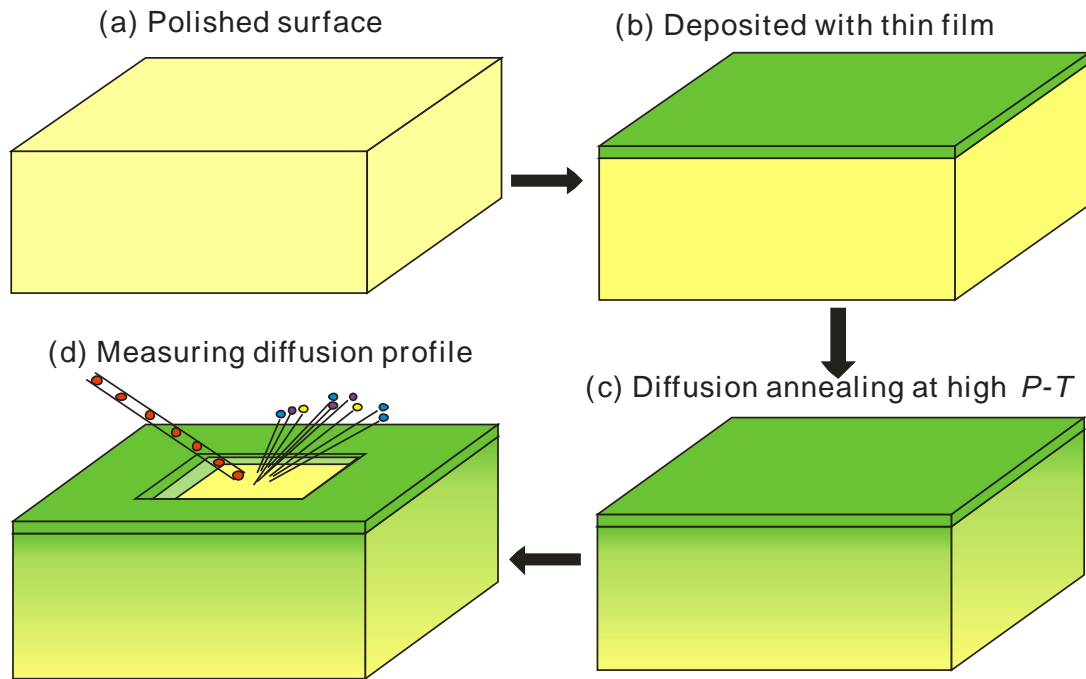


**Fig. 1.31.** Experimental procedure for silicon and oxygen diffusion measurements. (a) Highly polished sample. (b) Sample deposited with  $^{18}\text{O}$  and  $^{29}\text{Si}$  enriched thin film, while the substrate has natural ratios of  $^{18}\text{O}/\Sigma\text{O}$  and  $^{29}\text{Si}/\Sigma\text{Si}$ . (c) Sample annealed at high temperature. The deposited thin film forms a polycrystalline layer, with rough surface. The concentrations of  $^{18}\text{O}$  and  $^{29}\text{Si}$  decrease with increasing depth. (d) Crater after SIMS analysis.

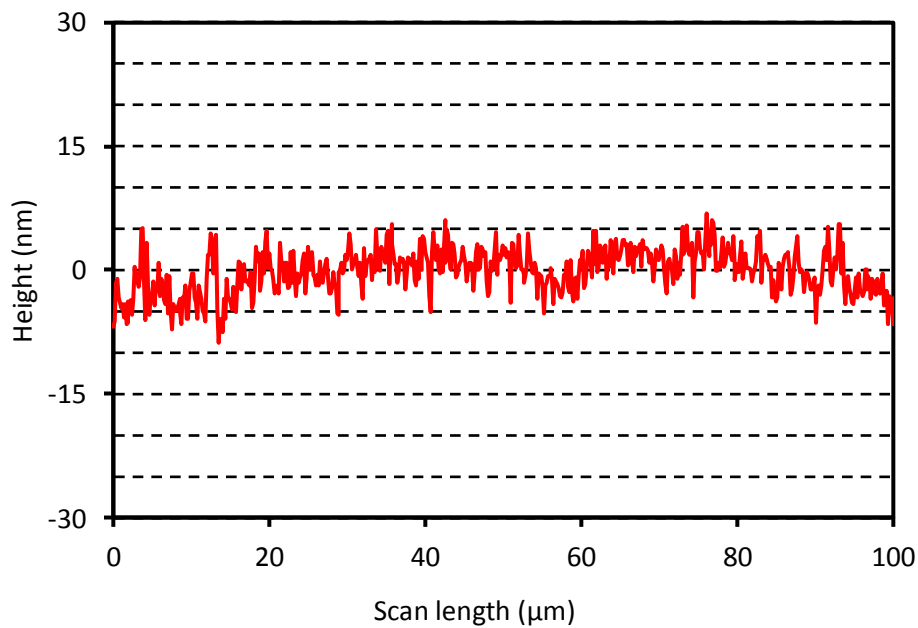


**Fig. 1.32.** Sample surface after fine polished in an alkaline colloidal silica solution measured by 3D-nanofocus microscope.

### 1.8.2 Thin film deposition

Subsequently, the highly polished sample surface is deposited with an isotopically enriched thin film ( $\text{Mg}_2^{29}\text{Si}^{18}\text{O}_4$  forsterite film was used in this study) for diffusion couple (**Fig. 1.31b**). The chemical composition of the thin film should be the same as the substrate but isotopically enriched. The thickness of thin film depends on the length of diffusion profile. In this study, a 300-500-nm thick film was used. **Fig. 33** shows the pulsed laser deposition system (PLD) available at Ruhr-University, Bochum, which is an efficient apparatus to deposit thin films of complex silicate and oxide compositions [*Dohmen et al.*, 2002]. The principle of the PLD system is shown in **Fig. 33a**. A pulsed beam of Excimer Laser with wavelength of 248/193 nm heats the rotating target (isotopically enriched), generating an isotopically enriched plasma, which depositing onto the substrate located under the target. The substrate is heated up to 400-700 K by a SiC heater in the vacuum sample chamber, which is necessary to remove the free water on the sample surface to make a good contact between thin film and substrate.

Note that the composition of the thin film may slightly differ from the target material, for example the thin film from a forsterite ( $\text{Mg}_2\text{SiO}_4$ ) target has a stoichiometry of  $\text{Mg}_2\text{SiO}_{4.3}$  [*Dohmen et al.*, 2002], which might lead to a non-equilibrium defect chemistry in a diffusion couple. However, this is not a serious problem in this study. As shown in the following chapters, the experimental results show highly symmetric diffusion profiles, which means the diffusion coefficients in the thin film and substrates should be very similar. It is reasonable because the annealing duration for diffusion is usually very long. The stoichiometry could reach the equilibrium in a short time at the beginning and the diffusion happens under an equilibrium state for most of the duration.

### 1.8.3 Diffusion annealing

After thin film deposition, the sample is annealed at a given pressure and temperature condition (**Fig. 1.31c**) for diffusion. During annealing,  $^{18}\text{O}$  and  $^{29}\text{Si}$  diffuse into the substrate. The concentrations of  $^{29}\text{Si}$  and  $^{18}\text{O}$  are functions of depth and annealing time. The diffusion depth depends on the experimental conditions and annealing duration. In this study, most diffusion annealing experiments were performed with Kawai-type multi-anvil apparatus (**Fig. 1.34**) installed at University of Bayreuth, Bayreuth, Germany, and at Okayama University,

Misasa, Japan. Some ambient pressure experiments were performed using an atmosphere or a gas mixing furnace at University of Bayreuth.

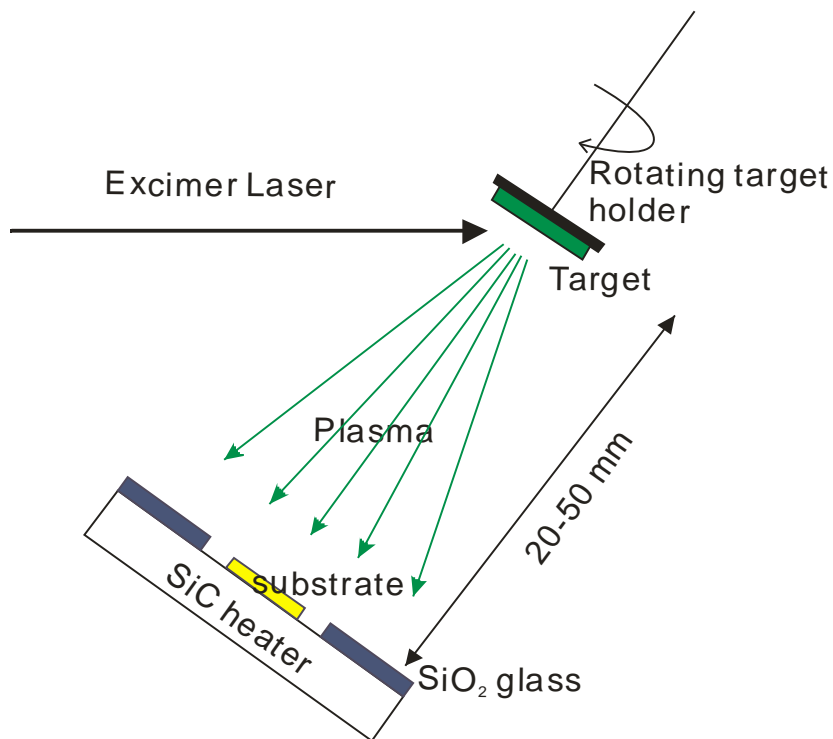


**Fig. 1.33.** (a) Principle of PLD system simplified from Dohmen et al. [2002]. (b) Pulsed laser deposition (PLD) available at Ruhr-University, Bochum.



**Fig. 1.34.** 1200 ton Kawai-type multi-anvil apparatus installed at University of Bayreuth.

#### **1.8.4 Diffusion profile analysis**

Different analytical techniques are used for analysis the diffusion profiles of different elements. For example, FT-IR spectrometer is a typical way for analyze hydrogen diffusion in mantle minerals because the hydrogen diffuses fast in minerals, which induces long diffusion profiles [Demouchy and Mackwell, 2003]. For Fe-Mg diffusion in minerals, electron microprobe analysis (EPMA) could be used [Holzapfel *et al.*, 2007]. For trace elements with high diffusion coefficients, ICP-MS is a suitable way because of its high mass resolution [Lerchbaumer and Audéat, 2012]. In the case of oxygen and silicon self-diffusion, high distance resolution technique, for example secondary ion mass spectrometry (SIMS) [Jaoul *et al.*, 1981] or Rutherford backscattering spectrometry (RBS) [Jaoul *et al.*, 1980] is required because of their short diffusion lengths (**Fig. 1.31d**).

In this study, we used SIMS operated at a depth profiling mode to determining the diffusion profiles of Si and O, in which the primary ion beam sputters a crater on the sample surface (**Fig. 1.35**), and the secondary ions from the crater are extracted by applying an accelerating voltage between the sample and an extraction plate, and this secondary ion beam is passed through a mass spectrometer for mass separation (**Fig. 1.36**). A Cameca 6f SIMS (**Fig. 1.37**) installed at

the Helmholtz Centre Potsdam, Germany was used in this project. Some profiles were obtained using a Cameca IMS-6f SIMS at Hokkaido University, Japan.

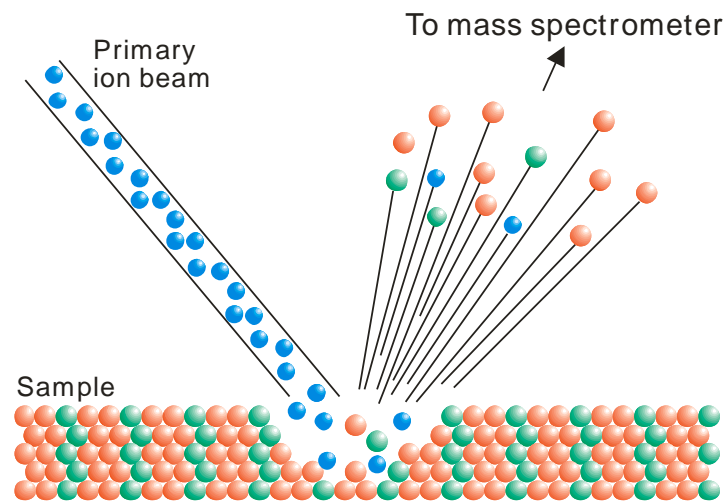


**Fig. 1.35.** SIMS sputtering. Primary ion beam sputters the sample surface, and ions from the sputtering crater are detected by a mass spectrometer.

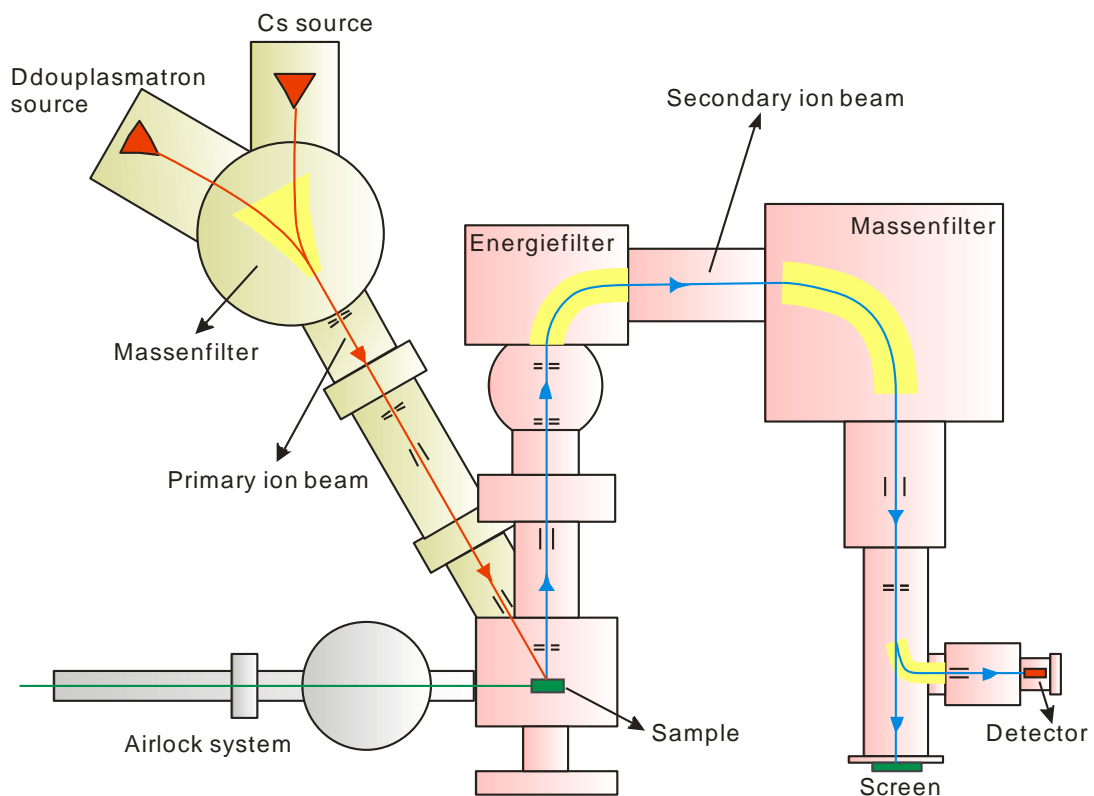


**Fig. 1.36.** Principle of SIMS. Sample with a holder is loaded into the sample stage from "Air lock". Primary Cs<sup>+</sup> or O<sup>-</sup> (duoplasmatron) ion beam through a mass filter sputters the high-

voltage charged sample surface. The secondary ions from the sputtering crater are then passed through a mass spectrometer for mass separation.



**Fig. 1.37.** Cameca 6f SIMS installed at the Helmholtz Centre Potsdam, Germany.

### 1.8.5 Obtain diffusion coefficients and other parameters

The diffusion coefficients of silicon and oxygen can be obtained by fitting the diffusion profiles to the solution of Fick's second law (**Eqs. 1.4**). Since diffusion coefficients of silicon and oxygen are functions of pressure, temperature, water content, silicon activity, oxygen fugacity, the obtained diffusion coefficients can be fitted to the Arrhenius equation to obtain the parameters for each factor:

$$D = A_0 (C_{\text{H}_2\text{O}})^r (a_{\text{SiO}_2})^s (f_{\text{O}_2})^p \exp\left(-\frac{\Delta H + P\Delta V}{RT}\right) \quad (1.41)$$

where  $D$  is the silicon or oxygen self-diffusion coefficient,  $A_0$  is the pre-factor,  $C_{\text{H}_2\text{O}}$  is the water content (or water fugacity,  $f_{\text{H}_2\text{O}}$ ),  $a_{\text{SiO}_2}$  is the silicon activity,  $f_{\text{O}_2}$  is the oxygen fugacity,  $\Delta H$  is the activation energy,  $P$  is the pressure,  $\Delta V$  is the activation volume,  $R$  is the gas constant,  $T$  is the absolute temperature.  $r$ ,  $s$ , and  $p$ , are the exponents for water content, silicon activity, and oxygen fugacity, respectively.

# Chapter 2

---

## Silicon self-diffusion in dry forsterite

### 2.1 Abstract

Silicon self-diffusion coefficients ( $D_{Si}$ ) in dry synthetic forsterite single crystals were measured at temperatures of 1600 and 1800 K, from ambient pressure up to 13 GPa using an ambient pressure furnace and Kawai-type multi-anvil apparatus. The water contents in the samples were carefully controlled at <1 wt. ppm. Diffusion profiles were obtained by secondary ion mass spectrometry in depth profiling mode. Small negative pressure dependence of  $D_{Si}$  is determined with an activation volume of  $1.7 \pm 0.4$  cm<sup>3</sup>/mol. The activation energy is found to be  $407 \pm 31$  kJ/mol.  $\text{Log}D_{Si}$  values ( $D_{Si}$  in m<sup>2</sup>/s) at 1600 and 1800 K at ambient pressure are determined to be  $-19.7 \pm 0.3$  and  $-18.1 \pm 0.1$ , respectively. These values are  $\sim 2.4$  orders of magnitude higher than those reported by Jaoul et al. (1981). We speculate that their low  $D_{Si}$  might reflect the effects of a horizontal migration of the isotopically enriched thin films applied on sample surfaces, which may inhibit diffusion into the substrate during diffusion annealing. Our results for  $D_{Si}$  resolves the inconsistency between  $D_{Si}$  measured in diffusion experiments and those deduced from dislocation climb rates measured in deformation experiments.

### 2.2 Introduction

Understanding dynamic flows in the mantle is essential for solid earth geophysics. Plastic deformation of minerals is controlled by diffusion and dislocation creep. Needless to say, diffusion creep is controlled by diffusion. Dislocation creep under the high-temperature and low-stress conditions as in the deep mantle is dominated by dislocation climb, which is also thought to be controlled by diffusion [Frost and Ashby, 1982; Weertman, 1999], although there are some arguments suggesting other factors play important roles in plastic deformation or other deformation mechanisms [Karato, 2010]. Thus, creep in mantle minerals is related to their diffusion coefficients, which largely define mantle viscosity [Yamazaki et al., 2000]. Silicon is the slowest diffusing species in most mantle minerals [Costa and Chakraborty, 2008; Dobson et al., 2008; Shimajuku et al., 2009], and it is therefore expected to be the element controlling creep

rate.  $(\text{Mg,Fe})_2\text{SiO}_4$  olivine is believed to represent approximately 60 vol. % of the upper mantle [Ringwood, 1991]. Hence, understanding the silicon self-diffusion in olivine is essential for understanding the rheological properties in the upper mantle.

Dohmen et al. [2002] measured silicon self-diffusion coefficients ( $D_{\text{Si}}$ ) in single crystals of natural olivine at ambient pressure under dry conditions. Hirth and Kohlstedt [2003] and Kohlstedt [2006] investigated the dislocation climb rate in olivine based on the results of Dohmen et al. [2002], from which they calculated a climb rate of only 1 nm at 1670 K in 1 hour under anhydrous conditions. In contrast, dislocation climb rates in natural olivine measured by Goetze and Kohlstedt [1973] were with  $\sim 100$  nm of prismatic dislocation loops after 1 hour at 1570 K and dry conditions. Therefore, the rates of silicon self-diffusion and dislocation creep are in disagreement by 2-3 orders of magnitude.

Forsterite is the Mg-rich end member of olivine. It is known that iron is important for upper mantle rheology because natural olivine is iron-bearing. Durham and Goetze compared the plastic deformation rates of single crystals of pure forsterite and iron-bearing olivine ( $\text{Fo}_{92}$ ), which they found to have almost identical strain rates. Hence, the rheological properties of forsterite should provide a basic understanding of upper mantle rheology.

Andersson et al. [1989] measured the  $D_{\text{Si}}$  in forsterite. However, their study shows a large range in activation energy from 150 to 620 kJ/mol in different analyses. Jaoul et al. [1981] measured  $D_{\text{Si}}$  in forsterite at ambient pressure under dry conditions, where they sputter coated samples with 10 nm  $^{30}\text{Si}$  enriched films of forsterite, which were subsequently annealed at 1600 – 1950 K and ambient pressure with durations of up to 1 month, and measured the diffusion profiles using Backscattering Spectrometry. Their results showed  $\log D_{\text{Si}} (\text{m}^2/\text{s}) = -22.1$  at 1600 K, again 2-3 orders of magnitude lower than the rates estimated from dislocation creep rate by Goetze and Kohlstedt [1973]. Hence, it is necessary to reexamine silicon self-diffusion in forsterite.

In this study we measured  $D_{\text{Si}}$  in forsterite at 1600 and 1800 K, at pressures from ambient pressure to 13 GPa, and under relatively dry conditions ( $C_{\text{H}_2\text{O}} < 1$  wt. ppm). Our results show a much higher diffusion rate of silicon compared to results reported either by Jaoul et al. [1981] in forsterite or by Dohmen et al. [2002] in natural olivine. Significantly, our results of silicon

diffusion are consistent with that derived from the dislocation creep rate by deformation experiments [Goetze and Kohlstedt, 1973].

## 2.3 Experimental and analytical methods

### 2.3.1 Starting material and sample preparing

A forsterite single crystal (**Fig. 2.1a**) with no cracks or optically visible inclusions was obtained from the Japanese company “Oxides”. The chemical composition of this crystal is essentially pure  $\text{Mg}_2\text{SiO}_4$ . No other elements were detected by electron microprobe. Its trace elements were examined by Inductively-Coupled-Plasma Mass-Spectrometry (ICP-MS) at University of Bayreuth, Germany, using a Geolas M 193 nm ArF-Excimer laser attached to an Elan DRC-e mass spectrometer, operated at a frequency of 10 Hz and output energy of 80 mJ, which resulted in an energy density of ca.  $10 \text{ J/cm}^2$  at the sample surface [Huang and Audéat, 2012]. The laser pit size was  $\sim 90 \mu\text{m}$ . The major impurity is Ir ( $\sim 80 \text{ wt. ppm}$ ), which was not too surprising because it was likely derived from the capsule used during crystal growth. The other determinable trace elements were: Mn ( $\sim 3 \text{ wt. ppm}$ ), Ni ( $\sim 2.0 \text{ wt. ppm}$ ), Fe ( $\sim 2.0 \text{ wt. ppm}$ ), Al ( $\sim 1.3 \text{ wt. ppm}$ ), and others (Sc, Cr, Cu, Zn, Ga, Lu, Re, Au, etc.) with concentrations of less than 1 wt. ppm each.

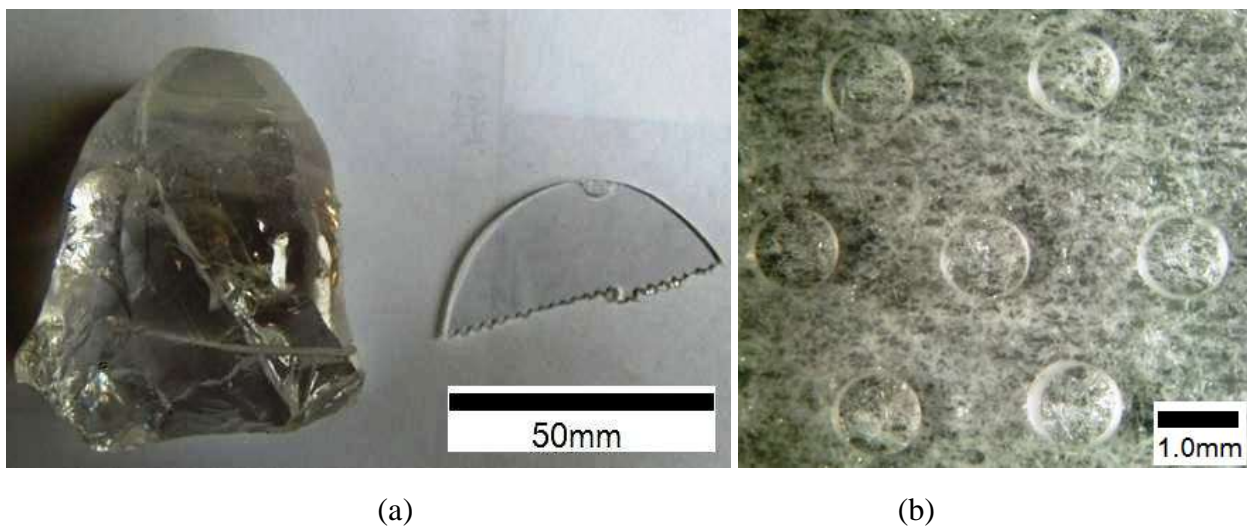


**Fig. 2.1** (a) Forsterite single crystal as starting material used in this study. (b) Cored forsterite disks with 1-mm diameter and 1-mm thickness.

Using an ultrasonic coring machine at Okayama University, Japan, the sample was cored along its *b*-axis, producing multiple disks with 1 mm in diameter and 1 mm in thickness (**Fig. 2.1b**). Jaoul et al. [1981] and Costa and Chakraborty [2008] reported that the anisotropy of silicon diffusion in forsterite and natural olivine is negligibly small. Therefore, only the diffusion rate along the *b*-axis, which is the longest crystallographic axis of the forsterite crystal structure, was investigated in this study.

The cored disks were carefully polished using diamond powder with grain sizes from 3 to 0.25  $\mu\text{m}$  until they were free of scratches. Subsequently, each test surface was chemically polished using an alkaline colloidal silica solution for 3-12 hours until any small scratches produced by polishing with the diamond powder were removed, thereby the surface roughness was reduced.

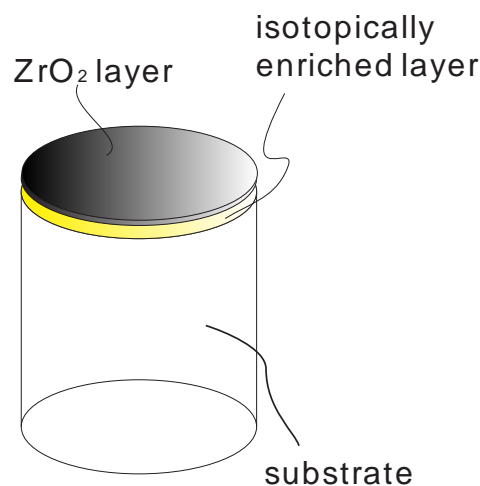


**Fig. 2.2.** Forsterite disks deposited with 300-500-nm thickness of isotopically enriched forsterite layer and covered with ~100-nm of ZrO<sub>2</sub> layer.

The highly polished surfaces of the forsterite disks were coated with thin films (300-500 nm thickness), possessing a forsterite major elements composition but enriched in <sup>29</sup>Si, using the pulsed laser deposition (PLD) system available at Ruhr-University of Bochum, Germany [Dohmen et al., 2002]. Prior to thin film deposition, the samples were heated up to 670 K for 10-15 min in the vacuum chamber of the PLD so as to remove water on the sample surfaces. Later it will be shown that crystallization and grain growth of the thin film coating during diffusion annealing causes significant surface roughness and possible poor contact between thin film and substrate. A second film of ZrO<sub>2</sub> with a thickness of 100 nm was deposited on the forsterite thin

film (**Fig. 2.2**) as recommended by Costa and Chakraborty [2008] who suggested that a  $ZrO_2$  film prevents the reaction of the isotopically enriched film coating with surrounding materials. Some samples were not coated with  $ZrO_2$ , and diffusion experiments were also carried out using these samples for comparison.

### 2.3.2 Annealing experiments

Before annealing experiments, the samples were pre-heated in an atmosphere furnace at 1273 K for 2 hours, or 1327 K for 15 min. This pre-heating induced the amorphous thin films to form a polycrystalline layer. Any water present in the thin films is expected to have been largely removed during this crystallization. The silicon diffusion in this pre-heating step should be negligible, because the diffusion depth in this procedure should be less than 1 nm if calculated using the  $D_{Si}$  given by Jaoul et al. [1981] and Costa and Chakraborty [2008]. This conclusion is also consistent with the diffusion coefficients obtained in this study.

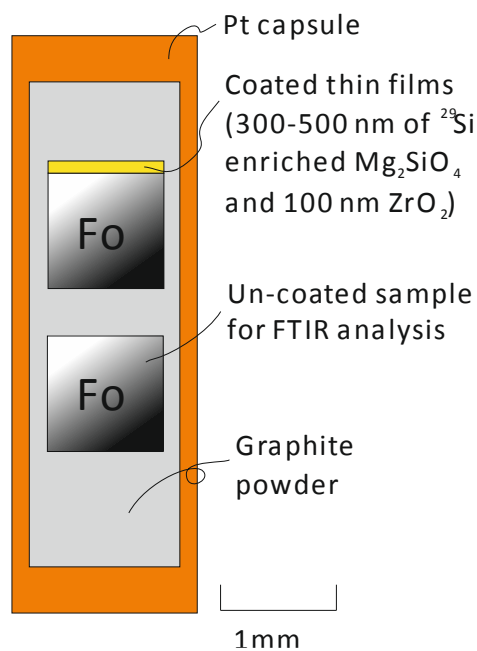


**Fig. 2.3.** Forsterite disks with graphite sealed in a platinum capsule.

After pre-heating, each coated forsterite disk was loaded in a platinum capsule with outer diameter of 1.6 mm and inner diameter of 1.3 mm (**Fig. 2.3**). Sealed at one end, an additional disk of forsterite, without the film deposition, was also loaded in the platinum capsule for determining water content. The space between samples and capsule wall was filled with graphite

powder, which was soft enough to protect the forsterite disk from mechanical damage at high pressures. The graphite powder also helped to remove water in forsterite crystal during high temperature annealing [Yamaoka *et al.*, 2000]. The capsule with two forsterite disks and graphite powder was closed, dried in a vacuum oven at 470 K for longer than 24 hours, and then immediately sealed by arc welding on a hot plate to minimize the amount of moisture absorbed from the atmosphere [Shatskiy *et al.*, 2009]. The final length of the capsules was 5 to 6 mm.

In ambient pressure experiments, each sealed capsule was put in a furnace at 1273 K and then temperature was increased to the target temperature (1600 K or 1800 K) within 5 min. The capsules were kept at the target temperatures for different durations and then quenched by taking them out from the furnace.

High pressure experiments were performed using Kawai-type multi-anvil apparatus at Okayama University and University of Bayreuth at pressures of 1, 3, 8 and 13 GPa and temperatures of 1600 and 1800 K. In each run, the sealed capsule surrounded by graphite powder was placed in a BN cylinder in graphite or LaCrO<sub>3</sub> stepped heater with a ZrO<sub>2</sub> thermal insulator. The pressure media were MgO + 5% Cr<sub>2</sub>O<sub>3</sub> octahedra with edge lengths of 25 and 14 mm for 1-8 and 13 GPa, respectively. Eight cubes of 32 mm tungsten carbide (WC) with 15 or 6 mm truncation edge lengths were used to generate high pressures. Pressure calibration was done at room temperature by phase transformation of Bi and ZnS, and temperature of 1473 K by the olivine-wadsleyite transition in Mg<sub>2</sub>SiO<sub>4</sub>. The sample temperatures were measured using a W97%Re3%-W75%Re25% thermocouple with a 0.25 mm diameter, with its junction placed at the bottom of the capsule (**Fig. 2.4**). The temperature gradient in the assembly was estimated to be less than 25 K/mm [Walter *et al.*, 1995]. The assembly was compressed to the target pressure in 2-4 hours, and then heated to the target temperature at a rate of  $\approx 100$  K/min. Annealing duration in a range from 0 to 42 hours was determined according to previous studies of silicon diffusion in forsterite [Andersson *et al.*, 1989; Jaoul *et al.*, 1981] and natural olivine [Bejjina and Jaoul, 1997; Costa and Chakraborty, 2008]. The temperature was under automatic control, thus limiting variation to less than 2 K during annealing. After annealing, the sample was quenched by switching off the heating power, and decompressed to ambient pressure a duration of 10-15 hours to prevent mechanical cracks during decompression.

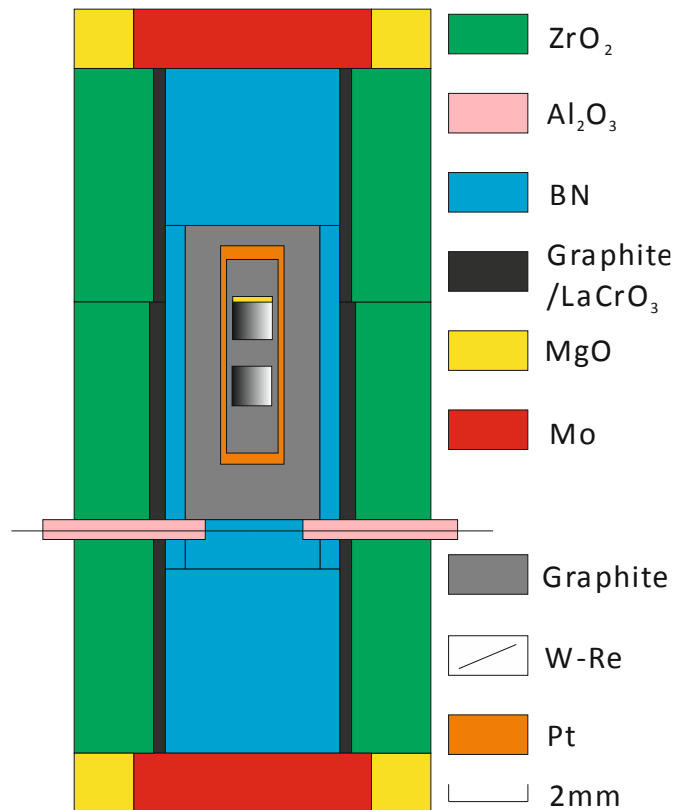


**Fig. 2.4.** A sketch of assembly for high pressure experiments. The thermocouple was located at the step of heater, while the coated sample surface was on the other step to minimize temperature uncertainty.

The forsterite disks were recovered by cutting into the platinum capsule using a steel blade. No obvious cracks were found in most forsterite disks, but some disks contained some horizontal cracks which should not have effects on the results of SIMS analyses.

In addition, some forsterite disks were pre-annealed buffered with enstatite ( $\text{MgSiO}_3$ ) before thin film deposition under the same pressure and temperature conditions as diffusion annealing experiments. Silicon should be excess in these samples. Although the silicon vacancy concentration of the starting material was unknown, the same results of  $D_{\text{Si}}$  in buffered and unbuffered samples demonstrated the silicon enriched condition of starting material.

### 2.3.3 FT-IR analysis

Each uncoated forsterite disk from the recovered capsule was doubly polished using a 0.25- $\mu\text{m}$  diamond powder and heated to 420 K for ~3 hours to remove the free water on the sample

surface prior to infrared analyses. The water contents in the samples were measured using the Bruker IFS 120 HR high resolution FTIR spectrometer coupled with a Bruker IR microscope at University of Bayreuth. Unpolarized infrared measurements were performed using a tungsten light source, a Si/CaF<sub>2</sub> beam splitter, and a high sensitivity narrow-band MCT (mercury-cadmium-telluride) detector cooled by liquid nitrogen. Two hundred scans were accumulated for each spectrum at a resolution of 1 cm<sup>-1</sup> [Demouchy and Mackwell, 2003].

The infrared beam was focused on the surface of forsterite disks with a spot diameter of ~100 μm. Two spectra were obtained for each sample in the center of the disk and near the edge. After a background baseline correction and thickness normalization to 1 cm, the water content was determined using the calibration given by [Bell *et al.*, 2003]:

$$C_{H_2O} = 0.188 \times \int k(\nu) d\nu \quad (2.1)$$

where  $k(\nu)$  is the absorption coefficient at wave number  $\nu$ . Integration was performed between the wave numbers 3000 and 4000 cm<sup>-1</sup>.

### 2.3.4 SIMS analysis

The isotopic depth profiles were determined by secondary ion mass spectrometry (SIMS). A Cameca IMS-6f ion probe instrument installed at Helmholtz Centre Potsdam, Germany was used. Some profiles were obtained using a Cameca IMS-3f ion probe at Hokkaido University, Japan. The forsterite disks recovered from diffusion annealing experiments were mounted in epoxy. The epoxy mounts containing the samples were coated with 35 nm thick gold films. A nominally 10 keV primary Cs<sup>+</sup> beam providing a ~4 nA current focused to a ~20 μm diameter on the sample surface was used for all analyses. In order to estimate the water contents, the count rate on the <sup>1</sup>H mass station (2 s per cycle) was determined in addition to <sup>28</sup>Si (2 s) and <sup>29</sup>Si (4 s) mass stations which made up our peak stepping sequence. Secondary ion intensities from central region (30 μm diameter) of the sputtered crater (80 x 80 μm raster) were collected as a function of sputtering time. The mass spectrometer was operated at a mass resolution of M/dM ≈ 4300 in conjunction with a 50 V energy band pass to which no offset voltage was applied. The depth of each SIMS crater was subsequently determined using a 3D-Nanofocus microscope at University of Bayreuth. Crater depths ranged from ~200 up to 1000 nanometers, depending on the length of diffusion

profiles. The time data of SIMS profiles was converted to depth data based on the assumption of a constant sputtering rate for each analysis.

The abundance of  $^{29}\text{Si}$  was expressed as  $^{29}\text{Si}/(^{28}\text{Si}+^{29}\text{Si})$ .  $D_{\text{Si}}$  was obtained by fitting to the solution of Fick's second law as:

$$c = \frac{c_0 - c_1}{2} \operatorname{erf}\left(\frac{x - h}{\sqrt{4Dt + L^2(\sigma)}}\right) + \frac{c_0 + c_1}{2} \quad (2.2)$$

where  $c$  is the observed abundance of  $^{29}\text{Si}$ ,  $c_1$  the is initial abundance of  $^{29}\text{Si}$  in the isotopic film,  $c_0$  is the initial abundance of  $^{29}\text{Si}$  in the substrate,  $x$  is the distance from the surface,  $h$  is the boundary position of isotopically enriched film and the substrate,  $D$  is the diffusion coefficient,  $t$  is the annealing time,  $L(\sigma)$  is the nominal diffusion length in zero-time diffusion runs, related to surface roughness (the calibration for the standard deviation for roughness,  $\sigma$ , is discussed in the next section), and  $\operatorname{erf}(z)$  is the error function defined as,

$$\operatorname{erf}(z) = \frac{2}{\pi} \int_0^z e^{-t^2} dt \quad (2.3)$$

### 2.3.5 Surface roughness

Due to silicon's slow diffusion rate, the diffusion lengths in this study are less than 1 micron even in samples which were annealed over long durations (40 h) and high temperatures (1800 K). As surface roughness adversely impacts the depth resolution of SIMS depth profiles, the quality of polished surfaces after diffusion experiments must be considered.

**Figure. 2.5.** Shows a typical example of how the surface roughness evolved through the entire experimental procedure measured by 3D-Nanofocus microscope at University of Bayreuth, Germany. In this example, the surface was quite smooth, with surface roughness of  $R_y < 10$  nm (**Fig. 2.5a**) after thin film deposition (here  $R_y$  is simply defined as the height difference between the highest and lowest points in the profile). However, roughness increased to  $R_y = 100\text{-}200$  nm (**Fig. 2.5b**) after crystallization at 1270 or 1370 K, and then to  $R_y = 200\text{-}400$  nm (**Fig. 2.5c**) after diffusion annealing. The roughening of the surface was presumably induced by grain growth of the coated films. The above surface roughness is comparable with the diffusion length, and would thus introduce to be a significant source of error for the depth profile analyses (**Fig. 2.6**).

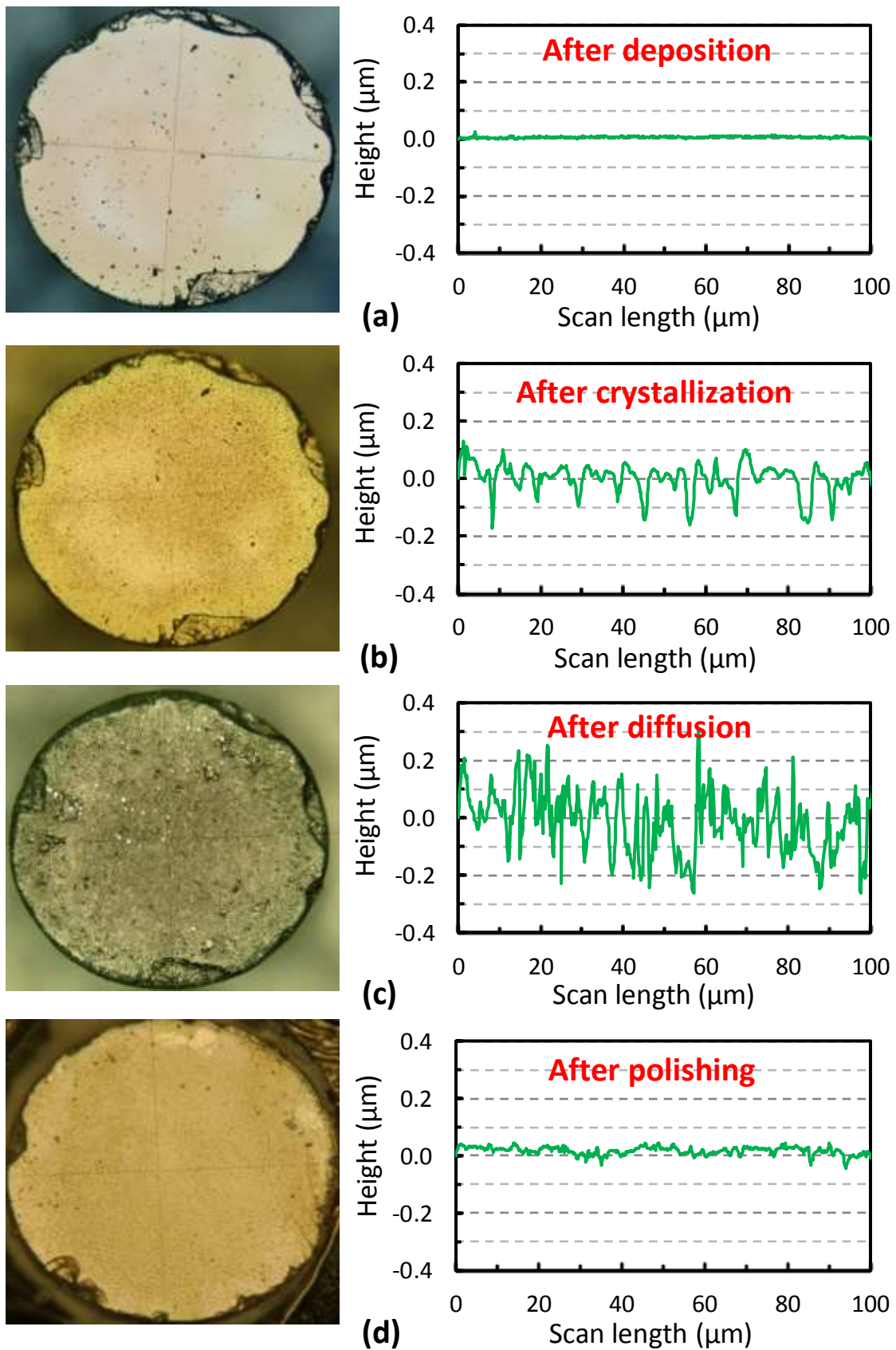


**Fig. 2.5.** Surface roughness after each step. **(a)** After thin films deposition. **(b)** After crystallization. **(c)** After diffusion annealing. **(d)** After second chemical polish.

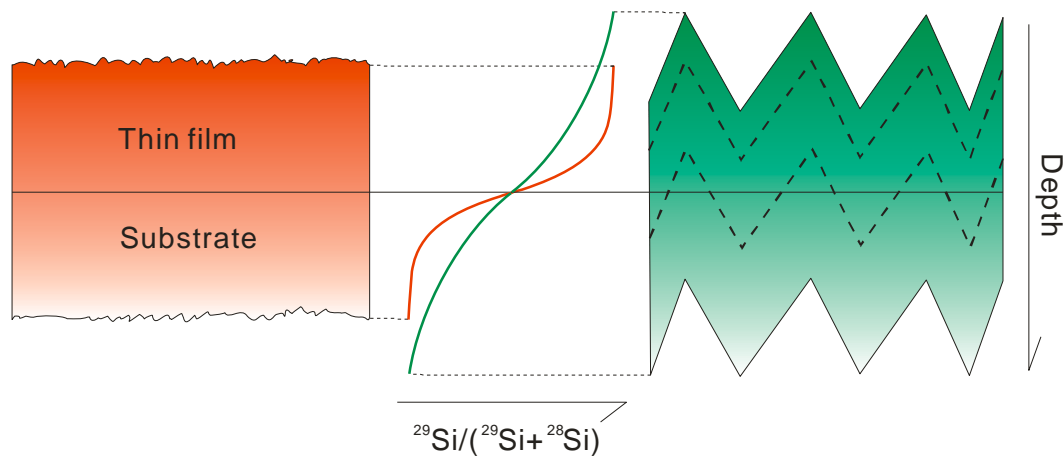


**Fig. 2.6.** Models of diffusion profiles measured in samples with small and large surface roughness. As SIMS determined the average concentration of  $^{29}\text{Si}$  in each cycle, if the surface roughness is large, the diffusion profile becomes much longer (green profile) in comparing with that measured in smooth sample (red color).

In order to solve this surface roughness problem, numerous methods were tested to obtain smooth surface required for determining the slow diffusion rate of silicon. Ultimately we found that conducting a chemical polish after diffusion annealing is the most practical solution. 100-200 nanometers on the sample surface was polished away in alkaline colloidal silica solution for several minutes to 1-2 hours until the surface roughness was reduced to  $R_y < 50 \text{ nm}$  (**Fig. 2.5d**). Combining our best estimation of the  $D_{\text{Si}}$  and carefully controlling both the temperature and annealing duration, the overall diffusion length was held to below 300 nm. As the total thickness of the thin films was 400-600 nm, only a thin layer located well beyond the apparent diffusion profile was removed during the final chemical polishing. Note that this procedure requires very careful treatment to prevent the films from being polished away completely. The duration for this polishing depends on many factors like the sample surface condition, the force used for holding the sample, the round or flat surface of epoxy for mounting the sample, etc.

Although the surface roughness can be reduced by chemical polishing,  $\sim 50 \text{ nm}$  roughness is still a significant source of error. In addition, there are other error sources, for example, the intrinsic depth resolution in SIMS analyses, which suggests a longer apparent diffusion length observed by SIMS than the real diffusion length [Tomita *et al.*, 2012]. In order to correct for these error sources, we conducted zero time diffusion runs in which the samples were heated to a given target temperature and then quenched immediately. Such samples were polished to

different surface roughnesses and then measured by SIMS. The results of such zero time runs suggest that the nominal diffusion length ( $L$ ) is approximated by a linear function (**Fig. 2.7a**) of the surface roughness standard deviation ( $\sigma$ ) of Ry in the bottom of the crater (**Fig. 2.7b**). The apparent diffusion length obtained by SIMS was corrected using such a calibration procedure in **Eqs. 2.2**.

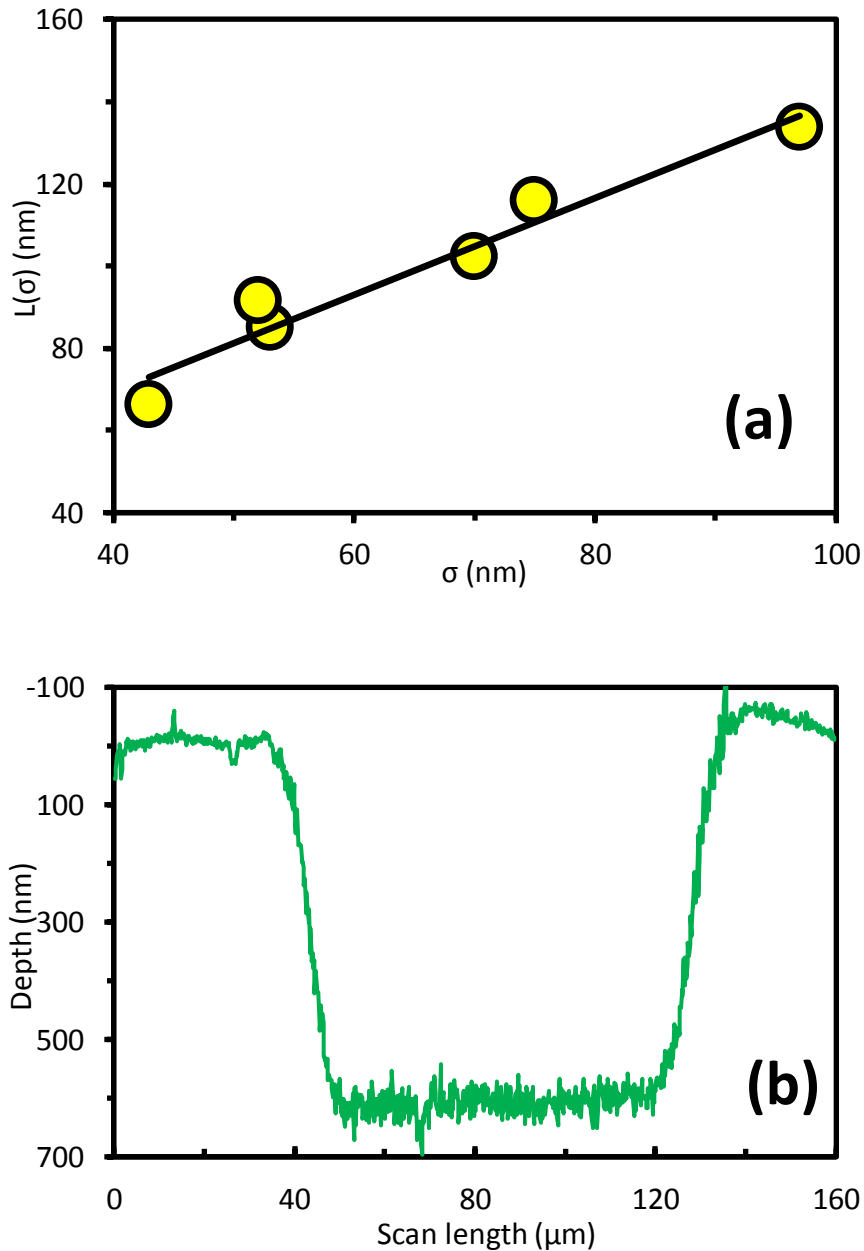


**Fig. 2.7.** (a) Nominal diffusion length  $L(\sigma)$  of silicon in zero-time diffusion runs is linear to standard deviation  $\sigma$  of surface. The surface standard deviation data are from the center ( $30 \times 30 \mu\text{m}^2$ ) of the crater bottom (b) after SIMS measurement.

## 2.4 Results

### 2.4.1 Water content

#### (1) Water content observed by FTIR

There are no –OH peaks determinable by FTIR in most samples after annealing (**Fig. 2.8**), which indicate water in the capsules in these experiments was efficiently removed before welding the capsule, but some samples contain a small amount (like the sample with ~3 wt. ppm of water shown in **Fig. 2.8**) of water. Only the samples without determinable –OH peaks were used for determining  $D_{Si}$  in this study.

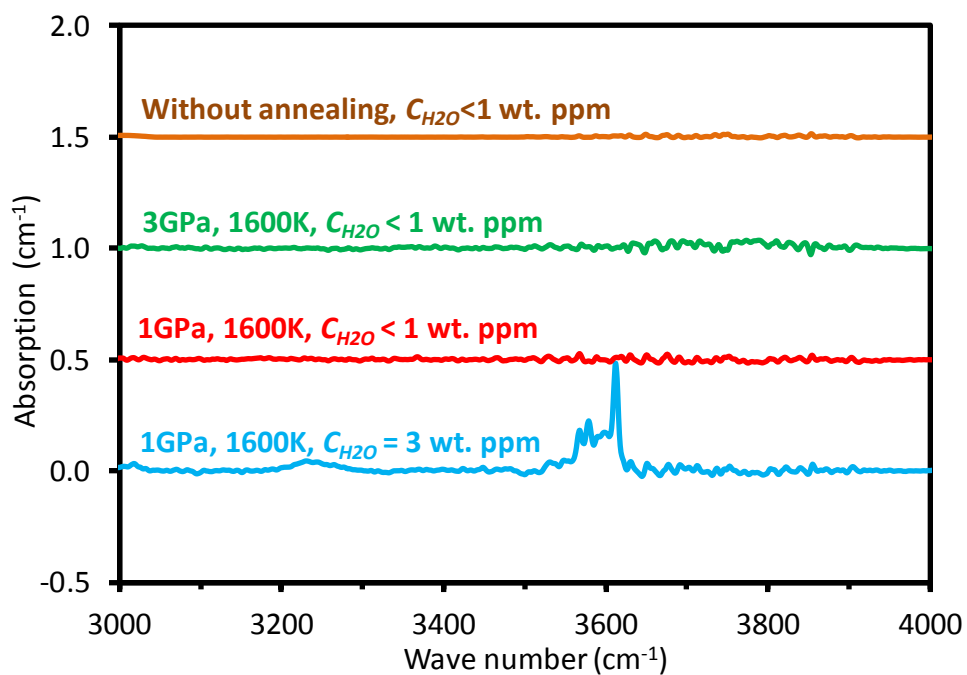


**Fig. 2.8.** Un-polarized infrared spectra of forsterite samples. Water contents are calculated using the calibration given by Bell et al. [2003] with integration from 3000 to 4000  $\text{cm}^{-1}$ . All the spectra are normalized to a thickness of 1 cm.

#### (2) Water content observed by SIMS

$C_{H_2O}$  determined by infrared spectra shows the average value for the water content in the crystal. On the other hand,  $^{29}\text{Si}$  diffusion only happens near the sample surface (within 2  $\mu\text{m}$ ) because of the slow diffusion rate of silicon. Therefore, water near the sample surface, which may significantly affect the  $D_{Si}$ , should be considered.

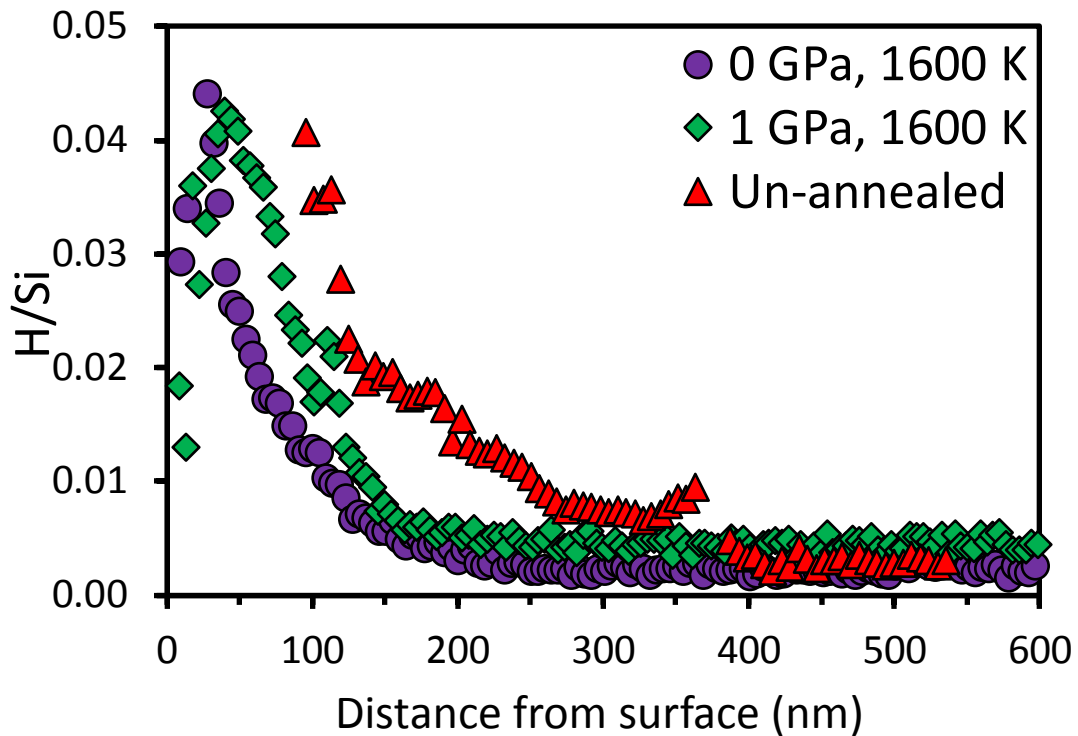


**Fig. 2.9.** Atomic ratio of H/Si with distance from the surface determined by SIMS. The initial thicknesses of coated films ( $\text{Mg}_2\text{SiO}_4+\text{ZrO}_2$ ) of un-annealed samples, ambient pressure ( $\sim 0$  GPa), and 1 GPa are 400 nm, 600 nm and 600 nm, respectively. The 0 GPa and 1 GPa samples were chemically polished after diffusion annealing, while the un-annealed sample was not. The difference of H/Si ratios between 1 atm and 1 GPa samples after 200 nm is mostly because of the background in different analyses.

**Figure 2.9** shows the ratio of H and Si intensities observed by SIMS from the surface to 600-nm depth. Although it is not an absolute value because of the lack of calibration, we can see in an un-annealed sample (after thin film deposition and without high temperature treatment), H/Si decreases to a constant value at  $\sim 400$  nm from the surface. The high H/Si ratio in thin film is not too surprising because water may have been absorbed from the air during and after thin film deposition. The sample annealed at high pressure shows that the H/Si ratio is high from the surface to 40-nm depth but decreased to a constant value in the region deeper than 200 nm. This trend is the same as for the sample annealed at ambient pressure. Certainly, the ambient pressure experiments were annealed at “dry” conditions. Therefore, the high H/Si ratio to 200 nm depth may be water absorbed after annealing, probably during chemical polishing, and does not affect silicon diffusion rates during annealing. Since  $C_{\text{H}_2\text{O}}$  determined by FTIR is lower than 1 wt. ppm,

which indicates the average value of  $C_{H_2O}$  in the crystal, and the H/Si ratio in the region deeper than 200 nm is constant, we can conclude that  $C_{H_2O}$  in the region where silicon diffusion profiles were obtained is lower than 1 wt. ppm.

The water contents estimated from H/Si ratios by SIMS are much higher than that by infrared analyses. That is because of the high level of background hydrogen in SIMS analyses endemic to typical analytical conditions, as hydrogen is a relatively abundant contaminant in mass spectrometer vacuums, in primary ion sources, and from epoxy used for mounting the samples [Koga *et al.*, 2003; Magee, 1981; Yurimoto *et al.*, 1989].

#### 2.4.2 Silicon diffusion coefficients

Results of silicon self-diffusion experiments in forsterite are summarized in **Table 2.1** and the  $\log D_{Si}$  are plotted against pressure in **Fig. 2.10**. The obtained  $D_{Si}$  are fit to the Arrhenius equation:

$$D = D_0 \exp\left(-\frac{\Delta H + P\Delta V}{RT}\right) \quad (2.4)$$

where  $D$  is diffusion coefficient,  $D_0$  is the pre-exponential factor,  $\Delta H$  is the activation energy,  $P$  is the pressure,  $\Delta V$  is the activation volume,  $R$  is the gas constant, and  $T$  is the absolute temperature. Here we assume that the pressure does not affect the pre-exponential factor. This fitting gives the  $\Delta H$ ,  $\Delta V$ , and  $D_0$  of  $407 \pm 31$  kJ/mol,  $1.7 \pm 0.4$  cm<sup>3</sup>/mol and  $3.6 \times 10^{-7}$  m<sup>2</sup>/s, respectively. The standard deviation of the data points at the same experimental conditions is  $<0.45 \log[\text{m}^2/\text{s}]$ . Although the data at ambient pressure and at high pressures are obtained using different experimental techniques, the data sets show quite consistent results. Small negative pressure dependence is recognized.  $\log D_{Si}$  at ambient pressure are determined to be  $-18.2 \pm 0.1 \log[\text{m}^2/\text{s}]$  at 1800 K and  $-19.7 \pm 0.3 \log[\text{m}^2/\text{s}]$  at 1600 K. These values are 2.4 orders of magnitude higher than those given by Jaoul *et al.* [1981] at 1600 and at 1800 K, respectively.

For bulk self-diffusion, the penetration depth has to be proportional to  $t^{1/2}$  ( $t$  is the annealing duration). In that case, the value of  $D_{Si}$  has to be independent of  $t$  [Jaoul *et al.*, 1980]. This is what came out in the present experiments, as is illustrated in **Fig. 2.11** for identical samples treated in the same conditions, but for different durations, yielding the same  $D_{Si}$  value.

**Table 2.1.** Summary of runs, experimental conditions (P: pressure, T: temperature, and t: annealing duration), and results of silicon self-diffusion coefficient ( $D_{Si}$ ).

Sample	$P$ (GPa)	$T$ (K)	$t$ (h)	$D_{Si}$ ( $m^2/s$ )	Error factor <sup>*4</sup>
0004 <sup>*(1)</sup>	$10^{-4}$	1600	13	$4.8 \times 10^{-20}$	2.8
0022a	$10^{-4}$	1600	13	$3.5 \times 10^{-20}$	2.3
0022b	$10^{-4}$	1600	13	$1.3 \times 10^{-20}$	2.4
0010 <sup>*(2)</sup>	$10^{-4}$	1600	12	$2.9 \times 10^{-22}$	-
D223a <sup>*(1)</sup>	1	1600	4	$3.2 \times 10^{-20}$	2.4
D223b <sup>*(1)</sup>	1	1600	4	$6.2 \times 10^{-21}$	3.4
D225 <sup>*(1)</sup>	1	1600	15	$1.7 \times 10^{-20}$	2.0
D220 <sup>*(1)(3)</sup>	1	1600	3.3	$2.2 \times 10^{-20}$	2.1
1K1120	3	1600	6	$2.5 \times 10^{-20}$	2.4
1K1123a	3	1600	22	$5.3 \times 10^{-21}$	3.2
1K1123b	3	1600	22	$1.6 \times 10^{-20}$	2.0
S5045a <sup>*(1)</sup>	8	1600	21	$4.8 \times 10^{-21}$	2.3
S5045b <sup>*(1)</sup>	8	1600	21	$1.3 \times 10^{-20}$	2.5
1K1119c	8	1600	42	$6.7 \times 10^{-21}$	2.9
1K1119a	8	1600	12	$9.8 \times 10^{-21}$	2.2
1K1119b	8	1600	12	$6.0 \times 10^{-21}$	2.1
1K1106	13	1600	15	$6.5 \times 10^{-21}$	2.0
0016a	$10^{-4}$	1800	2	$7.7 \times 10^{-19}$	2.1
0016b	$10^{-4}$	1800	2	$7.8 \times 10^{-19}$	2.1
1K1144	3	1800	3	$3.5 \times 10^{-19}$	2.0
1K1145	8	1800	5	$2.6 \times 10^{-19}$	2.0
1K1146a	8	1800	15	$1.8 \times 10^{-19}$	2.1
1K1146b	8	1800	15	$1.4 \times 10^{-19}$	2.3
1K1143	13	1800	7	$1.4 \times 10^{-19}$	2.0

\* (1): Pre-annealed before thin film deposition with enstatite buffer.

\* (2): Sample 0010 (without  $ZrO_2$  film) annealed at 1 atm.  $D_{Si}$  is approximately 2 orders of magnitude lower than that in  $ZrO_2$  coated sample (0022) with similar annealing conditions.

\* (3): Sample D220-2 (without  $ZrO_2$  thin film) annealed at 1 GPa.  $D_{Si}$  is consistent with other  $ZrO_2$  coated samples.

\* (4): Errors estimated from fitting in **Eqs. 2.3** and **2.4** estimated by 1 standard deviation of the fitting parameters.

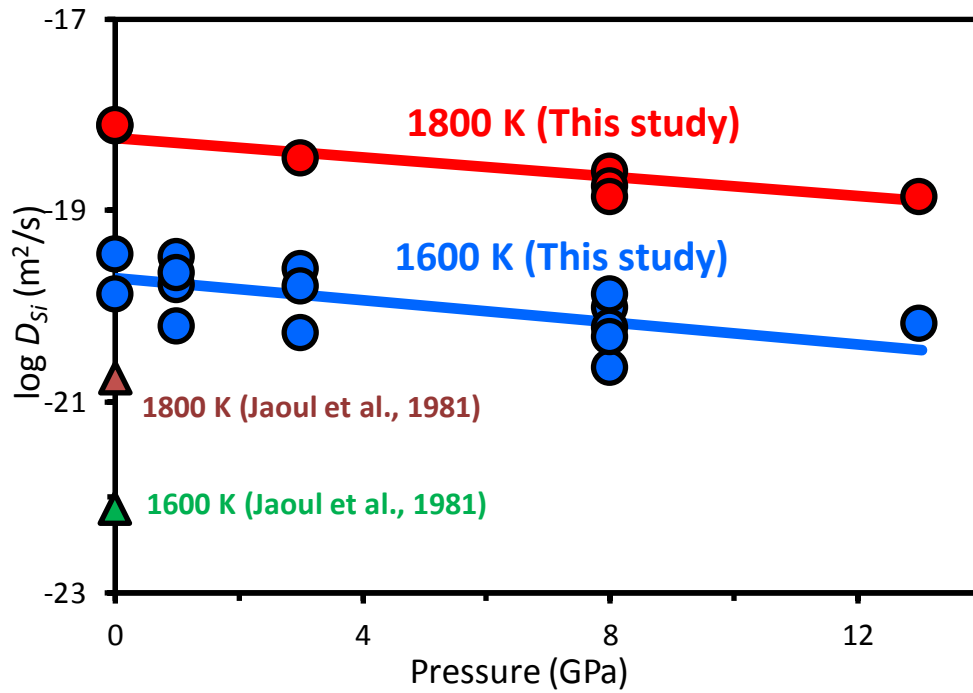


**Fig. 2.10.**  $\log D_{Si}$  with pressure at 1600 and 1800 K in comparison with Jaoul et al. [1981].  $D_{Si}$  at ambient pressure are approximately 2.4 orders of magnitude higher than that determined by Jaoul et al. [1981].

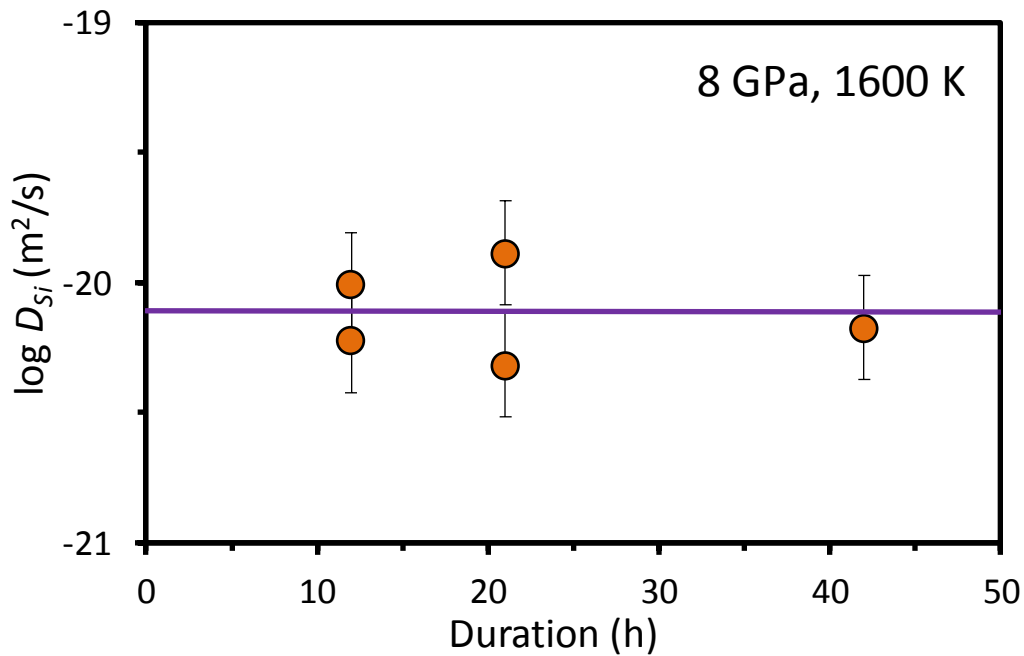


**Fig. 2.11.**  $\log D_{Si}$  at 1600 K and 8 GPa with different durations.

In ambient pressure experiments, the sealed capsules were usually broken due to the expansion of air in the capsule at high temperature, resulting in a higher oxygen fugacity as compared with high pressure experimental conditions. Houlier et al. [1990] reported a very small negative dependence of silicon diffusion rate on oxygen fugacity ( $D_{Si} \propto f_{O_2}^{-0.19 \pm 0.1}$ ). However, the data sets of Houlier et al. [1990] are rather scattered and could also be fitted without any dependency on oxygen fugacity [Costa and Chakraborty, 2008]. This is also confirmed by the consistent values of  $D_{Si}$  obtained at ambient pressure and at high pressures (**Fig. 2.10**). Therefore, the breakage of capsules does not introduce any significant additional uncertainties to our experimental results.

## 2.5 Discussion

### 2.5.1 “Dry” experimental conditions at high pressures

Water may have large effect on rheology properties of mantle minerals [Costa and Chakraborty, 2008; Karato et al., 1986; Mei and Kohlstedt, 2000a; b]. Even 10 wt. ppm of water in olivine is sufficient to cause a transition from “dry” to “wet” laws for the diffusion process and “wet” diffusion laws should be used to model geodynamics processes in the upper mantle. Therefore, it is important to assess whether our experimental conditions are “dry” or “wet”.

The  $D_{Si}$  obtained at ambient pressure are consistent with those at high pressures with negative pressure dependence in this study. In ambient pressure experiments, they are certainly “dry” conditions. The consistency of  $D_{Si}$  obtained at ambient and high pressures suggests that  $D_{Si}$  at high pressures can be considered as rheologically “dry” conditions, and that the effect of water on  $D_{Si}$  is negligible in this study. Such “dry” sample environments were successfully produced by the efficient removing and reduction of water in the sealed platinum capsules in our high pressure experiments.

### 2.5.2 Comparison with previous studies of $D_{Si}$ in forsterite

The  $D_{Si}$  in dry forsterite single crystals is 2.4 orders of magnitude higher than that reported in Jaoul et al. [1981] at ambient pressure. One difference between our and their study is that a  $ZrO_2$  thin film for protecting isotopically enriched film was used in our study but not in their study. Possibly, without the protection of  $ZrO_2$ , the isotopically enriched film tends to

horizontally shrink during recrystallization of the film instead of diffusing into the substrate during high temperature annealing. Because of the horizontal shrinking, the isotopically enriched film and substrate are not well contacted and  $^{29}\text{Si}$  cannot diffuse into the substrate though concentration gradient of  $^{29}\text{Si}$  exists ( $^{30}\text{Si}$  enriched  $\text{Mg}_2\text{SiO}_4$  thin films were used in Jaoul et al. [1981]. But this did not affect the arguments presented here). Such phenomenon was found in some no- $\text{ZrO}_2$  coated samples (0010, 0007, and 0011 shown in **Fig. 2.12, 2.13**) annealed at 1600 K and ambient pressure in our study. In these samples, isotopically enriched films shrink to small areas and formed islands on the crystal surface (**Fig. 2.13a, 2.13b**). SIMS analysis of sample 0010 shows a much shorter diffusion profile in comparison with a sample coated with  $\text{ZrO}_2$  and annealed under similar conditions (**Fig. 2.12**). The phenomenon of horizontal shrinking was not found in high pressure experiments even without a  $\text{ZrO}_2$  film (sample D220 in **Table 2.1**), which was not too surprising because the isotopically enriched film was compressed by the surrounding material and had good contact with the substrate at high pressure.

One might consider that the high  $D_{\text{Si}}$  in the  $\text{ZrO}_2$  coated sample could be because Zr ions diffused into forsterite and formed excess vacancies in forsterite due to the high valence (+4) of the Zr ion, which should have caused artificially high  $D_{\text{Si}}$ . However, we should note that even if the sample was not coated with  $\text{ZrO}_2$ , the thin film did not shrink at high pressure and showed a high  $D_{\text{Si}}$ , as mentioned above (sample D220-2). Hence, the magnitude of  $D_{\text{Si}}$  is related to the thin film shrinkage but not directly to the presence of  $\text{ZrO}_2$ .

Besides, the symmetrical apparent silicon diffusion profile also indicates the negligible effect of the presence of  $\text{ZrO}_2$ . If  $\text{ZrO}_2$  largely enhances the silicon diffusion rate by several orders of magnitude, the silicon diffusion rate in the film should be much larger than that in the substrate. In that case, we would not obtain such symmetrical apparent diffusion profiles (**Fig. 2.12, Sample 0022**).

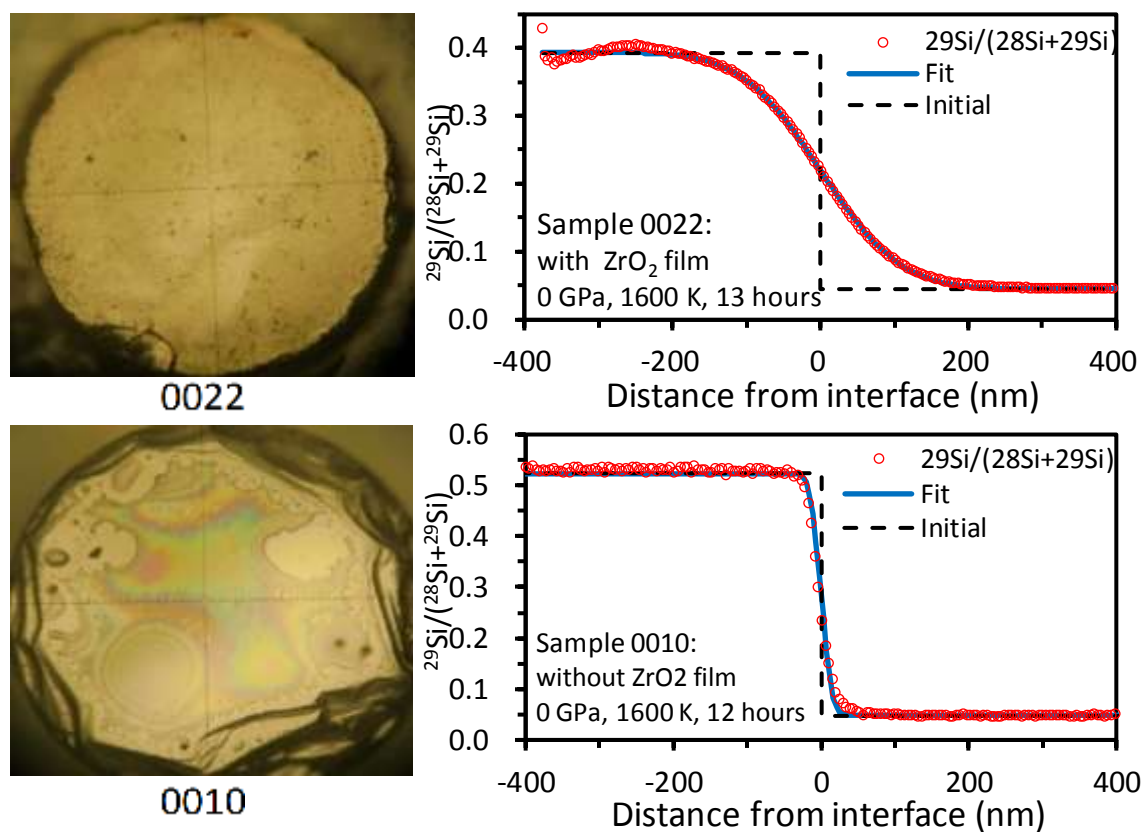


**Fig. 2-12.** Diffusion profiles of sample 0010 (1600 K, 1 atm, 12 h, without ZrO<sub>2</sub> film) and 0022 (1600 K, 1 atm, 13 h, with ZrO<sub>2</sub> film). The film coating horizontally shrank in sample 0010 and the diffusion profile is much shorter than sample 0022 even similar annealing conditions.

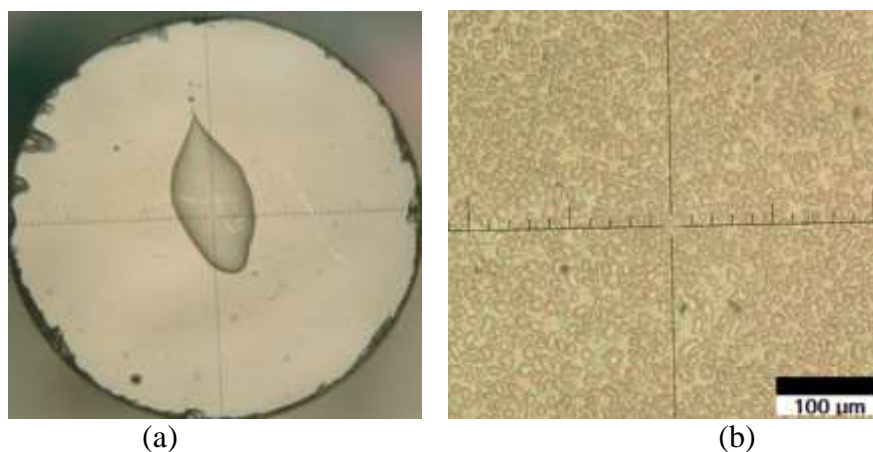


**Fig. 2.13** (a) Sample 0011 (without ZrO<sub>2</sub> film) annealed at 1600 K, 1 atm for 3 h. The isotopically enriched film horizontally shrank to a small area at the center. (b) Sample 0007 (without ZrO<sub>2</sub> film) annealed at 1273 K, 1 atm, for 2 h. The thin film horizontally shrank and formed islands on the surface.

Furthermore, in order to confirm the negligible effect of  $\text{ZrO}_2$  films on apparent diffusion profiles, a cross section vertical to the coating layer of one sample annealed at ambient pressure was observed with a scanning electron microscope (SEM) shown in **Fig. 2.14**. The interface of the thin film and substrate could not be observed with SEM. Electron backscatter diffraction (EBSD) showed the same crystallographic orientations between the film and substrate. It suggests that the forsterite thin film and substrate formed one single crystal. Judging from the diffusion profile of this sample, the interface should be located at around 400 nm of depth from the sample surface, and the concentration of  $^{29}\text{Si}$  starts to decrease at 200 nm of depth. We observed  $\text{ZrO}_2$  grains on the surface of the apparent coated layer. No Zr was found inside of forsterite. The thicknesses of most  $\text{ZrO}_2$  grains were less than 300 nm. Judging from the diffusion profile of this sample, the interface located at  $\sim 400$  nm depth from the surface, and the concentration of  $^{29}\text{Si}$  started to decrease at  $\sim 200$ -nm depth. We also note that presence of  $\text{ZrO}_2$  only affected the intensity of each silicon signal in SIMS analysis, but not the ratio of  $^{29}\text{Si}$  to  $^{28}\text{Si}$ . Therefore, the  $\text{ZrO}_2$  film did not affect the apparent diffusion profile in this study.

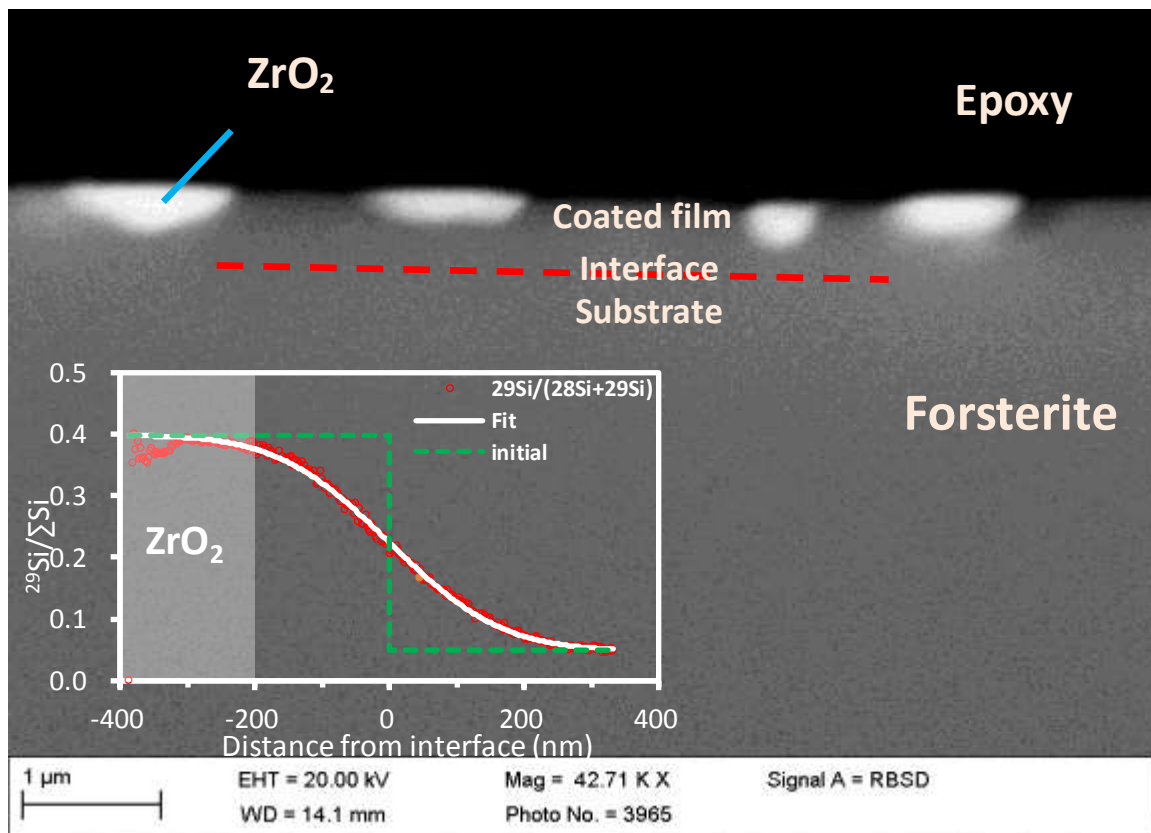


**Fig. 2.14.** SEM image of the cross section. The interface of thin film and substrate could not be observed from SEM. It is estimated to be located at  $\sim 400$  nm depth from the diffusion profile.

We infer that the shrinkage of the thin film could have occurred in the samples of Jaoul et al. [1981], which caused the apparent low  $D_{Si}$  as in our sample 0010. The thicknesses of their thin films are about 10 nm, which is by 1.5 orders of magnitude thinner than ours. The area to volume ratio of their films is thus higher than ours, which leads to greater possibility of thin film shrinkage.

Before Costa and Chakraborty [2008] introduced the technique,  $ZrO_2$  films were not used for protecting isotopically enriched thin films in silicon diffusion experiments ([Dohmen et al., 2002; Houlier et al., 1990; Jaoul et al., 1981] shown in **Fig. 2.15**). It is possible that the silicon diffusion coefficients were underestimated in the previous studies at ambient pressure.

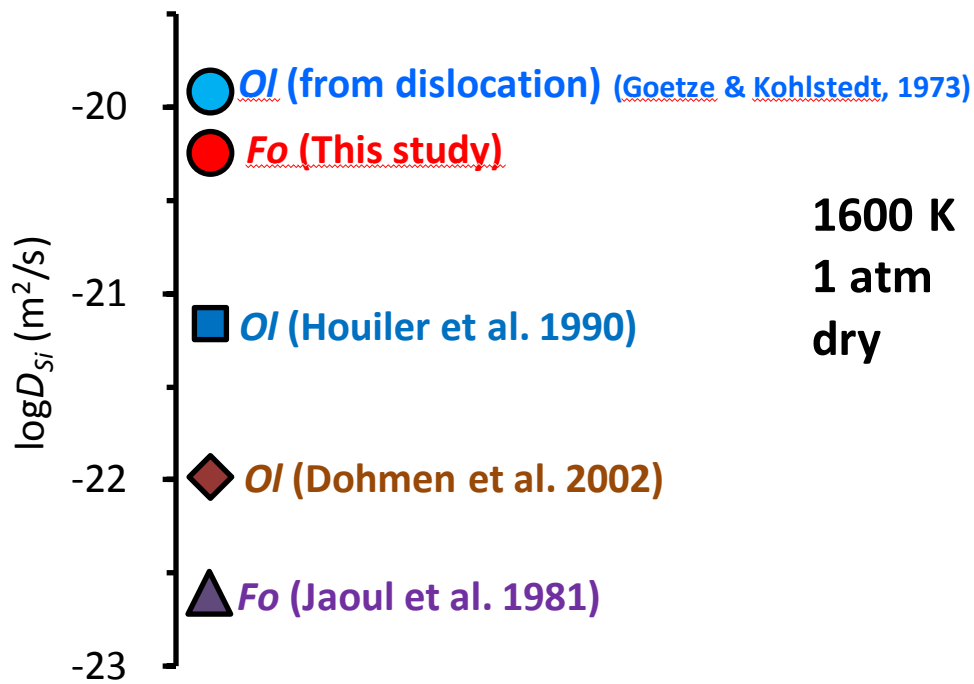


**Fig. 2.15.**  $D_{Si}$  in forsterite and in natural olivine at ambient pressure. Previous studies [Dohmen et al., 2002; Houlier et al., 1990; Jaoul et al., 1981] may underestimate the  $D_{Si}$  at ambient pressure. The  $D_{Si}$  obtained in this study is consistent with that estimated from dislocation experiments.

### 2.5.3 Comparison with dislocation climb rate

The diffusion coefficient and loop radius in dislocation are related as:

$$D_s = R_c / t_c [(1-\nu)kT_c / (\mu V_a)] \quad (2.5)$$

where  $D_s$  is the diffusion coefficient of the slowest species, which is silicon in forsterite and olivine,  $R_c$  is the loop radius,  $t_c$  is the time,  $T_c$  is the absolute temperature,  $k$  is the Boltzman's constant,  $V_a$  is the corresponding volume, with a value of  $20 \times 10^{-30} \text{ m}^3$  in olivine,  $\mu$  and  $\nu$  are the shear modulus and Poisson's ratio, respectively [Goetze and Kohlstedt, 1973]. With  $\mu/(1-\nu) = 0.8 \times 10^{16} \text{ dynes/m}^2$ , and  $R_c = 100 \text{ nm}$  in  $t_c = 1 \text{ hour}$  at  $T_c = 1563 \text{ K}$  [Goetze and Kohlstedt, 1973], we have  $D_{Si} = 3.7 \times 10^{-20} \text{ m}^2/\text{s}$ . It is consistent with our  $D_{Si}$  value ( $1.9 \times 10^{-20} \text{ m}^2/\text{s}$ ) within experimental errors ( $0.3 \log[\text{m}^2/\text{s}]$ ). The high dislocation creep rate is thus well explained by the silicon diffusion results from this study (**Fig. 2.15**).

#### 2.5.4 Activation energy and activation volume in forsterite and in natural olivine

Activation energy and activation volume for silicon diffusion, deformation, and dislocation recovery in forsterite and natural olivine are summarized in **Table 2.2**. The activation energy of silicon diffusion in forsterite in this study is determined to be  $407 \pm 31 \text{ kJ/mol}$ , which is slightly higher than that determined by Jaoul et al. [1981] with  $376 \pm 38 \text{ kJ/mol}$ , and slightly lower than that in forsterite deformation experiments with  $460 \pm 59 \text{ kJ/mol}$  by Darot and Gueguen [1981]. However, the differences of activation energy for silicon diffusion from these studies are within the range of the errors.

In natural iron-bearing olivine, the activation energy of silicon diffusion, deformation, and dislocation recovery is determined to be  $529 \pm 41 \text{ kJ/mol}$  [Dohmen et al., 2002] or  $291 \pm 15 \text{ kJ/mol}$  [Houlier et al., 1990],  $510 \pm 30 \text{ kJ/mol}$  [Karato and Jung, 2003], and  $389 \pm 30 \text{ kJ/mol}$  [Karato and Ogawa, 1982], respectively. The activation energy determined by deformation experiments is higher than that from silicon diffusion and dislocation recovery experiments except for that of [Dohmen et al., 2002] in both forsterite and natural olivine. It may be attributable to the energy required to form jogs along dislocations [Karato and Ogawa, 1982], or to the energy resulting from coupled diffusion of silicon and other faster species [Jaoul, 1990].

There are no published data on the activation volume for silicon diffusion in forsterite. Bějina et al. [1997; 1999] determined the activation volume for silicon diffusion in San Carlos olivine, summarized in **Table 2.2**, with results of  $-1.9 \pm 2.4$  and  $+0.7 \pm 2.3 \text{ cm}^3/\text{mol}$  in Bějina et al.

[1997] and Běřina et al. [1999], respectively. They concluded that the activation volume for silicon diffusion is likely close to zero, and therefore pressure has practically no effect upon silicon diffusion [Běřina et al., 1999]. Meanwhile, the activation volume for silicon diffusion in forsterite is determined to be  $1.7 \pm 0.4$  cm<sup>3</sup>/mol in this study, which indicates small negative pressure dependence. Due to short diffusion profiles in the silicon diffusion experiments, in Běřina et al. [1997; 1999], the small pressure dependence of  $D_{Si}$  was likely hidden by large experimental error with rather scattered data points.

**Table 2.2.** Activation energy ( $\Delta H$ ), activation volume ( $\Delta V$ ), pressure ( $P$ ), and pre-exponential factor ( $D_0$ ) in forsterite ( $Fo$ ) and iron-bearing olivine ( $Ol$ ) obtained at “dry” experimental conditions.

Method	$\Delta H$ (kJ/mol)	$\Delta V$ (cm <sup>3</sup> /mol)	$P$ (GPa)	Reference
<i>Fo</i> diffusion	407 $\pm$ 31	1.7 $\pm$ 0.4	10 <sup>-4</sup> -13	This study
<i>Fo</i> diffusion	376 $\pm$ 38	—	10 <sup>-4</sup>	[Jaoul et al., 1981]
<i>Ol</i> diffusion	529 $\pm$ 41	—	10 <sup>-4</sup>	[Dohmen et al., 2002]
<i>Ol</i> diffusion	291 $\pm$ 15	—	10 <sup>-4</sup>	[Houlier et al., 1990]
<i>Ol</i> diffusion	—	-1.9 $\pm$ 2.4	4-9	[Běřina et al., 1997]
<i>Ol</i> diffusion	—	0.7 $\pm$ 2.3	4-9	[Běřina et al., 1999]
<i>Ol</i> deformation	510 $\pm$ 30	14	1-2	[Karato and Jung, 2003]
<i>Fo</i> deformation	460 $\pm$ 59	—	10 <sup>-4</sup>	[Darot and Gueguen, 1981]
<i>Fo</i> deformation	112	1-3	2.1-7.5	[Raterron et al., 2007]
<i>Ol</i> recovery	389 $\pm$ 30	14	10 <sup>-4</sup> -2	[Karato and Ogawa, 1982]
<i>Ol</i> recovery	—	5 $\pm$ 1	10 <sup>-4</sup> -10	[Karato et al., 1993]

The activation volume in the literature for olivine or forsterite deformation is typically larger than 10 cm<sup>3</sup>/mol (e.g. Karato and Ogawa [1982], Karato and Jung [2003], see **Table 2.2**), which is much higher than that for diffusion. The high activation volumes in deformation experiments are all obtained at low pressures (< 2 GPa). Li et al. [2006] obtained a value of 0 $\pm$ 5 cm<sup>3</sup>/mol at higher pressure (9.6 GPa) deformation experiments and Raterron et al. [2007] obtained 1-3 cm<sup>3</sup>/mol at 2.1-7.5 GPa. Meanwhile, Karato et al. [1993] reported an activation volume of 5 $\pm$ 1 cm<sup>3</sup>/mol for dislocation recovery up to 10 GPa. These values obtained at high pressures are in

good agreement with those in diffusion experiments. Li et al. [2006] suggested that the discrepancy in activation volume deduced from high-pressure and low-pressure experiments may result from grain boundary deformation mechanisms, active at low pressure and corresponding to high-activation volume, which consequently would be “shut down” at high pressure [Raterron et al., 2007] and it explains the apparent decrease of activation volume with pressure in deformation experiments. Besides, in order to precisely determine the activation volume, a large pressure range is necessary [Béjina et al., 1999]. The high activation volumes in deformation experiments were always obtained in narrow pressure ranges (< 2 GPa). In this study, experiments were conducted from ambient pressure to 13 GPa, which covers almost the entire forsterite phase stability field.

### 2.5.5 Comparison with wadsleyite and ringwoodite

Olivine, wadsleyite and ringwoodite are the main constituents of the upper mantle [Ringwood, 1991]. We plot  $D_{Si}$  in forsterite at 1600 K against pressure with that in iron-bearing wadsleyite and ringwoodite by Shimojuku et al. [2009] adjusted to 1600 K for comparison in **Fig. 2.16**.

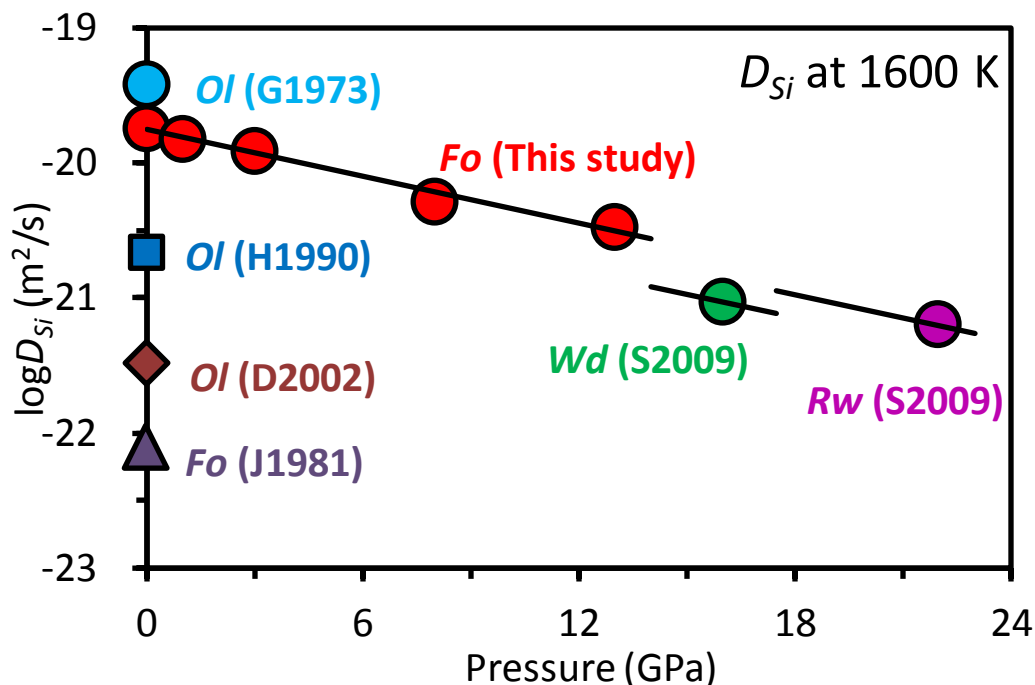


**Fig. 2.16.**  $\log D_{Si}$  with pressure at 1600 K. *Fo*: forsterite. *Ol*: natural olivine. *Wd*: iron-bearing wadsleyite. *Rw*: iron-bearing ringwoodite. S2009: Shimojuku et al. [2009]; H1990: Houlter et

al. [1990]; D2002: Dohmen et al. [2002]; J1981: Jaoul et al. [1981]. G1973: estimated from dislocation data by Goetze and Kohlstedt [1973].  $D_{Si}$  from previous studies are all calibrated to 1600 K. We assume the same activation volume for silicon diffusion in forsterite, wadsleyite and ringwoodite.

By extrapolating the data of  $\log D_{Si}$  in iron-free forsterite to higher pressures (at stability fields for  $\beta$  and  $\gamma$  phases), we found that it is  $\sim 0.2$ - $0.4$  orders of magnitude higher than those obtained in iron-bearing ( $Mg_{1.8}Fe_{0.2}SiO_4$ ) wadsleyite and ringwoodite determined by Shimojuku et al. [2009]. In Shimojuku et al. [2009], their wadsleyite samples contain 10-80 wt. ppm of water, while ringwoodite samples contain 130-220 wt. ppm water. Such a small difference in  $\log D_{Si}$  among dry forsterite, iron and water bearing wadsleyite and ringwoodite calibrated to the same temperature conditions implies that the effects of iron, water, and the structural difference among  $(Mg,Fe)_2SiO_4$  polymorphs on silicon diffusion are small.

#### 2.5.6 $D_{Si}$ in the upper mantle and mantle transition zone

As mentioned above, the  $D_{Si}$  has a negative dependence on pressure and positive dependence on temperature. By assuming the adiabatic geotherm [Katsura et al., 2010], we estimated the  $D_{Si}$  profile in the upper mantle and mantle transition zone (**Fig. 2.17**) neglecting effects of iron and water contents. As is seen in the figure,  $D_{Si}$  monotonically and slightly increases with depth in the olivine stability field. This means that pressure is not a significant factor in variations of  $D_{Si}$  whereas the temperature effect is significant in spite of the small temperature increase in the adiabatic temperature distribution (1-1.5 K/km). As the geothermal gradient decreases with increasing depth in the olivine stability field, the increasing rate of  $D_{Si}$  also decreases with increasing depth. At the 410 km depth discontinuity,  $D_{Si}$  increases by  $\sim 0.3$ - $0.4$  orders of magnitude due to the temperature increase. However, this magnitude of jump is within the range of experimental errors. In addition, other factors such as the iron content, water content and oxidation state may affect the magnitude of the jump.

If the mantle viscosity is primarily inversely proportional to  $D_{Si}$ , the mantle viscosity should slightly decrease monotonically with depth from the top of the upper mantle to the mantle transition zone by  $\sim 0.5$  orders of magnitude (**Fig. 2.17**). It is inconsistent with geophysical estimations of the mantle viscosity that indicate it decrease from 100 to 200 km with a minimum

value at 200 km depth and increases gradually from the bottom of the lithosphere at 200 km to deep mantle [Anderson, 1966].

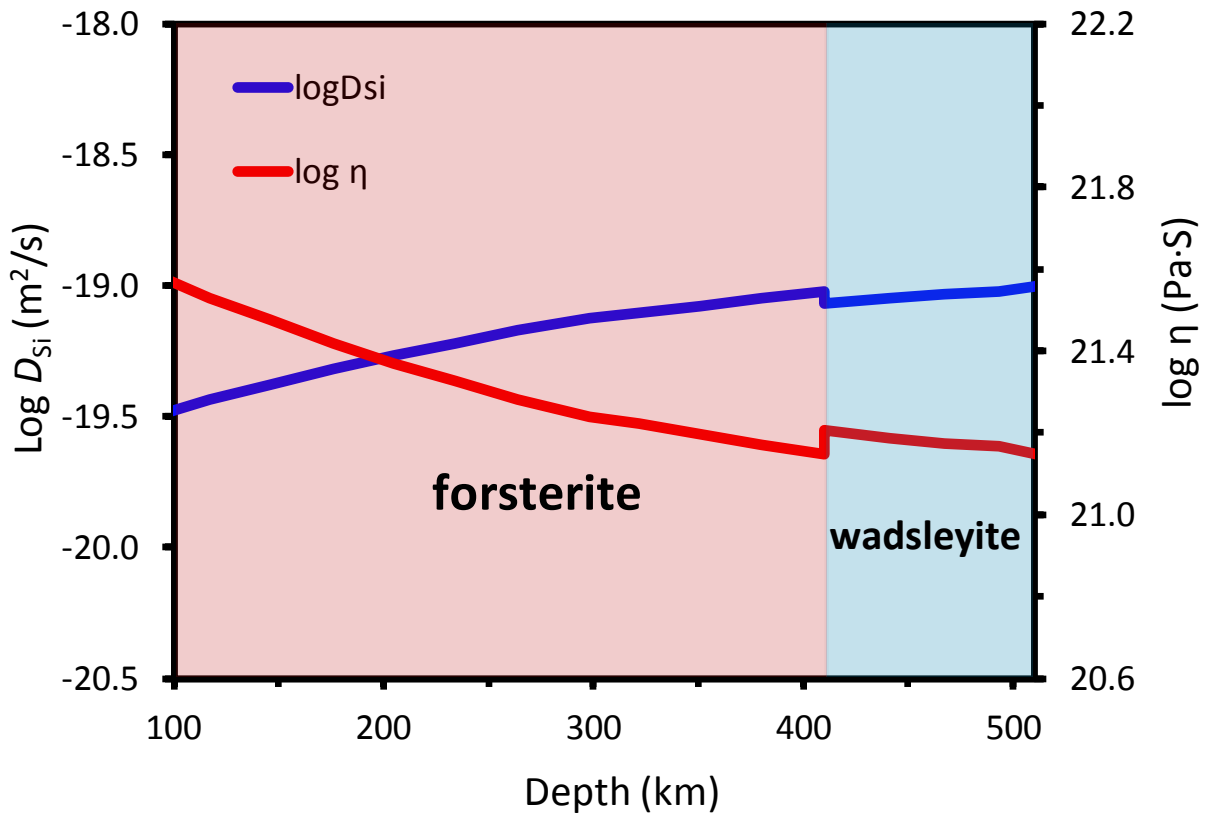


**Fig. 2.17.**  $D_{Si}$  and viscosity in the upper mantle. Data of  $D_{Si}$  in wadsleyite was from Shimojuku et al. [2009]. The viscosity was calculated using the inversely proportional relationship of  $D_{Si}$  and viscosity as:  $\eta=10kTr^2/(D_{Si}m_a)$ , where  $k$  is the Boltzmann constant,  $T$  was the absolute temperature based on adiabatic geothermal from Katsura et al. [2010],  $r$  was the radius of crystal, and  $m_a$  was the mass of a Si ion [McKenzie, 1967]. The grain size in the mantle was assumed to be  $\sim 1$  mm.  $D_{Si}$  was a function of temperature, and pressure in **Eqs. 2.4**.

Karato and Wu [1993] investigated the viscosity with depth in the upper mantle at different activation volumes of creep in olivine. They suggested that with larger activation volumes ( $>10$   $cm^3/mol$ ) the viscosity increases greatly with depth and if the activation volume is smaller than 5  $cm^3/mol$ , the viscosity is almost constant in the upper mantle. Experimental deformation studies [Borch and Green II, 1989; Karato and Ogawa, 1982; Karato and Jung, 2003] show high activation volume ( $> 10$   $cm^3/mol$ ), and therefore, the mantle viscosity increase with depth. On the other hand, if diffusion controlled dislocation creep in the mantle, the present results for  $D_{Si}$

with an activation volume for 1-2 cm<sup>3</sup>/mol (e.g. this study; Běřina et al. [1997; 1999]) clearly suggest that the viscosity in the upper mantle should be nearly constant, or even slightly decrease, and that there is no viscosity minimum in the upper mantle. If a viscosity minimum exists at 200 km depth that allows plate motion, we have to consider other reasons for it. Two ideas often considered are partial melting [*Hirth and Kohlstedt*, 1995a; b] and hydration [*Hirth and Kohlstedt*, 2003] in the asthenosphere.

## **2.6 Acknowledgments**

We make great acknowledgements to S. Chakraborty and R. Dohmen in Ruhr-University of Bochum for their help in the sample coating and comprehensive discussions throughout in this study. We also appreciate H. Keppler for his help of FTIR measurement, A. Audéat for ICP-MS analysis, K. Pollok for surface roughness measurement, F. Heidelbach for SEM analysis, and T. Boffa-Ballaran for single crystal X-ray diffraction analysis. We thank all the technicians in BGI and ISEI for sample and assembly preparation. We acknowledge the support by ENB (Elite Network Bavaria) programs. This research was partially supported by the Ministry of Education, Science, Sports and Culture, Japan, Grant-in-Aid for Scientific Research (S), No. 20224010, 2008-2010.

# Chapter 3

---

## Silicon self-diffusion in wet forsterite

### 3.1 Abstract

Water has been considered to largely affect the dynamical processes in the Earth's interior. In particular, experimental deformation results [Hirth and Kohlstedt, 2003; Jung and Karato, 2001; Karato *et al.*, 1986; Mei and Kohlstedt, 2000a; b] suggest that even several tens wt. ppm of water enhances the creep rates in olivine by orders of magnitude. However, those deformation studies have limitations such as a limited range of water concentrations, very high stresses, etc., which might affect the results. Rock deformation can also be understood by silicon self-diffusion coefficient ( $D_{Si}$ ) because the creep rates of minerals at high temperature, as that in the Earth's interior, are limited by self-diffusion of the slowest species [Frost and Ashby, 1982; Weertman, 1999]. Here we report our experimental results of  $D_{Si}$  in forsterite at 8 GPa, 1600-1800 K, as a function of water content ( $C_{H_2O}$ ) in the range from <1 up to ~800 wt. ppm, showing a relationship,  $D_{Si} \propto (C_{H_2O})^{0.32 \pm 0.07} \approx (C_{H_2O})^{1/3}$ . This  $C_{H_2O}$  exponent is strikingly lower than 1.2 that has been obtained by deformation experiments [Hirth and Kohlstedt, 2003]. The high nominal creep rates in the deformation studies under wet conditions may be caused by excess grain boundary water. We conclude that the effect of water on upper mantle rheology is very small based on the results of Si self-diffusion coefficients. The smooth motion of the Earth's tectonic plates cannot be caused by mineral hydration in the asthenosphere. Water cannot cause the viscosity minimum zone in the upper mantle. The dominant mechanism responsible for hotspot immobility cannot be  $C_{H_2O}$  differences between their source and surrounding regions.

### 3.2 Introduction

Diffusion and dislocation creeps are two important mechanisms that dominate the plastic deformation of rocks and minerals in the Earth's interior. Experimental deformation studies have suggested that incorporation of water in olivine significantly enhances both dislocation and diffusion creep rates [Hirth and Kohlstedt, 2003; Jung and Karato, 2001; Karato *et al.*, 1986; Mei and Kohlstedt, 2000a; b]. However, we note that those studies used polycrystalline olivine

samples with over-saturated water. In such setups, large amounts of free water may have existed on grain boundaries leading to a large enhancement of grain boundary sliding (or pressure solution accommodated creep), rather than dislocation or diffusion creeps in the grain interior. On the other hand, the upper mantle is water unsaturated and free water is unlikely to exist. Therefore, the enhancement of creep rates by free water cannot occur in the real upper mantle. We also note that the ranges of water contents ( $C_{H_2O} < 80$  wt. ppm) in these deformation studies [Hirth and Kohlstedt, 2003; Jung and Karato, 2001; Karato et al., 1986; Mei and Kohlstedt, 2000a; b] are too small to accurately determine the effect of water on stress-strain rate measurements. These can lead to large errors in estimating the effect of water on mantle rheology.

Another problem with the rock deformation experiments is the very high stress (typically  $\sim 10^2$  times higher than that in Earth's interior) needed to obtain experimentally determinable strain rates. High stress makes anomalously high-density dislocations, stacking faults, or sub-grain boundaries, which possibly lead to artificial results for the Earth's interior. Measurement of self-diffusion coefficients in minerals is an independent way to study mantle rheology because high temperature mineral creep is believed to be controlled by self-diffusion of the slowest species [Frost and Ashby, 1982; Weertman, 1999] (e.g. silicon in the case of olivine [Costa and Chakraborty, 2008; Houlier et al., 1990]). It allows much wider experimental conditions (e.g. pressure,  $C_{H_2O}$ ), and also does not induce unrealistically high defect densities.

Costa and Chakraborty [2008] measured silicon self-diffusion coefficients ( $D_{Si}$ ) in olivine single crystals with  $C_{H_2O}$  values of  $\sim 40$  and  $370$  wt. ppm and concluded that even  $45$  wt. ppm of water enhances  $D_{Si}$  by 2-3 orders of magnitude by comparing with that under dry conditions obtained by Dohmen et al. [2002]. However, the data of Costa and Chakraborty [2008] did not show a systematic change in  $D_{Si}$  with  $C_{H_2O}$  at  $\sim 40$  and at  $\sim 370$  wt. ppm. In addition, our previous study [Fei et al., 2012] showed that Dohmen et al. [2002] may have underestimated  $D_{Si}$  under dry conditions. We therefore propose that the water effect was overestimated in Costa and Chakraborty [2008].

In this study, we systematically measured  $D_{Si}$  in olivine as a function of  $C_{H_2O}$ . Because the effects of iron on  $D_{Si}$ , as well as on creep rates, are very small under upper mantle conditions [Durham and Goetze, 1977b; Fei et al., 2012], a single crystal forsterite sample is used. We

measured its  $D_{Si}$  at 8 GPa, 1600 and 1800 K, and with well controlled  $C_{H_2O}$  from <1 up to ~800 wt. ppm, which is realistic for the oceanic mantle. Our results indicate that the effect of water on upper mantle rheology is very small.

### 3.3 Experimental methods

#### 3.3.1 Starting material

A single crystal forsterite sample was obtained from Oxide Co., Japan. The chemical composition of the crystal is  $Mg_2SiO_4$ . Its trace elements compositions were shown in Fei et al. [2012]. No O-H absorption bands were detected by Fourier transform infrared (FT-IR), indicating that the water content was less than 1 wt. ppm. Disks cored from the crystal, with 1 mm diameter and 1 mm thick and the thickness oriented along the  $b$ -axis, were used in this study.

#### 3.3.2 Water-doping experiments

The cored forsterite disks were pre-annealed at 8 GPa, 1600 K in the presence of a water source. This step is necessary to equilibrate the water in the crystal before diffusion annealing.

Each forsterite disk was loaded in a platinum capsule, with an outer diameter 2.0 mm and inner diameter 1.6 mm, with one end sealed. A mixture of talc and brucite powders, weight ratio 4:1, was used as the water source and also to control the silica activity in the capsule. The space between the forsterite disk and capsule wall was filled with graphite or gold + enstatite (weight ratio 35:1) powder for low and high water content experiments, respectively, to protect the single crystal from mechanical damage at high pressure. The capsule was closed and sealed by arc welding in liquid nitrogen to minimize water escape from the capsule. The water content in the capsule was controlled by the ratio of water source to graphite or gold + enstatite. In dry experiments, graphite powder was loaded around the samples; the capsules were then dried in a vacuum oven at 470 K for at least 24 hours and sealed on a hot plate to minimize the amount of moisture absorbed from the atmosphere. The final length of capsules was 4 to 4.5 mm (**Fig. 3.1**).

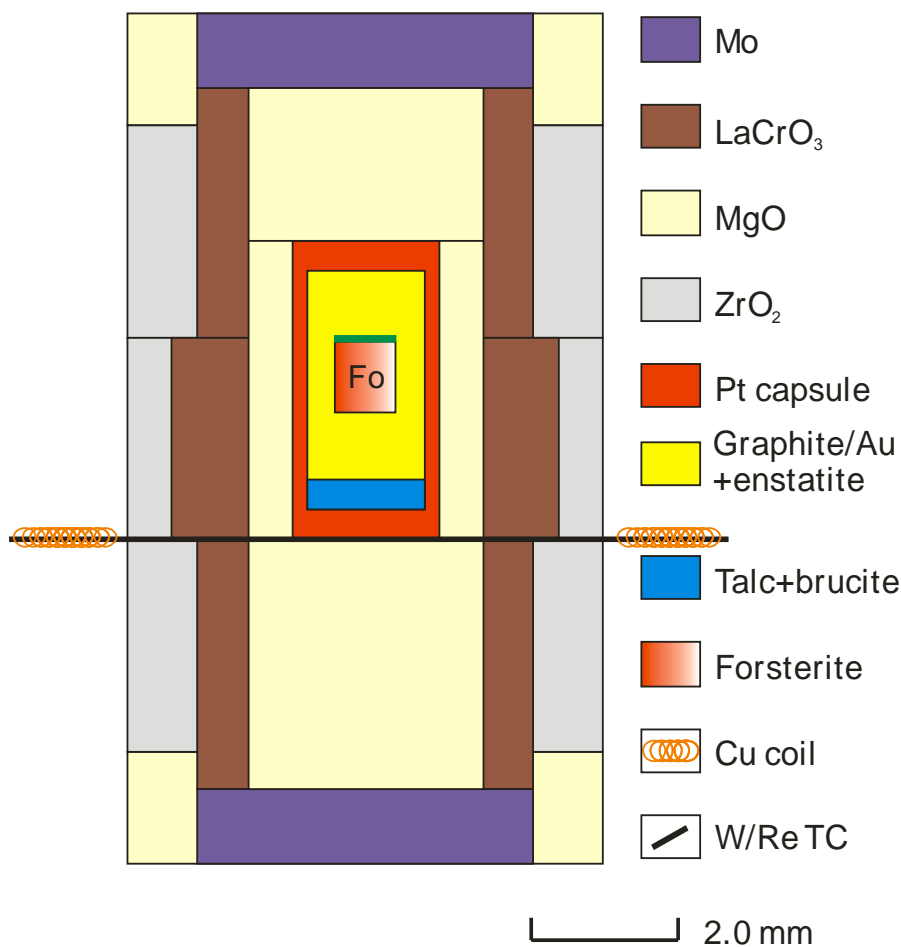


**Fig. 3.1.** Cross-section of high-pressure cell assembly used for water-doping and diffusion annealing experiments. The coated thin film for diffusion experiments (green) is located at the step of  $\text{LaCrO}_3$ , while the thermocouple is located at the other step to minimize temperature measurement uncertainties.

High pressure experiments were performed using a Kawai-type multi-anvil apparatus at the University of Bayreuth. All experiments were performed at 8 GPa and 1600 K. In each run, the sealed platinum capsule was located in an MgO cylinder in a  $\text{LaCrO}_3$  stepped heater with a  $\text{ZrO}_2$  thermal insulator. A MgO octahedron (with 5 wt. %  $\text{Cr}_2\text{O}_3$ ) with edge length of 14 mm was used as the pressure medium (**Fig. 3.1**). Eight tungsten carbide cubes with 32-mm edge length and 8-mm truncation edge length were used to generate high pressures. The temperatures were measured using a W97%Re3%-W75%Re25% thermocouple, 0.25 mm in diameter, whose junction was placed at the bottom of capsule. The assembly was compressed to the target pressure over 2-4 hours, heated to 1273 K at a rate of 50 K/min, kept at 1273 K for 1 hour to decompose talc and brucite and to make the water distribution homogenous in the capsule, the

assembly was then heated to 1600 K in 5 min and kept for a long duration for water equilibration (50-70 hours), as calculated from the hydrogen diffusion coefficients in forsterite [Demouchy and Mackwell, 2003]. The temperature was under automatic control, thus limiting variation to less than 2 K during annealing. After annealing, the sample was quenched by switching off the heating power and gradually decompressed to ambient pressure over a long period (15-20 hours) to prevent crystal breakage.

The forsterite disks were recovered by cutting into the platinum capsule using a steel blade. No obvious cracks were found in the samples if small amounts of water source were used. With high amounts of water source, the crystal always contained some cracks and broke into pieces. However, in such case we were still able to find usable pieces for diffusion experiments.

### 3.3.3 Deposition

The water doped samples were polished using diamond powders with grain sizes of 0.25  $\mu\text{m}$ , followed by an alkaline colloidal silica solution for >3 hours until all small scratches were removed. The highly polished surface was then coated with ~500 nm of  $^{29}\text{Si}$  enriched  $\text{Mg}_2\text{SiO}_4$  and 100 nm of  $\text{ZrO}_2$  using a pulsed laser deposition (PLD) system at Ruhr-University of Bochum [Dohmen *et al.*, 2002]. We also conducted some diffusion experiments without the  $\text{ZrO}_2$  film for comparison, and showed that the  $\text{ZrO}_2$  does not affect  $D_{\text{Si}}$ , which was already confirmed in our previous study. Prior to each deposition, the samples were heated up to 470 K for 10-15 min in the vacuum chamber of the PLD system so as to remove any free water from the sample surface. The structural water in the crystals did not escape during this step.

### 3.3.4 Diffusion annealing

Each thin film deposited sample was placed in a platinum capsule with the same ratio of water source and graphite or gold + enstatite as used for the corresponding water-doping experiment and was then annealed at 8 GPa, and 1600 or 1800 K using the same high pressure assembly (**Fig. 3.1**). The annealing durations, ranging from 5 - 41 hours as summarized in **Table 3.1**, were estimated from silicon diffusion coefficient data for olivine [Costa and Chakraborty, 2008] and forsterite [Fei *et al.*, 2012].

**Table 3.1.** Summary of experimental runs and results of silicon self-diffusion coefficients ( $C_{H_2O}^a$ : water content before diffusion annealing,  $C_{H_2O}^b$ : water content after diffusion annealing,  $t$ : duration of diffusion annealing,  $T$ : annealing temperature,  $D_{Si}$ : silicon self-diffusion coefficient).  $C_{H_2O}$  under dry conditions are below the detection limit of FT-IR (i.e.,  $< 1$  wt. ppm). All experiments were performed at a pressure of 8 GPa. We did not make time series in this study because we have previously examined [Fei *et al.*, 2012] that  $D_{Si}$  is constant within experimental error for different annealing durations under the same conditions after a zero-time calibration.

Run No.	$C_{H_2O}^a$ (wt. ppm)	$C_{H_2O}^b$ (wt. ppm)	$T$ (h)	$T$ (K)	$D_{Si}$ (m <sup>2</sup> /s)
H3390a	242	237	41	1600	$3.0 \times 10^{-20}$
H3390b	242	237	41	1600	$3.1 \times 10^{-20}$
H3507a	805	810	7	1600	$6.7 \times 10^{-20}$
H3507b	805	810	7	1600	$1.5 \times 10^{-19}$
H3389a	248	230	9	1600	$4.5 \times 10^{-20}$
H3389b	248	230	9	1600	$7.0 \times 10^{-20}$
H3389c	248	230	9	1600	$9.0 \times 10^{-20}$
V724a	183	114	18	1600	$5.1 \times 10^{-20}$
V724b	183	114	18	1600	$5.5 \times 10^{-20}$
1119a	<1	<1	12	1600	$9.8 \times 10^{-21}$
1119b	<1	<1	12	1600	$6.0 \times 10^{-21}$
1119c	<1	<1	12	1600	$6.7 \times 10^{-21}$
S5045a	<1	<1	21	1600	$4.8 \times 10^{-21}$
S5045b	<1	<1	21	1600	$1.3 \times 10^{-20}$
V720a	13	12	27	1600	$2.2 \times 10^{-20}$
V720b	13	12	27	1600	$2.5 \times 10^{-20}$
245a	<1	6	25.3	1600	$2.1 \times 10^{-20}$
1146a	<1	<1	15	1800	$1.8 \times 10^{-19}$
1146b	<1	<1	15	1800	$1.4 \times 10^{-19}$
1145	<1	<1	5	1800	$2.6 \times 10^{-19}$
H3509a	15	12	5	1800	$1.1 \times 10^{-18}$
H3509b	15	12	5	1800	$9.9 \times 10^{-19}$
H3509c	15	12	5	1800	$1.7 \times 10^{-18}$

### 3.3.5 FT-IR analysis

The water contents in the samples after water-doping experiments and also after diffusion annealing were measured using a high resolution FT-IR spectrometer at the University of Bayreuth, described in Fei et al. [2012]. Each forsterite sample for FT-IR analysis was polished on both faces normal to the  $b$ -axis using 0.25- $\mu\text{m}$  diamond powder. Two hundred scans were accumulated for each spectrum at a resolution of  $1\text{ cm}^{-1}$ . Two or three spectra were obtained for each sample with at least one near the center of the disk and one near the edge. One sample (V720) was also polished parallel to the  $b$ -axis, and the water content was obtained as a function of distance from the coated thin film at 60- $\mu\text{m}$  steps. After a background baseline correction and thickness normalization to 1 cm, the water contents were determined using the calibration given by Bell et al. [Bell et al., 2003]:

$$C_{H_2O} = 0.188 \times \int k(\nu) d\nu \quad (3.1)$$

where  $C_{H_2O}$  was the water content in wt. ppm and  $k(\nu)$  was the absorption coefficient at wave number  $\nu$ . Integration was performed between 3000 and 4000  $\text{cm}^{-1}$  [Fei et al., 2012].

### 3.3.6 SIMS analysis

The apparent diffusion profiles were measured by secondary ion mass spectrometry (SIMS) depth profiling using the Cameca IMS-6f installed at the Helmholtz Centre Potsdam, Germany, with the same setup for determining  $D_{Si}$  in dry forsterite as in our previous study [Fei et al., 2012]. The depth of each SIMS crater was determined using a 3D-Nanofocus vertical microscope at the University of Bayreuth. The  $D_{Si}$  was obtained by fitting the data to the solution of Fick's second law:

$$c = \frac{c_0 - c_1}{2} \operatorname{erf}\left(\frac{x - h}{\sqrt{4Dt + L^2(\sigma)}}\right) + \frac{c_0 + c_1}{2} \quad (3.2)$$

where  $c$  is the observed abundance of  $^{29}\text{Si}$ ,  $c_1$  is the initial abundance of  $^{29}\text{Si}$  in the isotopic film,  $c_0$  is the initial abundance of  $^{29}\text{Si}$  in the substrate,  $x$  is the distance from the surface,  $h$  is the position of the boundary between the thin film and substrate,  $t$  is the annealing time,  $L(\sigma)$  is the nominal diffusion length in zero-time diffusion runs related to surface roughness (discussed in

section 2.3.5), and  $erf(z)$  is the error function [Fei *et al.*, 2012]. An example of the diffusion profiles is shown in Fig. 3.2.

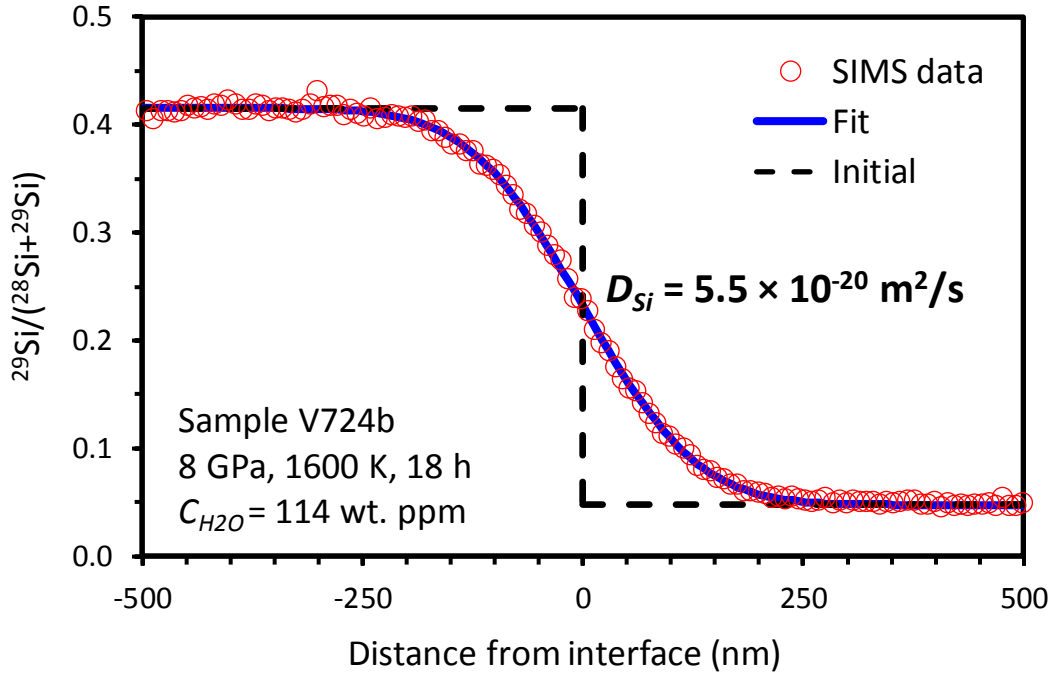


**Fig. 3.2.** An example of a SIMS diffusion profile. Sample with 114 wt. ppm of water, annealed at 8 GPa and 1600 K for 18 hours.

### 3.4 Results

Experimental results are shown in Fig. 3.3.  $D_{\text{Si}}$  systematically increases with increasing  $C_{\text{H}_2\text{O}}$ .  $D_{\text{Si}}$  values under wet conditions ( $C_{\text{H}_2\text{O}} > 1 \text{ wt. ppm}$ ) were fitted to the Arrhenius equation:

$$D_{\text{Si}} = A_0 C_{\text{H}_2\text{O}}^r \exp\left(-\frac{\Delta H}{RT}\right) \quad (3.3)$$

where  $A_0$  is the pre-exponential factor,  $r$  is the  $C_{\text{H}_2\text{O}}$  exponent,  $R$  is the gas constant,  $T$  is the absolute temperature, and  $\Delta H$  is the activation enthalpy.  $A_0$ ,  $r$ , and  $\Delta H$  are determined to be  $10^{5.8 \pm 0.7} \text{ m}^2/\text{s}$ ,  $0.32 \pm 0.07$ , and  $434 \pm 20 \text{ kJ/mol}$ , respectively. The activation energy,  $\Delta E$ , is  $420 \pm 23 \text{ kJ/mol}$  after a pressure correction (using an activation volume of  $1.7 \pm 0.4 \text{ cm}^3/\text{mol}$ ), which is essentially the same as that for dry conditions ( $410 \pm 30 \text{ kJ/mol}$ , [Fei *et al.*, 2012]).

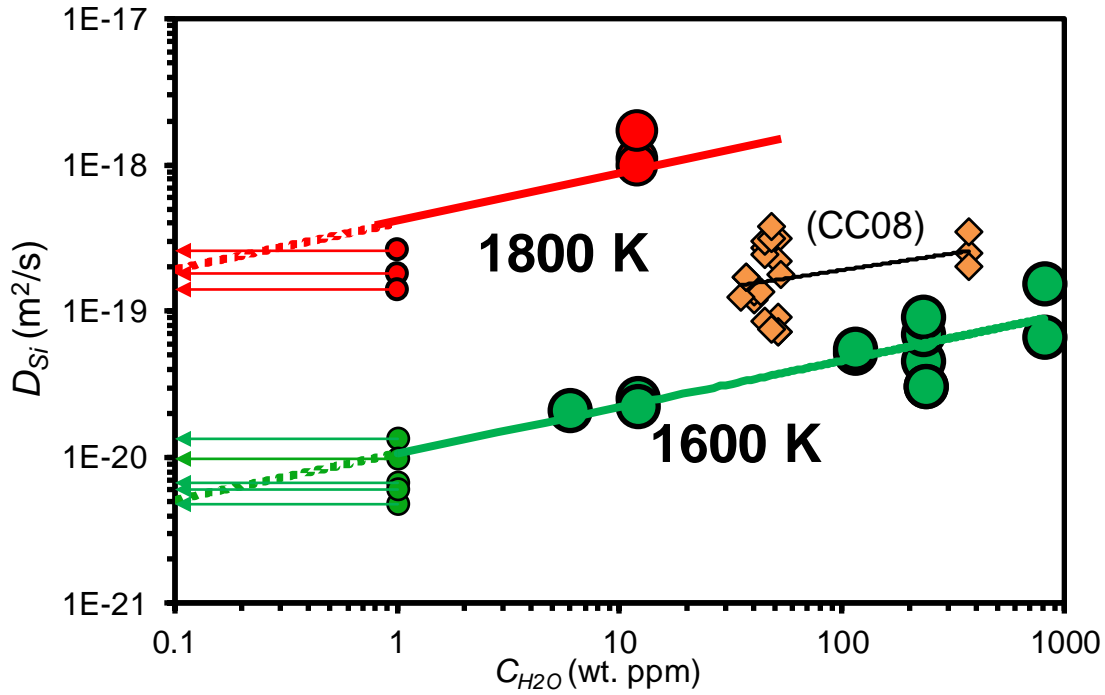


**Fig. 3.3.**  $D_{Si}$  versus  $C_{H_2O}$  at 1600 and 1800 K. The data points shown by small circles with an arrow are taken from Fei et al. [2012] on  $D_{Si}$  in dry forsterite at 8 GPa, with  $C_{H_2O} < 1$  wt. ppm, which are below the detection resolution of FT-IR and SIMS. It was impossible to obtain data points at 1800 K with high  $C_{H_2O}$  because of the low melting temperature of hydrous forsterite [Inoue, 1994]. Even when  $C_{H_2O}$  was low, the isotopically enriched thin film coating of the diffusion couple was often damaged during annealing at this temperature. CC08: data points taken from Costa and Chakraborty [2008] normalized to 1600 K and 8 GPa using the activation energy of 358 kJ/mol they reported and an activation volume of 1.7 cm<sup>3</sup>/mol [Fei et al., 2012].

### 3.5 Discussion

#### 3.5.1 Well-controlled $C_{H_2O}$ during diffusion annealing experiments

**Figure 3.4a** shows typical FT-IR spectra of samples after diffusion annealing experiments with a wide range of  $C_{H_2O}$  from  $< 1$  up to  $\sim 800$  wt. ppm, i.e. from “dry” conditions to close to the water solubility ( $\sim 900$  wt. ppm at 8 GPa [Kohlstedt et al., 1996]). In the dry experiments,  $C_{H_2O}$  are below the detection limit of FT-IR ( $C_{H_2O} < 1$  wt. ppm). Our previous study [Fei et al., 2012] shows that  $D_{Si}$  at high pressures with  $C_{H_2O} < 1$  wt. ppm are consistent with results obtained at ambient pressure. Certainly ambient pressure experiments have a practically dry condition,

therefore, less than 1 wt. ppm of water does not affect the Si self-diffusion rate. The condition with  $C_{H_2O} < 1$  wt. ppm is rheologically “dry”.

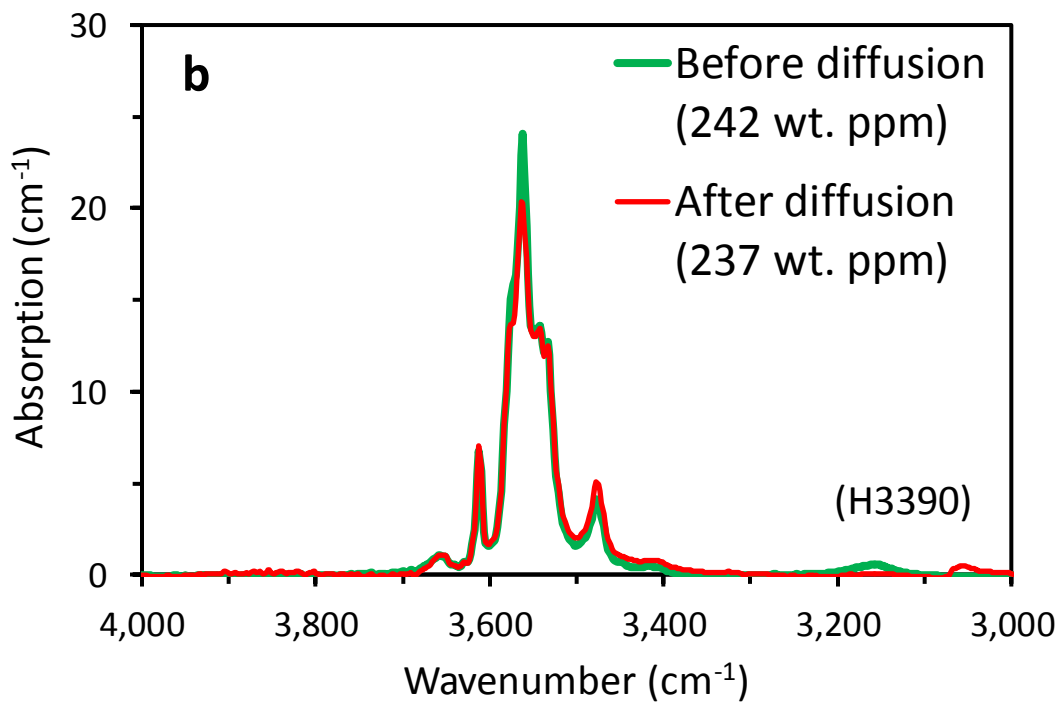
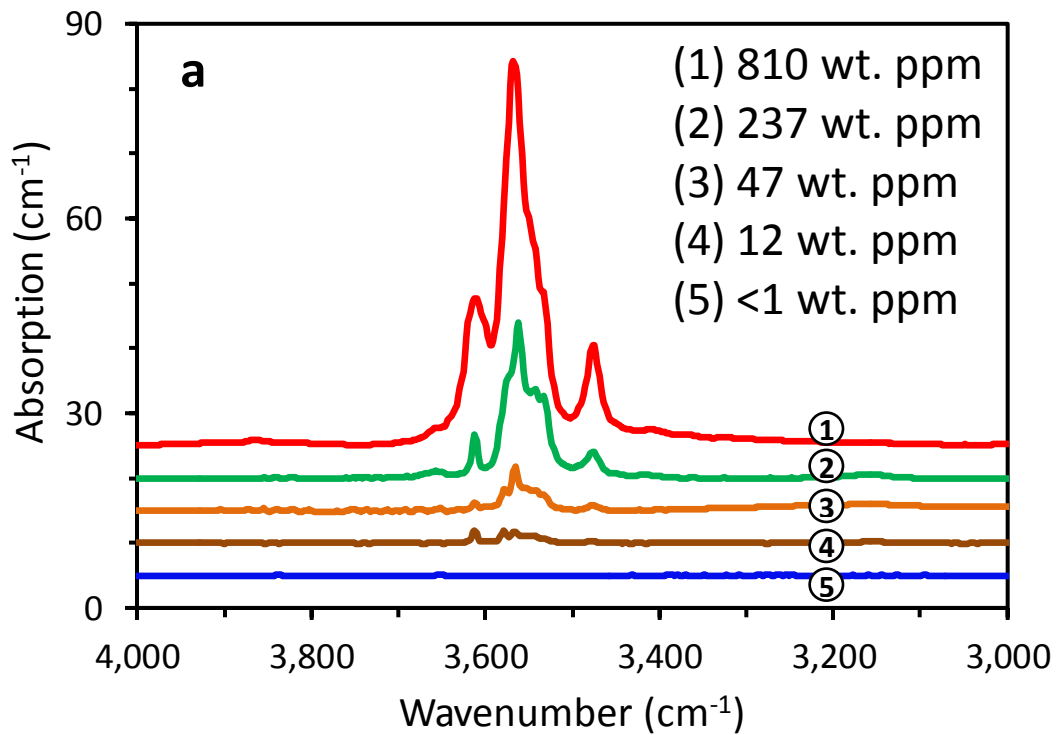
The water fugacity was not buffered to control the water contents in the crystal during diffusion annealing. However, we found almost the same values of  $C_{H_2O}$  before and after diffusion (**Fig. 3.4b**), indicating that the  $C_{H_2O}$  in the samples did not change during diffusion annealing.

One might expect that  $C_{H_2O}$  near the surface may be very different from the average in the crystal. However, we point out that the hydrogen diffusion rate in forsterite [Demouchy and Mackwell, 2003] is about nine orders of magnitude higher than that of Si self-diffusion. Even if  $C_{H_2O}$  in the forsterite crystal changes, it should essentially reach equilibrium quickly in comparison with the Si self-diffusion. In other words, the change of  $C_{H_2O}$  occurs instantaneously at the beginning of diffusion annealing, whereas Si self-diffusion occurs under the new water content condition for most of the annealing period.

The shortest diffusion length of hydrogen in the present study calculated from hydrogen diffusion rate in forsterite [Demouchy and Mackwell, 2003] is  $\sim 0.5$  mm; this is comparable to the radius of our sample and far longer than that of Si self-diffusion (about  $1 \mu\text{m}$ ). Therefore,  $C_{H_2O}$  should be homogenous in the samples in this study. To confirm this conclusion, FT-IR measurements were carried out on the cross section of sample V720. The difference in  $C_{H_2O}$  values near the sample surface with the thin film and in the center is within a factor of 2 ( $C_{H_2O} = \sim 12$  wt. ppm near the thin film, and  $\sim 6$  wt. ppm in the center, see **Fig. 3.4c**). In higher  $C_{H_2O}$  experiments, water in the crystals should be more homogeneous because the crystals usually included more cracks or broke to pieces, and water can easily enter such cracks during annealing.

We also measured the hydrogen concentration near the sample surface using SIMS. Examples of  $^{28}\text{Si}$ ,  $^{29}\text{Si}$ , and  $^1\text{H}$  counts are shown in **Fig. 3.4d**.  $^1\text{H}$  count within  $\sim 100$  nm of the sample surface is very high; this is likely to be water absorbed after annealing, probably during the chemical polishing [Fei et al., 2012]. The  $^1\text{H}$  count rapidly decreases to a constant value within a depth of 200 nm. On the other hand, the concentration of  $^{29}\text{Si}$  starts to decrease at depth  $> 200$  nm. Therefore, even if the high amount of water on the surface was introduced during annealing, it did not affect the  $D_{\text{Si}}$  results. The water content in the deeper region, where the

diffusion profile was measured, is homogenous. Thus, the  $C_{H_2O}$  data measured by FT-IR reflect the correct water contents for the regions where  $D_{Si}$  has been determined in this study.



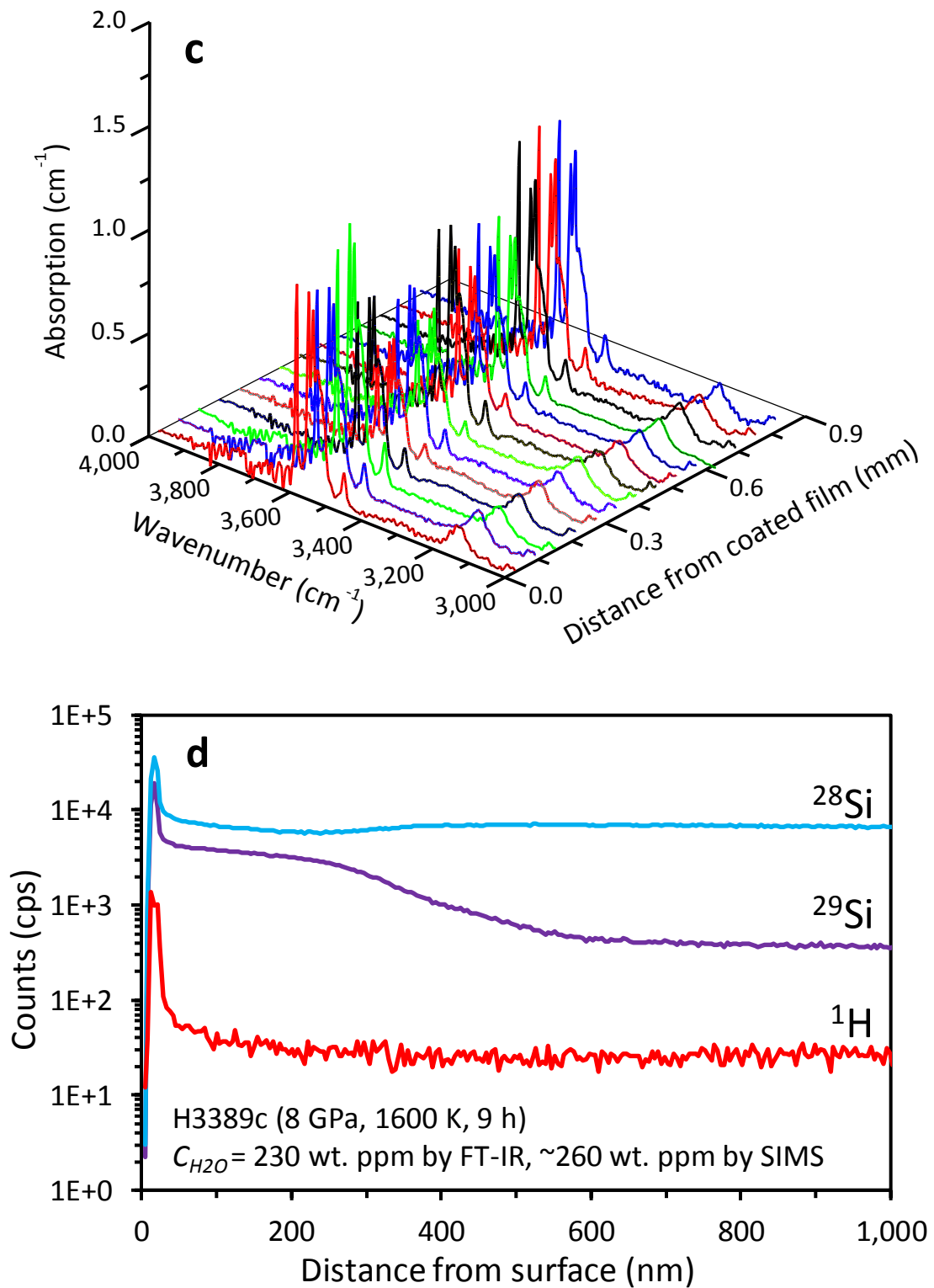


**Fig. 3.4.** Water contents in the samples. (a) Various  $C_{\text{H}_2\text{O}}$  values ranging from  $< 1$  up to  $\sim 800$  wt. ppm, as measured by FT-IR. (b) Constant  $C_{\text{H}_2\text{O}}$  from FT-IR spectra before and after diffusion annealing. (c) FT-IR spectra indicating homogenous  $C_{\text{H}_2\text{O}}$  measured across the cross-section at different distances from the thin film coated surface (sample V720). (d) Constant  $^1\text{H}$  counts in

the region deeper than 100 nm where silicon diffusion profiles were obtained.  $C_{H_2O}$  from FT-IR spectra were calculated using Bell's calibration [Bell *et al.*, 2003] after a background baseline correction and thickness normalization to 1 cm. The  $C_{H_2O}$  in (d) estimated from the H/Si ratio by SIMS is slightly higher than, but generally in agreement with that from FT-IR.

### 3.5.2 Activation energy for Si diffusion and deformation of olivine

The activation enthalpy  $\Delta H$  at pressure  $P$  can be expanded into  $\Delta H = \Delta E + P\Delta V$ , where  $\Delta E$  is the activation energy and  $\Delta V$  is the activation volume. Using the value of  $\Delta V = 1.7 \text{ cm}^3/\text{mol}$  [Fei *et al.*, 2012], we obtained  $\Delta E = 420 \pm 23 \text{ kJ/mol}$  for wet samples, which is essentially the same as that under dry conditions ( $410 \pm 30 \text{ kJ/mol}$ ) [Fei *et al.*, 2012]. Hence, the effect of water on activation energy for  $D_{Si}$  is small. Costa and Chakraborty [2008] reported a value of  $358 \pm 28 \text{ kJ/mol}$  of  $\Delta H$  for silicon diffusion in wet olivine. This value is slightly lower than that in forsterite determined in this study when normalized to the same pressure. On the other hand, Costa & Chakraborty [2008] also indicated that their activation energy for Si diffusion in wet olivine was  $\sim 450 \text{ kJ/mol}$  after an oxygen fugacity calibration, which is close to that determined in this study when analytical uncertainties are considered. Therefore, we conclude that the activation energy for Si diffusion in olivine or forsterite is  $\sim 400\text{-}450 \text{ kJ/mol}$  under both dry and wet conditions (**Table 3.2**).

**Table 3.2.** Activation energy for silicon diffusion and deformation in forsterite (*Fo*) and iron-bearing olivine (*Ol*) under “dry” and “wet” conditions.

Sample	Method	$T$ (K)	$P$ (GPa)	$\Delta E$ (kJ/mol)	Ref.
Wet <i>Fo</i>	Si diffusion	1600-1800	8	$420 \pm 23$	This study
Dry <i>Fo</i>	Si diffusion	1600-1800	$10^{-4}$ -13	$410 \pm 30$	Fei et al. [2012]
Wet <i>Ol</i>	Si diffusion	1473-1623	2	$358 \pm 28$	Costa and Chakraborty [2008]
Dry <i>Fo</i>	Deformation	1673-1873	$10^{-4}$	$460 \pm 59$	Darot and Gueguen [1981]
Wet <i>Ol</i>	Deformation	1473-1573	0.1-0.45	$470 \pm 40$	Mei and Kohlstedt [2000b]
Dry <i>Ol</i>	Deformation	1473-1573	0.1-0.45	$510 \pm 30$	Mei and Kohlstedt [2000b]

In dry forsterite,  $\Delta E$  values for Si diffusion and dislocation creep are 410 and 460 kJ/mol [Darot and Gueguen, 1981; Fei et al., 2012], respectively. In wet conditions, they are 420 (this study) and 470 kJ/mol [Mei and Kohlstedt, 2000b], respectively (**Table 3.2**). We find the activation energies for dislocation creep obtained in deformation experiments are slightly higher than that for Si diffusion under both dry and wet conditions. This could be attributed to the energy required to form jogs along dislocations [Karato and Jung, 2003], or to the energy resulting from coupled diffusion of silicon and other faster species [Jaoul, 1990].

### 3.5.3 Defect chemistry

The  $C_{H_2O}$  exponent for  $D_{Si}$  can be understood using defect chemistry. Formation of a Mg vacancy,  $V_{Mg}''$ , requires less energy than a Si vacancy,  $V_{Si}''''$  [Brodholt and Refson, 2000]. The concentration of  $V_{Mg}''$  is therefore much higher than that of  $V_{Si}''''$ ;  $[V_{Mg}''] \gg [V_{Si}''']$  in olivine [Kohlstedt, 2006]. Thus, the charge neutrality for  $H^+$  should be maintained by  $V_{Mg}''$ , namely,  $[(OH)_O^*] = 2[V_{Mg}'']$  [Kohlstedt et al., 1996]. This charge neutrality condition leads to [Kohlstedt, 2006]:

$$[V_{Si}'''] \propto (C_{H_2O})^{2/3} \quad (3.4)$$

$$[V_O^{\bullet\bullet}] \propto (C_{H_2O})^{-1/3} \quad (3.5)$$

The  $D_{Si}$  should be proportional to the density of silicon vacancies [Costa and Chakraborty, 2008; Kohlstedt, 2006]. In addition,  $Si^{4+}$  is surrounded by  $O^{2-}$  in tetrahedrons, and therefore,  $V_O^{\bullet\bullet}$  is also needed for  $Si^{4+}$  migration. We can expect a certain proportion of  $V_{Si}''''$  should be associated with  $V_O^{\bullet\bullet}$  due to the Coulomb force and the Si migration is dominated by  $V_O^{\bullet\bullet}$ -associated  $V_{Si}''''$ . Hence,  $D_{Si}$  should be also proportional to  $[V_O^{\bullet\bullet}]$ . This idea is supported by the oxygen partial pressure ( $P_{O_2}$ ) exponent for  $D_{Si}$  in olivine reported by Houlier et al. [1990],  $D_{Si} \propto (P_{O_2})^{-0.19} \approx (P_{O_2})^{-1/6}$ , which suggests  $D_{Si} \propto [V_O^{\bullet\bullet}]$  because  $[V_O^{\bullet\bullet}] \propto (P_{O_2})^{-1/6}$  [Stocker and Smyth, 1978]. Though Houlier et al.'s [1990] results were obtained in iron-bearing olivine, the proportional relationship between  $D_{Si}$  and  $[V_O^{\bullet\bullet}]$  should be also the case for iron-free forsterite. As a result, we have:

$$D_{Si} \propto [V_{Si}'''] \times [V_O^{\bullet\bullet}] \propto (C_{H_2O})^{1/3} \quad (3.6)$$

which agrees with our experimental results,  $D_{Si} \propto (C_{H2O})^{0.32 \pm 0.07}$ .

Natural olivine contains about 10 % of the  $Fe_2SiO_4$  component. The defect chemistry of iron-bearing olivine should be the same as that of forsterite if the iron ions are ferrous under reducing conditions. This means that the charge neutrality condition should be  $[(OH)_O^\bullet] = 2[V_{Me}^{\prime\prime}]$  for the  $C_{H2O}$  values as that in the present study. If the  $C_{H2O}$  is much higher, a large proportion of metal vacancies is occupied by  $H^+$  and the charge neutrality condition becomes  $[(OH)_O^\bullet] = [H_{Me}^\prime]$ .

On the other hand, if a sufficiently large proportion of ferric iron exists, namely under oxidizing conditions, the defect chemistry would be different because of the positively excess-charged  $Fe_{Me}^\bullet$ . In this case, if  $C_{H2O}$  is extremely low, the dominant charge neutrality condition in olivine is  $[Fe_{Me}^\bullet] = 2[V_{Me}^{\prime\prime}]$ . If  $C_{H2O}$  is higher, it would be replaced by  $[Fe_{Me}^\bullet] = [H_{Me}^\prime]$ . If  $C_{H2O}$  is extremely high, the contribution of  $Fe_{Me}^\bullet$  becomes negligible in comparison with that of  $(OH)_O^\bullet$  and the charge neutrality condition should be  $[(OH)_O^\bullet] = [H_{Me}^\prime]$  as also found for reducing conditions.

Now let us consider which charge neutrality condition applies for the upper mantle conditions. In the upper mantle, the ratio of  $[Fe_{Me}^\bullet]/[Me_{Me}^\times]$  is around  $10^{-5}$ - $10^{-6}$  in anhydrous olivine [Karato, 2008]. Consequently,  $10^{-5}$  of  $[H^+]/[Me_{Me}^\times]$  (i.e.,  $\sim 1 \mu\text{g/g}$  of  $H_2O$  in olivine) is enough to satisfy the condition  $[(OH)_O^\bullet] > [Fe_{Me}^\bullet]$ . Therefore, the dominant charge neutrality condition will be  $[(OH)_O^\bullet] = 2[V_{Me}^{\prime\prime}]$  when  $C_{H2O} > 1$  wt. ppm. On the other hand, If all  $H^+$  ions enter  $V_{Me}^{\prime\prime}$  to form  $H_{Me}^\prime$  at  $C_{H2O} = 1$  wt. ppm, we have  $[H_{Me}^\prime] \approx 1.6 \times 10^{-5}$ . By using the relationships  $[V_{Me}^{\prime\prime}] \propto (C_{H2O})^{1/3}$  and  $[H_{Me}^\prime] \propto (C_{H2O})^{2/3}$  (**Table 3.3**), and the experimental result that  $[V_{Me}] \approx [V_{Me}^{\prime\prime}] + [H_{Me}^\prime] \approx 4.2 \times 10^{-4}$  at  $C_{H2O} \approx 16$  wt. ppm [Wang *et al.*, 2004],  $C_{H2O} > 3700$  wt. ppm is required to make the condition  $[H_{Me}^\prime] > 2[V_{Me}^{\prime\prime}]$  true. Therefore,  $[(OH)_O^\bullet] = [H_{Me}^\prime]$  dominates the charge neutrality condition only if  $C_{H2O}$  is at least  $> 3700$  wt. ppm. Hence,  $[(OH)_O^\bullet] = 2[V_{Me}^{\prime\prime}]$  is the charge neutrality condition for olivine under upper mantle conditions where  $C_{H2O}$  is at the level of several hundred wt. ppm [Hirschmann, 2006; Workman and Hart, 2005].

We also have to consider the case in which  $H^+$  is incorporated into the Si vacancies. If  $C_{H2O}$  is relatively low, the dominant Si vacancy should be  $V_{Si}^{\prime\prime\prime}$ . With increasing  $C_{H2O}$ ,  $H^+$  is trapped

in the Si vacancies and the dominant Si vacancy should change from  $V_{Si}^{''''}$  to  $H_{Si}^{''}$ ,  $(2H)_{Si}^{''}$ ,  $(3H)_{Si}^{'}$ , and finally  $(4H)_{Si}^{\times}$ .

Let us consider the  $C_{H_2O}$  exponent for  $D_{Si}$  when the dominant Si vacancy is  $V_{Si}^{''''}$ . When the charge neutrality conditions are  $[Fe_{Me}^{\bullet}] = 2[V_{Me}^{''}]$ , as well as  $[(OH)_O^{\bullet}] = [H_{Me}^{\bullet}]$ ,  $[V_{Si}^{''''}]$  and  $[V_O^{\bullet\bullet}]$  are independent with  $C_{H_2O}$ . Therefore,  $D_{Si} \propto [V_{Si}^{''''}] \times [V_O^{\bullet\bullet}] \propto (C_{H_2O})^0$ . When  $[Fe_{Me}^{\bullet}] = 2[H_{Me}^{\bullet}]$ , we have  $D_{Si} \propto (C_{H_2O})^{-0.5}$ . This relationship indicates that increasing  $C_{H_2O}$  makes olivine even harder under oxidizing conditions. For the charge neutrality condition of  $[(OH)_O^{\bullet}] = 2[V_{Me}^{''}]$ , we have  $D_{Si} \propto (C_{H_2O})^{1/3}$ , which is the case in this study. Thus, the  $C_{H_2O}$  exponent of 1/3 is the largest value that can be obtained if the dominant Si vacancy is  $V_{Si}^{''''}$  (**Table 3.3**).

Next, let us consider the case that  $H^+$  ions are trapped in the Si vacancies. When the dominant Si vacancy is  $H_{Si}^{''}$ , the  $C_{H_2O}$  exponent for  $D_{Si}$  is 1/2 or 2/3. In the case of  $(2H)_{Si}^{''}$ , the  $C_{H_2O}$  exponent will be 1. If the dominant Si vacancy is  $(3H)_{Si}^{'}$  or  $(4H)_{Si}^{\times}$ , the  $C_{H_2O}$  exponent will be even higher, i.e. up to 2.5 (**Table 3.3**). Thus, the  $C_{H_2O}$  exponent will be higher than 1/3 if  $H^+$  ions are incorporated into Si vacancies.

We can expect a certain proportion of  $V_{Si}^{''''}$  are associated with  $V_O^{\bullet\bullet}$  due to the Coulomb force, and Si diffusion is dominated by  $V_O^{\bullet\bullet}$  associated  $V_{Si}^{''''}$ . Since  $V_{Si}^{''''}$  has four charges, and  $H_{Si}^{''}$ ,  $(2H)_{Si}^{''}$ ,  $(3H)_{Si}^{'}$ , or  $(4H)_{Si}^{\times}$  has three or less charges, the probability of association of  $V_{Si}^{''''}$  and  $V_O^{\bullet\bullet}$  should be much higher than that of hydrated  $V_{Si}^{''''}$  and  $V_O^{\bullet\bullet}$ . Therefore,  $H_{Si}^{''}$ ,  $(2H)_{Si}^{''}$ ,  $(3H)_{Si}^{'}$ , or  $(4H)_{Si}^{\times}$  could dominate Si diffusion only if  $C_{H_2O}$  is extremely high and all of Si vacancies are hydrated.

We note that the incorporation of  $H^+$  ions into Si vacancies is unlikely in the upper mantle, at least in the oceanic mantle. Our experimental results demonstrate that the species of Si vacancies that dominates Si self-diffusion should not change with  $C_{H_2O}$  from 1 to 800 wt. ppm. However, our experimental results do not show increase of  $C_{H_2O}$  exponent up to 800 wt. ppm. Higher  $C_{H_2O}$  conditions are unlikely in upper mantle judging from petrological studies (i.e., ~70-160 wt. ppm of water in depleted mantle [Workman and Hart, 2005], and four to five times higher in enriched mantle [Hirschmann, 2006]). Therefore, the  $C_{H_2O}$  exponent of 1/3 should be the maximum for the realistic mantle.

**Table 3.3.** Dependencies of defect species and  $D_{Si}$  on  $C_{H_2O}$  under four charge neutrality conditions, expressed as the exponent  $r$  in the relationship  $[A] \propto (C_{H_2O})^r$ .  $V_{Si}$  denotes the silicon vacancy species, namely,  $V_{Si}^{''''}$ ,  $(H)_{Si}^{''}$ ,  $(2H)_{Si}{'}$ ,  $(3H)_{Si}'$ , or  $(4H)_{Si}^{\times}$ . Defect species exponent data in the table are from Kohlstedt [2006]. Note that the  $H^+$  should not be trapped by Si vacancies under the charge neutrality condition of  $[Fe_{Me}^{\bullet}] = 2[V_{Me}{'}]$  because this condition is the case where  $C_{H_2O}$  is extremely low.

Charge neutrality condition	$[V_{Me}{'}]$	$[H_{Me}{'}]$	$[V_O^{\bullet}]$	Si defect species	$[V_{Si}]$	$D_{Si}$
$[Fe_{Me}^{\bullet}] = 2[V_{Me}{'}]$	0	1/2	0	$V_{Si}^{''''}$	0	0
$[(OH)_O^{\bullet}] = 2[V_{Me}{'}]$	1/3	2/3	-1/3	$V_{Si}^{''''}$	2/3	1/3
				$(H)_{Si}^{''}$	1	2/3
				$(2H)_{Si}{'}$	4/3	1
				$(3H)_{Si}'$	5/3	4/3
				$(4H)_{Si}^{\times}$	2	5/3
$[Fe_{Me}^{\bullet}] = [H_{Me}{'}]$	-1/2	1/4	1/2	$V_{Si}^{''''}$	-1	-1/2
				$(H)_{Si}^{''}$	0	1/2
				$(2H)_{Si}{'}$	1/2	1
				$(3H)_{Si}'$	5/4	7/4
				$(4H)_{Si}^{\times}$	2	5/2
$[(OH)_O^{\bullet}] = [H_{Me}{'}]$	0	1/2	0	$V_{Si}^{''''}$	0	0
				$(H)_{Si}^{''}$	1/2	1/2
				$(2H)_{Si}{'}$	1	1
				$(3H)_{Si}'$	3/2	3/2
				$(4H)_{Si}^{\times}$	2	2

### 3.5.4 Comparing with deformation experiments

Diffusion and dislocation creeps in olivine under high temperatures are believed to be controlled by Si self-diffusion [Frost and Ashby, 1982; Weertman, 1999]. Therefore, the  $C_{H_2O}$  exponent for  $D_{Si}$  should be identical to that for creep rates. However, deformation studies [Hirth and Kohlstedt, 2003; Jung and Karato, 2001; Karato et al., 1986; Mei and Kohlstedt, 2000a; b] on olivine aggregates claimed a much larger  $C_{H_2O}$  exponent,  $1.2 \pm 0.4$  (Fig. 3.5). In this paper, we have concluded that the  $C_{H_2O}$  exponent value  $r = 1.2 \pm 0.4$  [Hirth and Kohlstedt, 2003], obtained from deformation experiments, is an overestimate.

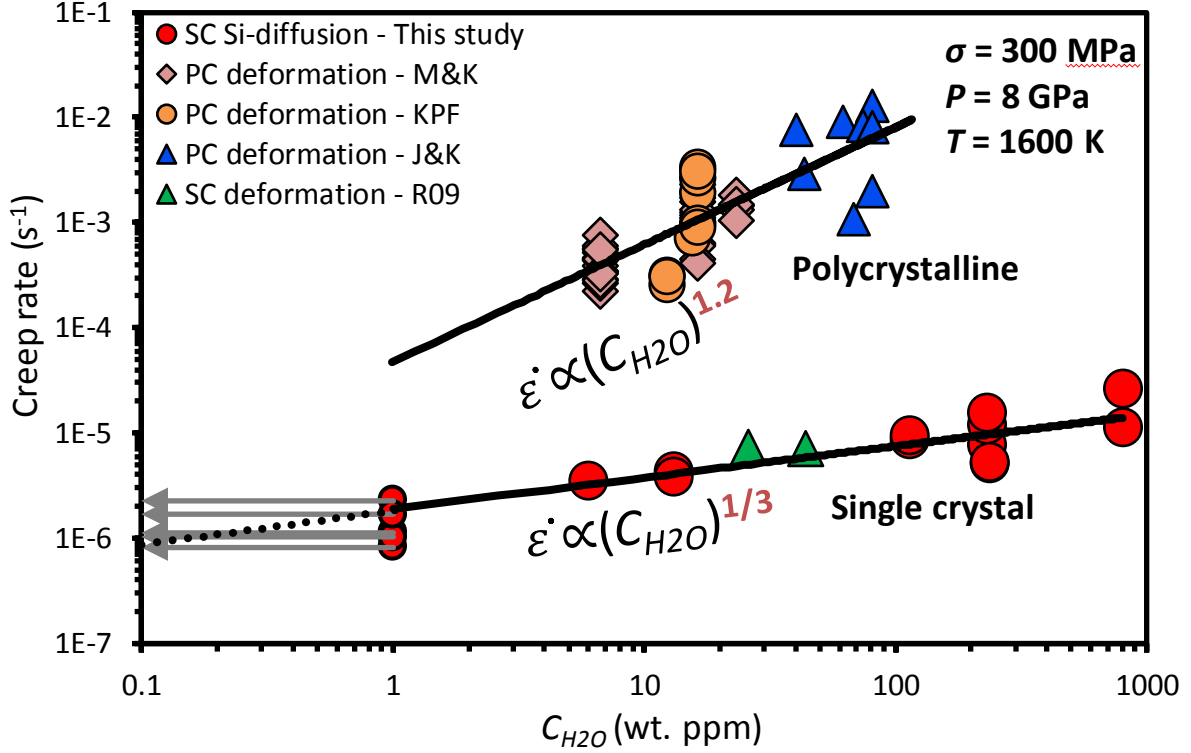


**Fig. 3.5.** Strain rate ( $\dot{\epsilon}$ ) versus  $C_{H_2O}$ .  $D_{Si}$  from this study is converted to strain rate using the proportional relationship of  $D_{Si}$  and  $\dot{\epsilon}$  [Weertman, 1999] with parameters from Kohlstedt [Kohlstedt, 2006]. All data are normalized to a pressure of 8 GPa, a temperature of 1600 K, and a stress of 300 MPa using an activation volume of  $1.7 \text{ cm}^3/\text{mol}$  [Fei et al., 2012], activation energy of 420 kJ/mol, and a stress exponent of 3.5. The data points for  $C_{H_2O} < 1 \text{ wt. ppm}$  are treated in the same way as in **Fig. 3.3**. SC: single crystal. PC: polycrystalline. M&K: Mei and Kohlstedt [2000b]. KPF: Karato et al. [1986]. J&K: Jung and Karato [2001]. R09: Raterron et al. [2009].

Here we discuss possible reasons for the overestimation of the effect of water on creep rates in deformation experiments. First, those deformation studies were performed on polycrystalline olivine samples with small grain size ( $< 70 \mu\text{m}$ ). We have plotted the dislocation creep data (with stress  $\sigma > 100 \text{ MPa}$ ) from Mei and Kohlstedt [2000a; b], corrected to a temperature of 1523 K and stress of 150 MPa using values of activation energy  $\Delta H = 470 \text{ kJ/mol}$  and stress exponent  $n = 3$  which were reported by Mei and Kohlstedt [2000a; b], as a function of grain size in **Fig. 3.6**. At dry conditions, no grain size dependence of dislocation creep is found [grain size exponent  $m \approx 0$  within experimental error (**Fig. 3.6a**)], in agreement with the accepted idea that dislocation creep rate is independent of grain size [Karato et al., 1986]. However, under wet conditions, with water fugacity  $f_{H_2O} = \sim 100 \text{ MPa}$ , we find a large grain size dependence of creep rate, with

an exponent of  $m = -1.8 \pm 0.4$  (**Fig. 3.6b**). With higher water fugacity ( $f_{H_2O} = \sim 300$  MPa), the effect of grain size on dislocation creep rates becomes even larger ( $m = -4.4 \pm 0.8$  in **Fig. 3.6c**). Also in Karato et al. [1986], although there is a large scatter in the relationship between strain rate and grain size, we could still find a negative dependence of strain rate on grain size for wet conditions, but strain rate is almost independent of grain size under dry conditions (**Fig. 3.6d**). These data contradict the notion that dislocation creep rate is independent of grain size. Therefore, their high strain rates under wet conditions should not be attributed to the effect of water on dislocation creep.

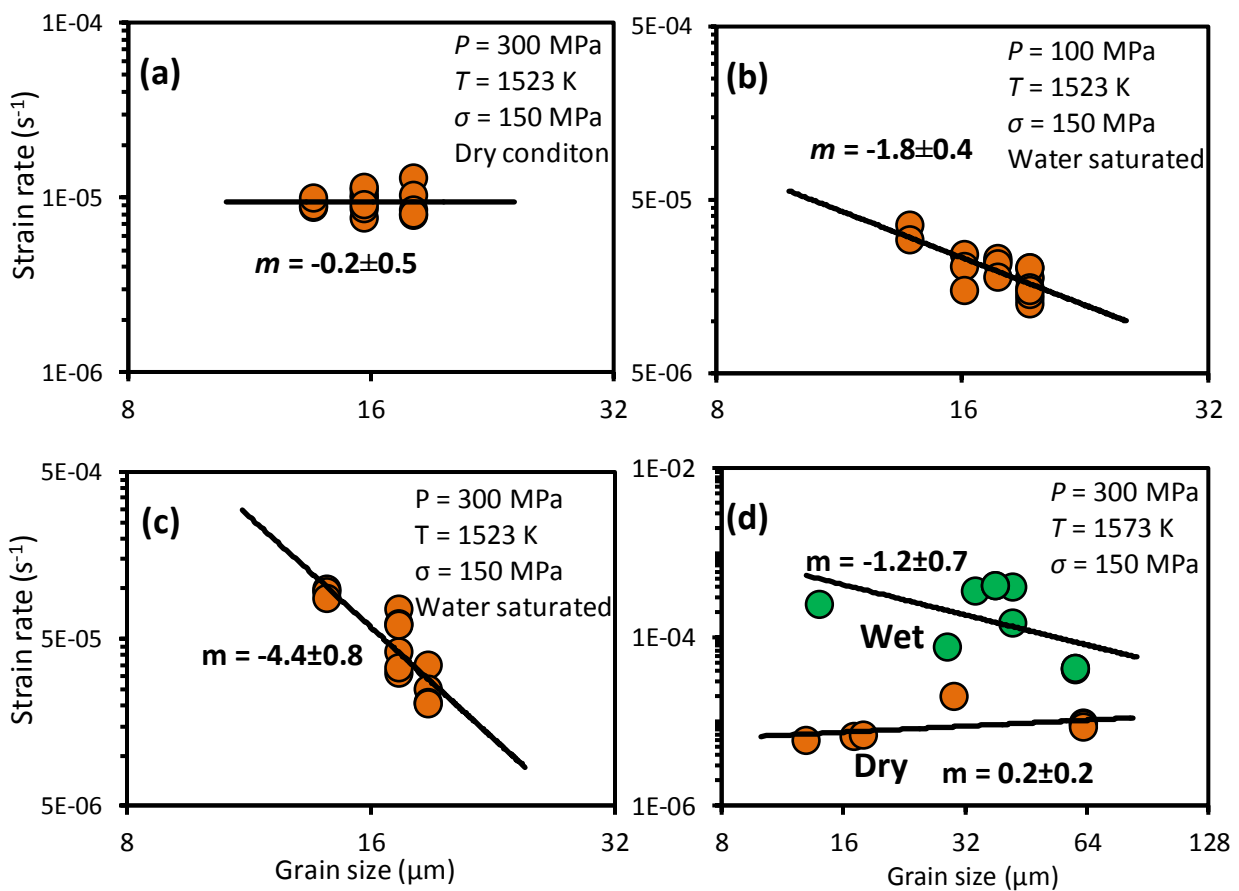


**Fig. 3.6.** Grain size dependence of nominal dislocation creep rates in previous deformation studies. **(a)** At pressure of 300 MPa and dry condition. **(b)** At pressure of 100 MPa and water saturated condition. **(c)** At pressure of 300 MPa and water saturated condition. **(d)** At both dry and wet conditions. Data points in **(a-c)** and **(d)** are from Mei and Kohlstedt [2000a; b] and Karato et al. [1986], respectively, normalized to 150 MPa using values of activation energies and

stress exponents they reported. Only dislocation creep data ( $\sigma > 100$  MPa) are plotted in the figure.

The large grain size exponent implies that the main deformation mechanism in these studies is grain boundary sliding. Their experimental setup should have caused oversaturation of water in the samples. Therefore, free fluid phases probably existed on the grain boundaries in these experiments. With higher  $f_{H_2O}$  and smaller grain sizes, grain boundary sliding is further enhanced by the larger amounts of fluid phases. As a result, the creep rate decreases with increasing grain size, and the grain size exponent  $m$  decreases with increasing  $f_{H_2O}$  under wet conditions in Mei and Kohlstedt [2000a; b] and Karato et al. [1986] (**Fig. 3.6**). The FT-IR spectra shown by Mei and Kohlstedt [2000a; b] and by Karato et al. [1986] for polycrystalline olivine also indicated that the majority of the water in their samples was not structural water but existed on grain boundaries (very wide bands, but no sharp peaks in the FT-IR spectra).

Second, because water solubility in olivine increases with increasing pressure [Kohlstedt et al., 1996], the ranges of  $C_{H_2O}$  used in the deformation experiments were very narrow owing to their low pressure conditions (**Table 3.4**). The data points collected by Mei and Kohlstedt [2000a; b] for the experimental condition of 300 MPa water fugacity are scattered by a factor of at least 4 (**Fig. 3.7a**). On the other hand, the difference in strain rates between dry and water saturated conditions was reported as a factor of 5-6. Karato et al. [1986] compared the strain rates at dry and water saturated conditions (~16 wt. ppm water), and found a strain rate contrast of 1 order of magnitude. However, the error bars for their strain rates under wet conditions were also about factor 10 (**Fig. 3.7b**). In Jung and Karato [2001], the water dependence of strain rates is essentially invisible because of the experimental errors (**Fig. 3.5**). Hence, the ranges of  $C_{H_2O}$  used in those deformation studies were not wide enough to obtain systematical changes in strain rates; this then led to large error in estimating the effect of water on strain rates.

Third, previous studies have exaggerated the effect of water on creep rates. For example, Mei and Kohlstedt [2000a; b] used data points (PI-258) which were higher than average for their linear fitting to compare with those at dry conditions (**Fig. 3.7a**), and thus overestimated the effect of water on strain rates. Although Hirth and Kohlstedt [2003] obtained a water content exponent of  $r = 1.2 \pm 0.4$  from their fitting, the largely scattered data points can also be fitted with a smaller  $C_{H_2O}$  exponent.

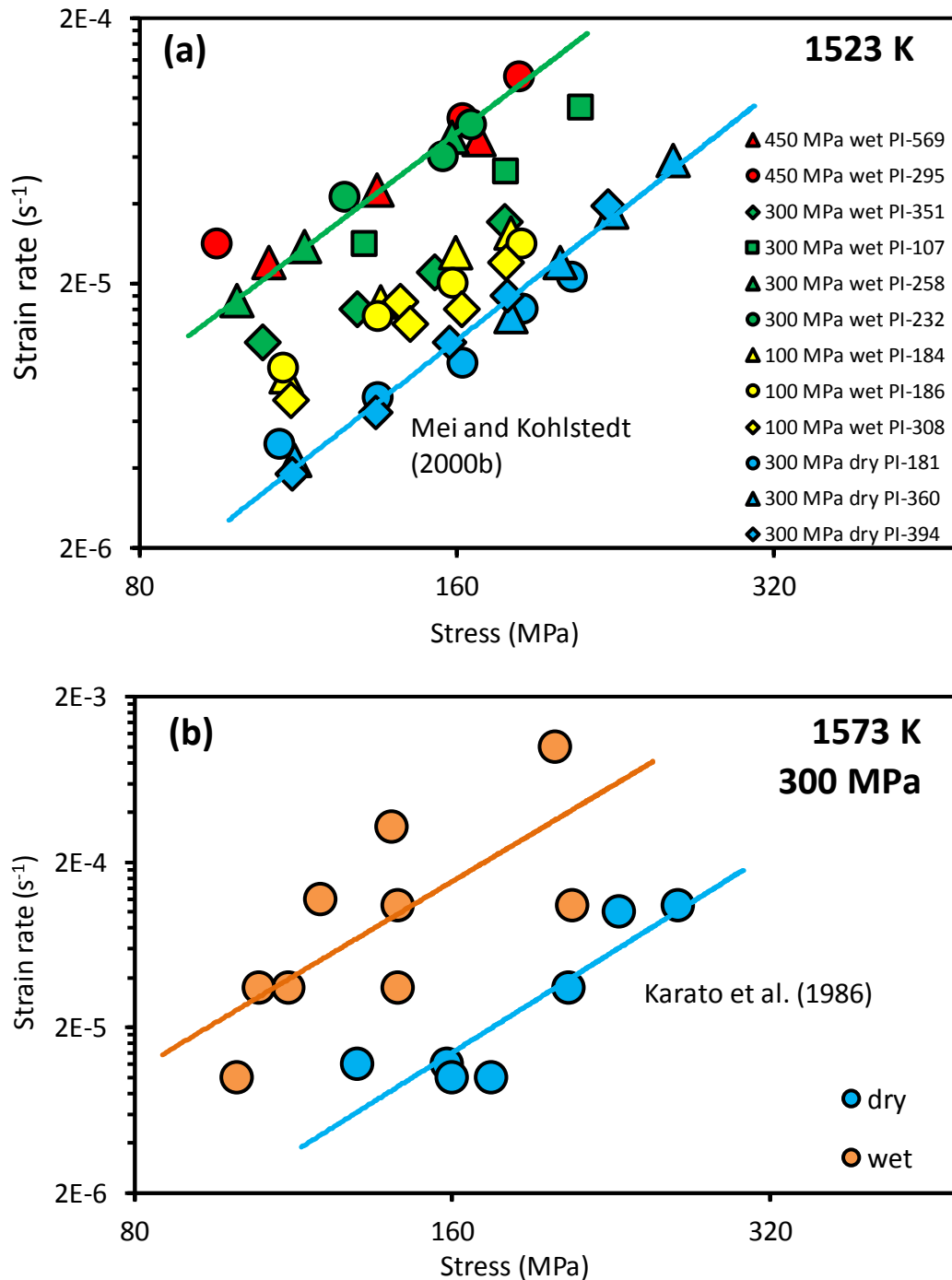


**Fig. 3.7.** Dislocation creep rate versus stress. (a) Data from Mei and Kohlstedt [2000a; b] at 1523 K. Data points with the same color indicate the same experimental conditions (pressure and water fugacity). Different types of symbols indicate independent experimental runs. The straight lines are linear fits of PI-258 and PI-360, which were used by Mei and Kohlstedt [2000a; b] to estimate the effect of water on creep rates. (b) Data from Karato et al. [1986] at 1573 K, 300 MPa for both dry and wet conditions.

**Table 3.4.** Summary of  $C_{H_2O}$  exponent ( $r$ ) values for rheological properties obtained in different studies (*Fo*: forsterite. *Ol*: iron-bearing olivine. SC: single crystal. PC: polycrystalline).

Method	Sample	$r$	$P$ (GPa)	$C_{H_2O}$ (wt. ppm)	Reference
Si diffusion	<i>Fo</i> SC	0.32±0.07	8	<1–810	This study
Si diffusion	<i>Ol</i> SC	0.2-1.0	2	~40 and ~370	[Costa and Chakraborty, 2008]
Deformation	<i>Ol</i> PC	0.7-1.0	0.1-0.45	“dry” and 7–25	[Mei and Kohlstedt, 2000a]
Deformation	<i>Ol</i> PC	0.69-1.25	0.1-0.45	“dry” and 7–25	[Mei and Kohlstedt, 2000b]
Deformation	<i>Ol</i> PC	—	0.3	“dry” and 16	[Karato <i>et al.</i> , 1986]
Deformation	<i>Ol</i> PC	—	0.5-2.2	6–80	[Jung and Karato, 2001]
Deformation	<i>Ol</i> PC	1.2±0.4	0.1-2.2	“dry” and 6-80	[Hirth and Kohlstedt, 2003]

In addition, the high water content exponent ( $r = 1.2 \pm 0.4$ ) was obtained by combining results from different studies that use different experimental techniques and apparatus, and should have their own different intrinsic errors. All these problems could cause large uncertainty in estimating the water dependence of creep rates.

Furthermore, Girard *et al.* [2013] investigated the hydrolytic weakening of olivine single crystal at high pressure with un-saturated water. They discussed the water content exponent based on assuming different activation volumes. If assuming an activation volume of 17.3 cm<sup>3</sup>/mol, the water content exponent should be ~1.2 based on their experimental results. With assuming lower activation volume, the water content exponent becomes small. If the volume is 12.1 cm<sup>3</sup>/mol, there is almost no water content dependence for creep rate. Since the activation volume for silicon diffusion and deformation is small (~1.7 cm<sup>3</sup>/mol for silicon diffusion, and <10 cm<sup>3</sup>/mol in most deformation studies [e.g., Karato *et al.*, 1993; Raterron *et al.*, 2007; Li *et al.*, 2006], and >10 cm<sup>3</sup>/mol in some studies [e.g., Karato and Ogawa, 1981; Karato and Jung, 2003; Borch and Green, 1989], discussed in detail in **Section 2.5.4**), Girard *et al.* [2013]’s results actually also show a small water content exponent for olivine deformation.

We note that Paterson’s calibration [Paterson, 1982] was used to calculate the  $C_{H_2O}$  in the deformation studies, while Bell’s calibration [Bell *et al.*, 2003] was used in this study. However, the difference in calibration methods only changes the absolute values of  $C_{H_2O}$ , and not the ratio of  $C_{H_2O}$  between different samples. Therefore, it does not affect the values of the  $C_{H_2O}$  exponent.

Based on the above discussion, we conclude that previous studies using deformation experiments on olivine aggregates have overestimated the effect of water on rheological properties. This idea is also supported by the much lower creep rates obtained in single crystals of hydrous olivine [Raterron *et al.*, 2009] than those in polycrystalline (**Fig. 3.5**). Free water is unlikely to be present in the upper mantle due to the water un-saturated conditions except for the mantle wedge or subducting slabs. In addition, the grain size is on the order of millimeter to centimeter in the upper mantle [Karato, 1984], meaning grain boundary sliding would be negligible in comparison with diffusion creep or dislocation creep as discussed in Hirth and Kohlstedt [2003]. Therefore, the creep rates of minerals in the real upper mantle cannot be enhanced by free water on grain boundaries at least in the depleted mantle with under-saturated water.

### 3.5.5 Implications to upper mantle rheology

Based on the small  $C_{H_2O}$  exponent ( $r = 1/3$ ) determined in this study, the difference in  $D_{Si}$ , as well as creep rates, between rheologically dry ( $<1$  wt. ppm) and maximum  $C_{H_2O}$  of olivine in upper mantle ( $< 1000$  wt. ppm [Dixon *et al.*, 2002; Hirschmann, 2006; Workman and Hart, 2005]) is within one order of magnitude. Because the variance of  $C_{H_2O}$  in the upper mantle is very small, i.e.  $\sim 10^2$ - $10^3$  wt. ppm [Dixon *et al.*, 2002; Hirschmann, 2006; Workman and Hart, 2005], such a small range only causes  $\sim 0.3$  orders of magnitude difference in creep rates. This is much smaller than other factors that affect rheological properties like temperature or shear stress. Hence, we conclude that the effect of water on upper mantle rheology is not significant, which completely contradicts the commonly accepted idea [Costa and Chakraborty, 2008; Hirth and Kohlstedt, 1996; Hirth and Kohlstedt, 2003; Karato and Jung, 1998]

Since water has only a small effect on upper mantle rheology, many geodynamical problems must be reconsidered. Two ideas, partial melting and hydration [Hirth and Kohlstedt, 1995a; b; 1996], have been commonly considered to explain plate motion because both could soften the oceanic asthenosphere. Previous overestimates of water effects on creep rates have erroneously supported the idea that hydration is the main reason [Hirth and Kohlstedt, 1996; Hirth and Kohlstedt, 2003; Karato and Jung, 1998]. Using the  $C_{H_2O}$  exponent of  $1/3$ , if 75 % of the original water is extracted during mantle dehydration ( $\sim 110$  wt. ppm of water before dehydration [Workman and Hart, 2005], and  $\sim 28$  wt. ppm after dehydration [Ito *et al.*, 1999]), the creep rates

are only changed by a factor of 1.6. On the other hand, the melt fraction in the asthenosphere is estimated to be 1.25-0.25 % or less [Hirschmann, 2010; Kawakatsu *et al.*, 2009]. Such a small melt fraction enhances the creep rates by at most a factor of three [Hirth and Kohlstedt, 1995a; b]. However, the high geothermal gradient in the oceanic mantle at < 200 km, and especially at < 100 km (~12 K/km) [Green and Ringwood, 1967], causes the creep rates to increase at least 6 orders of magnitude from 60 to 200-km depth. Thus, the effect of temperature gradient on creep rates appears to be much larger than that of  $C_{H_2O}$  or melt fraction. The softening of the oceanic asthenosphere that allows plate motion cannot occur by hydration or by partial melting.

The presence of a viscosity minimum zone has been expected in the asthenosphere based on the seismically observed low velocity and high attenuation zone [Anderson, 1966]. However, because the effects of pressure on  $D_{Si}$  is also small [Fei *et al.*, 2012], the viscosity in the upper mantle, which is calculated using the inverse relationship between  $D_{Si}$  and viscosity [McKenzie, 1967] based on oceanic geotherm [Green and Ringwood, 1967], decreases monotonically with increasing depth (Fig. 3.8) even if the geothermal gradient is very small (i.e., <1 K/km) at a depth > 200 km. Thus, the viscosity minimum zone does not appear in the asthenosphere based on  $D_{Si}$  by taking the effects of pressure, temperature, and water content into account.

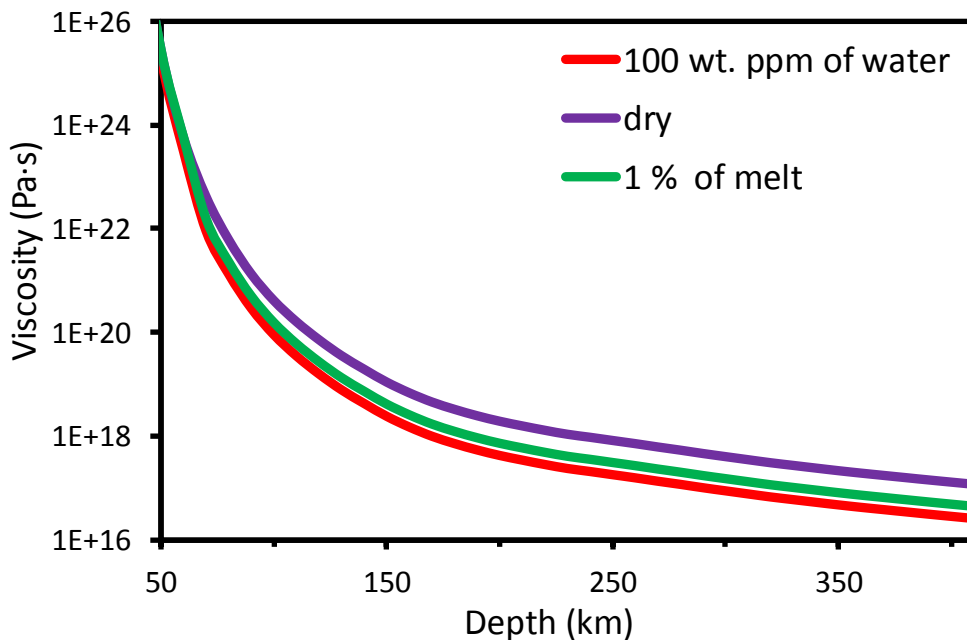


**Fig. 3.8.** Viscosity ( $\eta$ ) in upper mantle.  $\eta$  is calculated from  $D_{Si}$  using the inverse relationship of  $\eta$  and  $D_{Si}$  [McKenzie, 1967] as:  $\eta=10kTr_c^2/(D_{Si}m_a)$ , where  $k$  is the Boltzmann constant,  $T$  is the

absolute temperature based on the oceanic geotherm [Green and Ringwood, 1967],  $r_c$  is the crystal radius, and  $m_a$  is the mass of a Si ion. The grain size in the mantle is assumed to be ~1 mm.  $D_{Si}$  is a function of temperature,  $C_{H_2O}$ , and pressure, as given by **Eqs. 3.3** with  $\Delta H = \Delta E + P\Delta V$ , for which activation energy ( $\Delta E$ ) and activation volume ( $\Delta V$ ) values of 420 kJ/mol and 1.7 cm<sup>3</sup>/mol were used [Fei *et al.*, 2012], respectively. The influence of partial melting on viscosity is calculated from the melt fraction dependence of creep rates [Mei *et al.*, 2002].

An open question in mantle dynamics is why hotspots are so immobile against plate motion. If the large effect of water on mantle rheology was accepted, the high  $C_{H_2O}$  in the source regions of hotspots in comparison to that in surrounding regions would be a possible explanation. However, our results demonstrate this idea is not valid. Taking the Hawaii hot spot as an example, the  $C_{H_2O}$  in its source is ~750 wt. ppm, and ~110 wt. ppm in its surrounding regions [Dixon *et al.*, 2002]. Our results indicate that this difference would cause a viscosity contrast by a factor of two, which is rather small in comparison with that caused by temperature difference (~200 K hotter than surrounding mantle [Putirka, 2005], resulting in a viscosity decrease by more than one order of magnitude). Hence, the  $C_{H_2O}$  contrast cannot be the major reason for the immobility of hotspots.

### 3.6 Acknowledgments

We are very grateful to S. Chakraborty and R. Dohmen at Ruhr-University of Bochum for thin film deposition, and also discussions about experimental methods. We also appreciate A. Yoneda at Okayama University providing the single crystal, H. Keppler for FT-IR measurement, A. Audéat for ICP-MS analysis, and T. Boffa-Ballaran for X-ray diffraction analysis. We acknowledge support from the ENB (Elite Network Bavaria) programs.

# Chapter 4

---

## Oxygen self-diffusion in forsterite

### 4.1 Abstract

In order to examine the effects of water on creep reported by rock deformation experiments, we systematically measured oxygen self-diffusion coefficients ( $D_O$ ) in forsterite at a pressure of 8 GPa and temperatures of 1600 – 1800 K, over a wide range of  $C_{H_2O}$  from <1 up to ~800 wt. ppm. Experimental results suggest that  $D_O \propto (C_{H_2O})^{0.06 \pm 0.1} \approx (C_{H_2O})^0$ . From our data we conclude that water has almost no effect on  $D_O$ . Together with the small effect of water on silicon self-diffusion coefficients [Fei *et al.*, 2013], we conclude that the role of water on upper mantle rheology is insignificant.

### 4.2 Introduction

Water is thought to play an essential role in the dynamical processes in the Earth's interior. A number of studies has reported water's significant influence on the physical properties of mantle minerals (e.g., electrical conductivity [Karato, 1990; Yoshino *et al.*, 2009], elastic moduli [Jacobsen *et al.*, 2008], creep rates [Karato *et al.*, 1986; Mei and Kohlstedt, 2000a; b], and deformation fabric [Jung and Karato, 2001]). In the case of rheological properties, it was believed that even several tens of wt. ppm water could enhance the creep rates in olivine by orders of magnitude [Karato *et al.*, 1986; Mei and Kohlstedt, 2000a; b]. However, because of the technical difficulty in rock deformation experiments, the effect of water on the rheological properties may have been misunderstood [Fei *et al.*, 2013]. Therefore, it is necessary to examine the results from deformation experiments independently. Since the high temperature creep in minerals is controlled by self-diffusion of the slowest species [Frost and Ashby, 1982; Weertman, 1999], which is silicon in the case of olivine [Costa and Chakraborty, 2008; Houlier *et al.*, 1990], measurement of silicon self-diffusion coefficients ( $D_{Si}$ ) can be used to estimate the effect of water on creep rates in olivine [Fei *et al.*, 2013]. In contrast to earlier rock deformation experiments, Fei *et al.* [2013] demonstrated that the effect of water on  $D_{Si}$  is very small.  $D_{Si}$  was found to increase with increasing water content ( $C_{H_2O}$ ) with an exponent of only 1/3, although

previous results from deformation experiments [Jung and Karato, 2001; Karato et al., 1986; Mei and Kohlstedt, 2000a; b] suggested a  $C_{H_2O}$  exponent of 1.2 [Hirth and Kohlstedt, 2003].

Oxygen is the second slowest diffusion species in olivine and has similar diffusion rate with that of silicon. Its self-diffusion coefficient is only about one order of magnitude higher than that of silicon [Costa and Chakraborty, 2008; Fei et al., 2012; Gérard and Jaoul, 1989; Jaoul et al., 1980; Ryerson et al., 1989]. Therefore, it is expected that oxygen diffusion also plays an essential role in the creep of olivine.

Costa and Chakraborty [2008] measured oxygen self-diffusion coefficients ( $D_O$ ) in natural olivine at 2 GPa, 1473-1623 K, with  $C_{H_2O}$  of 30-50 wt. ppm. By comparing their results with those determined at ambient pressure under dry conditions [Dohmen et al., 2002], they concluded that even ~45 wt. ppm of water could enhanced  $D_O$  by one order of magnitude. However, as pointed out by Fei et al. [2012], comparison of experimental results obtained at ambient pressure and at high pressures could lead to misinterpretations because different experimental setups have different error sources. Actually, although Costa and Chakraborty [2008] claimed a very large  $C_{H_2O}$  dependence of  $D_{Si}$  by comparing the data sets obtained at high-pressure and at ambient pressure, their high-pressure data shows a similarly small  $C_{H_2O}$  dependence of  $D_{Si}$  as that of Fei et al. [2013]. For these reasons, in order to clarify the effects of water on  $D_O$  in olivine, experiments should be conducted with the same setup over a wide range of  $C_{H_2O}$  under constant pressure and temperature conditions.

In this study we systematically measured  $D_O$  in an iron-free synthetic forsterite single crystal at 8 GPa, 1600 - 1800 K, over a wide range of  $C_{H_2O}$  from <1 up to ~800 wt. ppm. Our results showed that water has no effect on  $D_O$  under upper mantle conditions.

#### **4.3 Experimental and analytical methods**

The experimental approach used in this study is essentially the same as those in our previous studies [2013]. Therefore, the experimental procedure in this study is briefly described here.

Previous silicon and oxygen self-diffusion studies [Bégin et al., 1997; Bégin et al., 1999; Costa and Chakraborty, 2008; Fei et al., 2012; Gérard and Jaoul, 1989; Jaoul et al., 1980; Ryerson et al., 1989] suggested that the effect of iron on  $D_{Si}$  and  $D_O$  is insignificant. Therefore, a

synthetic iron-free forsterite ( $\text{Mg}_2\text{SiO}_4$ ) single crystal, with the only major impurity of ~80 wt. ppm of Ir [Fei *et al.*, 2012], was used as a starting material. Disks with (010) faces were cored from the single crystal.

Water was doped into the forsterite disks at a pressure of 8 GPa and a temperature of 1600 K using a mixture of talc+brucite (4:1 weight ratio) as a water source with graphite/gold + enstatite buffer in a multi-anvil apparatus. Variation of water contents in the samples were made by varying the ratio of the water source to the graphite/gold + enstatite. For dry condition experiments, the samples were annealed under these pressure and temperature conditions but without the water source.

The faces of the water doped forsterite disks were polished using 0.25  $\mu\text{m}$  diamond powder, followed by an alkaline colloidal silica solution. The polished surface was then coated with ~500-nm thick layer of  $^{18}\text{O}$  enriched  $\text{Mg}_2\text{SiO}_4$  and 100-nm of  $\text{ZrO}_2$  using a Pulsed laser deposition (PLD) system at Ruhr-University Bochum [Dohmen *et al.*, 2002]. The coating of  $\text{ZrO}_2$  was made to follow the technique of Costa and Chakraborty [2008]. We also conducted some diffusion experiments without the  $\text{ZrO}_2$  film for comparison, which showed that the  $\text{ZrO}_2$  does not affect  $D_{\text{O}}$ . The coated disks were annealed at 8 GPa, 1600 and 1800 K for diffusion with the same surrounding material and experimental set up as those for water-doping experiments. The annealing conditions are listed in **Table 4.1**.  $C_{\text{H}_2\text{O}}$  for each sample both before and after diffusion annealing was determined by Fourier transform infrared (FT-IR) spectroscopy using Bell's [2003] calibration described in detail in Fei *et al.* [2013].

The isotopic profiles of the annealed samples were obtained from the Cameca IMS-6f SIMS at the Helmholtz Centre Potsdam using a  $\text{Cs}^+$  primary beam. The counting times for  $^{16}\text{O}$  and  $^{18}\text{O}$  mass stations were 2 and 4 s, respectively. The depth of each SIMS crater was subsequently measured using a 3D-nanofocus microscope [Fei *et al.*, 2012; Fei *et al.*, 2013]. An example of an isotope profile is shown in **Fig. 4.1**.

The  $D_{\text{O}}$  was obtained by fitting the data to the solution of Fick's second law:

$$c = \frac{c_0 - c_1}{2} \operatorname{erf}\left(\frac{x - h}{\sqrt{4D_{\text{O}}t + L^2(\sigma)}}\right) + \frac{c_0 + c_1}{2} \quad (4.1)$$

where  $c$  is the observed abundance of  $^{18}\text{O}$ ,  $c_I$  is the initial abundance of  $^{18}\text{O}$  in the  $^{18}\text{O}$  enriched film,  $c_0$  is the initial abundance of  $^{18}\text{O}$  in the substrate,  $x$  is the distance from the surface,  $h$  is the boundary position of the thin film and the substrate,  $t$  is the annealing time,  $\text{erf}(z)$  is the error function, and  $L(\sigma)$  is the nominal diffusion lengths obtained as a function of surface roughness ( $\sigma$ ) by several zero-time runs (**Fig. 4.2**) [Fei *et al.*, 2012; Fei *et al.*, 2013].

**Table 4.1.** Summary of experimental conditions ( $T$ : temperature,  $t$ : annealing duration,  $C_{\text{H}_2\text{O}}^{*1}$ : water content before diffusion,  $C_{\text{H}_2\text{O}}^{*2}$ : water content after diffusion), and results of oxygen self-diffusion coefficients ( $D_O$ ).

Run No.	$T$ (K)	$T$ (h)	$C_{\text{H}_2\text{O}}^{(a)}$ (wt. ppm)	$C_{\text{H}_2\text{O}}^{(b)}$ (wt. ppm)	$D_O$ (m <sup>2</sup> /s)	Buffer
S5045a	1600	21	<1	<1	$5.7 \times 10^{-19}$	graphite+enstatite
S5045b	1600	21	<1	<1	$6.8 \times 10^{-19}$	graphite+enstatite
V716a	1600	52	<1	<1	$5.7 \times 10^{-19}$	graphite+enstatite
V716b	1600	52	<1	<1	$1.1 \times 10^{-18}$	graphite+enstatite
H3390a	1600	41	242	237	$4.8 \times 10^{-19}$	graphite+enstatite
H3390b	1600	41	242	237	$7.1 \times 10^{-19}$	graphite+enstatite
H3389a	1600	9	248	230	$1.4 \times 10^{-18}$	graphite+enstatite
H3389b	1600	9	248	230	$2.1 \times 10^{-18}$	graphite+enstatite
H3389c	1600	9	248	230	$2.0 \times 10^{-18}$	graphite+enstatite
H3394a	1600	20	248	135	$5.2 \times 10^{-19}$	graphite+enstatite
H3394b	1600	20	248	135	$5.7 \times 10^{-19}$	graphite+enstatite
V724a	1600	18	183	114	$5.8 \times 10^{-19}$	graphite+enstatite
V724b	1600	18	183	114	$7.5 \times 10^{-19}$	graphite+enstatite
V723	1600	23	40	47	$6.9 \times 10^{-19}$	graphite+enstatite
V720a	1600	27	13	12	$8.1 \times 10^{-19}$	graphite+enstatite
V720b	1600	27	13	12	$1.0 \times 10^{-18}$	graphite+enstatite
H3507a	1600	7	805	810	$1.9 \times 10^{-18}$	enstatite
H3507b	1600	7	805	810	$2.0 \times 10^{-18}$	enstatite
3509a	1800	5	15	12	$9.8 \times 10^{-18}$	graphite+enstatite
3509b	1800	5	15	12	$2.1 \times 10^{-17}$	graphite+enstatite

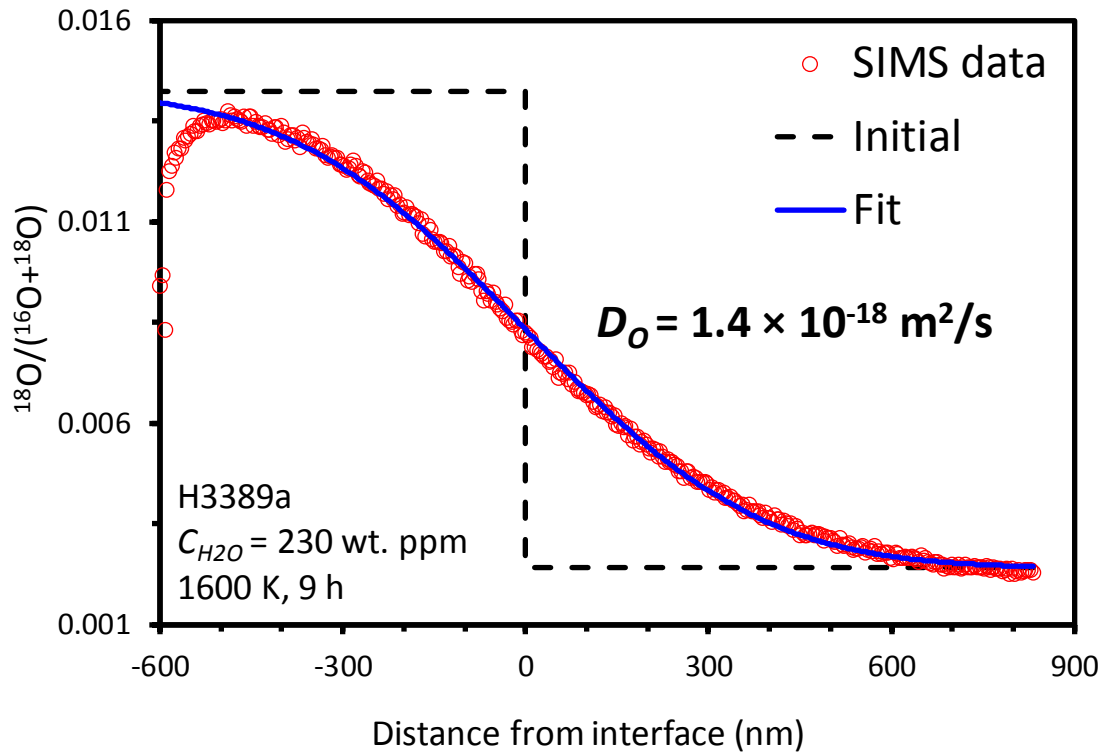


**Fig. 4.1.** An example of an apparent diffusion profile.

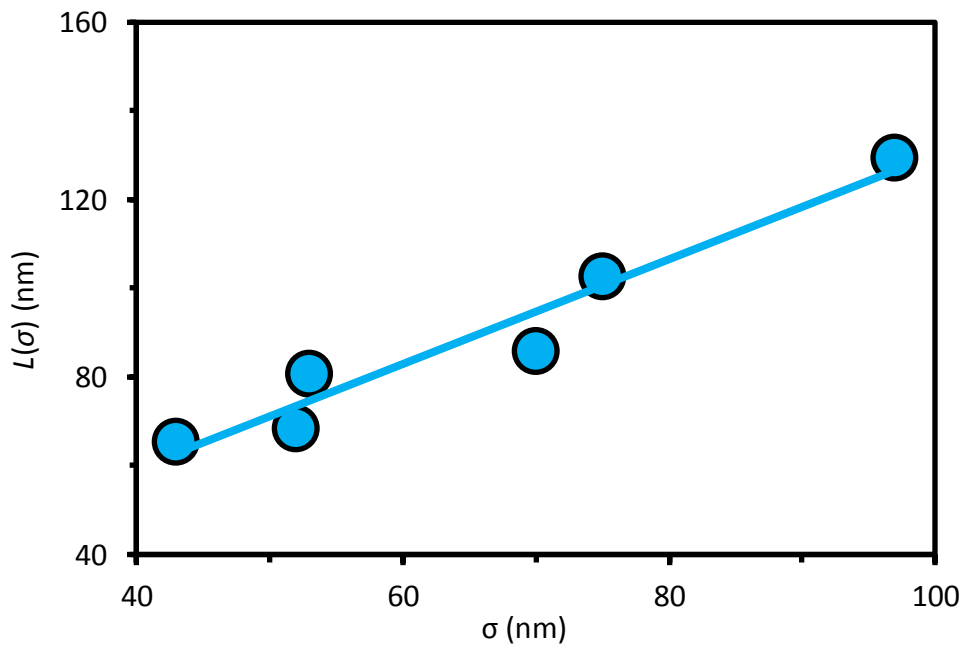


**Fig. 4.2.** Relationship between nominal diffusion length and surface standard deviation as used for the roughness calibration.

#### 4.4 Results

The measured results of  $D_O$  listed in **Table 4.1** are plotted against  $C_{H_2O}$  in **Fig. 4.3**. The  $D_O$  at 1600 K is essentially constant with increasing  $C_{H_2O}$  from <1 to ~800 wt. ppm. Although the redox environments were changed by using different surrounding material (graphite+enstatite or only enstatite), no differences were observed.

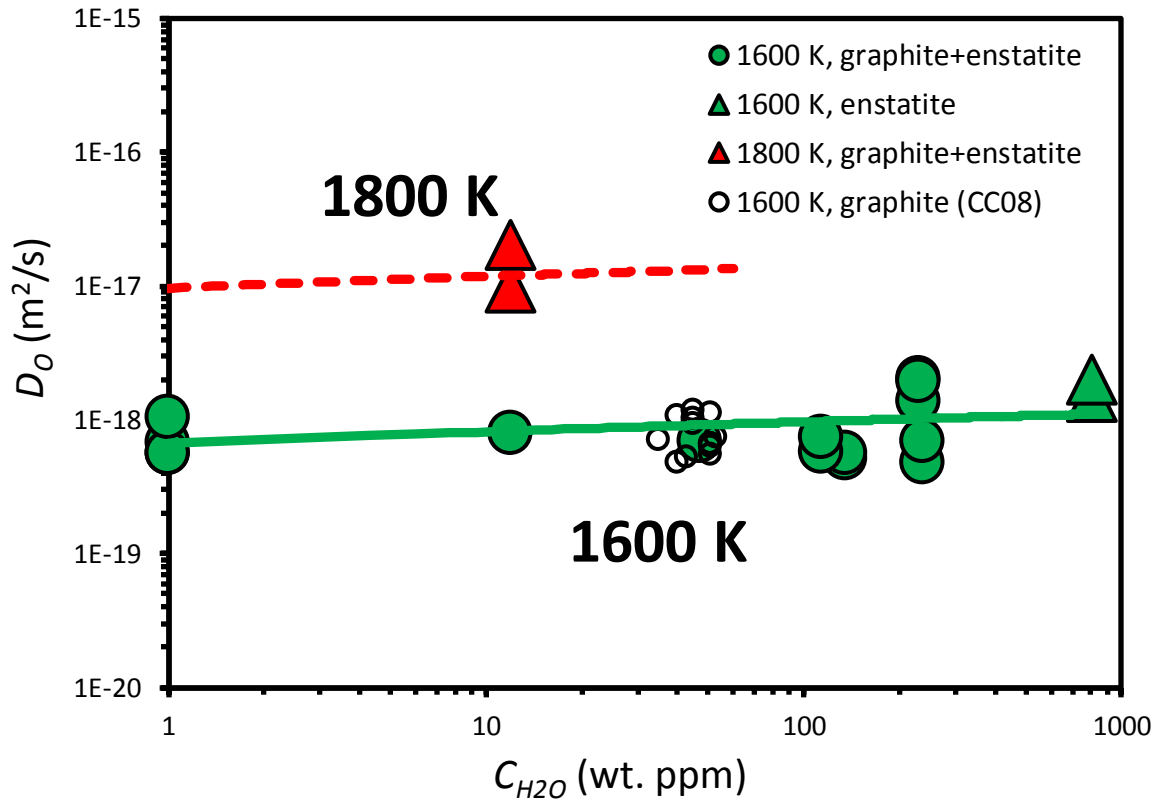


**Fig. 4.3.** Plot of  $D_O$  against  $C_{H_2O}$  at 8 GPa, 1600 and 1800 K, buffered with graphite or gold. The  $C_{H_2O}$  data at dry condition are below the detection limit of our FT-IR equipment, which is less than 1 wt. ppm. These values of  $D_O$  are plotted at  $C_{H_2O} = 1$  wt. ppm with smaller symbols. CC08: data points from *Costa and Chakraborty*, [2008] corrected to 1600 K.

The present results of  $D_O$  are fitted to the Arrhenius equations:

$$D_O = A_0 C_{H_2O}^r \exp\left(-\frac{\Delta H}{RT}\right) \quad (4.2)$$

where  $A_0$  is the pre-exponential factor,  $r$  is the water content exponent,  $R$  is the ideal gas

constant,  $T$  is the absolute temperature, and  $\Delta H$  is the activation enthalpy.  $A_0$ ,  $r$ , and  $\Delta H$  are found to be  $10^{-6.7\pm 1.8}$  m<sup>2</sup>/s,  $0.06\pm 0.14$ , and  $352\pm 60$  kJ/mol, respectively. The  $C_{H_2O}$  exponent for  $D_O$  is thus zero, which means water has no significant effect on oxygen self-diffusion rate.

Diffusion coefficients should be independent of annealing duration [Jaoul *et al.*, 1980]. In order to examine the validity of our results, we performed annealing experiments under the same pressure and temperature conditions but with different durations, which yield the same  $D_O$  values as shown in **Fig.4.4**.

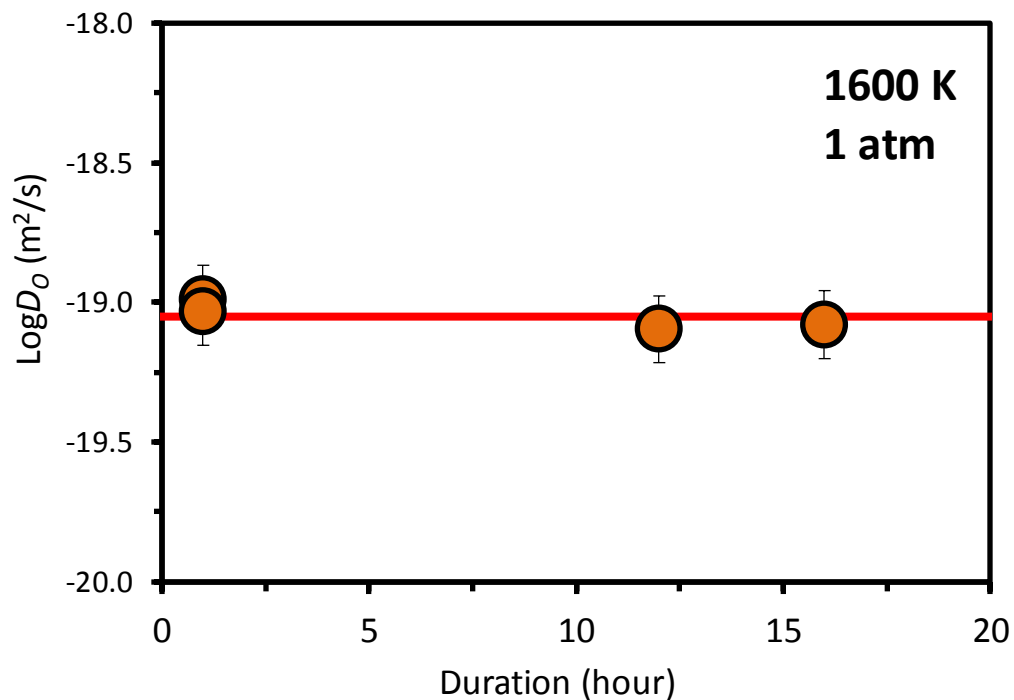


**Fig. 4.4.** Plot of  $D_O$  at 1 atm, 1600 K with different durations.

## 4.5 Discussion

### 4.5.1 Activation energy and activation volume

The activation energy for oxygen diffusion in this study is determined to be  $352\pm 60$  kJ/mol at 8 GPa. This value is lower than that for silicon diffusion ( $\sim 410$ - $430$  kJ/mol, [Fei *et al.*, 2012; Fei *et al.*, 2013]). By comparing to the activation energy determined at ambient pressure ( $\sim 302$ - $322$  kJ/mol [Andersson *et al.*, 1989; Jaoul *et al.*, 1980] shown in **Table 4.2**), the activation volume is between  $3.8$  -  $6.3$  cm<sup>3</sup>/mol calculated using the equation:  $\Delta H = \Delta E + P\Delta V$ , where  $\Delta H$

is the activation enthalpy at pressure  $P$ ,  $\Delta E$  is the activation energy, and  $\Delta V$  is the activation volume. The  $\Delta V$  for oxygen diffusion is higher than that for silicon self-diffusion ( $1.7 \pm 0.4$  cm<sup>3</sup>/mol [Fei et al., 2012]), and identical with that for Fe-Mg diffusion (4-7 cm<sup>3</sup>/mol, [Hier-Majumder et al., 2005]).

**Table 4.2.** Activation energy for oxygen diffusion determined in forsterite and natural olivine ( $T$ : temperature,  $P$ : pressure,  $\Delta E$ : activation energy).

Sample	H <sub>2</sub> O	$T$ (K)	$P$ (GPa)	$\Delta E$ (kJ/mol)	Reference
Forsterite	Wet	1600-1800	8	352±60 <sup>*a</sup>	This study
Forsterite	Dry	1423-1873	10 <sup>-4</sup>	322±42	[Jaoul et al., 1980]
Forsterite	Dry	1523-1793	10 <sup>-4</sup>	302±13	[Andersson et al., 1989]
Olivine	Wet	1473-1623	2	437±17 <sup>*b</sup>	[Costa and Chakraborty, 2008]
Olivine	Dry	1473-1673	10 <sup>-4</sup>	266±11	[Ryerson et al., 1989]
Olivine	Dry	1363-1773	10 <sup>-4</sup>	318±17	[Gérard and Jaoul, 1989]
Olivine	Dry	1373-1773	10 <sup>-4</sup>	338±14	[Dohmen et al., 2002]

\*a:  $\Delta E$  is ~296-320 kJ/mol if corrected to ambient pressure using the  $\Delta V = 4-7$  cm<sup>3</sup>/mol from Fe-Mg diffusion [Farber et al., 2000; Holzapfel et al., 2007].

\*b:  $\Delta E$  is reported as 324 kJ/mol after pressure correction using  $\Delta V = 7$  cm<sup>3</sup>/mol from Fe-Mg diffusion [Holzapfel et al., 2007] and  $f_{O_2}$  correction using an assumed exponent of 1/4 intermediate between the 1/3 and 1/5 exponents determined by Gérard and Jaoul [1989] and Ryerson et al. [1989], respectively.

In Fei et al. [2012], we suppose that the horizontal migration of thin films occurred in previous ambient pressure silicon diffusion experiments, which could also occur in oxygen diffusion studies. However, the activation energy determined in this study agrees well with previous oxygen diffusion studies. This is reasonable because when horizontal migration occurs, there should be a nano size vacant layer between the thin film and substrate which could be an obstacle for silicon diffusion, but not for oxygen since oxygen ions in forsterite (both in the thin film and in substrate) could exchange with that in the vacant layer which is filled with air. As a result, even if the horizontal migration occurred in previous oxygen diffusion studies at ambient

pressure, the measured oxygen diffusion coefficient is not influenced and therefore the activation energy determined in this study agrees well with that determined in previous studies.

Costa and Chakraborty [2008] reported an activation energy of  $\sim 437$  kJ/mol at 2 GPa in hydrous olivine. Additionally, they also pointed out that it is 324 kJ/mol after  $f_{O_2}$  and pressure normalization (using  $\Delta V = 7$  cm<sup>3</sup>/mol from Fe-Mg diffusion [Holzapfel *et al.*, 2007] and a  $f_{O_2}$  exponent of 1/4 [Gérard and Jaoul, 1989; Ryerson *et al.*, 1989]), which overlaps with that in dry olivine [Dohmen *et al.*, 2002; Gérard and Jaoul, 1989; Ryerson *et al.*, 1989]. Therefore, the activation energy for oxygen diffusion in forsterite and natural olivine is  $\sim 300$ -340 kJ/mol under both dry and wet conditions (**Table 4.2**). Water does not largely affect the activation energy, which agrees with computer simulations by Walker *et al.* [2003], who proposed the same mechanism for oxygen diffusion in dry and water-bearing forsterite.

#### 4.5.2 Defect chemistry

The zero- $C_{H_2O}$  dependence for  $D_O$  can be understood on the basis of defect chemistry. We use the Kröger-Vink [1956] notation (see **Appendix I**), e.g.  $V_{Si}''''$  indicates four effective negative charges for a vacancy in the silicon site, whereas  $(OH)_O^\bullet$  indicates an H<sup>+</sup>-associated O in the O site with an effective charge of +1. Square brackets [-] denote concentration of the corresponding units. The self-diffusion coefficient of an ion,  $D_{ion}$ , is proportional to the vacancy concentration of that ion,  $[V_{ion}]$  [Kohlstedt, 2006]. Hence,  $D_O \propto [V_O^{\bullet\bullet}]$ . In a hydrous olivine crystal, water exists as hydroxyl,  $(OH)_O^\bullet$  [Kohlstedt *et al.*, 1996]. Thus, there are two possibilities for the oxygen ions hopping in hydrous olivine: (a) hopping of O in O site, and (b) hopping of O in  $(OH)_O^\bullet$ . Because H<sup>+</sup>-associated O has a lower Coulomb force due to the excess charge by H<sup>+</sup>, the hopping probability of O in  $(OH)_O^\bullet$  should be higher than that of  $O_O^\times$ . Thus, the O diffusion should be dominated by O from  $(OH)_O^\bullet$ . Besides, if an O in  $(OH)_O^\bullet$  jumps, the H<sup>+</sup> cannot remain in an O vacancy because the  $V_O^{\bullet\bullet}$  already has two excess positive charges, and also the mobility of H<sup>+</sup> is much higher than that of  $O^{2-}$  [Costa and Chakraborty, 2008; Demouchy and Mackwell, 2003]. Therefore, oxygen diffusion is probably dominated by hopping of OH<sup>-</sup> in  $(OH)_O^\bullet$ .

There are mainly three types of  $(OH)_O^\bullet$  in hydrous olivine: (a)  $(OH)_O^\bullet$  associated with metal vacancies, i.e.,  $\{(OH)_O^\bullet - V_{Mg}''\}'$  and  $\{2(OH)_O^\bullet - V_{Mg}''\}^\times$ ; (b)  $(OH)_O^\bullet$  associated with Si vacancies, i.e.,  $\{(OH)_O^\bullet - V_{Si}''''\}''''$ ,  $\{2(OH)_O^\bullet - V_{Si}''''\}''''$ ,  $\{3(OH)_O^\bullet - V_{Si}''''\}'$ , and  $\{4(OH)_O^\bullet - V_{Si}''''\}^\times$ ; (c)

(OH)<sub>o</sub>• without associating with any cation vacancies [Brodholt and Refson, 2000]. The third type should have much higher mobility because the association of (OH)<sub>o</sub>• with V<sub>Si</sub>'''' or V<sub>Mg</sub>'' should cause lower mobility of (OH)<sub>o</sub>• due to the additional Coulomb force between (OH)<sub>o</sub>• and V<sub>Si</sub>'''' or V<sub>Mg</sub>''. Therefore, oxygen diffusion should be dominated by un-associated (OH)<sub>o</sub>•, namely,  $D_o \propto [(OH)_o^\bullet]^{un-associated}$ . Thus, we have,

$$D_o \propto [V_o^{\bullet\bullet}] \times [(OH)_o^\bullet]^{un-associated} \quad (4.3)$$

In wet olivine, the concentration of V<sub>Mg</sub>'' is much higher than that of V<sub>Si</sub>'''' [Brodholt and Refson, 2000; Kohlstedt, 2006]. Thus, the charge neutrality for H<sup>+</sup> is mainly kept by V<sub>Mg</sub>'', namely, [(OH)<sub>o</sub>•] = 2[V<sub>Mg</sub>''] [Kohlstedt, 2006]. This charge neutrality condition leads to the relationships between [V<sub>o</sub>''], [(OH)<sub>o</sub>•], and water fugacity,  $f_{H_2O}$  as follows [Costa and Chakraborty, 2008; Kohlstedt, 2006; Mei and Kohlstedt, 2000a]:

$$[V_o^{\bullet\bullet}] \propto (f_{H_2O})^{-1/3} \quad (4.4)$$

$$[(OH)_o^\bullet]^{un-associated} \propto (f_{H_2O})^{1/3} \quad (4.5)$$

**Eqs. (4.3)-(4.5)** lead to,

$$D_o \propto [V_o^{\bullet\bullet}] \times [(OH)_o^\bullet]^{un-associated} \propto (f_{H_2O})^{-1/3} \times (f_{H_2O})^{1/3} = (f_{H_2O})^0 \quad (4.6)$$

It suggests that  $D_o$  is independent from  $C_{H_2O}$  ( $C_{H_2O} \propto f_{H_2O}$  [Kohlstedt, 2006; Zhao et al., 2004]), which agrees well with our experimental results,  $D_o \propto C_{H_2O}^{0.06 \pm 0.14}$ .

In the enstatite buffered samples, oxygen fugacity ( $f_{O_2}$ ) is relatively higher in comparison with graphite+enstatite buffered samples. However, both systems show almost the same value of  $D_o$ , which indicates that  $D_o$  in forsterite is independent with  $f_{O_2}$ . This observation is consistent with Jaoul et al. , who suggested  $f_{O_2}$  has no effect on  $D_o$  in dry forsterite at ambient pressure.

Natural olivine contains about 10 % of the Fe<sub>2</sub>SiO<sub>4</sub> component. The charge neutrality condition could be different if a significant proportion of ferric iron exists. However, the  $D_o$  in pure forsterite determined in this study is essentially the same as that obtained in iron-bearing

olivine determined by Costa and Chakraborty [2008] after correcting to the same temperature (Fig. 4.3). Therefore, presence of ferric iron in natural olivine is not essential for oxygen diffusion at least at the  $C_{H_2O}$  levels of several hundred wt. ppm, which is the case for the major part of upper mantle conditions [Dixon *et al.*, 2002; Hirschmann, 2006; Workman and Hart, 2005].

#### 4.5.3 Geophysical implications

We compared  $D_O$ ,  $D_{Si}$ , and  $D_{Me}$  (Mg-Fe diffusion) against  $C_{H_2O}$  shown in Fig. 4.5. Under dry conditions ( $C_{H_2O} < 1$  wt. ppm),  $D_{Mg-Fe} \gg D_O \gg D_{Si}$ , and therefore, the plastic deformation of dry olivine is controlled by Si diffusion. With  $C_{H_2O}$  at the level of several hundred wt. ppm, we have  $D_{Mg-Fe} \gg D_O \gg D_{Si}$ , oxygen diffusion plays an essential role on the rheological properties of olivine as well as Si. With increasing water content, the difference between  $D_{Si}$  and  $D_O$  becomes smaller. If  $C_{H_2O}$  is extremely high,  $D_O$  could be almost the same or even higher than  $D_{Si}$ . Therefore, it is possible that oxygen diffusion dominates the rheological properties of olivine.

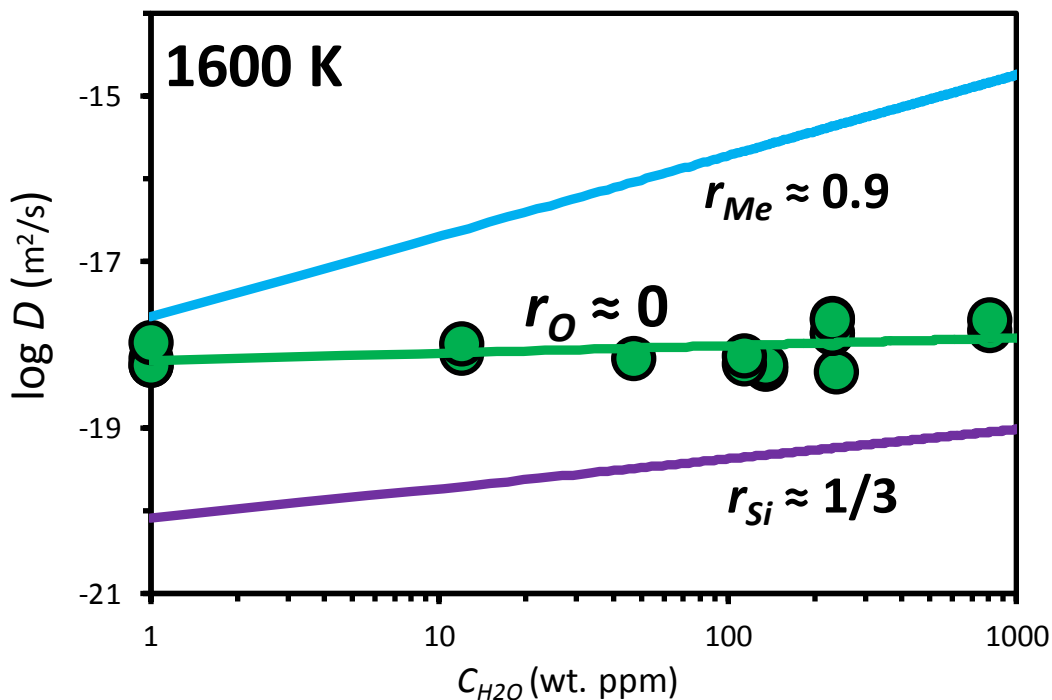


**Fig. 4.5.** Water content dependence for  $D_O$  (this study),  $D_{Si}$  [Fei *et al.*, 2013], and  $D_{Me}$  [Hier-Majumder *et al.*, 2005]. The  $D_{Me}$  data are calibrated to 8 GPa, 1600 K using an activation energy

of 220 kJ/mol [Hier-Majumder *et al.*, 2005], activation volume of 7 cm<sup>3</sup>/mol [Holzapfel *et al.*, 2007], and  $f_{H_2O}$  converted to  $C_{H_2O}$  using the calibration given by Zhao *et al.* [Zhao *et al.*, 2004].

Fei *et al.* [2013] demonstrated the relationship of  $D_{Si} \propto C_{H_2O}^{1/3}$  at water contents up to ~800 wt. ppm, which is the case for most parts of upper mantle, e.g.,  $C_{H_2O} = \sim 70\text{-}160$  wt. ppm in the depleted mantle, and it is four to five times higher in enriched mantle [Dixon *et al.*, 2002; Hirschmann, 2006; Workman and Hart, 2005]. They concluded a very small effect of water on olivine rheology under upper mantle conditions based on  $D_{Si}$ . In this study, we obtained  $D_O \propto C_{H_2O}^0$ . Therefore, the effect of water on upper mantle rheology could be even smaller than that suggested by Fei *et al.* [2013]. If water content is higher, for example in the mantle wedge, the  $C_{H_2O}$  dependence of  $D_{Si}$  could become greater than an exponent of 1/3 due to incorporation of more H<sup>+</sup> in  $V_{Si}''''$  [Fei *et al.*, 2013]. However, the difference between  $D_{Si}$  and  $D_O$  becomes smaller with increasing  $C_{H_2O}$  (**Fig. 4.5**), such that the role of oxygen diffusion on mantle rheology becomes more significant at high  $C_{H_2O}$ . Therefore, even though  $D_{Si}$  largely increases with  $C_{H_2O}$ , the creep rate should be limited by oxygen diffusion under high  $C_{H_2O}$  conditions. In conclusion, the role of water in upper mantle rheology is much smaller than previously considered. Water is not a significant factor that affects mantle dynamics.

## 4.6 Acknowledgments

We are very grateful to S. Chakraborty and R. Dohmen at Ruhr-University of Bochum for their help in sample coating, and A. Yoneda at Okayama University for giving us the high quality single crystal. We also appreciate the help of H. Keppler for FT-IR measurements, A. Audéat for ICP-MS analysis, F. Heidelbach for SEM analysis, and T. Boffa-Ballaran for single crystal X-ray diffraction analysis. We thank all the technicians at BGI. We acknowledge support from the ENB (Elite Network Bavaria) programs.

# Chapter 5

---

## Silicon grain boundary diffusion in forsterite

### 5.1 Abstract

Dislocation creep causes non-Newtonian viscosity and seismic anisotropy whereas diffusion creep doesn't. Determination of deformation mechanism in Earth's interior is thus essential to understand mantle dynamics. We have measured silicon grain-boundary diffusion coefficient in forsterite as a function of pressure, temperature, and water content. The diffusion and dislocation creep rates calculated from silicon grain-boundary and lattice diffusion coefficients suggest a dominant diffusion creep in cold mantles and mantle wedges. In the asthenosphere, dislocation creep always dominates because of the high temperature. In the lithosphere, diffusion creep dominates in shallow regions and dislocation creep dominates in deeper regions. In mantle wedges, olivine does not form lattice-preferred orientation: their strong anisotropy is caused not by olivine but by serpentine. Dominance of diffusion creep in cold continental lithosphere accounts for the mid-lithospheric seismic discontinuity and the Newtonian rheology suggested by postglacial rebound.

### 5.2 Introduction

Plastic deformation of rocks and minerals in the Earth's interior is controlled by diffusion creep and dislocation creep. An open question in geodynamics is which type of creep is dominant in various parts of Earth's upper mantle. If dislocation creep dominates, the strain rate will be proportional to 3.0-3.5 powers of stress, namely, the mantle flow will be non-Newtonian. In addition, the dominant slip system will produce the lattice-preferred-orientation (LPO), which causes seismic anisotropy. In contrast, if diffusion creep dominates, the strain rate will be proportional to stress and the mantle flow will be Newtonian. It does not cause seismic anisotropy. Thus, assessment of dominant creep mechanism is significant for understanding the solid geophysics.

Based on experimental deformation results in dry and wet olivine [Hirth and Kohlstedt, 2003; Jung and Karato, 2001; Karato et al., 1993; Karato et al., 1986; Karato and Jung, 2003; Mei and Kohlstedt, 2000a; b], it has been considered that the deformation mechanism in the upper mantle changes from anisotropic dislocation creep to isotropic diffusion creep in the asthenosphere at a depth of ~200-250 km [Hirth and Kohlstedt, 2003; Karato and Wu, 1993]. However, as suggested by Fei et al. [2012; 2013], the reported water and pressure dependences on rheology are very problematic because of the limited water content and uncertainty of stress-strain rate relations. Therefore, it is necessary to examine the deformation mechanisms in Earth's mantle by independent ways from the deformation experiments.

Diffusion and dislocation creep are considered to be controlled by self-diffusion of the slowest species [Frost and Ashby, 1982; Weertman, 1999], which is silicon in olivine [Costa and Chakraborty, 2008; Houlier et al., 1990]. Especially, Coble diffusion creep is controlled by grain-boundary diffusion, while Nabarro-Herring diffusion creep and dislocation creeps are controlled by lattice diffusion [Frost and Ashby, 1982; Weertman, 1999]. Therefore, measurement of silicon lattice and grain-boundary diffusion-coefficients ( $D_{\text{Si}^{\text{lat}}}$  and  $D_{\text{Si}^{\text{gb}}}$ , respectively), which allows much wider experimental conditions than rock deformation studies [e.g., pressure ( $P$ ), temperature ( $T$ ), and water content ( $C_{\text{H}_2\text{O}}$ )] and also does not create unrealistically high-density defects, provides useful information to understand the upper mantle rheology. We have already reported results of  $D_{\text{Si}^{\text{lat}}}$  as a function of  $T$ ,  $P$ , and  $C_{\text{H}_2\text{O}}$  in the lattice ( $C_{\text{H}_2\text{O}}^{\text{lat}}$ ) [Fei et al., 2012; Fei et al., 2013]. The  $D_{\text{Si}^{\text{gb}}}$  was measured by Farver and Yund [2000] using forsterite aggregates. However, Farver and Yund [2000]'s results of  $D_{\text{Si}^{\text{gb}}}$  were obtained under dry and ambient pressure conditions, which cannot be applied to the Earth's interior because of its wet and high-pressure conditions. Therefore, we have systematically measured  $D_{\text{Si}^{\text{gb}}}$  in this study as a function of  $P$ ,  $T$ , and  $C_{\text{H}_2\text{O}}^{\text{gb}}$  (water content on the grain boundaries) in a fine-grained forsterite aggregates sample. The results suggest that diffusion creep dominates in cold lithosphere and mantle wedge.

## 5.3 Experimental and analytical procedures

### 5.3.1 Starting material

We use forsterite ( $\text{Mg}_2\text{SiO}_4$ ) aggregates (**Fig. 5.1**) as starting material synthesized from a mixture of  $\text{SiO}_2$  and  $\text{Mg}(\text{OH})_2$  powder following the procedure reported by Hiraga et al. [2010], Koizumi et al. [2010], and Sano et al. [2006]. Nano-sized powders of  $\text{SiO}_2$  (particle size of 50 nm) and  $\text{Mg}(\text{OH})_2$  (particle size of 40 nm) were analyzed with thermogravimetry and differential thermal analyses to  $T = 1273$  K to estimate the water contents on the powder surfaces absorbed from the air, which were extremely high (nearly 20 wt. %) due to the large surface area per unit volume [Hiraga et al., 2010; Koizumi et al., 2010; Sano et al., 2006]. The two powders were well mixed in ethanol, dried, cooked at  $T = 1273$  K to synthesize forsterite powder, and then cold-pressed into pellets at 200 MPa in an isostatic press [Hiraga et al., 2010; Koizumi et al., 2010]. The cold-pressed forsterite pellets ( $\sim 5$ -mm diameter and  $\sim 4$ -mm thickness) were heated to 1633 K with a ramping rate of 300 K/h under a vacuum condition of  $P = \sim 5 \times 10^{-3}$  Pa in an alumina tube furnace at University of Tokyo, Japan. The annealing duration at 1630 K was about 3 hours [Hiraga et al., 2010; Koizumi et al., 2010].

The average grain size of the synthesized forsterite aggregates was  $\sim 0.6$   $\mu\text{m}$  estimated from scanning electron microscopy (SEM) images (**Fig. 5.1**). The concentration of trace elements (Ti, Al, Fe, Mn, Ca, Na, K, P, Ba, Co, Cr, Cu, Nb, Sc, V, Ni, Zn, Rb, Zr, Sr, and V) in the synthesized samples was found to be  $< 10$  wt. ppm each [Hiraga et al., 2010]. The bulk water content ( $C_{\text{H}_2\text{O}}^{\text{bulk}}$ ) was  $< 1$  wt. ppm determined by Fourier transform infrared (FT-IR). Forsterite aggregates ( $\sim 0.7 \times 0.7 \times 0.6$   $\text{mm}^3$ ) cored from the synthesized pellets was used for diffusion experiments in the following procedures.

Several forsterite aggregate samples were further heated at 1700 K for 20 hours to enhance the grain growth, after which the average grain sizes were  $\sim 2$   $\mu\text{m}$  (**Fig. 5.1**). Diffusion experiments were also performed for these samples.

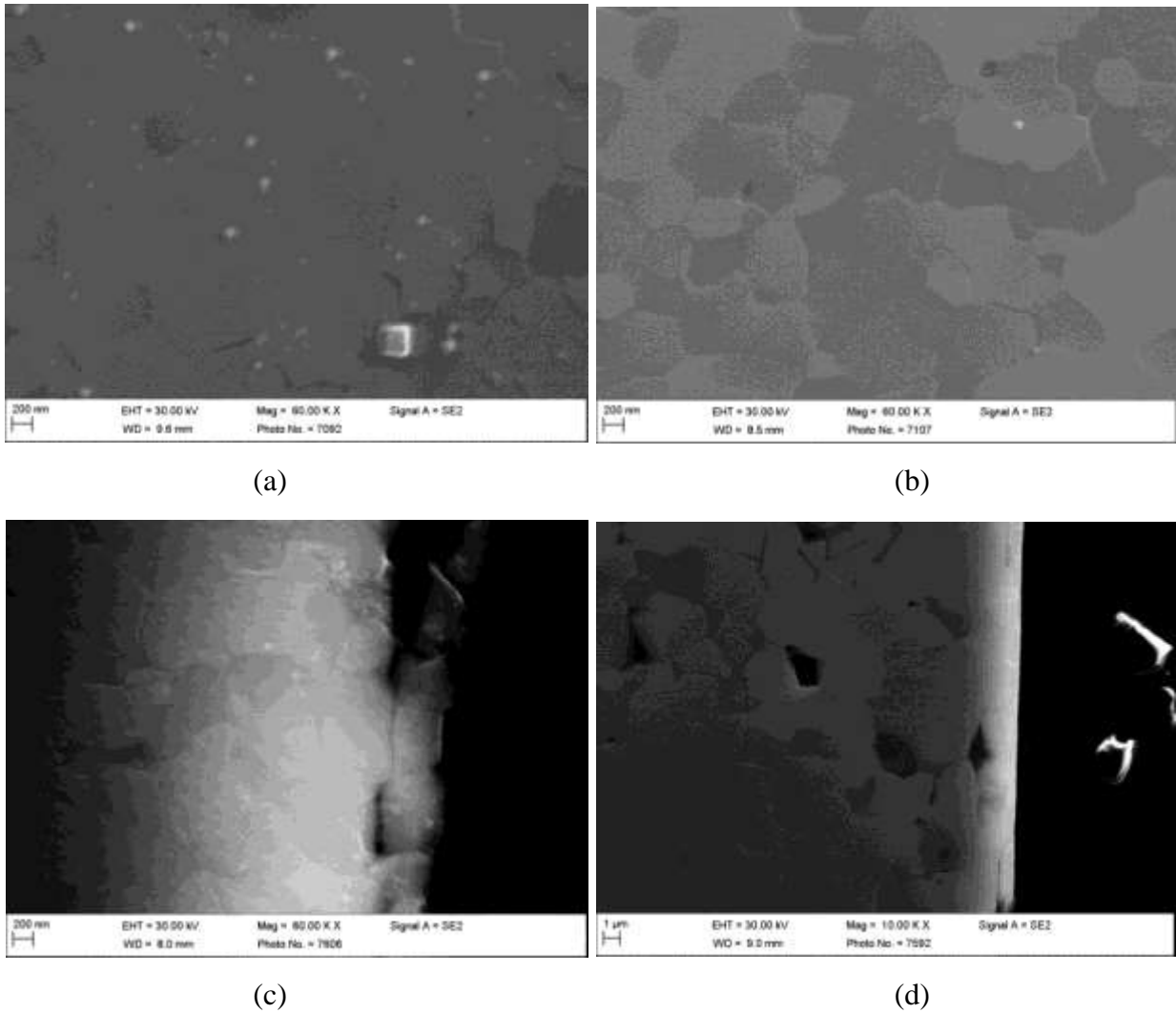


**Fig. 5.1.** Secondary electron images of the forsterite aggregates. **(a)** Before water-doping experiments. **(b)** After water-doping experiments. **(c)** After diffusion annealing. The coated thin film has similar grain size as that in the substrate after diffusion. **(d)** After diffusion annealing (starting material treated at 1700 K for 20 h). No grain growth was observed in each step. The grain boundaries were chemically etched using dilute HCl+HNO<sub>3</sub> (~5 %) acid before SEM analysis. Triple junctions are well defined. The difference in intensity among grains is due the channeling effect.

### 5.3.2 Pre-annealing experiments

In order to obtain samples with various  $C_{H_2O}^{gb}$ , the dry forsterite aggregate cubes were pre-annealed at 8 GPa, 1100-1600 K with talc and brucite as a water source. Each forsterite cube was loaded into a one-end sealed platinum capsule with outer diameter of 2.0-mm and inner diameter

of 1.6-mm and a mixture of talc+brucite powders (weight ratio of 4:1) located at the bottom [Fei *et al.*, 2013]. The space between sample and capsule inner wall was filled with a mixture of graphite and enstatite ( $\text{MgSiO}_3$ ) powder (20:1 volume ratio) to prevent the sample from mechanical damage and to buffer the silicon activity, respectively. The platinum capsule was closed, cooled in liquid nitrogen, and sealed by arc welding. The water content in the capsule was controlled by the ratio of talc+brucite to graphite+enstatite [Fei *et al.*, 2013] and the oxygen fugacity ( $f_{\text{O}_2}$ ) was at the enstatite-magnesite-olivine-graphite (EMOG) stable field [Eggler, 1979], which is close to that in the Earth's interior, i.e.,  $\log f_{\text{O}_2} \approx \sim \text{FMQ}-1$  [Wood *et al.*, 1990].

High pressure experiments were performed using a Kawai-type multi-anvil apparatus at University of Bayreuth. In each run, the capsule was placed in an MgO cylinder in a stepped graphite heater with a  $\text{ZrO}_2$  thermal insulator. A W97%Re3%-W75%Re25% thermocouple with its junction placed at the bottom of the capsule was used to measure the temperature (**Fig. 5.2**). The pressure media was MgO+5%  $\text{Cr}_2\text{O}_3$  octahedra with edge lengths of 14 mm. Eight tungsten carbide cubes with 32-mm edge length and 8-mm truncation edge lengths were used to generate high pressures. The cell assembly was compressed to the target pressure (1 - 13 GPa) at room temperature in 2-4 hours, heated up to the target temperature (1200 – 1600 K) at a rate of 50 K/min, kept at high temperature for a duration of 4-10 hours which was sufficient to equilibrate water in sample [Demouchy and Mackwell, 2003; Demouchy, 2010], and then quenched by switching off the heating power. The temperature variation during annealing was less than 2 K under automatic control. After annealing, the sample assembly was decompressed to ambient pressure over a period of 10-16 hours.

For dry condition experiments, the samples were pre-annealed in the same way described above but without the water source for defect equilibrium. Additionally, the capsules with samples and graphite+enstatite powders were dried in a vacuum furnace ( $P < 30$  mbar) at 473 K for >24 hours and sealed on a hotplate to minimize the moisture in the capsule absorbed from the atmosphere [Fei *et al.*, 2012; Shatskiy *et al.*, 2009].

In ambient pressure experiments, samples with enstatite buffer were loaded in platinum capsules without sealing and pre-annealed in a gas mixing furnace at 1100 – 1600 K for over 12 hours for defect equilibrium. The oxygen partial pressure was controlled at extrapolation of the EMOG buffer [Eggler, 1979] to the ambient total pressure using a mixture of CO and  $\text{CO}_2$ .

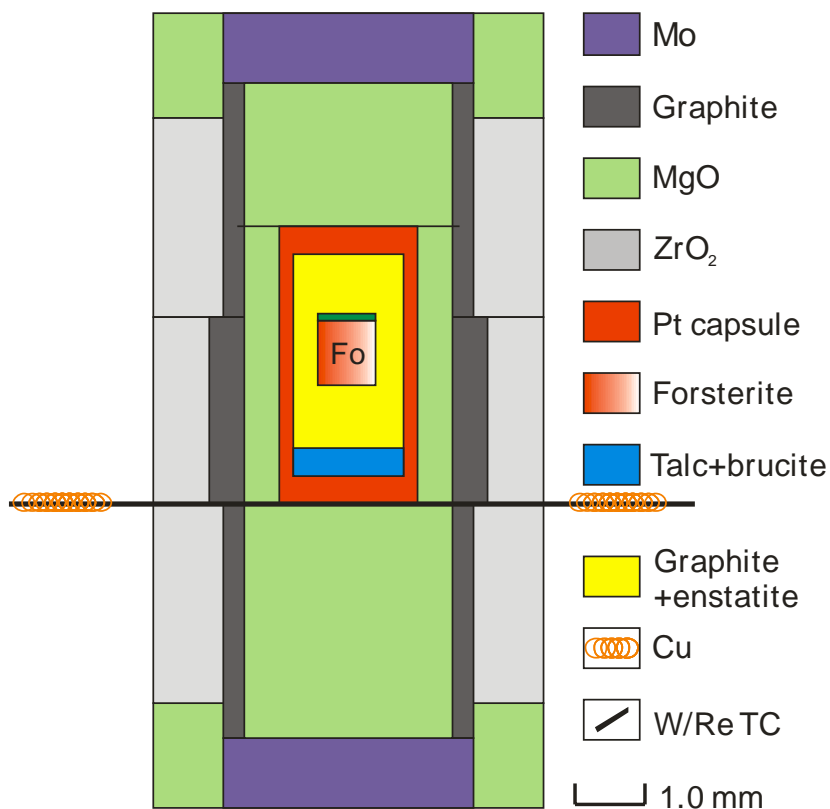


**Fig. 5.2.** A sketch of multi-anvil assembly used for water-doping and diffusion annealing experiments. The coated thin film for diffusion experiments (green) is located at the step of graphite, while the thermocouple is located at the other step to minimize temperature measurement errors.

### 5.3.3 Deposition

The samples after pre-annealing were finely polished using 1/4  $\mu\text{m}$  diamond powder and subsequently using an alkaline colloidal silica solution. The roughness of the sample surfaces after polishing was less than 10 nm including the grain boundaries confirmed by a confocal microscope. The sample surfaces were deposited with 1000-nm thick  $^{29}\text{Si}$  enriched  $\text{Mg}_2\text{SiO}_4$  forsterite thin film using the pulsed laser deposition (PLD) system at Ruhr-University of Bochum [Dohmen *et al.*, 2002]. An additional  $\text{ZrO}_2$  thin film ( $\sim 100$  nm) was deposited to protect the  $^{29}\text{Si}$  enriched forsterite film, which does not affect the silicon diffusion rate confirmed in our previous studies [Fei *et al.*, 2012; Fei *et al.*, 2013].

### 5.3.4 Diffusion annealing

After thin-film deposition, each sample was annealed again for diffusion using exactly the same experimental set up, the same  $P$ - $T$  conditions, and the same ratio of (talc+brucite)/(graphite+enstatite) as that used for the corresponding pre-annealing experiment, which successfully made constant  $C_{\text{H}_2\text{O}}^{\text{gb}}$  during annealing [Fei *et al.*, 2013]. A summary of run conditions were listed in **Table 5.1**.

**Table 5.1.** Experimental conditions and results of  $\delta D_{\text{Si}}^{\text{gb}}$ . \*a: total  $C_{\text{H}_2\text{O}}^{\text{bulk}} \approx C_{\text{H}_2\text{O}}^{\text{lat}} + 2\delta C_{\text{H}_2\text{O}}^{\text{gb}}/d$  determined using Thomas' calibration [Thomas *et al.*, 2009]. \*b:  $C_{\text{H}_2\text{O}}^{\text{lat}}$  determined using Thomas' calibration [Thomas *et al.*, 2009]. \*c:  $\delta C_{\text{H}_2\text{O}}^{\text{gb}}$  determined using Bell's calibration [Bell *et al.*, 2003], \*d:  $\delta C_{\text{H}_2\text{O}}^{\text{gb}}$  determined using Thomas' calibration [Thomas *et al.*, 2009].

Sample	$P$ (GPa)	$T$ (K)	$t$ (h)	*a $C_{\text{H}_2\text{O}}^{\text{bulk}}$ (wt. ppm)	*b $C_{\text{H}_2\text{O}}^{\text{lat}}$ (wt. ppm)	*c $\delta C_{\text{H}_2\text{O}}^{\text{gb}}$ (wt. ppm · $\mu\text{m}$ )	*d $\delta C_{\text{H}_2\text{O}}^{\text{gb}}$ (wt. ppm · $\mu\text{m}$ )	$d$ ( $\mu\text{m}$ )	$\delta D_{\text{Si}}^{\text{gb}}$ ( $\text{m}^3/\text{s}$ )
H3670#1	8	1200	3	157	41	32	35	0.6	$6.2 \times 10^{-28}$
H3670#2	8	1200	3	157	41	32	35	0.6	$2.1 \times 10^{-28}$
H3675B#1	8	1200	3	29	12	5.1	5.1	0.6	$3.5 \times 10^{-28}$
H3675B#2	8	1200	3	29	12	5.1	5.1	0.6	$2.5 \times 10^{-28}$
H3675T	8	1200	3	43	13	8.4	9.0	0.6	$4.9 \times 10^{-28}$
H3681B#1	8	1200	7	<1	<1	<1	<1	2	$1.5 \times 10^{-28}$
H3681B#2	8	1200	7	<1	<1	<1	<1	2	$8.0 \times 10^{-29}$
H3681T#1	8	1200	7	<1	<1	<1	<1	2	$1.4 \times 10^{-28}$
S5752L	8	1200	30	39	12	25	27	2	$2.9 \times 10^{-28}$
S5752S	8	1200	30	33	23	4	3	0.6	$3.1 \times 10^{-28}$
V758#1	8	1200	2	320	99	64	66	0.6	$9.1 \times 10^{-28}$
V758#2	8	1200	2	320	99	64	66	0.6	$4.6 \times 10^{-28}$
V758#3	8	1200	2	320	99	64	66	0.6	$4.9 \times 10^{-28}$
V797B	8	1200	30	149	79	20	21	0.6	$2.2 \times 10^{-28}$
V797M	8	1200	30	58	26	29	32	2	$5.7 \times 10^{-28}$
V797T	8	1200	30	171	56	34	35	0.6	$4.0 \times 10^{-28}$
H3667B#1	8	1300	1	209	71	40	41	0.6	$3.4 \times 10^{-27}$
H3667B#2	8	1300	1	209	71	40	41	0.6	$2.4 \times 10^{-27}$
H3667T#1	8	1300	2	200	71	123	129	2	$3.8 \times 10^{-27}$
H3667T#2	8	1300	2	200	71	123	129	2	$3.6 \times 10^{-27}$
H3673#1	8	1300	1	<1	<1	<0.3	<0.3	0.6	$1.1 \times 10^{-27}$
H3673#2	8	1300	1	<1	<1	<0.3	<0.3	0.6	$4.2 \times 10^{-28}$

(Continued)

**Table 5.1** (continue)

Sample	$P$ (GPa)	$T$ (K)	$t$ (h)	$^{*a}C_{H_2O}^{bulk}$ (wt. ppm)	$^{*b}C_{H_2O}^{lat}$ (wt. ppm)	$^{*c}\delta C_{H_2O}^{gb}$ (wt. ppm $\cdot \mu m$ )	$^{*e}\delta C_{H_2O}^{gb}$ (wt. ppm $\cdot \mu m$ )	$d$ ( $\mu m$ )	$\delta D_{Si}^{gb}$ ( $m^3/s$ )
H3679T#1	8	1300	1	31	22	2.4	2.7	0.6	$2.4 \times 10^{-27}$
H3679T#2	8	1300	1	31	22	2.4	2.7	0.6	$1.8 \times 10^{-27}$
H3699B	8	1300	10	<1	<1	<0.3	<0.3	0.6	$7.2 \times 10^{-28}$
H3699T	8	1300	10	<1	<1	<1	<1	2	$5.8 \times 10^{-28}$
H3734	8	1300	10	52	24	6.9	8.4	0.6	$2.3 \times 10^{-27}$
S5746B	8	1300	30	<1	<1	<0.3	<0.3	0.6	$3.8 \times 10^{-28}$
H3741L	8	1300	6	36	11	25.0	25.0	2	$4.0 \times 10^{-27}$
H3741S	8	1300	6	80	41	11.1	11.7	0.6	$1.9 \times 10^{-27}$
S5746T	8	1300	30	<1	<1	<1	<1	2	$6.1 \times 10^{-28}$
V757#1	8	1300	0.5	274	71	58	61	0.6	$4.5 \times 10^{-27}$
V757#2	8	1300	0.5	274	71	58	61	0.6	$3.9 \times 10^{-27}$
V760#1	8	1300	0.5	563	215	100	104	0.6	$7.9 \times 10^{-27}$
V760#2	8	1300	0.5	563	215	100	104	0.6	$3.8 \times 10^{-27}$
H3740L	8	1400	8	<1	<1	<1	<1	2	$2.7 \times 10^{-27}$
H3740S	8	1400	8	<1	<1	<0.3	<0.3	0.6	$4.3 \times 10^{-27}$
H3747M	8	1400	5	87	64	6.6	6.9	0.6	$1.7 \times 10^{-26}$
H3747T	8	1400	5	<1	<1	<0.3	<0.3	0.6	$3.3 \times 10^{-27}$
H3736B	8	1500	5	<1	<1	<0.3	<0.3	0.6	$7.7 \times 10^{-27}$
H3736T	8	1500	5	<1	<1	<0.3	<0.3	0.6	$1.2 \times 10^{-26}$
H3746	8	1500	5	20	9	3.0	3.3	0.6	$3.5 \times 10^{-26}$
H3715B	8	1600	7	27	12	3.9	4.5	0.6	$2.7 \times 10^{-25}$
H3715T	8	1600	7	27	21	7.0	6.0	2	$1.7 \times 10^{-25}$
H3735B	8	1600	4	<1	<1	<0.3	<0.3	0.6	$7.8 \times 10^{-26}$
H3735T	8	1600	4	80	50	27	30	2	$3.0 \times 10^{-25}$
V798B	1	1300	9	<1	<1	<0.3	<0.3	0.6	$8.9 \times 10^{-28}$
V798T	1	1300	9	<1	<1	<0.3	<0.3	0.6	$2.0 \times 10^{-27}$
V789	4	1300	9	<1	<1	<0.3	<0.3	0.6	$1.6 \times 10^{-27}$
H3749T#1	13	1300	9	<1	<1	<0.3	<0.3	0.6	$1.7 \times 10^{-28}$
H3749T#2	13	1300	9	<1	<1	<0.3	<0.3	0.6	$3.0 \times 10^{-28}$
D20L	$10^{-4}$	1100	71.3	<1	<1	<1	<1	2	$2.6 \times 10^{-29}$
D20S#1	$10^{-4}$	1100	71.3	<1	<1	<0.3	<0.3	0.6	$2.9 \times 10^{-29}$
D20S#2	$10^{-4}$	1100	71.3	<1	<1	<0.3	<0.3	0.6	$7.3 \times 10^{-29}$
D15L	$10^{-4}$	1200	38	<1	<1	<1	<1	2	$3.2 \times 10^{-28}$
D15S	$10^{-4}$	1200	38	<1	<1	<0.3	<0.3	0.6	$3.2 \times 10^{-28}$
D13L	$10^{-4}$	1300	15	<1	<1	<1	<1	2	$1.6 \times 10^{-27}$
D13S	$10^{-4}$	1300	15	<1	<1	<0.3	<0.3	0.6	$2.6 \times 10^{-27}$

(Continued)

**Table 5.1** (continue)

Sample	$P$ (GPa)	$T$ (K)	$t$ (h)	* <sup>a</sup> $C_{\text{H}_2\text{O}}^{\text{bulk}}$ (wt. ppm)	* <sup>b</sup> $C_{\text{H}_2\text{O}}^{\text{lat}}$ (wt. ppm)	* <sup>c</sup> $\delta C_{\text{H}_2\text{O}}^{\text{gb}}$ (wt. ppm · $\mu\text{m}$ )	* <sup>c</sup> $\delta C_{\text{H}_2\text{O}}^{\text{gb}}$ (wt. ppm · $\mu\text{m}$ )	$d$ ( $\mu\text{m}$ )	$\delta D_{\text{Si}}^{\text{gb}}$ ( $\text{m}^3/\text{s}$ )
D21	$10^{-4}$	1300	22.2	<1	<1	<0.3	<0.3	0.6	$1.9 \times 10^{-27}$
D22	$10^{-4}$	1300	6	<1	<1	<0.3	<0.3	0.6	$1.6 \times 10^{-27}$
D23	$10^{-4}$	1300	40.2	<1	<1	<0.3	<0.3	0.6	$2.4 \times 10^{-27}$
D2L	$10^{-4}$	1300	1	<1	<1	<1	<1	2	$3.4 \times 10^{-27}$
D2S	$10^{-4}$	1300	1	<1	<1	<0.3	<0.3	0.6	$2.2 \times 10^{-27}$
D5S	$10^{-4}$	1300	0.25	<1	<1	<0.3	<0.3	0.6	$3.1 \times 10^{-27}$
D6S	$10^{-4}$	1300	3	<1	<1	<0.3	<0.3	0.6	$1.9 \times 10^{-27}$
D16L	$10^{-4}$	1400	11	<1	<1	<1	<1	2	$9.6 \times 10^{-27}$
D16S	$10^{-4}$	1400	11	<1	<1	<0.3	<0.3	0.6	$6.5 \times 10^{-27}$
D4S	$10^{-4}$	1400	0.25	<1	<1	<0.3	<0.3	0.6	$1.0 \times 10^{-26}$
D17L	$10^{-4}$	1500	6	<1	<1	<1	<1	2	$2.4 \times 10^{-26}$
D17S#1	$10^{-4}$	1500	6	<1	<1	<0.3	<0.3	0.6	$9.5 \times 10^{-26}$
D17S#2	$10^{-4}$	1500	6	<1	<1	<0.3	<0.3	0.6	$3.1 \times 10^{-26}$
D19S	$10^{-4}$	1600	4	<1	<1	<0.3	<0.3	0.6	$2.8 \times 10^{-25}$

Besides, a series of zero-time diffusion runs were performed at 8 GPa, 1200 K, in which the sample assemblies were heated up to the target temperature and quenched immediately. By measuring the diffusion profiles of these zero-time run samples, a linear correction line of zero-time nominal-diffusion profile slope against surface roughness was obtained for the roughness calibration [Fei *et al.*, 2012; Fei *et al.*, 2013] shown in **Fig. 5.3**. Note that the surface roughness was usually ~100-200 nm after diffusion annealing. The sample surfaces were slightly polished by an alkaline colloidal silica solution to obtain a smooth surface with a roughness less than 40 nm. The variation of surface roughness in **Fig. 5.3** was obtained by varying the degree of the polishing after diffusion annealing.

Additionally, the grain sizes of the forsterite aggregates during pre-annealing and diffusion annealing did not increase, and the grain sizes in the thin film were similar as those in the substrates confirmed by secondary electrons image shown in **Fig. 5.1c** and **5.1d**. That is because the annealing temperature is relatively low (1100-1600 K) and duration is relatively short (less than 10 h when the temperature is higher than 1400 K, and less than 72 h when lower than 1300 K). Even if the sample is annealed at 1630 K for 50 h, the average grain size only increases by less than factor 2.5 [Hiraga *et al.*, 2010]. Therefore, the grain growth is negligible in this study.

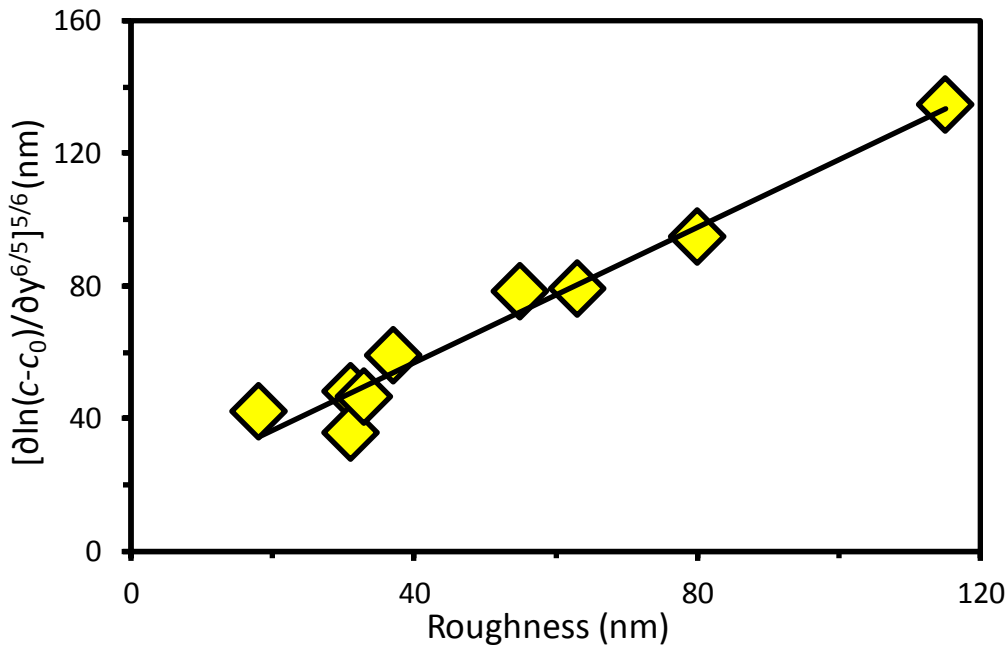


**Fig. 5.3.** A linear relationship between the standard deviation of surface roughness ( $\sigma$ ) and slope of the grain-boundary diffusion profile obtained in zero-time runs for roughness correction.

### 5.3.5 FT-IR analysis

#### (1) FT-IR measurement

The water content of each sample before and after diffusion annealing was determined by un-polarized Fourier transform infrared (FT-IR) spectroscopy using a Bruker IFS 120 high-resolution FT-IR spectrometer coupled with a Bruker IR microscope performed at room pressure and temperature. The measurements were performed using a tungsten light source, a Si/CaF<sub>2</sub> beam splitter and a high-sensitivity narrow-band mercury-cadmium-telluride detector cooled by liquid nitrogen [Demouchy and Mackwell, 2003].

The infrared beam was focused to  $\sim 100 \mu\text{m}$  on the sample surface for analysis. Two hundred scans were accumulated for each spectrum at a resolution of  $1 \text{ cm}^{-1}$ . More than three spectra were obtained for each forsterite sample both in the center and near the edge to confirm the homogeneity of water content in the sample [Fei *et al.*, 2012; Fei *et al.*, 2013]. Examples of FT-IR spectra after a background baseline correction and thickness normalization to 1 cm are shown in **Fig. 5.4**.

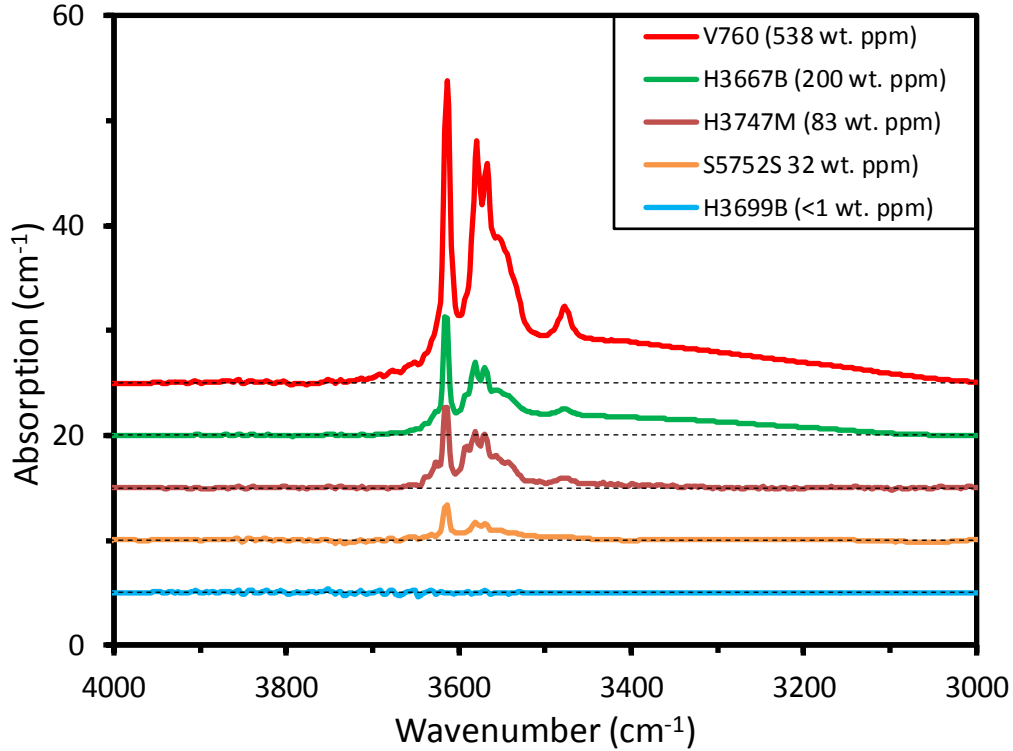


**Fig. 5.4.** Examples of FT-IR spectra after baseline correction and thickness normalization to 1 cm.

## (2) Calculate water content

Water in aggregates can exist both in grain-interior and on grain-boundaries [structured -OH in grain interior and on grain boundaries, there should be no molecular water in this study because of the unsaturated-water conditions [Fei *et al.*, 2013]. Thus, the FT-IR spectrum taken from polycrystalline contains the absorptions due to the -OH bonds on the grain boundaries ( $C_{H_2O}^{bulk(gb)}$ ) as well as those in the lattice ( $C_{H_2O}^{lat}$ ) [Katayama and Karato, 2008] (**Fig. 5.5**). In order to determine the effect of water on silicon grain-boundary diffusion, water contents on the grain boundaries are needed to be determined.

Since the lattice and grain-boundary water in olivine are reflected in the FT-IR spectra as sharp peaks and broad bands, respectively [Aubaud *et al.*, 2007; Katayama and Karato, 2008], the water content on grain-boundaries which affects the silicon grain-boundary diffusion rate in this study can be determined by the broad bands. We have synthesized a profile of a randomly oriented single crystal which was obtained by averaging polarized single crystal spectra measured in the three vibrational orientations. The contribution of the lattice part is subtracted

from the polycrystalline spectrum using this synthetic profile to obtain the contribution of the grain boundary water (**Fig. 5.5**). The contributions of  $C_{\text{H}_2\text{O}}^{\text{bulk (gb)}}$  and  $C_{\text{H}_2\text{O}}^{\text{lat}}$  were calculated from the grain-boundary part and lattice part –OH absorptions, respectively (**Fig. 5.5**), using calibration given by Thomas et al. [Thomas et al., 2009]:

$$C_{\text{H}_2\text{O}} = \int \frac{M \times A(\nu)}{k \times \rho \times t} d\nu \quad (5.1)$$

where  $C_{\text{H}_2\text{O}}$  is the  $C_{\text{H}_2\text{O}}^{\text{bulk (gb)}}$  or  $C_{\text{H}_2\text{O}}^{\text{bulk (lat)}}$  in wt. ppm,  $A(\nu)$  is the absorption coefficient at wave number  $\nu$ ,  $k$  is molar absorption coefficient [ $k = 28,000 \text{ L}/(\text{mol} \times \text{cm}^2)$ ] [Thomas et al., 2009]],  $M$  is the molecular weight of water ( $M = 18.02 \text{ g/mol}$ ),  $t$  is the sample thickness, and  $\rho$  is the density of forsterite ( $\rho = 3.27 \text{ g/cm}^3$ ). The integration was performed between 3000 and 4000  $\text{cm}^{-1}$  [Fei et al., 2012; Fei et al., 2013].

The total  $C_{\text{H}_2\text{O}}^{\text{bulk}}$  in **Table 5.1** is [Kirchheim, 2001],

$$C_{\text{H}_2\text{O}}^{\text{bulk}} = C_{\text{H}_2\text{O}}^{\text{bulk(lat)}} + C_{\text{H}_2\text{O}}^{\text{bulk(gb)}} = (1-f)C_{\text{H}_2\text{O}}^{\text{lat}} + fC_{\text{H}_2\text{O}}^{\text{gb}} \approx C_{\text{H}_2\text{O}}^{\text{lat}} + \frac{2\delta}{d}C_{\text{H}_2\text{O}}^{\text{gb}} \quad (5.2)$$

where  $f = 2\delta/(d+2\delta)$  is the volume fraction of grain boundaries,  $d$  is the grain size, and  $\delta$  is the grain boundary width [Kirchheim, 2001].

The water content on grain boundaries,  $\delta C_{\text{H}_2\text{O}}^{\text{gb}}$ , was obtained from the grain boundary contribution,  $C_{\text{H}_2\text{O}}^{\text{bulk (gb)}}$  [Kirchheim, 2001],

$$\delta C_{\text{H}_2\text{O}}^{\text{gb}} = \frac{d}{2} C_{\text{H}_2\text{O}}^{\text{bulk(gb)}} \quad (5.3)$$

Note that the absolute value of grain boundary width,  $\delta$ , was not used in the calculation.

Since different parameters or calibration equations have been reported to calculate the water content in olivine from infrared spectrum [Paterson, 1982; Thomas et al., 2009], we compared the water contents calculated by different calibrations and the results were shown in **Table 5.1**. We found that the uncertainty of  $\delta C_{\text{H}_2\text{O}}$  values by different calibrations is within factor 1.5,

which is much smaller than the experimental uncertainty of silicon diffusion coefficients. On the other hand, using different calibrations only slightly changes the absolute values of  $C_{\text{H}_2\text{O}}$ , but does not change the ratio of  $C_{\text{H}_2\text{O}}$  between high- $C_{\text{H}_2\text{O}}$  and low- $C_{\text{H}_2\text{O}}$  samples, and therefore the  $C_{\text{H}_2\text{O}}$  exponents for silicon diffusion coefficients obtained using different calibration equations are almost the same. Because the Bell's calibration [Bell *et al.*, 2003] was used in our previous  $D_{\text{Si}^{\text{lat}}}$  measurement [Fei *et al.*, 2013], we also recalculated the effect of water on  $D_{\text{Si}^{\text{lat}}}$  using the Thomas' calibration [Thomas *et al.*, 2009] and the results did not change.

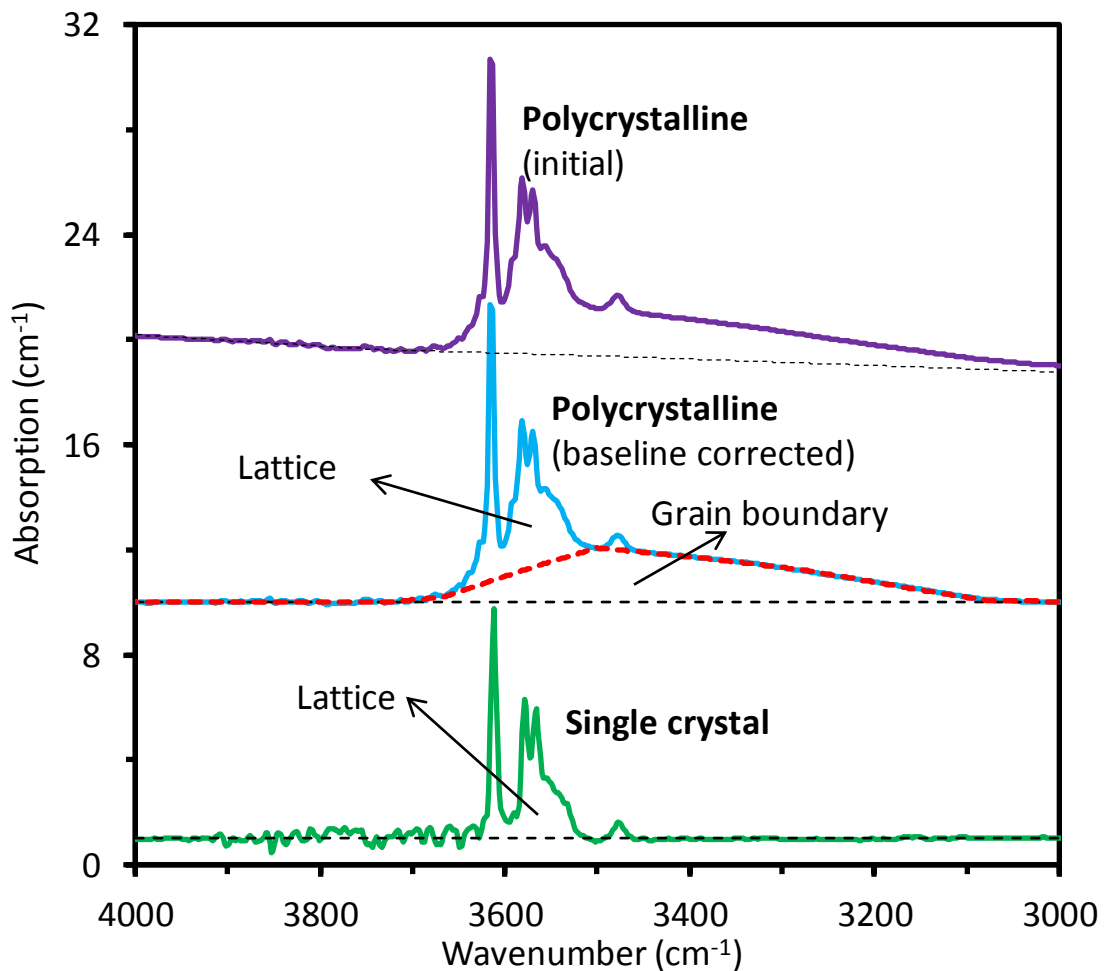


**Fig. 5.5.** Lattice and grain-boundary -OH absorptions. Bottom: a synthetic spectrum of a randomly oriented crystal which is obtained by averaging polarized spectra measured in the three vibrational orientations of a forsterite single crystal. Top: a real spectrum of a polycrystalline sample. The grain-boundary -OH absorptions (red dash line) is obtained by subtracting the contribution of the lattice part, which is estimated from the synthetic randomly oriented single crystal spectrum.

Strictly speaking, the calibrations should be different for the lattice and grain-boundary water. However, no calibration for the grain-boundary water has been reported so far and therefore we use the calibration for the lattice water, namely, Thomas' calibration [Thomas *et al.*, 2009] to calculate the grain-boundary water in this study.

### 5.3.6 SIMS analysis

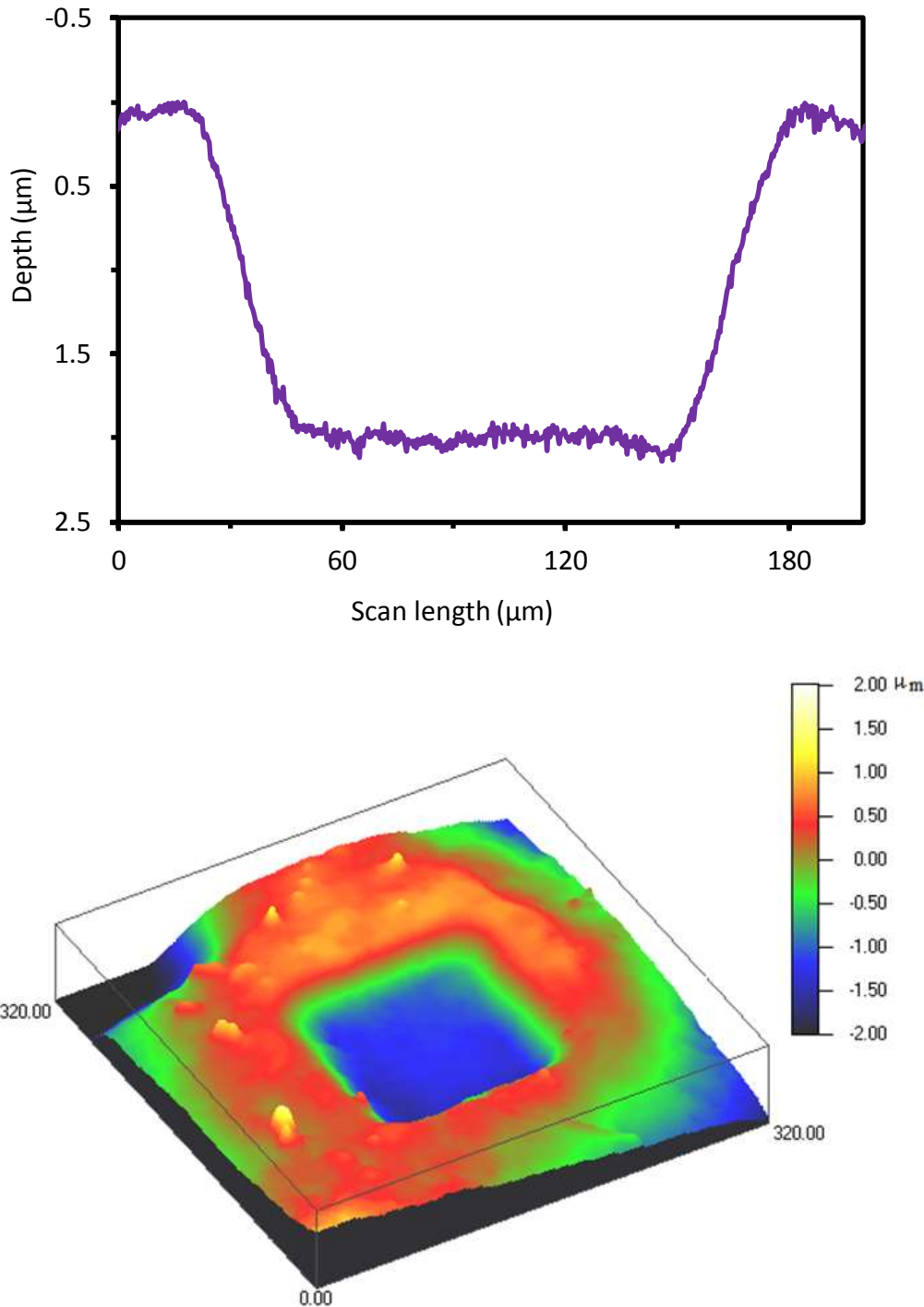
The samples after diffusion annealing were mounted in epoxy and deposited with ~50-nm gold thin films for secondary ion mass spectrometry (SIMS) analysis. The diffusion profiles were determined using a Cameca-6f SIMS at Hokkaido University, Japan. An O<sup>-</sup> primary beam (40 nA, 13 kV) was focused to the sample surface with a diameter of 50 μm. Secondary ions of <sup>28</sup>Si and <sup>29</sup>Si from the central regions (~30- μm diameter) of the sputtered crater (~100 × 100 μm<sup>2</sup> raster size) were detected with counting time of 2 s each. The crater depths were subsequently determined using a 3D-Nanofocus microscope at University of Bayreuth [Fei *et al.*, 2012; Fei *et al.*, 2013]. Examples of SIMS craters and diffusion profiles are shown in **Fig. 5.6** and **Fig. 5.7**, respectively.

There are different types of diffusion profiles in polycrystalline samples depending upon the annealing duration ( $t$ ), the grain size ( $d$ , 0.6 and ~2 μm in this study), the grain boundary width ( $\delta$ , 0.5-1 nm [Hiraga and Kohlstedt, 2007; Ricoult and Kohlstedt, 1983]), and the magnitude of  $D_{\text{Si}}^{\text{gb}}$  and  $D_{\text{Si}}^{\text{lat}}$ . In this study, the profiles were mainly controlled at type-B kinetics regime, in which both lattice diffusion and grain boundary diffusion contribute to the diffusion profile,  $\delta < 5(D_{\text{Si}}^{\text{lat}}t)^{1/2} < d$  [Harrison, 1961; Yamazaki *et al.*, 2000], by controlling the annealing duration estimated from previous studies of silicon lattice diffusion coefficients [Fei *et al.*, 2012; Fei *et al.*, 2013]. The results of  $\delta D_{\text{Si}}^{\text{gb}}$  were obtained by fitting the SIMS data to the equation [Farver *et al.*, 1994; Yamazaki *et al.*, 2000]:

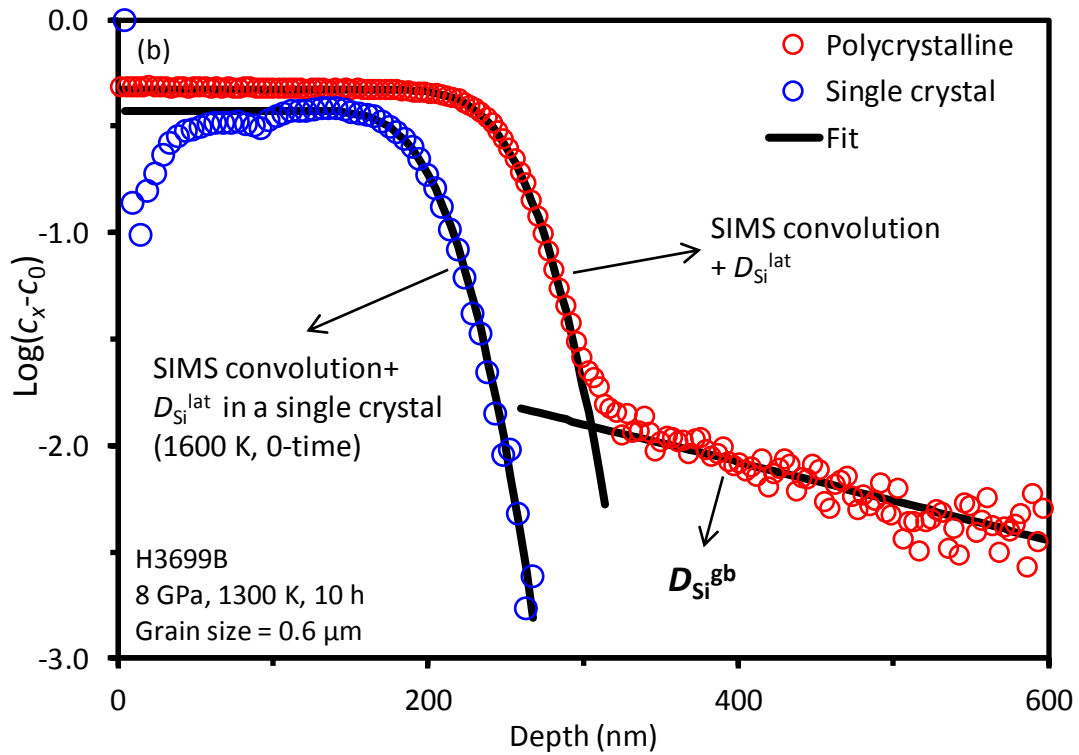
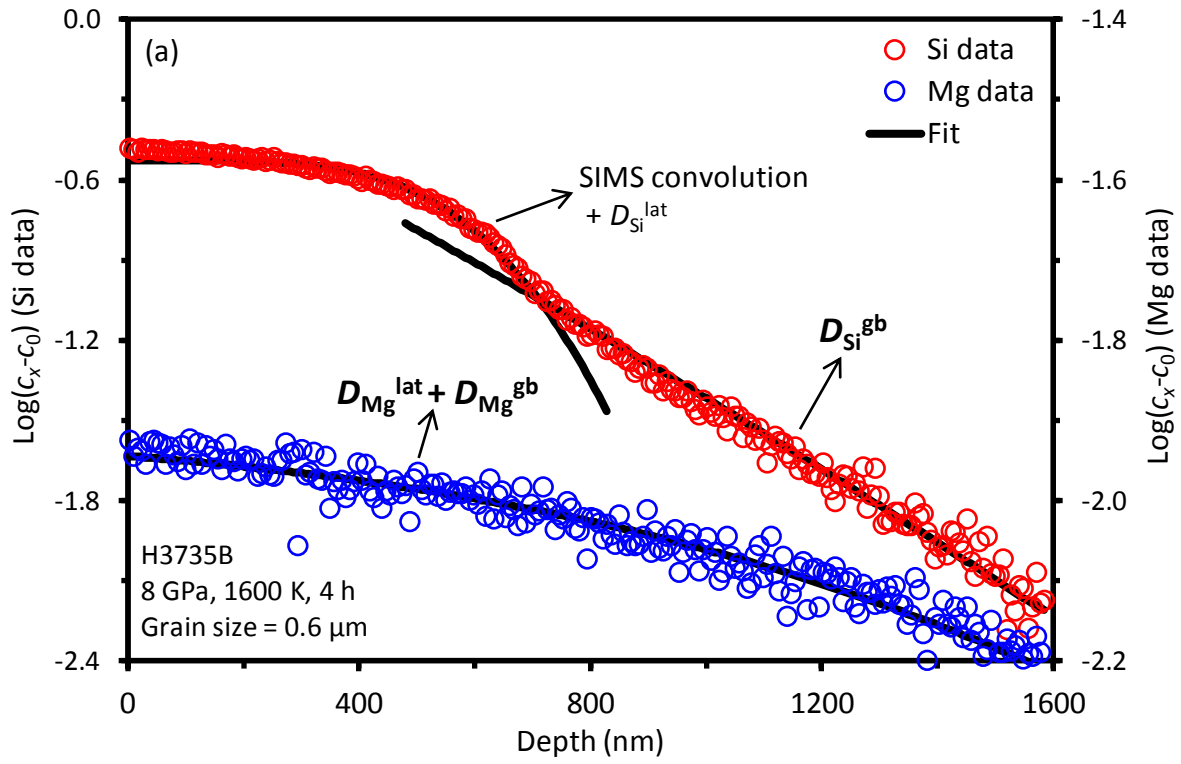
$$\delta D_{\text{Si}}^{\text{gb}} = 0.66 \left( -\frac{\partial \ln(c - c_0)}{\partial x^{6/5}} \right)^{-5/3} \left( \frac{4D_{\text{Si}}^{\text{lat}}}{t} \right)^{1/2} \quad (5.4)$$

where  $D_{\text{Si}}^{\text{lat}}$  is the Si lattice diffusion coefficient,  $c$  is the concentration of <sup>29</sup>Si expressed as <sup>29</sup>Si/(<sup>28</sup>Si+<sup>29</sup>Si) measured by SIMS,  $c_0$  is the concentration of <sup>29</sup>Si in the substrates,  $x$  is the distance from the surface, and  $t$  is the annealing duration. The slope of profile in the grain

boundary region,  $\partial \ln(c-c_0)/\partial x^{6/5}$ , is corrected by the slope obtained in 0-time experiments (**Fig. 5.3**).



**Fig. 5.6.** An example of SIMS crater measured by 3D-Nanofocus microscope. Top: Line scanning. Bottom: 3D-view of the crater.



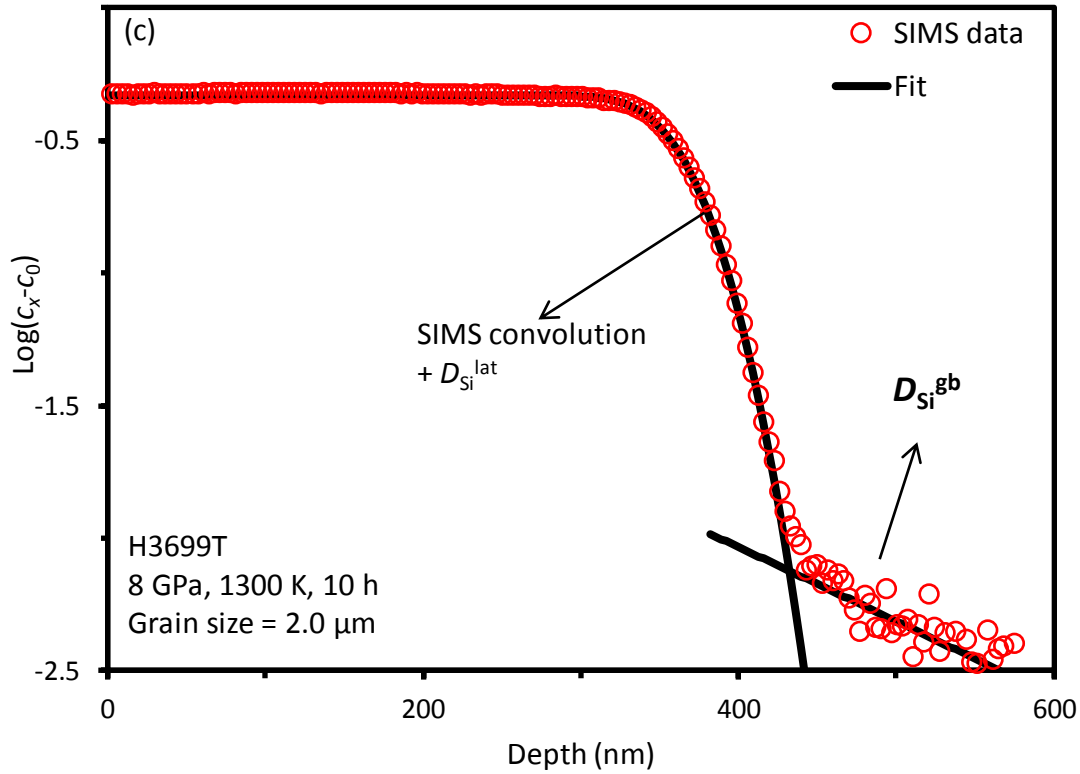


**Fig. 5.7.** Examples of diffusion profiles. (a) A comparison of Si and Mg diffusion profile obtained from the same SIMS crater. (b) A sample with grain size of  $\sim 0.6 \mu\text{m}$ . The single crystal silicon diffusion profile is taken from our previous studies [Fei *et al.*, 2012; Fei *et al.*, 2013]. (c) A sample with grain size of  $\sim 2 \mu\text{m}$ .

The lattice diffusion in a diffusion couple could be fitted to the error function, which is a solution of Fick's second law. On the other hand, the nominal diffusion profile caused by the convolution problem in measuring a diffusion profile, e.g., the rough surface, can also be fitted to the error function [Fei *et al.*, 2012; Ganguly *et al.*, 1988; Shimojuku *et al.*, 2009]. Therefore, the lattice diffusion regions of the profiles (**Fig. 5.7**) were fitted to,

$$c = \frac{c_0 - c_1}{2} \operatorname{erf} \left( \frac{x - H}{\sqrt{4D_{Si}^{lat}t + L}} \right) + \frac{c_0 + c_1}{2} \quad (5.5)$$

where  $c_1$  is the concentration of  $^{29}\text{Si}$  in the thin film,  $H$  is the boundary position between the thin film and substrate,  $\operatorname{erf}(z)$  is the error function, and  $L$  is a factor related to SIMS convolution including roughness effect which is approximately linear to surface roughness [Fei *et al.*, 2012].

However, since the experimental temperature conditions for determine  $\delta D_{\text{Si}}^{\text{gb}}$  are usually much lower than that for  $D_{\text{Si}}^{\text{lat}}$  because  $\delta D_{\text{Si}}^{\text{gb}}/d \gg D_{\text{Si}}^{\text{lat}}$ , the lattice diffusion length ranges from a few to several tens nanometer in this study, which is much shorter than that of a nominal profile caused by convolution of the SIMS measurement, i.e., a sample with rough surface could lead to an ~100-nm nominal diffusion profile even without annealing [Fei *et al.*, 2012]. Namely,  $4D_{\text{Si}}^{\text{lat}}t \ll L$  in this study. For example the apparent “lattice-diffusion” regions of a polycrystalline sample (**Fig. 5.7b**) is nearly the same as that measured in a single crystal after 0-time annealing from our previous study [Fei *et al.*, 2012], which means the “lattice-diffusion” regions of the profiles in this study are majorly contributed by SIMS convolution, especially in low temperature experiments (**Fig. 5.7b, Fig. 5.7c**). Therefore, even though the  $D_{\text{Si}}^{\text{lat}}$  could be determined in this study, the uncertainty is quite large and thus we used  $D_{\text{Si}}^{\text{lat}}$  in **Eqs. 5.5** determined from our previous studies which were measured using the same techniques but at higher temperatures and longer durations [Fei *et al.*, 2012; Fei *et al.*, 2013].

### 5.3.7 Calculations of creep rates from silicon diffusion coefficients

The rates of Coble creep, Nabarro-Herring creep, and dislocation creep can be calculated using the following equations based on Weertman [1999] and Frost & Ashby [1982] diffusion-controlled deformation models [Costa and Chakraborty, 2008; Farver and Yund, 2000; Frost and Ashby, 1982; Kohlstedt, 2006; Shimojuku *et al.*, 2009; Weertman, 1999]:

$$\dot{\epsilon}_{Co}(\text{Coble}) = A\sigma\pi \frac{\delta D_{\text{Si}}^{\text{gb}} V_m}{d^3 RT} \quad (5.6)$$

$$\dot{\epsilon}_{NH}(\text{Nabarro – Herring}) = A\sigma \frac{D_{\text{Si}}^{\text{lat}} V_m}{d^2 RT} \quad (5.7)$$

$$\dot{\epsilon}_{dis}(\text{dislocation}) = 2\pi \frac{GV_m}{RT} \left(\frac{\sigma}{G}\right)^3 \frac{D_{\text{Si}}^{\text{lat}}}{b^2} \frac{1}{\ln(G/\sigma)} \frac{l_g}{l_c} \quad (5.8)$$

where  $\dot{\epsilon}$  is the creep rate,  $A$  is a constant ( $A \approx 13.3$  [Farver and Yund, 2000; Shimojuku *et al.*, 2009]),  $\sigma$  is the shear stress,  $\delta$  is the grain boundary width ( $\delta \approx 0.5\text{-}1$  nm [Hiraga and Kohlstedt, 2007; Ricoult and Kohlstedt, 1983], actually, this value is not needed for this calculation),  $d$  is the grain size,  $G$  is the shear modulus ( $G = 52$  GPa for olivine [Kohlstedt, 2006]),  $V_m$  is the molar

volume ( $V_m = 43.8 \text{ cm}^3/\text{mol}$  for olivine [Kohlstedt, 2006]),  $b$  is the Burgers vector ( $b = 0.485 \text{ nm}$  [Kohlstedt, 2006]), and  $l_g/l_c$  is the ratio of dislocation glide distance to the climb distance ( $l_g/l_c = 1$  for olivine). Previously, the value of  $l_g/l_c$  was reported as 1 for dry olivine and 200 for wet olivine [Costa and Chakraborty, 2008; Kohlstedt, 2006]. However, the wet condition value,  $l_g/l_c = 200$ , was estimated based on deformation studies on wet olivine aggregates [Karato *et al.*, 1986; Mei and Kohlstedt, 2000b], in which the creep rates were demonstrated to be overestimated [Fei *et al.*, 2013], and  $l_g/l_c = 1$  is more realistic for wet olivine based on the single crystal silicon diffusion [Costa and Chakraborty, 2008; Fei *et al.*, 2013] and deformation studies [Raterron *et al.*, 2009; Raterron *et al.*, 2011]).

Under a given pressure, temperature,  $C_{\text{H}_2\text{O}}^{\text{bulk}}$ , grain size, and stress condition, the rates of Coble creep, Nabarro-Herring creep and dislocation creep can be obtained using **Eqs. 5.6-5.8** based on temperature, pressure, and water content dependence of  $\delta D_{\text{Si}}^{\text{gb}}$  determined in this study and  $D_{\text{Si}}^{\text{lat}}$  determined in our previous studies [Fei *et al.*, 2012; Fei *et al.*, 2013], and the one which has the fastest creep rate dominates the plastic deformation of olivine.

Note that a ratio of  $\sim 0.17 \times 10^{-6}$  between  $\delta C_{\text{H}_2\text{O}}$  and  $C_{\text{H}_2\text{O}}^{\text{bulk}}$  was found (**Table 5.1**) for a sample grain size of  $0.6 \text{ }\mu\text{m}$ , namely,  $\delta C_{\text{H}_2\text{O}}^{\text{gb}} \approx 0.17 \times 10^{-6} C_{\text{H}_2\text{O}}^{\text{bulk}}$ . For a given  $C_{\text{H}_2\text{O}}^{\text{bulk}}$  and  $d$ , values of  $\delta C_{\text{H}_2\text{O}}^{\text{gb}} \approx 0.17 \times 10^{-6} C_{\text{H}_2\text{O}}^{\text{bulk}}$  and  $C_{\text{H}_2\text{O}}^{\text{lat}} \approx C_{\text{H}_2\text{O}}^{\text{bulk}} (1 - 0.34 \times 10^{-6}/d)$  were used to determine the  $D_{\text{Si}}^{\text{lat}}$  and  $\delta D_{\text{Si}}^{\text{gb}}$ .

Additionally, the deformation of olivine in above models is driven by thermally activated defects at high temperatures. Material deformation is also possible at low temperature without thermal activation, namely, low temperature plasticity [Karato, 2008]. However, this is only the case when the stress is very high, reaching the yield stress, and the temperature is below  $770 - 1000 \text{ K}$  for olivine [Hunt *et al.*, 2009; Raterron *et al.*, 2004]. The yield stress in olivine is  $\sim 5 \text{ GPa}$  at  $\sim 370 \text{ K}$  [Evans and Goetze, 1979]. Though it decreases with increasing temperature, it is still several hundred MPa at  $1000 \text{ K}$  [Raterron *et al.*, 2004], much higher than the stress condition of most part of Earth's upper mantle ( $0.1-1 \text{ MPa}$ ). Thus, the low temperature plasticity is negligible in most part of the Earth's upper mantle.

## 5.4 Results

The experimental results listed in **Table 5.1** are plotted in **Fig. 5.8** against pressure, temperature, and water content. By fitting the results of  $\delta D_{\text{Si}}^{\text{gb}}$  and  $\delta C_{\text{H}_2\text{O}}^{\text{gb}}$  (The effective grain boundary thickness contribute grain-boundary diffusion is not clear, although the  $\delta$  is estimated by various methods. Therefore, we used  $\delta D_{\text{Si}}^{\text{gb}}$  and  $\delta C_{\text{H}_2\text{O}}^{\text{gb}}$  instead of  $D_{\text{Si}}^{\text{gb}}$  and  $C_{\text{H}_2\text{O}}^{\text{gb}}$  in this paper. The value of  $\delta$  is not used to calculate  $\delta D_{\text{Si}}^{\text{gb}}$  and  $\delta C_{\text{H}_2\text{O}}^{\text{gb}}$  as shown above) at 8 GPa and wet conditions ( $\delta C_{\text{H}_2\text{O}}^{\text{gb}} > 1$  wt. ppm  $\cdot \mu\text{m}$ ) (**Fig. 5.8a**) to the equation:

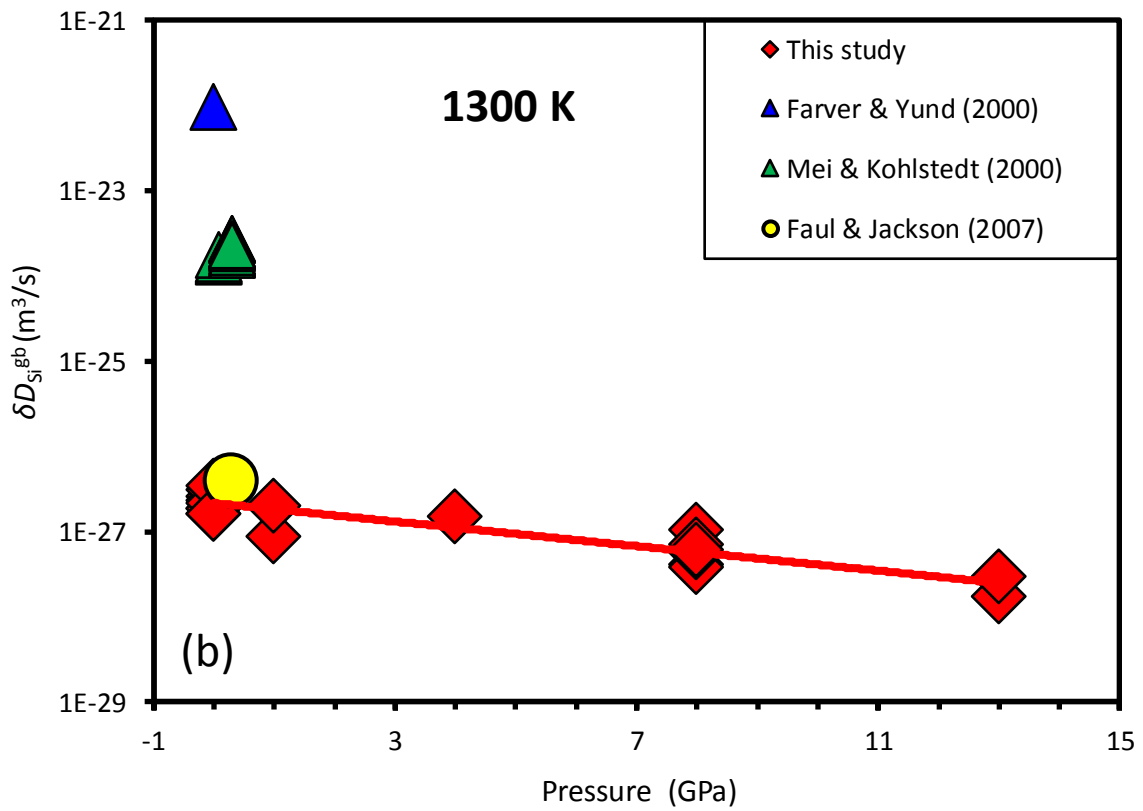
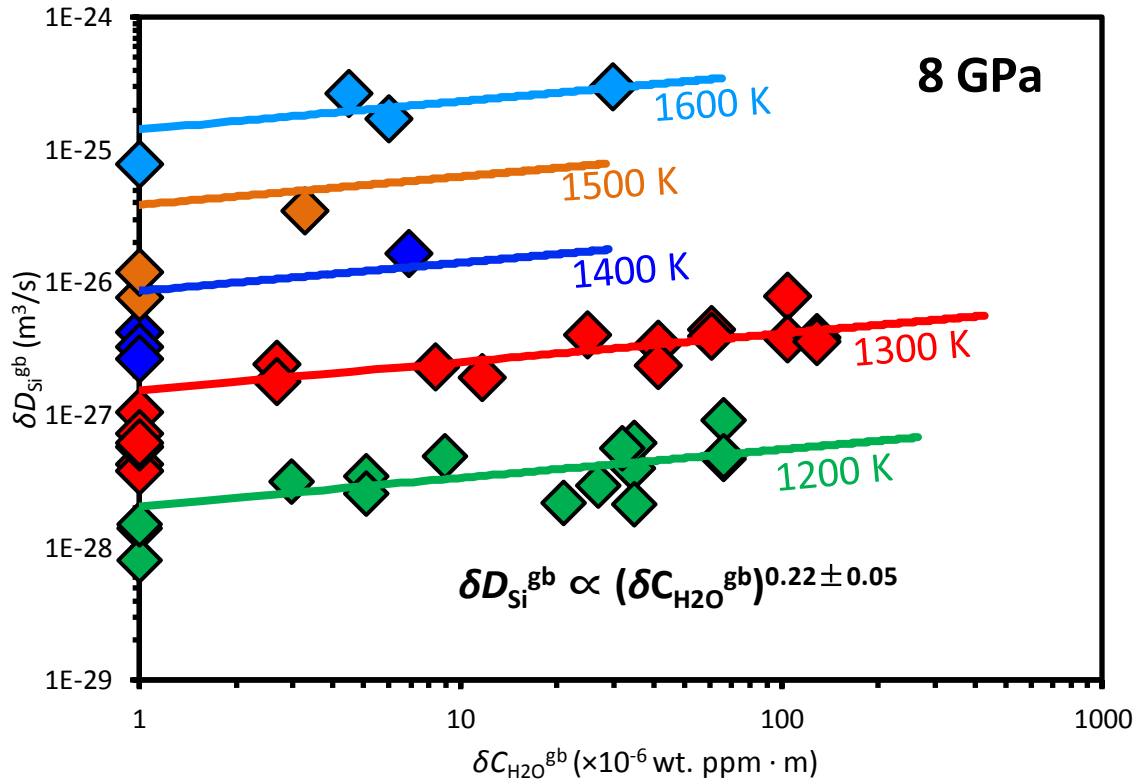
$$\delta D_{\text{Si}}^{\text{gb}} = D_0^{\text{gb,wet}} \left( \delta C_{\text{H}_2\text{O}}^{\text{gb}} \right)^{r^{\text{gb}}} \exp \left( - \frac{\Delta H^{\text{gb,wet}}}{RT} \right) \quad (5.9)$$

the pre-exponential factor ( $D_0^{\text{gb,wet}}$ ), activation enthalpy of  $\delta D_{\text{Si}}^{\text{gb}}$  under wet conditions ( $\Delta H^{\text{gb,wet}}$ ), and  $\delta C_{\text{H}_2\text{O}}^{\text{gb}}$  exponent ( $r^{\text{gb}}$ ) are determined to be  $10^{-15.1 \pm 0.4}$  m<sup>3</sup>/s,  $261 \pm 10$  kJ/mol, and  $0.22 \pm 0.05$ , respectively ( $\delta$  is the grain-boundary width,  $R$  is the ideal gas constant).

The dry condition results (the bulk water content below the detect limitation of infrared spectroscopy, i.e.,  $C_{\text{H}_2\text{O}}^{\text{bulk}} < 1$  wt. ppm,) (**Fig. 5.8b, 5.8c**) are fit to:

$$\delta D_{\text{Si}}^{\text{gb}} = D_0^{\text{gb,dry}} \exp \left( - \frac{\Delta E^{\text{gb,dry}} + P\Delta V^{\text{gb}}}{RT} \right) \quad (5.10)$$

and the activation volume ( $\Delta V^{\text{gb}}$ ) is determined to be  $1.8 \pm 0.2$  cm<sup>3</sup>/mol. The activation energy,  $\Delta E^{\text{gb,dry}}$ , is  $241 \pm 11$  kJ/mol, which is essentially the same as  $\Delta E^{\text{gb,wet}}$  ( $\Delta E^{\text{gb,wet}} = 247 \pm 12$  kJ/mol calculated from the equation  $\Delta H^{\text{gb,wet}} = \Delta E^{\text{gb,wet}} + P\Delta V^{\text{gb}}$  assuming the same activation volume between dry and wet conditions).



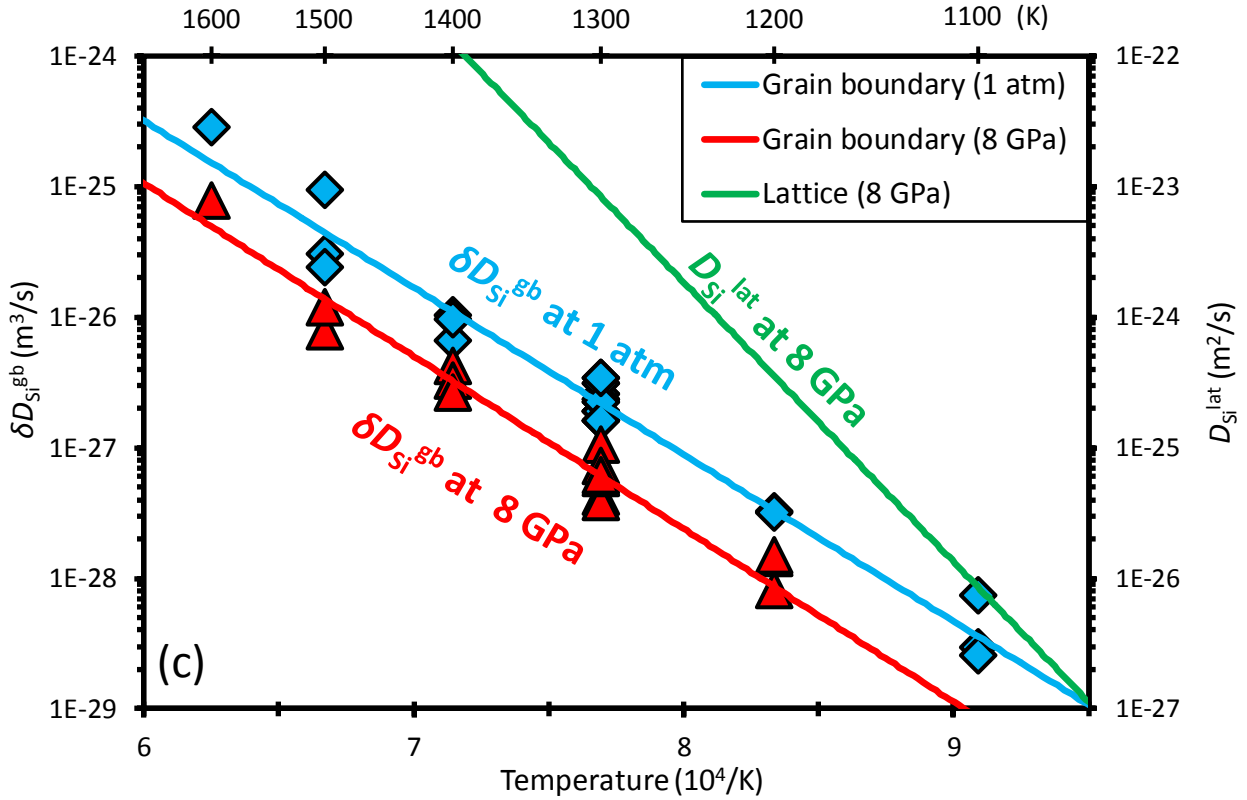


**Fig. 5.8.** Silicon grain-boundary diffusion in forsterite. (a)  $\delta D_{\text{Si}^{\text{gb}}}$  against  $\delta C_{\text{H}_2\text{O}^{\text{gb}}}$  at 8 GPa. The dry condition data points ( $\delta C_{\text{H}_2\text{O}^{\text{gb}}} < 1 \mu\text{m} \cdot \text{wt. ppm}$ ) are plotted at  $\delta C_{\text{H}_2\text{O}^{\text{gb}}} = 1 \mu\text{m} \cdot \text{wt. ppm}$ . (b)  $\delta D_{\text{Si}^{\text{gb}}}$  against pressure at 1300 K and  $C_{\text{H}_2\text{O}^{\text{bulk}}} < 1 \text{ wt. ppm}$ .  $\delta D_{\text{Si}^{\text{gb}}}$  from Faul and Jackson [2007] and Mei and Kohlstedt [2000a] are estimated from creep rate using Frost and Ashby model [Frost and Ashby, 1982]. (c)  $\delta D_{\text{Si}^{\text{gb}}}$  against temperature at 1 atm and 8 GPa with  $C_{\text{H}_2\text{O}^{\text{bulk}}} < 1 \text{ wt. ppm}$ .  $D_{\text{Si}^{\text{lat}}}$  data is taken from our previous study [Fei *et al.*, 2012].

## 5.5 Discussion

### 5.5.1 Examine the validity of results

Because of the low diffusion coefficient of silicon, the diffusion profiles are usually very short, within a few microns. Therefore, artificial results could be made by a series of error sources, for example, the edge effect from the SIMS crater, the SIMS convolution in measurement [Dohmen *et al.*, 2002] including rough surface problem [Fei *et al.*, 2012], and so on. We have examined the validity of experimental results from the following ways.

### (1) Time series

The diffusion coefficient should be independent with annealing duration [Jaoul *et al.*, 1980]. In order to examine the validity of results, we performed time-series experiments, in which the samples were annealed under the same pressure and temperature conditions but different annealing durations. The differences of  $\delta D_{\text{Si}^{\text{gb}}}$  obtained in these samples are very small, less than factor three (**Fig. 5.9**), which is within experimental uncertainty.

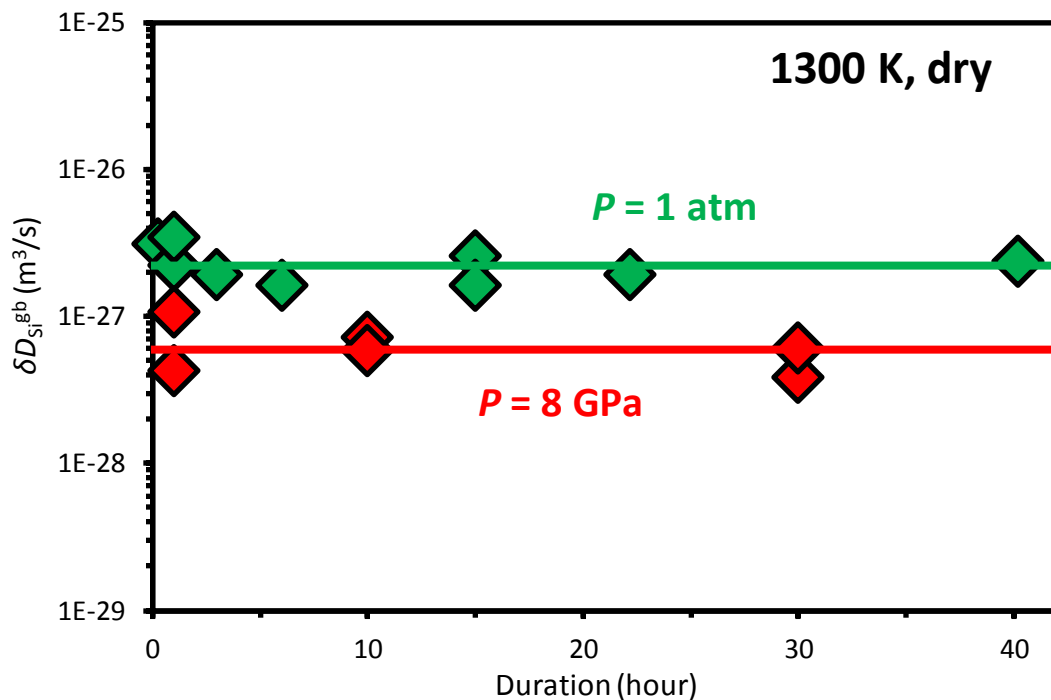


**Fig. 5.9.** Samples annealed under the same pressure, temperature, and  $\text{C}_{\text{H}_2\text{O}^{\text{gb}}}$  conditions but different durations, generating the same results of diffusion coefficient.

### (2) Comparison with Mg diffusion profile

The type-B grain boundary diffusion profiles usually have two segments, the lattice diffusion region in the shallow part of the profile, and the grain boundary region in the deeper part showing a very long tail. Such a profile is very similar as an artificial profile shape caused by edge effect from the SIMS crater. In order to examine whether the long tail in the profiles is caused by edge effect or real grain-boundary diffusion, we have also measured the magnesium, which is  $^{25}\text{Mg}$  enriched in the thin films. The comparison of silicon and magnesium profiles is shown in **Fig. 5.7a**. If the profile were an artifact caused by edge effect, Mg and Si should have

similar profiles. But it is not the case in this study because the Mg diffusion profile is much longer than that of Si as shown in **Fig. 5.7a** (The slope of Mg profile is much smaller. It is reasonable because the Mg diffuses much faster than Si in olivine [*Dohmen et al.*, 2007]).

#### (2) *Comparison with Si diffusion profile in single crystal*

The type-B grain-boundary diffusion profile measured in a polycrystalline sample usually has lattice diffusion segment (the isotopic concentration rapidly decreases) and grain boundary diffusion segment (long tail). It should be different from the diffusion profile measured in a single crystal in which only lattice diffusion occurs. We have compared the Si diffusion profiles measured in polycrystalline samples in this study with those obtained in single crystals from our previous studies [*Fei et al.*, 2012; *Fei et al.*, 2013]. As shown in **Fig. 5.7b**, the value of  $c-c_0$  in a single crystal Si diffusion profile decreases rapidly without appearing a long tail, whereas the profiles measured in polycrystalline samples (**Fig. 5.7a-c**) clearly show two segments: the lattice diffusion region in the shallow part and the grain boundary region in the deeper part because  $\delta D_{\text{Si}^{\text{gb}}}/d \gg D_{\text{Si}^{\text{lat}}}$ .

#### (4) *Grain size dependence*

For the kinetics of grain boundary diffusion, the value of bulk diffusion rate decreases with increasing grain size, but  $\delta D_{\text{Si}^{\text{gb}}}$  should be independent with grain size. In order to examine the validity of experimental results, we performed experiments on samples with two different grain-size conditions:  $\sim 0.6$  and  $\sim 2.0$   $\mu\text{m}$ . The results of  $\delta D_{\text{Si}^{\text{gb}}}$  obtained from these two sets of samples with different grain sizes show almost the same values both at ambient pressure and high pressures (**Fig. 5.10**).

Besides, the absolute value of  $c-c_0$  near the interface of thin film and substrate should be approximately proportional to  $d^{-1}$  when  $\delta \ll d$ , where  $d$  is the grain size. We find that the values of  $c-c_0$  near the interfaces for 0.6 and 2.0- $\mu\text{m}$  samples differ by factor 3-4, which is consistent with the theory that  $c-c_0 \propto d^{-1}$ . For example, as shown in **Fig. 5.7b, 5.7c**,  $\log(c-c_0)$  is  $\sim -1.8$  and  $\sim -2.3$  in 0.6 and 2.0  $\mu\text{m}$  samples, respectively.

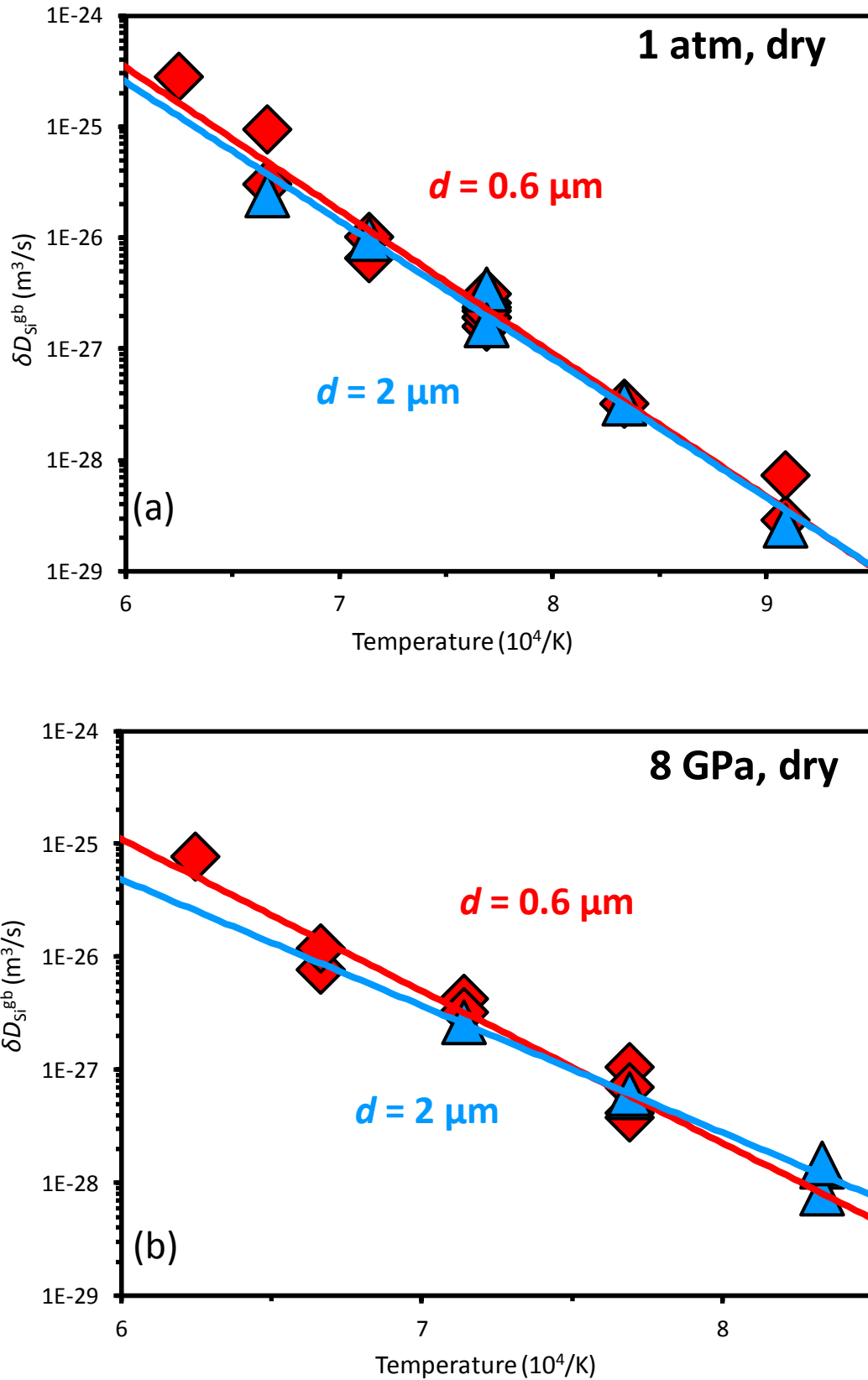


**Fig. 5.10.** Samples with different grain sizes generate the same  $\delta D_{\text{Si}}^{\text{gb}}$ . (a) at 1 atm. (b) at 8 GPa.

Additionally, the absolute value of  $c-c_0$  near the interface should be approximately proportional to the volume fraction of grain boundaries + depth of lattice diffusion from grain boundaries. Taking the sample shown in **Fig. 5.7b** as an example, the lattice diffusion depth is about 3 nm at 1300 K for 10 hours [Fei *et al.*, 2012] using  $\delta = \sim 1$  nm and  $d = 0.6$   $\mu\text{m}$ , the volume fraction of grain boundaries + lattice diffused regions is about 0.4 %. Since we have  $c-c_0 = 0.45$  in the original thin film,  $\log(c-c_0)$  should be -1.7 near the interface, which is consistent with the observation that  $\log(c-c_0) \approx -1.8$  (**Fig. 5.7b**). Also in **Fig. 5.7a**, the lattice diffusion depth is  $\sim 70$  nm at 1600 K for 4 hours, leading to a volume fraction of 40 % of grain boundaries + lattice diffused regions, which makes  $\log(c-c_0) \approx -0.8-0.9$  as shown in the figure.

### 5.5.2 $P$ , $T$ , $C_{\text{H}_2\text{O}}$ , and grain size dependences of $D_{\text{Si}^{\text{gb}}}$ , $D_{\text{Si}^{\text{lat}}}$ , and creep rates

Using the Weertman [1999] and Ashby and Frost [1982] models, the rates of Coble creep, Nabarro-Herring creep, and dislocation creep can be calculated from  $D_{\text{Si}^{\text{gb}}}$  determined in this study and  $D_{\text{Si}^{\text{lat}}}$  from our previous studies [Fei *et al.*, 2012; Fei *et al.*, 2013]. The mechanism which gives the fastest creep rate is the dominant mechanism shown in **Fig. 5.11** at given conditions (i.e.,  $P$ ,  $T$ , stress, grain size, and  $C_{\text{H}_2\text{O}}^{\text{bulk}}$ ).

The absolute value of  $D_{\text{Si}^{\text{gb}}}$  is much smaller than that obtained in previous studies (**Fig. 5.8b**). Therefore, diffusion creep should be much less dominant in olivine deformation than considered before. The activation energy for  $D_{\text{Si}^{\text{gb}}}$  is much lower than that for  $D_{\text{Si}^{\text{lat}}}$  ( $\Delta E^{\text{lat}} = \sim 410-420$  kJ/mol [Fei *et al.*, 2012; Fei *et al.*, 2013]) (**Fig. 5.8c**). Hence, Coble diffusion creep should be dominant at low temperature (**Fig. 5.11**) corresponding to shallow region of Earth's mantle. This is an opposite idea from the previous understandings [Hirth and Kohlstedt, 2003; Karato, 1992; Karato and Wu, 1993]. The activation volume for  $D_{\text{Si}^{\text{gb}}}$  is nearly the same as that for  $D_{\text{Si}^{\text{lat}}}$  ( $1.7 \pm 0.4$  cm<sup>3</sup>/mol [Fei *et al.*, 2012]), which means pressure effects on different creep mechanisms are the same and almost negligible. Therefore, pressure does not change a dominant creep mechanism. Besides, although we found a very small  $C_{\text{H}_2\text{O}}^{\text{lat}}$  exponent ( $r^{\text{lat}} = 0.32 \pm 0.07$ ) for  $D_{\text{Si}^{\text{lat}}}$  [Fei *et al.*, 2013], the  $r^{\text{gb}}$  for  $D_{\text{Si}^{\text{gb}}}$  is found to be even smaller ( $r^{\text{gb}} = 0.22 \pm 0.05$ ). Thus, the role of water on olivine creep rate is insignificant.

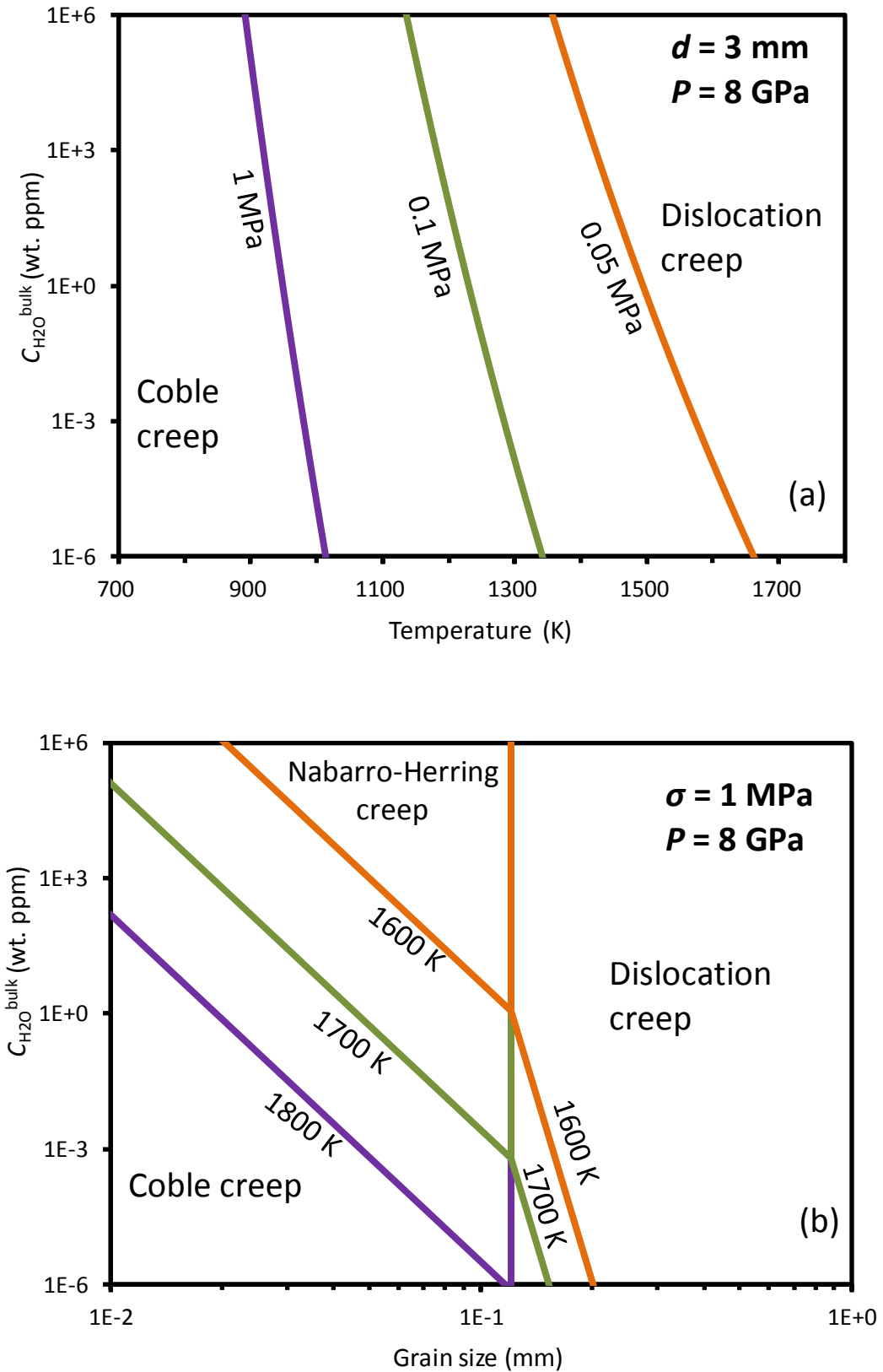


**Fig. 5.11.** Deformation-mechanism maps at 8 GPa calculated from  $D_{\text{Si}^{\text{gb}}}$  and  $D_{\text{Si}^{\text{lat}}}$  using Frost & Ashby [1982] and Weertman [1999] models. The dislocation creep, Coble creep, and Nabarro-Herring creep rates are calculated as functions of temperature, water content, grain size, stress,

pressure, and the one which gives the fastest creep rate at a given pressure, temperature, stress, water content, and grain size condition is the dominant deformation mechanism. (a)  $C_{\text{H}_2\text{O}}^{\text{bulk}}$  and temperature dependences at different stress. (b)  $C_{\text{H}_2\text{O}}^{\text{bulk}}$  and grain size dependences at different temperature. The labeled lines indicate the boundary conditions between different mechanisms.  $\sigma$ : stress.  $d$ : grain size.

In addition, diffusion creep (both Coble and Nabarro-Herring) has negative grain size dependences [Frost and Ashby, 1982], whereas dislocation creep rate is independent with grain size [Weertman, 1999]. As a result, diffusion and dislocation creep dominate deformation of olivine with small and large grain size, respectively.

Hansen et al. [2011] also introduced a grain-boundary-sliding mechanism near the diffusion and dislocation transition boundary. We note that their experimental results could also be explained by a combination of diffusion creep and dislocation creep. Therefore, we simplified the deformation mechanism by diffusion creep and dislocation creep here.

### 5.5.3 Defect chemistry

The  $C_{\text{H}_2\text{O}}^{\text{lat}}$  and  $C_{\text{H}_2\text{O}}^{\text{gb}}$  exponents for  $D_{\text{Si}}^{\text{lat}}$  and  $D_{\text{Si}}^{\text{gb}}$ , respectively, can be understood on the basis of defect chemistry because the diffusion coefficient of ion is proportional to the concentration of the corresponding defect [Kohlstedt, 2006]. The Kröger-Vink [Kröger and Vink, 1956] notation (see **Appendix I**) is used for point defects here, e.g.,  $V_{\text{Si}}^{''''}$  indicates four effective negative charges for a vacancy in the silicon site, whereas  $(\text{OH})_{\text{O}}^{\bullet}$  indicates an  $\text{H}^+$ -associated O in the O site with an effective charge of +1. Square brackets [-] denote concentration of the corresponding units.

For lattice diffusion, we have proposed a  $(V_{\text{Si}}^{''''}-V_{\text{O}}^{\bullet})$ -dominated  $D_{\text{Si}}^{\text{lat}}$  model in which  $D_{\text{Si}}^{\text{lat}}$  is proportional to both  $[V_{\text{Si}}^{''''}]$  and  $[V_{\text{O}}^{\bullet}]$  because silicon ions are surrounded by oxygen in tetrahedrons and therefore a missing of oxygen ion would largely enhance the hopping probability of  $V_{\text{Si}}^{''''}$ . As a result, we have  $D_{\text{Si}}^{\text{lat}} \propto [V_{\text{Si}}^{''''}] \times [V_{\text{O}}^{\bullet}] \propto (C_{\text{H}_2\text{O}}^{\text{lat}})^{1/3}$  [Fei et al., 2013] calculated from the dependences of point defect concentrations on water fugacity [Kohlstedt, 2006]. However, such a model does not work for  $D_{\text{Si}}^{\text{gb}}$ . The crystal lattices in the grain interior are almost perfect and their defects concentrations should be largely increased by the

incorporation of water and sequentially the grain-interior diffusion coefficients rate be increased, whereas the structure on the grain boundaries are already highly (not completely) distorted without water incorporation and the distortion of structure by water incorporation should be relatively small. Therefore, the  $C_{H_2O}^{gb}$  exponent for  $D_{Si}^{gb}$  should be smaller than that for  $D_{Si}^{lat}$  ( $0.32 \pm 0.07$ ), but larger than zero, as a value of  $0.22 \pm 0.05$  is determined in this study.

#### 5.5.4 Comparison with previous diffusion and deformation studies

##### (1) Diffusion creep

The diffusion creep rates (including Coble diffusion creep and Nabarro-Herring diffusion creep) versus water content calculated from  $\delta D_{Si}^{gb}$  and  $D_{Si}^{lat}$  are shown in **Fig. 5.12**. The diffusion creep rate estimated from silicon diffusion coefficients in this study is about three orders of magnitude lower than those from olivine deformation experiments by Mei and Kohlstedt [2000a] and forsterite diffusion experiments by Farver and Yund [2000], but consistent with those from deformation experiments in olivine by Faul and Jackson [2007] and in pure forsterite by Tasaka et al. [2013]. Faul and Jackson [2007] attributed this discrepancy to the effect of very small amounts of partial melt. However, the melt fraction in Mei and Kohlstedt [2000a] is very low ( $< 1\%$ ). Even 3% partial melt enhances the creep rate only by less than a factor of two [Hirth and Kohlstedt, 1995; Mei et al., 2002]. Besides, Farver and Yund's [2000] samples were also melt-free.

The reason for the discrepancy between ref. [Farver and Yund, 2000; Mei and Kohlstedt, 2000a] and ref. [Faul and Jackson, 2007; Tasaka et al., 2013], and this study is still unclear. One possible explanation for this discrepancy is that the starting material used in this study, as well as that in Faul and Jackson [2007]'s experiments were well sintered with almost no visible or very small pores within the grains or between grain boundaries (**Fig. 5.1** in this study, and in Faul and Jackson [2007]), in contrast, significantly large pores existed in the samples in Mei and Kohlstedt [2000a; 2002], which could largely weaken the olivine aggregates and therefore enhance the creep rates.

(2) *Dislocation creep*

The comparison of dislocation creep against water content is shown in **Fig. 5.13**. The dislocation creep rate calculated from  $D_{Si}^{lat}$  is consistent with that measured by Raterron et al. [2009; 2011] in single crystal deformation experiments, but much lower than that measured in polycrystalline samples [Jung and Karato, 2001; Karato et al., 1986; Mei and Kohlstedt, 2000b]. Our previous study [Fei et al., 2013] already demonstrated that the dislocation creep rates in those polycrystalline olivine deformation studies have been overestimated due to free water on grain boundaries.

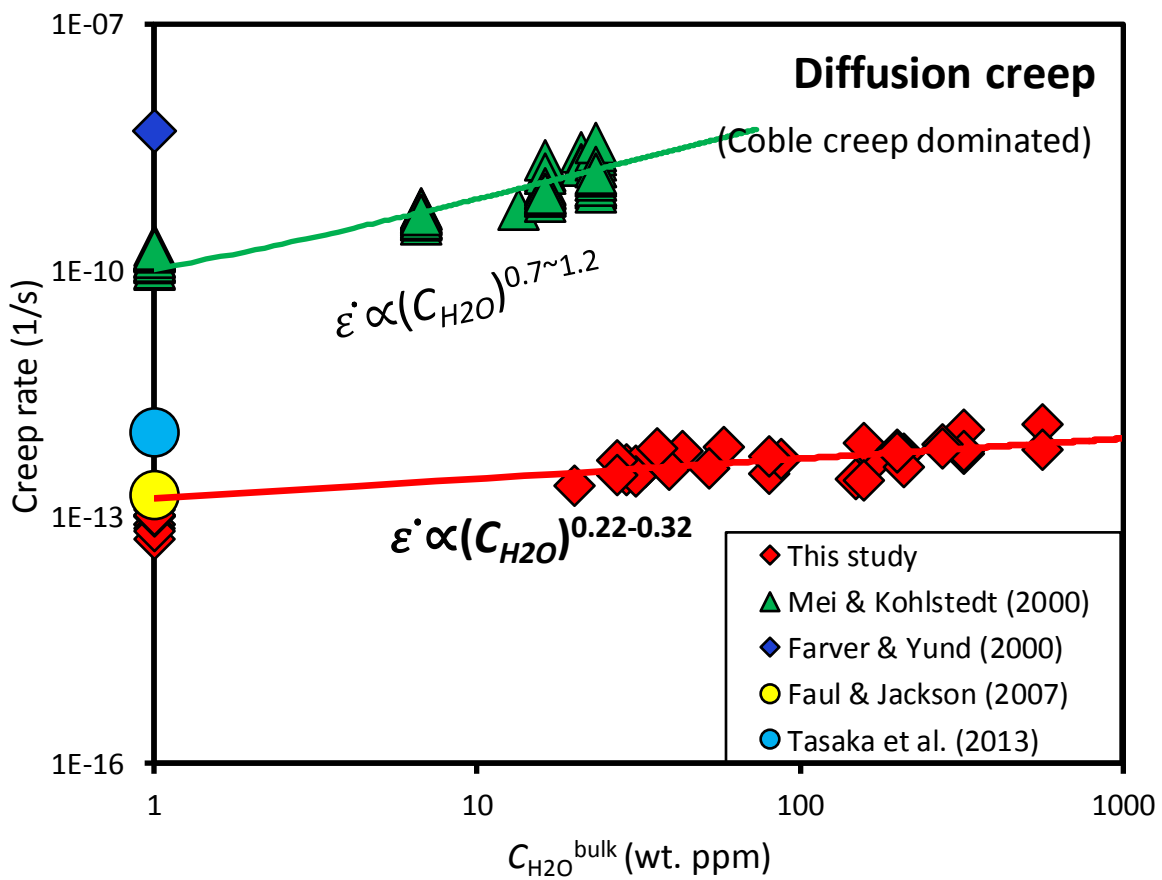


**Fig. 5.12.** A comparison of diffusion creep (Coble and Nabarro-Herring) rates at 8 GPa, 1300 K, stress of 1 MPa, and grain size of 10  $\mu\text{m}$  estimated from  $D_{Si}^{gb}$  with those measured in deformation experiments. All data are corrected to the same pressure, temperature, grain size, and stress conditions using the parameters they reported. Data points from dry conditions experiments are plotted at  $C_{H_2O}^{bulk} = 1$  wt. ppm.

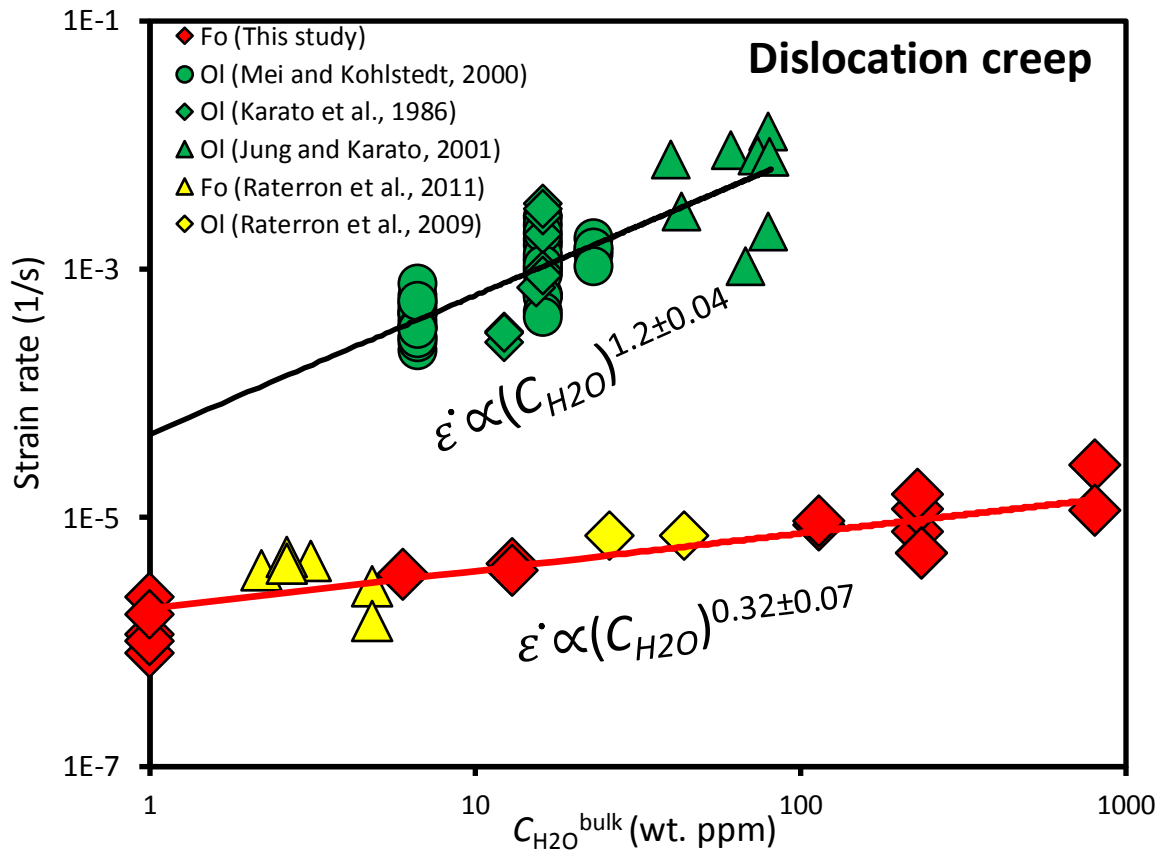


**Fig. 5.13.** A comparison of dislocation creep rates estimated from  $D_{\text{Si}^{\text{lat}}}$  with those measured in deformation experiments corrected to 8 GPa, 1600 K, and stress of 300 MPa using the parameters they reported. Data points from dry conditions experiments are plotted at  $C_{\text{H}_2\text{O}}^{\text{bulk}} = 1$  wt. ppm. This figure is modified from Fei et al. [2013]. Fo: iron-free forsterite. Ol: iron-bearing olivine.

### (3) Iron content effect

Natural olivine in Earth's upper mantle contains about 10 % of  $\text{Fe}_2\text{SiO}_4$  component and an iron content correction is necessary to imply the present results obtained in iron-free forsterite to Earth's interior.

As mentioned above, Faul and Jackson [2007] measured diffusion creep rate in dry  $(\text{Mg}_{0.9}\text{Fe}_{0.1})_2\text{SiO}_4$  olivine, with a result almost the same as that induced from silicon diffusion coefficients in pure forsterite determined in this study after a correction to the same condition (**Fig. 5.12**). Raterron et al. [2009; 2011] measured the dislocation creep rates in both natural olivine and pure forsterite, which also showed consistent values with those induced from silicon

diffusion coefficients in forsterite (**Fig. 5.13**). Therefore, we conclude that the effect of iron on olivine rheology is almost negligible.

Though the  $D_{Si^{lat}}$  measured in natural olivine [Costa and Chakraborty, 2008] is slightly higher than that in pure forsterite [Fei et al., 2013] by factor 3-4 (**Fig. 3.3**), we note that a chemical polishing after diffusion and a roughness correction was applied in Fei et al. [2013] whereas it was not in Costa and Chakraborty [2008]. If a similar treatment were applied to the natural olivine data points, the difference of  $D_{Si^{lat}}$  between natural olivine [Costa and Chakraborty, 2008] and pure forsterite [Fei et al., 2013] would be very small.

### 5.5.5 Stress and strain rate in the upper mantle

The velocity of plate motion is several centimeters per year. Using a value of 5 cm/year [e.g. Pacific plate [Sella et al., 2002]]. Taking a value of 5 cm/year (for most plates), the velocity of plate motion,  $V_{plate}$ , is  $\sim 1.6 \times 10^{-9}$  m/s. Thus, the velocity of flow at the top of asthenosphere ( $\sim 70$ -km depth in oceanic asthenosphere) is assumed to be  $1.6 \times 10^{-9}$  m/s here. Here we use two models to estimate the stress and strain rate in the asthenosphere: (a) assume a constant strain rate, (b) assume a constant stress.

#### (1) Constant strain rate model

We assume a constant strain rate in the asthenosphere from 70 to 410 or 660 km depth. Therefore, the total strain rate,

$$\dot{\epsilon}(total) = \dot{\epsilon}_{dis}(\sigma, x) + \dot{\epsilon}_{Co}(\sigma, x) + \dot{\epsilon}_{NH}(\sigma, x) = V_{plate}/x \quad (5.11)$$

where  $x$  is depth, i.e., from 70 to 410 or 660 km, and the total creep rate,  $\dot{\epsilon}$  (total), is a constant. Using **Eqs. 5.6-5.8**, the stress is calculated as a function of depth, and each component of creep rate also calculated shown in **Fig. 5.14a** ( $x = 410$  km) and **Fig. 5.14b** ( $x = 660$  km).

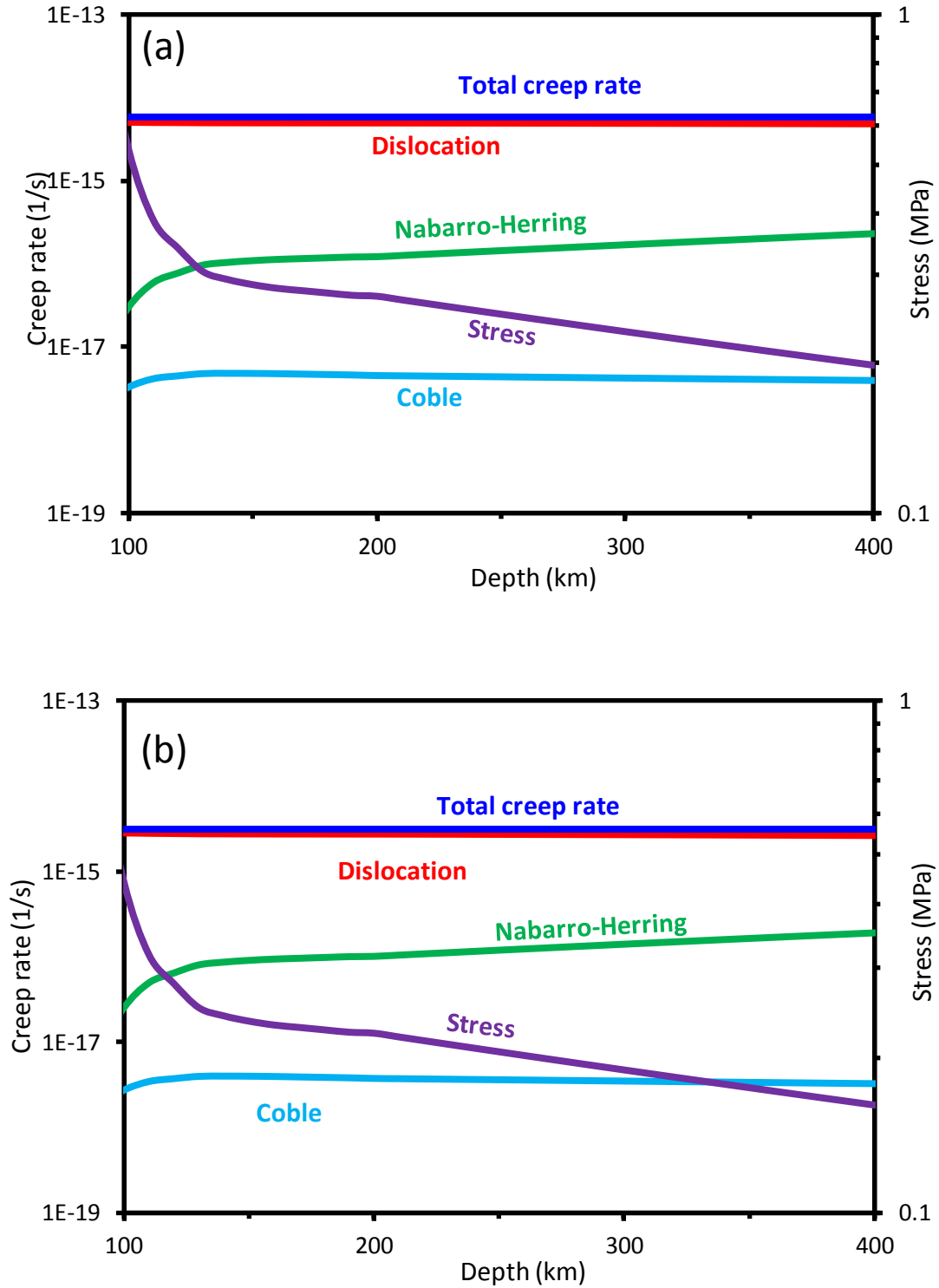


**Fig. 5.14.** Estimated stress and creep rate in upper mantle as a function of depth using the constant strain rate model. **(a).** Constant total creep rate from 70 to 410 km depth. **(b).** Constant total creep rate from 70 to 660 km depth. The  $C_{\text{H}_2\text{O}^{\text{bulk}}}$  and grain size for the calculations are assumed to be 100 wt. ppm and 3 mm, respectively. The temperature data is from oceanic

geotherm [Turcotte and Schubert, 2002]. The stress and strain rate calculated using these two models show very small difference (within factor two).

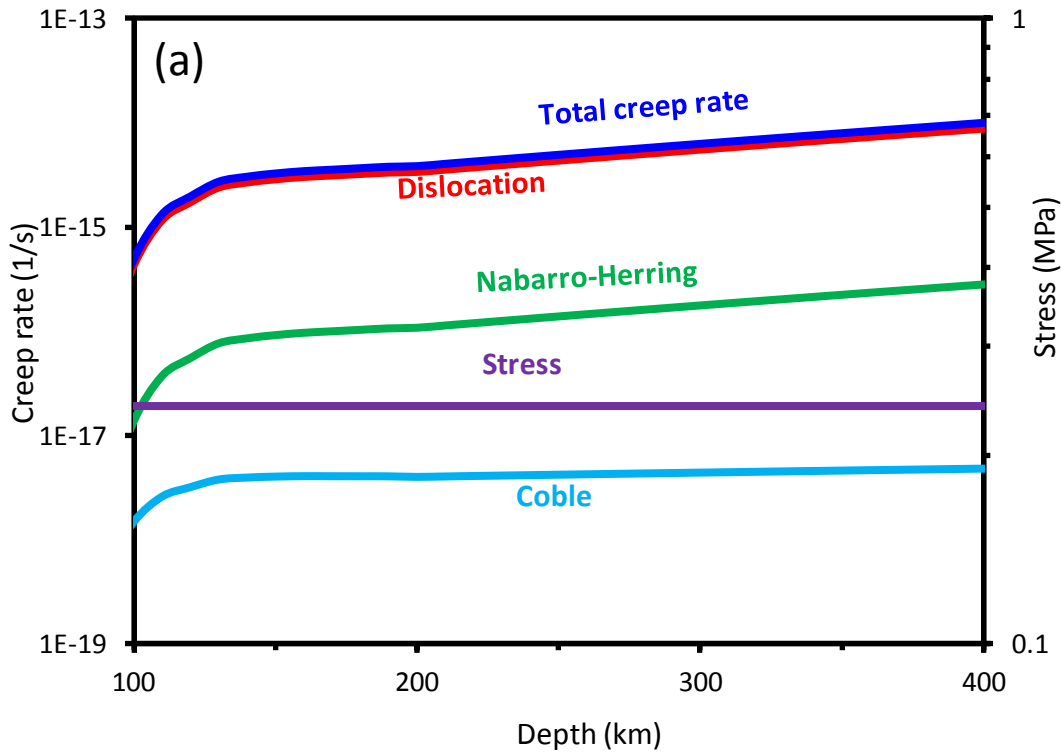
(2) *Constant stress model*

In the constant-stress model, we assume a constant stress value in the upper mantle and the flow velocity is zero at 410 or 660 km depth. Therefore, the flow velocity at the top of asthenosphere is an integration of total creep rate with depth  $x$ ,

$$\int \dot{\epsilon}(\text{total})dx = \int \dot{\epsilon}_{dis}(\sigma, x) + \dot{\epsilon}_{Co}(\sigma, x) + \dot{\epsilon}_{NH}(\sigma, x)dx = V_{plate} \quad (5.12)$$

Using **Eqs. 5.6-5.8**, the stress is  $\sim 0.25$  MPa to generate a  $V_{plate}$  of  $\sim 1.6 \times 10^{-9}$  m/s in **Eqs. 5.12** if integrating to 410-km depth (**Fig. 5.15a**), and  $\sim 0.15$  MPa if integrating to 660-km depth (**Fig. 5.15b**), and the creep rate of each component is calculated as a function of depth.

The stress estimated from constant strain rate model is  $\sim 0.1-0.4$  MPa, and that from constant stress model is  $\sim 0.15-0.25$  MPa. Therefore, the differences of stresses and strain rates estimated by different models are very small (**Fig. 5.14, 5.15**).



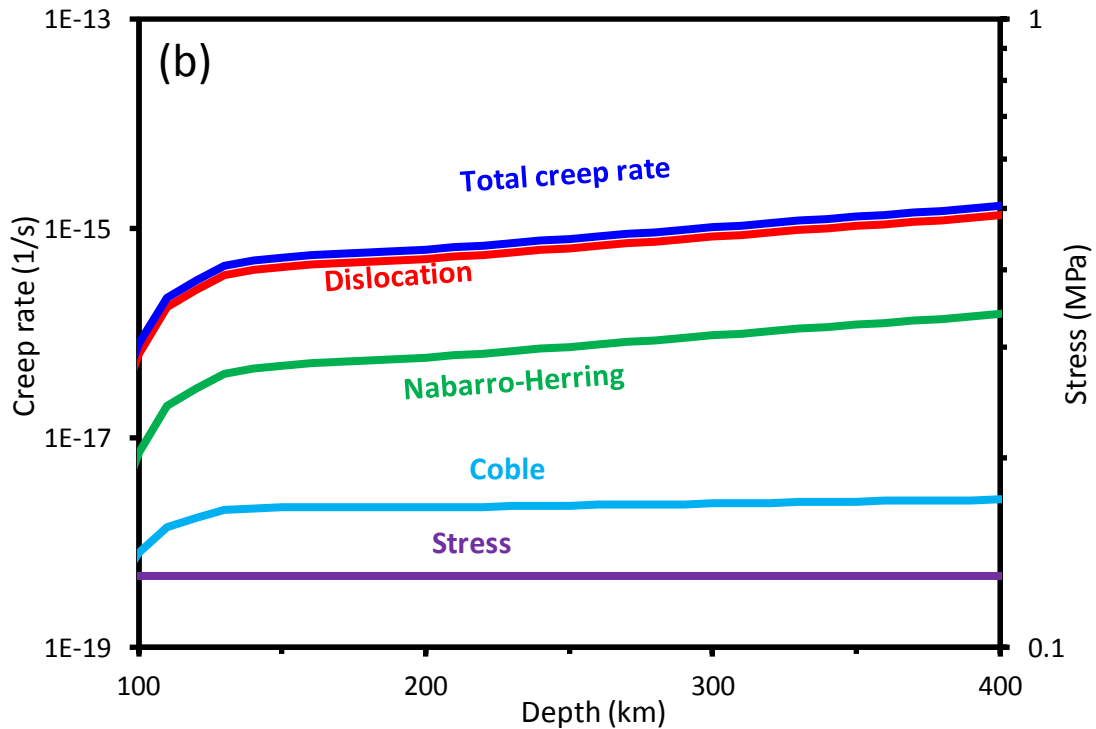


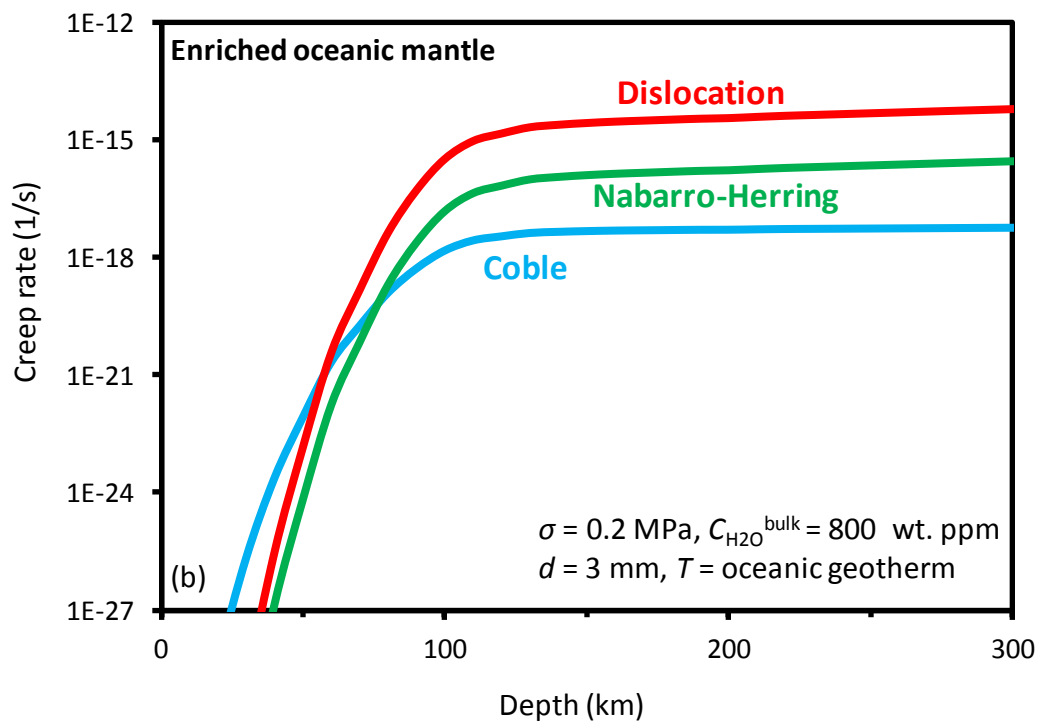
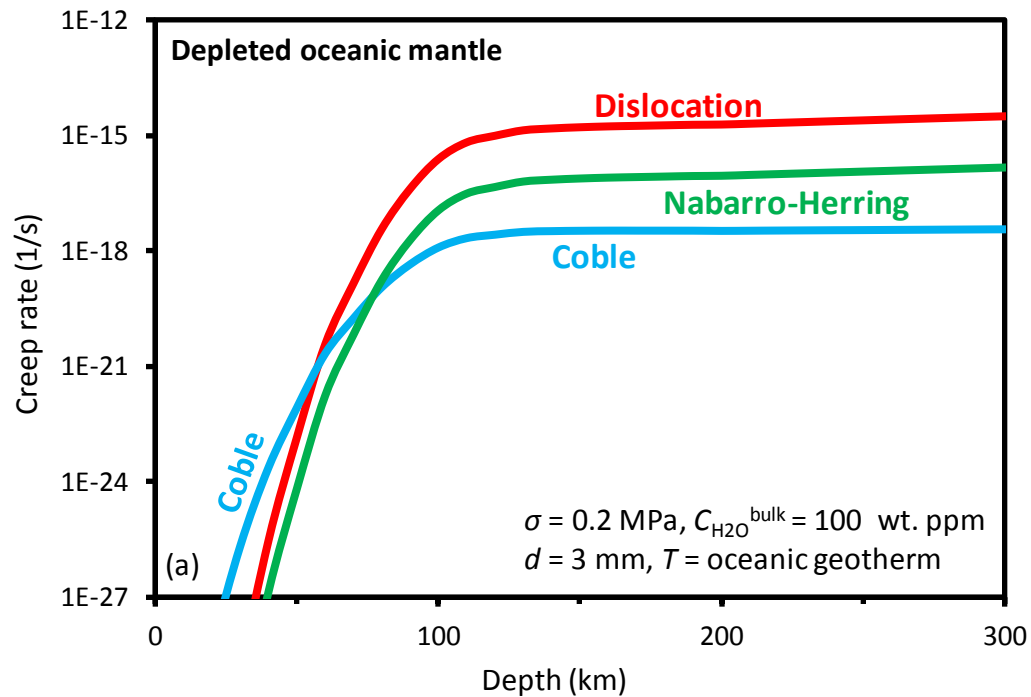
**Fig. 5.15.** Estimated stress and creep rate in upper mantle as a function of depth using the constant stress model. (a). Constant stress with flow velocity = 0 m/s at 410-km depth. (b). Constant stress with flow velocity = 0 m/s at 660-km depth. The  $C_{H_2O}^{bulk}$  and grain size for the calculations are assumed to be 100 wt. ppm and 3 mm, respectively. The temperature data is from oceanic geotherm [Turcotte and Schubert, 2002]. The stress and strain rate calculated using these two models show very small difference (within factor two).

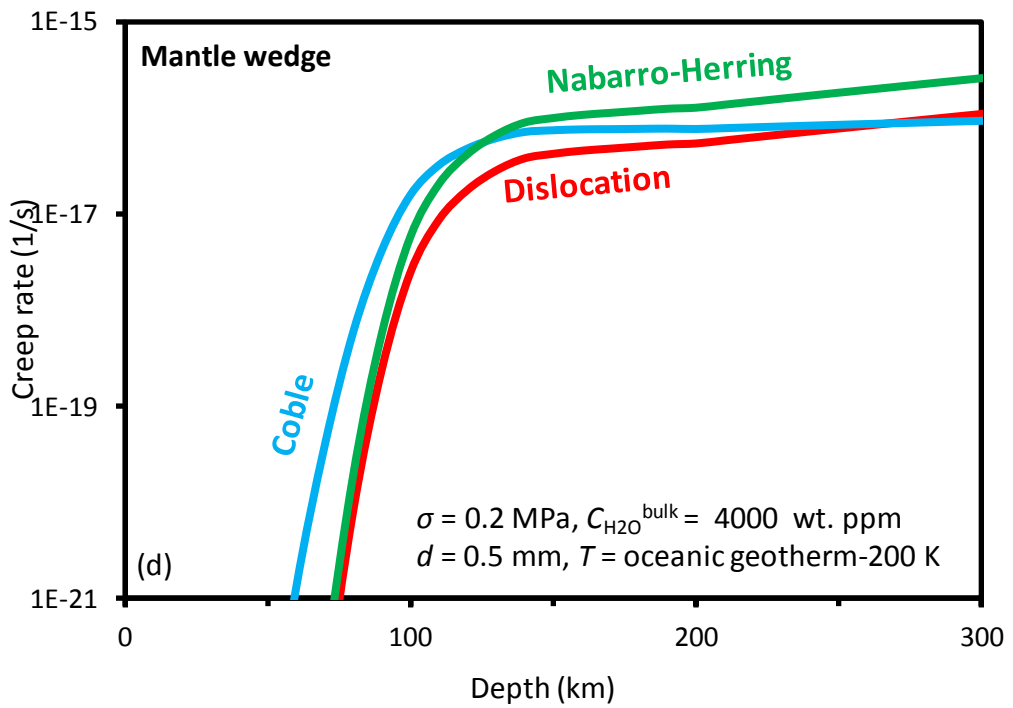
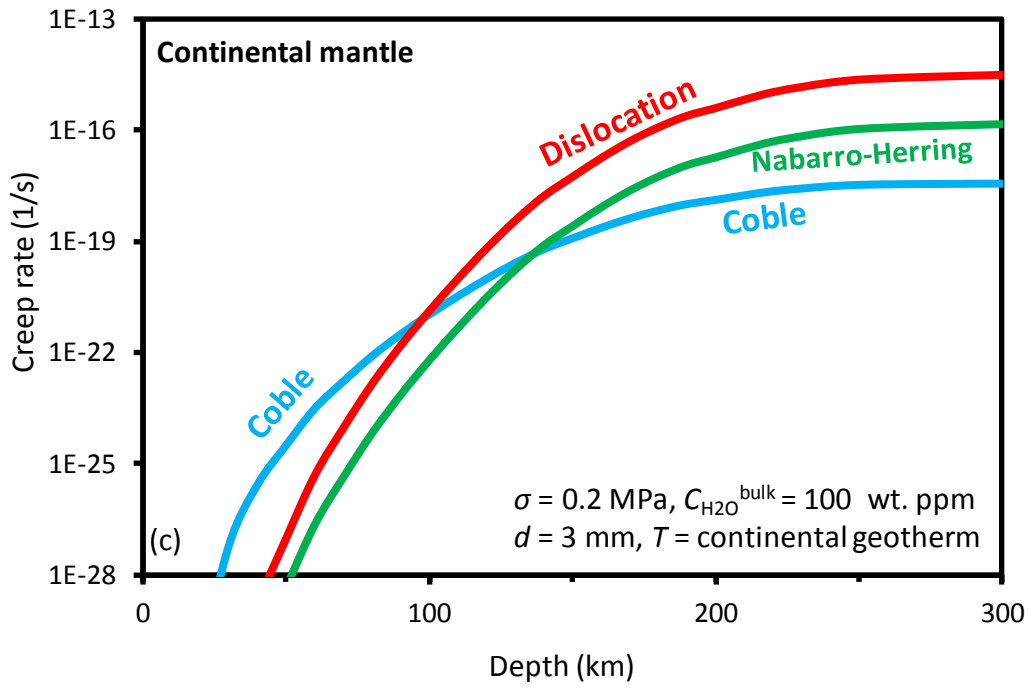
### 5.5.6 Deformation mechanisms in Earth's upper mantle

As discussed above, the stress and strain-rate in the asthenosphere are estimated to be  $\sim 10^{-14}$ - $10^{-15}$  s<sup>-1</sup> and 0.1-0.3 MPa, respectively, from the velocity of plate motion. Based on this assumption, the Coble creep, Nabarro-Herring creep, and dislocation creep rate components in the upper mantle are calculated as a function of depth (**Fig. 5.16**).

The bulk water content ( $C_{H_2O}^{bulk}$ ) in most parts of the Earth's asthenosphere is about  $\sim 10^2$ - $10^3$  wt. ppm [Hirschmann, 2006; Workman and Hart, 2005], and temperatures about 1500-1800 K [Turcotte and Schubert, 2002]. By assuming a grain size of  $\sim 3$  mm (1-5 mm in the upper-most of asthenosphere [Faul and Jackson, 2005]), the dislocation creep rate is at least one order of

magnitude higher than diffusion creep rate in both continental and oceanic asthenosphere (**Fig. 5.16a-c**). Besides, the grain size in the upper mantle is believed to increase with increasing depth [*Faul and Jackson, 2005; Karato, 1984*], which would further reduce the diffusion creep contribution. Thus, dislocation creep dominates olivine deformation in the entire asthenosphere.





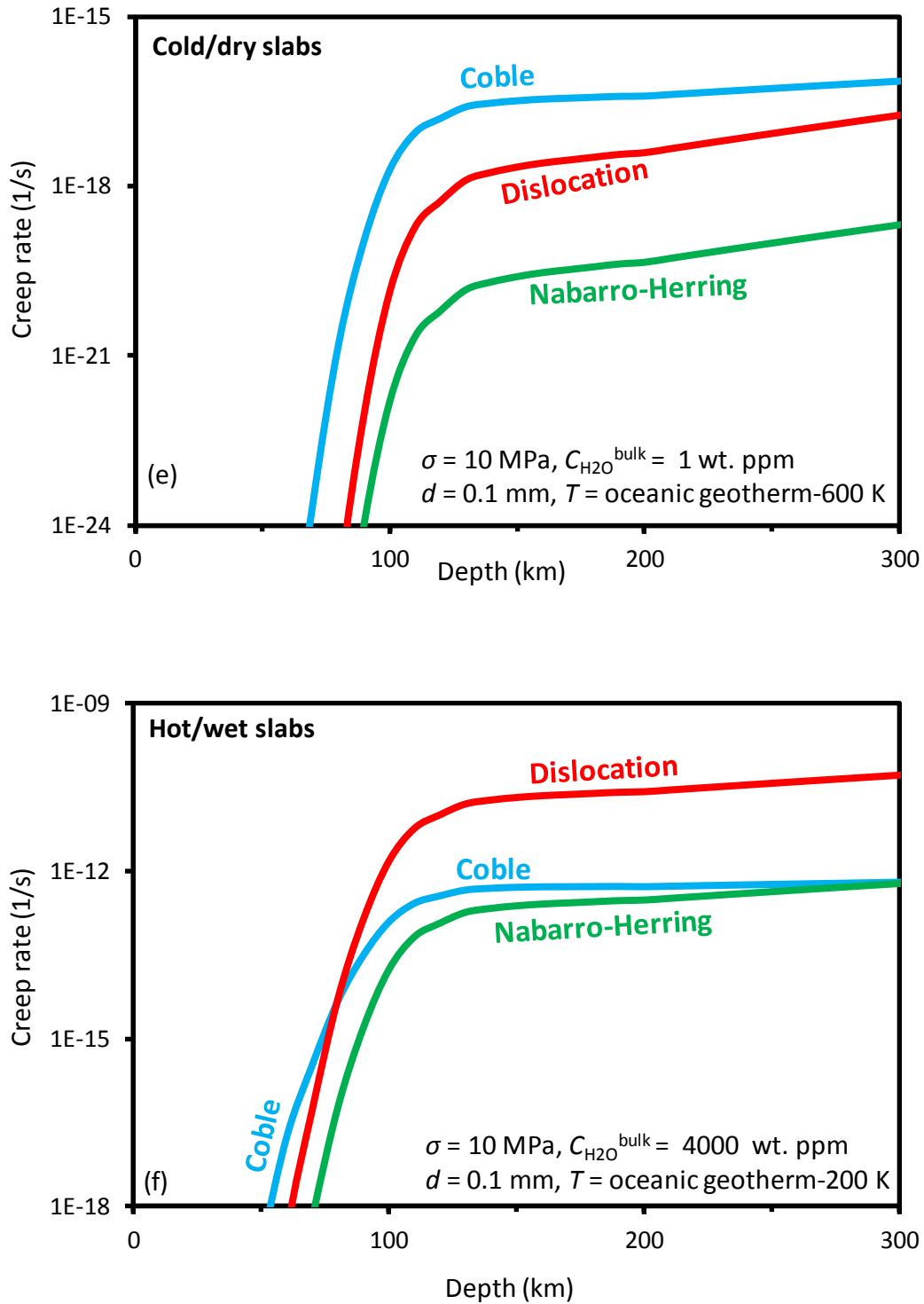


**Fig. 5.16.** Rates of Coble creep, Nabarro-Herring creep, and dislocation creep under various conditions changing with depth. (a) Depleted oceanic mantle. (b) Enriched mantle. (c) Continental mantle. (d) Mantle wedge. (e) Cold/dry subducting slab. (f) Hot/wet subducting slab. The oceanic and continental geotherm is taken from Turcotte and Schubert [2002].  $\sigma$ : stress.  $d$ : grain size.

Temperatures in both oceanic and continental lithospheres are much lower than those in asthenosphere. As a result, the Coble creep rate, which has smaller activation enthalpy than Nabarro-Herring and dislocation creeps should dominate, especially in the shallow region of continental lithosphere. We have found that a mechanism transition from Coble diffusion creep to dislocation creep should occur at ~100-150 km depth in the mid-continental lithosphere, and at ~50-70 km depth in the oceanic mantle near the lithosphere-asthenosphere boundary (**Fig. 5.16a, c**).

In mantle wedge, the  $C_{\text{H}_2\text{O}}^{\text{bulk}}$  will be very high [i.e., 0.4-1.0 % [Iwamori and Nakakuki, 2013]], the grain size is small (i.e.,  $10^{-2}$ - $10^0$  mm [Wada *et al.*, 2011]), and the temperature is cooled down due to the subducted slabs. If we consider a  $C_{\text{H}_2\text{O}}^{\text{bulk}} = 4000$  wt. ppm, a grain size of 0.5 mm, and 200 K lower than oceanic geotherm [Kelemen *et al.*, 2003], the Nabarro-Herring diffusion creep rate is about 0.5-1.5 orders of magnitude higher than dislocation creep rate (**Fig. 5.16d**). With lower temperature close to the subducting slab, the diffusion creep contribution should be even higher because of the contribution of Coble creep. Thus, the plastic deformation in mantle wedge should be controlled by diffusion creep.

In the subducting slab, if we assume a stress of 10 MPa and grain size of 0.1 mm, the Coble diffusion creep and dislocation creep could dominate the deformation mechanism in the cold/dry (e.g., Alaska Japan) and hot/wet slab (e.g., Southwest Japan), respectively (**Fig. 5.16e and 5.16f**).

As a summary, the plastic deformation in both depleted mantle and enriched mantle is dominated by dislocation creep. Coble diffusion creep could only dominate in the regions with low temperature (e.g., oceanic and topmost of continental lithosphere) or low  $C_{\text{H}_2\text{O}}^{\text{bulk}}$  and small grain size conditions (e.g., dry/cold subducting slab). Nabarro-Herring creep could be the dominant mechanism in mantle wedge with high  $C_{\text{H}_2\text{O}}^{\text{bulk}}$  and small grain size (**Fig. 5.17**).

Note that the above discussion is based on the silicon diffusion measured in a single phase. On the other hand, the Earth's upper mantle contains ~40 % of OPX and CPX, which may affect the rheological properties of olivine because the diffusion creep in a polyphase system might be controlled by the interaction between phases and therefore rate-limited by Mg or O diffusion [Sundberg and Cooper, 2008; Wheeler, 1992]. Recent study [Tasaka *et al.*, 2013] found that the strength of forsterite+enstatite aggregates decreases with increasing enstatite volume fraction ( $f_{\text{En}}$ )

for samples with  $0 < f_{En} < 0.5$  and increases with increasing  $f_{En}$  for samples with  $0.5 < f_{En} < 1$ . Based on their results, the strength of aggregates with 60 % of forsterite and 40 % of enstatite ( $f_{En} = 0.4$ ) is about one order of magnitude lower than that of pure forsterite in the diffusion creep regime. However, based on our results, the dislocation creep in the asthenosphere is more than two orders of magnitude faster than diffusion creep in both continental and oceanic mantles (**Fig. 5.16a, 5.16c**). Even when the effects from the second phase, the dislocation creep is still the dominant deformation mechanism in the asthenosphere, and the transition depth from Coble diffusion creep to dislocation creep becomes slightly deeper.

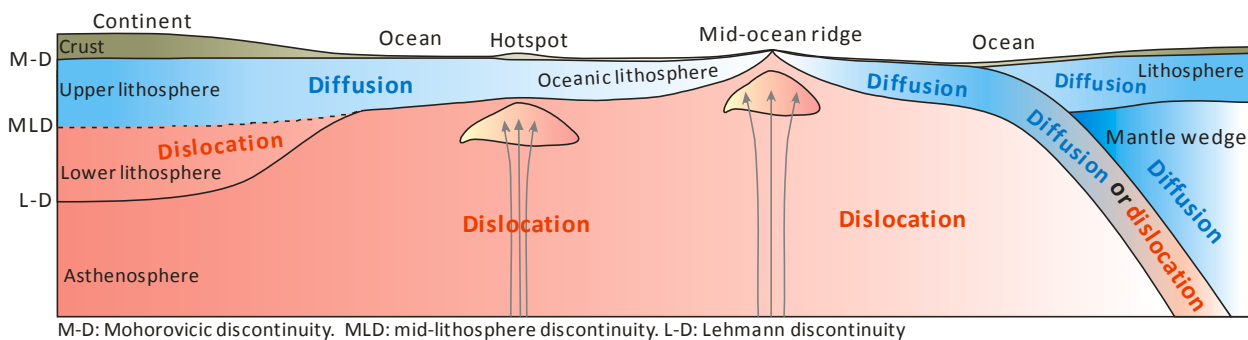


**Fig. 5.17.** Deformation mechanisms in Earth’s upper mantle. “Diffusion” indicates a region where diffusion creep dominates and “dislocation” indicates where dislocation creep dominates.

### 5.5.7 Geophysical implications

Previously, a creep-mechanism transition at ~220-km depth from dislocation creep in the shallow regions of upper mantle to diffusion creep in the deeper regions has been proposed [Hirth and Kohlstedt, 2003; Karato, 1992; Karato and Wu, 1993] based on deformation experimental studies on olivine. However, as suggested by Fei et al. [2013a; 2013b], the reported creep rates by deformation experiments are problematic. Our results demonstrate that such a creep-mechanism transition should not exist in the asthenosphere. Instead, we find a transition from Coble diffusion creep in the shallow cold lithosphere to dislocation creep in the deeper and hotter regions at 100-150 km depth near the mid-continental lithosphere beneath continents and at 50-70 km depth near the lithosphere-asthenosphere boundary (Gutenberg seismic discontinuity) beneath oceans (**Fig. 5.16a-c, Fig. 5.17**). This is consistent with the seismic anisotropy jumps observed at corresponding depths [Fischer et al., 2010; Gung et al., 2003; Nettles and Dziewonski, 2008; Snyder and Bruneton, 2007]. Besides, anisotropy beneath hotspots is stronger than their surrounding regions [Montagner and Guillot, 2000]. Furthermore,

the microstructures of olivine from shallow regions show weaker LPO than those from the base of lithosphere [Vauchez *et al.*, 2005], all of which support our idea. Though seismic anisotropy is also observed in the cold lithospheres, it could be interpreted as a fossil anisotropy formed at spreading ridges [Savage, 1999], which is weakened with time by diffusion creep and thus old lithosphere has weaker anisotropy than younger lithosphere as observed [Fischer *et al.*, 2010; Nettles and Dziewonski, 2008].

The Lehmann seismic discontinuity was once attributed to the dislocation-diffusion creep transition at 220-km depth [Karato, 1992]. However, our results suggest this is incorrect. The 220-km discontinuity should be caused by other mechanisms, e.g., a transition from weak-anisotropic lithosphere to anisotropic asthenosphere due to the temperature contrast and the Lehmann discontinuity may be associated with the lithosphere-asthenosphere boundary beneath continents [Gung *et al.*, 2003].

The origin of the seismic discontinuity at ~100-150 km depth beneath continents named mid-lithosphere discontinuity has not been well understood previously [Karato, 2012]. From our results, we find a creep mechanism transition at this depth beneath continents and the mid-lithosphere discontinuity could be attributed to this transition.

Besides, a diffusion creep dominated Newtonian rheology in the asthenosphere has been supposed by the linear postglacial rebound induced from relative sea levels (*RSL*) in continents [Karato and Wu, 1993; Wu, 1995]. However, this is not strictly true because a non-linear (power law) mantle could also fit the observed *RSL* data to some degree [Wu, 2001]. Our results suggested that asthenosphere should be non-linear dislocation creep dominated. In contrast, a diffusion creep dominated continental lithosphere at shallow region due to its low temperature as discussed above is found. Thus, the linear postglacial rebound should be attributed to the linear continental lithosphere in shallow regions, but not the previously considered Newtonian rheology in the asthenosphere. Recent study on glacial isostatic adjustment in Iceland supposed a non-linear rheology [Schmidt *et al.*, 2012] which strongly supports our idea because the geotherm beneath Iceland is much higher than that in continents and thus diffusion creep should be less dominant (**Fig. 5.16a, 5.16c**).

Seismic studies reported an anisotropic mantle wedge, for example, beneath the Ryukyu arc [Long and van der Hilst, 2006]. Previously, it was considered to be caused by dislocation-creep dominated olivine [Long and van der Hilst, 2006] because olivine deformed by dislocation creep shows a LPO and leads to a seismic anisotropy [Karato and Wu, 1993]. However, from our results, LPO should not be formed in mantle wedges because of dominant diffusion creep in such regions close to the subducting slabs. Recent studies proposed a responsibility of deformed serpentine for the seismic anisotropy in mantle wedge [Jung, 2011] and our results support this idea. Therefore, the seismically observed anisotropy in mantle wedge is most likely caused by serpentine in the limited regions above the subducted slabs, whereas most part of mantle wedge should be isotropic.

## **5.6 Acknowledgments**

We appreciate S. Chakraborty and R. Dohmen at Ruhr-University of Bochum for thin film deposition, F. Heidelbach for SEM analysis, A. Audétat for gas-mixing furnace experiments, and H. Keppler for FT-IR measurements. H. Fei acknowledges the support by the ENB (Elite Network Bavaria) program. This work is also supported by JSPS KAKENHI Grant Number 20002002 to H. Yurimoto, and by Earthquake Research Institute, The University of Tokyo.

# Chapter 6

---

## Conclusions

1. The silicon lattice diffusion coefficient in dry forsterite determined in this study is ~2-3 orders of magnitude higher than those determined previous studies. The discrepancy between dislocation creep rate measured in deformation experiments and that induced from silicon diffusion coefficient is resolved.
2. The effect of water on silicon lattice diffusion coefficient in forsterite is very small:  $D_{Si} \propto (C_{H_2O})^{0.32 \pm 0.07}$ . This  $C_{H_2O}$  exponent is much lower than that determined in deformation experiments. Water has a much small effect on upper mantle rheology than people considered before. Therefore, the softening of asthenosphere cannot be caused by olivine hydration.
3. Water has no significant effect on oxygen diffusion coefficient in forsterite:  $D_{Si} \propto (C_{H_2O})^{0.06 \pm 0.14}$ , which further demonstrates that water does not play essential role in upper mantle rheology.
4. The activation volume, activation energy, and water content exponent for silicon grain-boundary diffusion in forsterite are  $1.8 \pm 0.2$  cm<sup>3</sup>/mol,  $245 \pm 12$  kJ/mol, and  $0.22 \pm 0.05$ , respectively. The Coble, Nabarro-Herring, and dislocation creep rates calculated from silicon lattice and grain boundary diffusion coefficients suggest that diffusion creep dominates in cold mantles and mantle wedges, whereas dislocation creep dominates in both enriched and depleted asthenosphere.

# APPENDIX

---

## Appendix I: Kröger-Vink notation

Kröger-Vink notation [Kröger and Vink, 1956] is a commonly used notation for the description of defects in ionic materials [Chiang *et al.*, 1997]. The basic rules of the notation are outlined below:

### (1) Description of point defects

A point defect is described by three parts: main body, subscript, and superscript.

The main body is the name of the species, e.g.,

- A silicon atom is written as Si.
- A vacancy site is noted as V.

The subscript denotes the site that the defect occupies, e.g.,

- $\text{Mg}_{\text{Mg}}$  is an Mg ion occupies an Mg site.
- $\text{Fe}_{\text{Mg}}$  denote an iron ion as point defect occupies an Mg site.
- $\text{V}_{\text{Mg}}$  is a vacancy on Mg site.
- $\text{Mg}_i$  means an Mg ion occupies an interstitial site.

The superscript denotes the effective charge of the defect relative to the perfect crystal:

- Positive effective charges are represented by  $\bullet$ .
- Negative effective charges are represented by  $'$ .
- Charge neutrality is showed by  $\times$ .

Some examples:

- $\text{V}_{\text{O}}^{\bullet\bullet}$  is a vacancy occupies an O site, and the effective charge is +2.
- $\text{Al}_{\text{Fe}}^{\times}$  means an Al ion on Fe site, with an effective charge of 0.

- $\text{Fe}_{\text{Fe}}^{\bullet}$  means a ferric Fe ion occupies a ferrous Fe site, with +1 effective charge.
- $\text{O}_i^{\prime\prime}$  means an interstitial O ion. The effective charge is -2.
- $e'$  and  $h^{\bullet}$  denote electron and electron hole, respectively.

## (2) Description of clustered defects or defect associates

Clustered defects or defect associates are denoted with parentheses that group together the defects that are bound to on another by electrostatic attraction [*Chiang et al.*, 1997]. For example:

- $(\text{V}_{\text{Na}}^{\bullet} - \text{V}_{\text{Cl}}^{\bullet})^{\times}$  is a clustered pair with a Na vacancy and a Cl vacancy. The effective charge of the clustered pair is 0.
- $\{(\text{OH})_{\text{O}}^{\bullet} - \text{V}_{\text{Si}}^{\prime\prime\prime\prime} - (\text{OH})_{\text{O}}^{\bullet}\}^{\prime\prime}$  means, two hydroxyls, which occupy on two O sites respectively, associate with a vacancy on Si site, and the total effective charge is -2.

## (3) Concentration of defects

The concentration of defects is denoted by square brackets, for example,  $[\text{V}_{\text{Mg}}^{\prime\prime}]$ ,  $[\{(\text{OH})_{\text{O}}^{\bullet} - \text{V}_{\text{Si}}^{\prime\prime\prime\prime} - (\text{OH})_{\text{O}}^{\bullet}\}^{\prime\prime}]$ , and  $[h^{\bullet}]$ .

## (4) Point defect equations

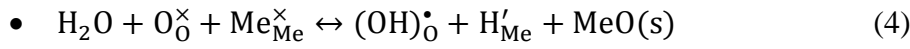
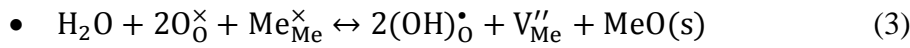
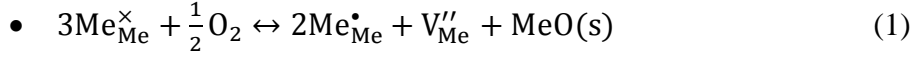
The rules to write point defect equations are similar as writing general chemical reactions, with the rules: charge conservation, atomic species conservation, and atomic sites conservation. For example:

- $3\text{MgO} = 3\text{Mg}_i^{\bullet\bullet} + 3\text{O}_0^{\times} + 2\text{V}_{\text{Al}}^{\prime\prime\prime}$
- $2(\text{OH})_{\text{O}}^{\bullet} + \text{V}_{\text{Si}}^{\prime\prime\prime\prime} = \{(\text{OH})_{\text{O}}^{\bullet} - \text{V}_{\text{Si}}^{\prime\prime\prime\prime} - (\text{OH})_{\text{O}}^{\bullet}\}^{\prime\prime} \equiv (2\text{H})_{\text{Si}}^{\prime\prime}$
- $e' + h^{\bullet} = \text{null}$

## Appendix II: water content exponents for defect species in olivine

The water content exponents for concentrations of defect species in olivine under each charge neutrality conditions can be derived by equations of reactions between different species.

The reactions of incorporation of water in olivine are listed below:



where “Me” indicates metal ions, i.e., Mg or Fe in olivine.

Assuming the equilibrium constant for reaction equation (i) is  $K_i$  in this section, we have:

$$\bullet \quad K_1 = \frac{[a_{\text{MeO}}][V_{\text{Me}}''][\text{Me}_{\text{Me}}^{\bullet}]^2}{[f_{\text{O}_2}]^{1/2}[\text{Me}_{\text{Me}}^{\times}]^3} \quad (6)$$

$$\bullet \quad K_2 = \frac{[a_{\text{MeO}}][H_{\text{Me}}'][\text{Me}_{\text{Me}}^{\bullet}]}{[f_{\text{O}_2}]^{1/4}[\text{Me}_{\text{Me}}^{\times}]^2[f_{\text{H}_2\text{O}}]^{1/2}} \quad (7)$$

$$\bullet \quad K_3 = \frac{[a_{\text{MeO}}][V_{\text{Me}}''][(\text{OH})_{\text{O}}^{\bullet}]^2}{[\text{O}_{\text{O}}^{\times}]^2[\text{Me}_{\text{Me}}^{\times}][f_{\text{H}_2\text{O}}]} \quad (8)$$

$$\bullet \quad K_4 = \frac{[a_{\text{MeO}}][H_{\text{Me}}'][(\text{OH})_{\text{O}}^{\bullet}]}{[\text{O}_{\text{O}}^{\times}][\text{Me}_{\text{Me}}^{\times}][f_{\text{H}_2\text{O}}]} \quad (9)$$

$$\bullet \quad K_5 = \frac{[a_{\text{MeO}}][H_{\text{Me}}']^2}{[V_{\text{Me}}''][\text{Me}_{\text{Me}}^{\times}][f_{\text{H}_2\text{O}}]} \quad (10)$$

Because Me and O are structure elements in olivine, we assume  $[\text{Me}_{\text{Me}}^{\times}] = 1$ , and  $[\text{O}_{\text{O}}^{\times}] = 1$ .

Therefore,  $K_1$ - $K_5$  can be simplified as:

$$\bullet \quad K_1 = m[V_{\text{Me}}''][\text{Me}_{\text{Me}}^{\bullet}]^2 \quad (11)$$

$$\bullet \quad K_2 = n \frac{[H_{\text{Me}}'][\text{Me}_{\text{Me}}^{\bullet}]}{[f_{\text{H}_2\text{O}}]^{1/2}} \quad (12)$$

$$\bullet \quad K_3 = p \frac{[V_{\text{Me}}''][(\text{OH})_{\text{O}}^{\bullet}]^2}{[f_{\text{H}_2\text{O}}]} \quad (13)$$

$$\bullet \quad K_4 = q \frac{[H_{\text{Me}}'][(\text{OH})_{\text{O}}^{\bullet}]}{[f_{\text{H}_2\text{O}}]} \quad (14)$$

- $K_5 = r \frac{[H'_{Me}]^2}{[V''_{Me}][f_{H_2O}]}$  (15)

Where  $m, n, p, q,$  and  $r$  are constants related to  $a_{MeO}$  and  $f_{O_2}$ .

Take the charge neutrality condition of  $[(OH)_O^\bullet] = 2[V_{Me}'']$  for example, using **Eqs. (11)-(15)** and the equation  $[(OH)_O^\bullet] = 2[V_{Me}'']$ , we obtain:

- $[V''_{Me}] = \left(\frac{K_3[f_{H_2O}]}{4p}\right)^{1/3} \propto [f_{H_2O}]^{1/3}$  (16)

- $[Me^\bullet_{Me}] = \left(\frac{K_1}{m[V''_{Me}]}\right)^{1/2} \propto [f_{H_2O}]^{-1/6}$  (17)

- $[H'_{Me}] = \frac{K_2[f_{H_2O}]^{1/2}}{n[Me^\bullet_{Me}]} \propto [f_{H_2O}]^{2/3}$  (18)

- $[(OH)_O^\bullet] = 2[V''_{Me}] \propto [f_{H_2O}]^{1/3}$  (19)

(The main idea of above derivation is from Kohlstedt [2006]).

Additionally, because:

- $2(OH)_O^\bullet + V''_{Me} \leftrightarrow \{(OH)_O^\bullet - V''_{Me} - (OH)_O^\bullet\}^\times \equiv (2H)^\times_{Me}$  (20)

We obtain:

- $[(2H)^\times_{Me}] = K_{20}[V''_{Me}][(OH)_O^\bullet]^2 \propto [f_{H_2O}]^1$  (21)

For defects on Si sites, we have the equations:

- $(OH)_O^\bullet + V_{Si}'''' \leftrightarrow \{(OH)_O^\bullet - V_{Si}''''\}'''' \equiv H_{Si}''''$  (22)

- $2(OH)_O^\bullet + V_{Si}'''' \leftrightarrow \{2(OH)_O^\bullet - V_{Si}''''\}'' \equiv (2H)''_{Si}$  (23)

- $3(OH)_O^\bullet + V_{Si}'''' \leftrightarrow \{3(OH)_O^\bullet - V_{Si}''''\}' \equiv (3H)'_{Si}$  (24)

- $4(OH)_O^\bullet + V_{Si}'''' \leftrightarrow \{4(OH)_O^\bullet - V_{Si}''''\}^\times \equiv (4H)^\times_{Si}$  (25)

- $2H_2O + Si^\times_{Si} \leftrightarrow SiO_2(s) + (4H)^\times_{Si}$  (26)

- $Si^\times_{Si} \leftrightarrow V_{Si}'''' + Si_i^{\bullet\bullet\bullet}$  (27)

and the equilibrium constants,

- $K_{22} = \frac{[H_{Si}''']}{[V_{Si}'''][(OH)_O^\bullet]} \quad (28)$

- $K_{23} = \frac{[(2H)_{Si}''']}{[V_{Si}'''][(OH)_O^\bullet]^2} \quad (29)$

- $K_{24} = \frac{[(3H)_{Si}''']}{[V_{Si}'''][(OH)_O^\bullet]^3} \quad (30)$

- $K_{25} = \frac{[(4H)_{Si}^\times]}{[V_{Si}'''][(OH)_O^\bullet]^4} \quad (31)$

- $K_{26} = \frac{[(4H)_{Si}^\times]}{[f_{H_2O}]^2} \quad (32)$

- $K_{27} = [V_{Si}'''] [Si_i^{\bullet\bullet\bullet}] \quad (33)$

Therefore, under the charge neutrality condition of  $[(OH)_O^\bullet]=2[V_{Me}''']$ , we have,

- $[(4H)_{Si}^\times] = K_{26}[f_{H_2O}]^2 \propto [f_{H_2O}]^2 \quad (34)$

- $[V_{Si}'''] = \frac{[(4H)_{Si}^\times]}{K_{25}[(OH)_O^\bullet]^4} \propto [f_{H_2O}]^{2/3} \quad (35)$

- $[(3H)_{Si}'''] = K_{24}[V_{Si}'''][(OH)_O^\bullet]^3 \propto [f_{H_2O}]^{5/3} \quad (36)$

- $[(2H)_{Si}'''] = K_{23}[V_{Si}'''][(OH)_O^\bullet]^2 \propto [f_{H_2O}]^{4/3} \quad (37)$

- $[H_{Si}'''] = K_{22}[V_{Si}'''][(OH)_O^\bullet] \propto [f_{H_2O}]^1 \quad (38)$

- $[Si_i^{\bullet\bullet\bullet}] = \frac{K_{27}}{[V_{Si}''']} \propto [f_{H_2O}]^{-2/3} \quad (39)$

The water content exponent for total concentrations of depends on Si sites,  $[V_{Si}^{total}] = [V_{Si}'''] + [H_{Si}'''] + [(2H)_{Si}'''] + [(3H)_{Si}'''] + [(4H)_{Si}^\times]$ , depends on which type of defects dominant the Si vacancies.

For defects on O sites, we have the equations:



And

- $K_{40} = \frac{[O_i''][(OH)_O^\bullet]^2}{[f_{H_2O}]} \quad (42)$

- $K_{41} = [O_i''] [V_O^{\bullet\bullet}] \quad (43)$

Therefore, we get,

$$\bullet \quad [O_i''] = \frac{K_{40}[f_{H_2O}]}{[(OH)_O^*]^2} \propto [f_{H_2O}]^{1/3} \quad (44)$$

$$\bullet \quad [V_O^{**}] = \frac{K_{41}}{[O_i'']} \propto [f_{H_2O}]^{-1/3} \quad (45)$$

under the charge neutrality condition of  $[(OH)_O^*]=2[V_{Me}^{**}]$ .

Above derivation is based on the charge neutrality condition of  $[(OH)_O^*]=2[V_{Me}^{**}]$  as an example. The water content exponents for each species under other charge neutrality conditions of  $[Fe_{Me}^*]=2[V_{Me}^{**}]$ ,  $[Fe_{Me}^*]=[H_{Me}']$ , and  $[(OH)_O^*]=[H_{Me}']$  listed in **Table 1.1** can be derived using the same method.

### Appendix III: Linkages between self-diffusion, creep rate, and viscosity

The linkages between atomic diffusion coefficient and Coble diffusion creep rate, Nabarro-Herring creep rate, and dislocation creep rate are systematically described in Frost and Ashby [Frost and Ashby, 1982], Weertman [1999], Nabarro [1948], Herring [1950], Coble [1963], and the connection between self-diffusion and viscosity is given in Mckenzie [1967]. Here I describe the inducing of equations in a brief.

#### (1) Self-diffusion and Nabarro-Herring diffusion creep

Let's consider a grain show in **Fig. 1**. The concentration of vacancies in the grain interior is  $C_0$ ,

$$C_0 = A \exp\left(-\frac{\Delta E_f}{kT}\right) \quad (1)$$

where  $A$  is a constant,  $\Delta E_f$  to the energy required to form a vacancy,  $k$  is the Boltzmann constant, and  $T$  is the temperature (See **Section 1.1.5**).

When the grain is deformed under a compressive stress of  $\sigma$ , the energy for the vacancy formation at the boundary is reduced/increased by  $\sigma\Omega$ , namely,  $\Delta E_f' = \Delta E_f \pm \sigma\Omega$ . Therefore, the concentrations of vacancies near the boundaries along the compressive stress and tensile stress,  $C^+$  and  $C^-$  shown in **Fig. 1**, are,

$$C^+ = A \exp\left(-\frac{\Delta E_f - \sigma\Omega}{kT}\right) = C_0 \exp\left(\frac{\sigma\Omega}{kT}\right) \quad (2)$$

$$C^- = A \exp\left(-\frac{\Delta E_f + \sigma\Omega}{kT}\right) = C_0 \exp\left(\frac{-\sigma\Omega}{kT}\right) \quad (3)$$

From Fick's first law, the flow of vacancy,  $J_v$ , should be proportional to the concentration gradient of vacancy,

$$J_v = \alpha D_v \frac{\partial c}{\partial x} = \alpha D_v \frac{C^+ - C^-}{d} \quad (4)$$

where  $D_v$  is the diffusion coefficient of vacancies,  $d$  is the grain size,  $\alpha$  is the geometry factor.

In contrast, the flow of atoms,  $J_A$ , in the opposite direction is,

$$J_A = -\alpha D_A \frac{\partial c}{\partial x} = -\alpha D_A \frac{c^+ - c^-}{d} \quad (5)$$

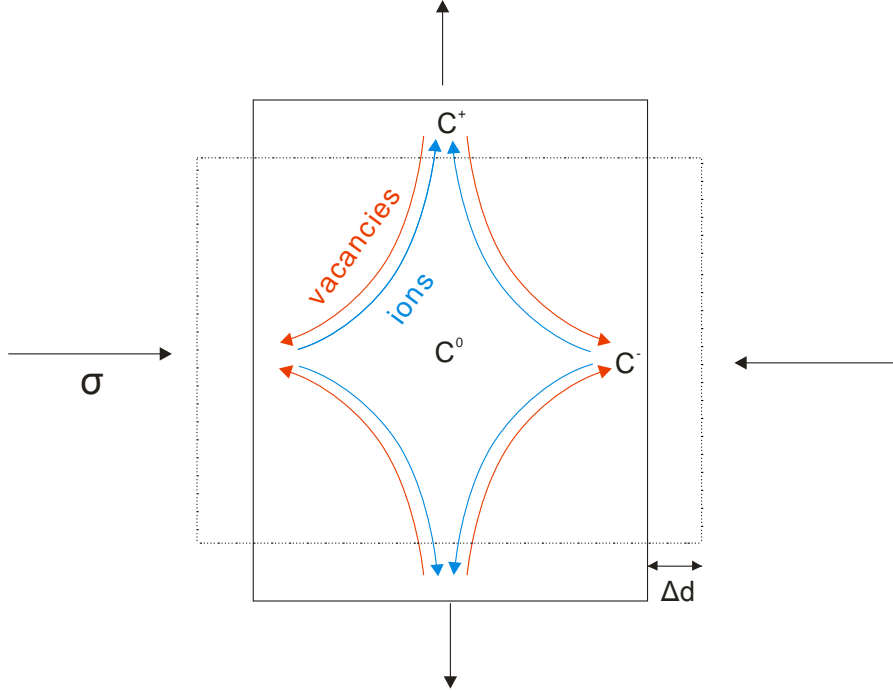


**Fig 1.** Nabarro-Herring diffusion creep. A grain is shortened in horizontal direction and elongated in vertical direction under a stress of  $\sigma$  by the diffusion of atoms and vacancies in the grain interior.

Since diffusion of atoms is the hopping from its normal site to its neighbor vacancy site, we have  $J_A = J_V = J$ .

The rate of shortening of the grain is,

$$\frac{\partial \Delta d}{\partial t} = \Delta \dot{d} = J V_m \quad (6)$$

The Nabarro-Herring creep rate is thus,

$$\dot{\epsilon} = \frac{\partial \epsilon}{\partial t} = \frac{\partial \Delta d}{d \partial t} = \Delta \dot{d} / d = \frac{J V_m}{d} = \alpha D_V V_m \frac{c^+ - c^-}{d^2} = \alpha D_V V_m C_0 \frac{\exp\left(\frac{\sigma \Omega}{kT}\right) - \exp\left(-\frac{\sigma \Omega}{kT}\right)}{d^2} \quad (7)$$

where  $V_m$  is the mole volume of the material. In the nature, the relationship,  $\sigma\Omega \ll kT$  always holds and therefore we have,

$$\dot{\epsilon} = \alpha D_V V_m C_0 \frac{\exp\left(\frac{\sigma\Omega}{kT}\right) - \exp\left(-\frac{\sigma\Omega}{kT}\right)}{d^2} \cong \alpha D_V V_m C_0 \frac{\sinh\left(\frac{\sigma\Omega}{kT}\right)}{d^2} \cong \alpha \sigma \frac{D_V V_m C_0 \Omega}{d^2} \quad (8)$$

Because the self-diffusion coefficient of atoms in a lattice,  $D_A = D_V V_m C_0$ , we obtained that the Nabarro-Herring creep rate is linearly proportional to  $D_A$ ,  $\sigma$ , and  $d^{-2}$ ,

$$\dot{\epsilon} \cong \alpha \sigma \frac{D_A \Omega}{kT d^2} = \alpha \sigma \frac{D_A V_m}{RT d^2} \quad (9)$$

## (2) Self-diffusion and Coble diffusion creep

Coble diffusion creep happens due to diffusion of atoms and vacancies along grain boundaries (**Fig. 2**). Similar as Nabarro-Herring creep, the flow of vacancies is,

$$J_V = \alpha D_v^{gb} \frac{\partial c}{\partial x} = \alpha D_v^{gb} \frac{c^+ - c^-}{d} \quad (10)$$

For grain boundary diffusion, the effective diffusion coefficient is,

$$D_V = \pi \frac{\delta}{d} D_v^{gb} \quad (11)$$

Therefore, the shorten rate along the compressive stress by diffusing of atoms to the tensile direction (**Fig. 2**) is,

$$\frac{\partial \Delta d}{\partial t} = \Delta \dot{d} = \alpha \pi \frac{\delta}{d} D_v^{gb} \frac{c^+ - c^-}{d} V_m \quad (12)$$

As a result, the Coble diffusion creep rate is obtained from **Eqs. (11), (12), (2), and (3)**,

$$\dot{\epsilon} = \frac{\Delta \dot{d}}{d} = \alpha \pi D_v^{gb} \frac{\delta}{d^2} V_m \frac{c^+ - c^-}{d} \cong \alpha \pi D_v^{gb} \frac{\delta}{d^2} V_m \frac{\sinh\left(\frac{\sigma\Omega}{kT}\right)}{d} \cong \alpha \pi \sigma \frac{\delta D_v^{gb} V_m C_0 \Omega}{kT d^3} = \alpha \pi \sigma \frac{\delta D_A^{gb} V_m}{RT d^3} \quad (13)$$

Therefore, the Coble creep is controlled by grain boundary diffusion of the slowest diffusing species and the creep rate is proportional to  $D_A^{gb}$ ,  $\sigma$ , and  $d^{-3}$ .

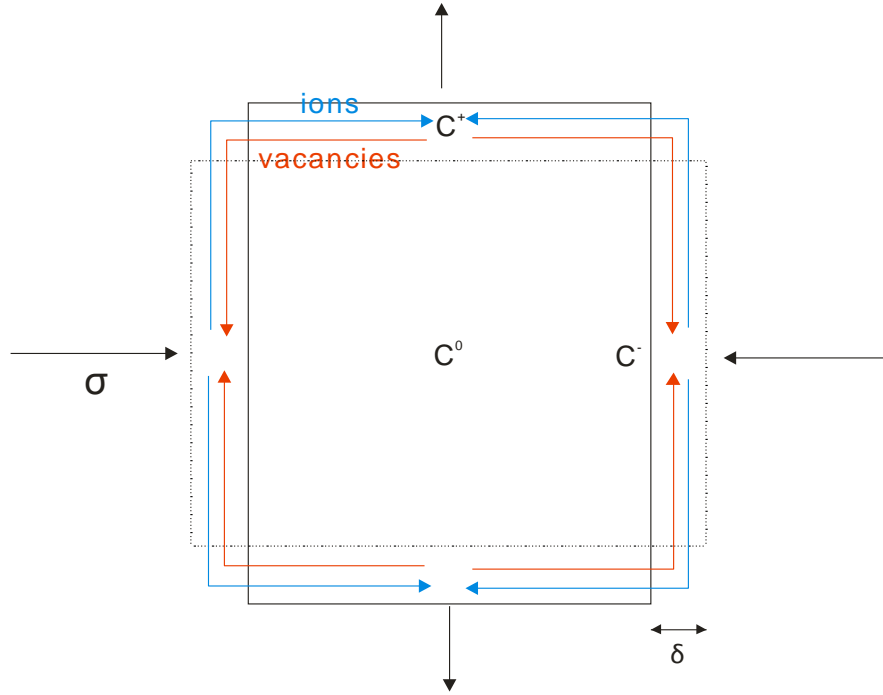


**Fig 2.** Coble diffusion creep. A grain is shorten in horizontal direction and elongated in vertical direction under a stress of  $\sigma$  by the diffusion of atoms and vacancies along the grain boundaries.

**(3) Self-diffusion and dislocation creep**

In a high temperature dislocation creep process, the strain is produced primarily by dislocation glide while strain rate is controlled by the rate of dislocation climb [Weertman, 1955], and the average dislocation motion velocity is,

$$\bar{v} = \frac{l_g}{l_c} v_c \tag{14}$$

where  $l_g$  is the glide distance,  $l_c$  is the climb distance, and  $v_c$  is the climb velocity. For dislocations with Burgers vector,  $b$ , the strain rate can be calculated from the Orowan Equation,

$$\dot{\epsilon} = \rho b \bar{v} \tag{15}$$

which physically means the rate of deformation is proportional to the amount of unit displacement caused by dislocation (Burgers vector), the dislocation density, and the average velocity of dislocation motion [Kohlstedt, 2006; Weertman, 1999].

The dislocation density,  $\rho$ , can be expressed by the stress  $\sigma$ , the Burgers vector, and the shear Modulus,  $G$ ,

$$\rho = \left(\frac{\sigma}{Gb}\right)^2 \quad (16)$$

and the climb velocity of the dislocation is [Hirth and Lothe, 1982],

$$v_c = 2\pi \frac{GV_m}{RT} \left(\frac{\sigma}{G}\right)^3 \frac{D_A}{b} \frac{1}{\ln\left(\frac{R_0}{r_c}\right)} \quad (17)$$

where  $R_0$  is the average spacing between dislocations, and  $r_c$  is the radius of a dislocation core which is generally taken to be as  $r_c \approx b$ .

From **Eqs. 14-17**, one obtains,

$$\dot{\epsilon} = 2\pi \frac{GV_m}{RT} \left(\frac{\sigma}{G}\right)^3 \frac{D_A}{b^2} \frac{1}{\ln\left(\frac{G}{\sigma}\right)} \frac{l_g}{l_c} \quad (18)$$

Therefore, the dislocation creep is controlled by lattice diffusion of the slowest diffusing species and the creep rate is proportional to  $D_A$ ,  $\sigma$ , and independent with grain size.

#### (4) *Self-diffusion and viscosity*

From the Fick's second law, we have,

$$\frac{\partial c}{\partial t} = D \frac{\partial^2 c}{\partial x^2} \quad (19)$$

and therefore we get the Einstein-Smoluchowski Equation,

$$D = \frac{\bar{\Delta}^2}{2t} \quad (20)$$

where  $\bar{\Delta}^2$  is the mean square of the deviation in a given direction in time  $t$ . By assuming that the particles have the same kinetic energy as gas molecules at the same temperature, we have,

$$\bar{\Delta}^2 = \frac{2RT}{N} \frac{t}{C} \quad (21)$$

where  $R$  is the gas constant,  $N$  is the Avogadro's number,  $T$  is the absolute temperature, and  $C$  is a constant which means the frictional resistance of the molecule.

Therefore, we have (Nernst-Einstein Equation),

$$D = \frac{RT}{N} \frac{1}{C} \quad (22)$$

For a spherical particles moving in a medium of proportionately small molecules,

$$C = 6\pi r \eta \quad (23)$$

where  $r$  is the radius of a diffusing particle and  $\eta$  is the viscosity.

Thus, one obtains the Stokes-Einstein Equation,

$$\eta = \frac{RT}{N} \frac{1}{6\pi r D} = kT \frac{1}{6\pi r D} \quad (24)$$

Therefore, the viscosity is inversely proportional to diffusion coefficient.

By assuming the density, the volume and mass fraction of ions in mantle minerals, we have,

$$\eta \approx 10kT \frac{r^2}{mD} \quad (25)$$

where  $m$  and  $r$  are the mass and radius of the diffusing ion.

# REFERENCES

---

## References

- Abt, D.L., K.M. Fischer, S.W. French, H.A. Ford, H. Yuan, and B. Romanowicz (2010), North American lithospheric discontinuity structure imaged by Ps and Sp receiver functions. *J. Geophys. Res.* **115**, B09301, doi: 10.1029/2009JB006914.
- Anderson, D. L. (1966), Earth's viscosity. *Science* **151**, 321-322.
- Andersson, K., G. Borchardt, S. Scherrer, and S. Weber (1989), Self-diffusion in Mg<sub>2</sub>SiO<sub>4</sub> (forsterite) at high temperature. *Fresenius. J. Analytical Chem.* **333**, 383-385.
- Aubaud, C., A.C. Withers, M.M. Hirschmann, Y.B. Guan, L.A. Leshin, S.J. Mackwell, and D.R. Bell (2010), A new calibration of H measurements by SIMS in glasses and nominally anhydrous minerals: application to experimental determinations of H partitioning. *Am. Geophys. Union abs.* **41**, 1419.
- Aubaud, C., A.C. Withers, M.M. Hirschmann, Y.B. Guan, L.A. Leshin, S.J. Mackwell, and D.R. Bell (2007), Intercalibration of FTIR and SIMS for hydrogen measurements in glasses and nominally anhydrous minerals. *Am. Miner.* **92**, 811-828.
- Aubaud, C., H. Bureau, C. Raepsaet, H. Khodja, A.C. Withers, M.M. Hirschmann, and D.R. Bell (2009), Calibration of the infrared molar absorption coefficients for H in olivine, clinopyroxene and rhyolitic glass by elastic recoil detection analysis. *Chem. Geol.* **262**, 78-86.
- Ando, K., H. Kurokawa, Y. Oishi, and H. Takei (1981), Self-diffusion coefficient of oxygen in single-crystal forsterite. *Com. Am. Ceramic Soci.* **64**, 30.
- Bai, Q., and D. L. Kohlstedt (1992), High-temperature creep of olivine single crystals, 2. dislocation structures. *Tectonophysics* **206**, 1-29.
- Bai, Q., and D. L. Kohlstedt (1992), Substantial hydrogen solubility in olivine and implications for storage in the mantle. *Nature* **357**, 672-674.
- Bai, Q., and D. L. Kohlstedt (1993), Effect of chemical environment on the solubility and incorporation mechanism for hydrogen in olivine. *Phys. Chem. Miner.* **19**, 460-471.
- Balan, E., J. Ingrin, S. Delattre, Kov, I. Cs, N, and M. Blanchard (2011), Theoretical infrared spectrum of OH-defects in forsterite. *Eur. J. Miner.* **23**, 285-292.

- Bali, E., N. Bolfan-Casanova, and K. T. Koga (2008), Pressure and temperature dependence of H solubility in forsterite: An implication to water activity in the Earth interior. *Earth Planet. Sci. Lett.* **268**, 354-363.
- Baxter, E. F. (2010), Diffusion of noble gases in minerals, *Rev. Min. Geochem.* **72**, 509-557.
- Bejina, F., and O. Jaoul (1996), Silicon self-diffusion in quartz and diopside measured by nuclear micro-analysis methods. *Phys. Earth Planet. Int.* **97**, 145-162.
- Bejina, F., and O. Jaoul (1997), Silicon diffusion in silicate minerals. *Earth Planet. Sci. Lett.* **153**, 229-238.
- Bejina, F., O. Jaoul, and R. C. Liebermann (2003), Diffusion in minerals at high pressure: a review. *Phys. Earth Planet. Int.* **139**, 3-20.
- Béjina, F., P. Raterron, J. Zhang, O. Jaoul, and R. C. Liebermann (1997), Activation volume of silicon diffusion in San Carlos olivine. *Geophys. Res. Lett.* **24**, 2597-2600.
- Béjina, F., O. Jaoul, and R. C. Liebermann (1999), Activation volume of Si diffusion in San Carlos olivine: Implications for upper mantle rheology. *J. Geophys. Res.* **104**, 25529-25542.
- Bell, D. R., and G. R. Rossman (1992), Water in Earth's mantle: the role of nominally anhydrous minerals. *Science* **255**, 1391-1397.
- Bell, D. R., G. R. Rossman, J. Maldener, D. Endisch, and F. Rauch (2003), Hydroxide in olivine: A quantitative determination of the absolute amount and calibration of the IR spectrum. *J. Geophys. Res.* **108**, 2105B2.
- Borg, R. J., and G. J. Dienes (1988), *An introduction to solid state diffusion*. Academic Press, Inc. Harcourt Brace Jovanovich Publishers.
- Brady, J. B. (1983), Intergranular diffusion in metamorphic rocks. *Am. J. Sci.* **293**, 181-200.
- Bruhn, D. F., D. L. Olgaard, L. N. Dell'Angelo (1999), Evidence for enhanced deformation in two-phase rocks: Experiments on the rheology of calcite-anhydrite aggregates. *J. Geophys. Res.* **104**, 707-724.
- Borch, R. S., and H. W. Green II (1989), Deformation of peridotite at high pressure in a new molten salt cell: comparison of traditional and homologous temperature treatments. *Phys. Earth Planet. Int.* **55**, 269-276.
- Brodholt, J. P., and K. Refson (2000), An ab initio study of hydrogen in forsterite and a possible mechanism for hydrolytic weakening. *J. Geophys. Res.* **105**, 18977-18982.
- Chadwick, A. V., and M. Terenzi (1985), *Defects in solids*. Plenum Press, New York and London.

- Chakraborty, S. (1997), Rate and mechanisms of Fe-Mg interdiffusion in olivine at 980 – 1300 °C, *J. Geophys. Res.* **102**, 12317-12331.
- Chakraborty, S. (2010), Diffusion coefficients in olivine, wadsleyite, and ringwoodite. *Rev. Min. Geochem.* **72**, 603-639.
- Chakraborty, S., J. R. Farver, R. A. Yund, and D. C. Rubie (1994), Mg tracer diffusion in synthetic forsterite and San Carlos olivine as a function of  $P$ ,  $T$ , and  $f_{O_2}$ . *Phys. Chem. Min.* **21**, 489-500.
- Chiang, Y. M., D. P. Birnie, and W. D. Kingery (1997), *Physical ceramics*. Wiley Chichester, UK.
- Chopra, P. N., and M. S. Paterson (1984), The role of water in the deformation of dunite. *J. Geophys. Res.* **89**, 7861-7876.
- Coble, R.L. (1963), A model for boundary diffusion controlled creep in polycrystalline materials, *J. Appl. Phys.* **34**, 1679-1682.
- Cooper, R. F., and D. L. Kohlstedt (1984), Solution-precipitation enhanced diffusional creep of partially molten olivine-basalt aggregates during hot-pressing. *Tectonophysics* **107**, 207-233.
- Costa, F., and S. Chakraborty (2008), The effect of water on Si and O diffusion rates in olivine and implications for transport properties and processes in the upper mantle. *Phys. Earth Planet. Int.* **166**, 11-29.
- Crank, J. (1975), *The mathematics of diffusion* (2nd edition). Oxford University Press.
- Darot, M., and Y. Gueguen (1981), High-temperature creep of forsterite single crystals *J. Geophys. Res.* **86**, 6219-6234.
- Demouchy, S., and S. Mackwell (2003), Water diffusion in synthetic iron-free forsterite. *Phys. Chem. Min.* **30**, 486-494.
- Demouchy, S., S. J. Mackwell, and D. L. Kohlstedt (2005), Effect of Hydrogen on Mg-Fe Interdiffusion in Ferro-periclase. *American Geophysical Union Fall Meeting* **41**, 902.
- Demouchy, S. (2010), Diffusion of hydrogen in olivine grain boundaries and implications for the survival of water-rich zones in the Earth's mantle. *Earth Planet. Sci. Lett.* **295**, 305-313.
- Dixon, J. E., L. Leist, C. Langmuir, and J. Schilling (2002), Recycled dehydrated lithosphere observed in plume-influenced mid-ocean-ridge basalt. *Nature* **420**, 385-389.
- Dobson, D. P., R. Dohmen, and M. Wiedenbeck (2008), Self-diffusion of oxygen and silicon in MgSiO<sub>3</sub> perovskite. *Earth Planet. Sci. Lett.* **270**, 125-129.

- Dohmen, R., S. Chakraborty, and H. W. Becker (2002), Si and O diffusion in olivine and implications for characterizing plastic flow in the mantle. *Geophys. Res. Lett.* **29**, 203021.
- Dohmen, R., H. Becker, E. Meissner, T. Etzel, and S. Chakraborty (2002), Production of silicate thin films using pulsed laser deposition (PLD) and applications to studies in mineral kinetics. *Eur. J. Min.* **14**, 1155-1168.
- Dohmen, R., and S. Chakraborty (2007), Fe-Mg diffusion in olivine II: point defect chemistry, change of diffusion mechanisms and a model for calculation of diffusion coefficients in natural olivine. *Phys. Chem. Min.* **34**, 409-430.
- Dohmen, R., H. W. Becker, and S. Chakraborty (2007), Fe-Mg diffusion in olivine I: experimental determination between 700 and 1,200 degrees C as a function of composition, crystal orientation and oxygen fugacity. *Phys. Chem. Min.* **34**, 389-407.
- Durham, W. B., and C. Goetze (1977a), Plastic flow of oriented single crystal of olivine 1. Mechanical data. *J. Geophys. Res.* **82**, 5737-5753.
- Durham, W. B., and C. Goetze (1977b), A comparison of the creep properties of pure forsterite and iron-bearing olivine. *Tectonophysics* **40**, T15-T18.
- Eggler, D. H. (1979), Studies on the role of CO<sub>2</sub> and CO in magma genesis in planetary interiors. *Lunar Planet. Institute Sci. Conference*, 03-01.
- Evans, B., and C. Goetze (1979), The temperature variation of hardness of olivine and its implication for polycrystalline yield stress. *J. Geophys. Res.* **84**, 5505-5524.
- Farber, D. L., Q. Williams, and F. J. Ryerson (2000), Divalent cation diffusion in Mg<sub>2</sub>SiO<sub>4</sub> spinel (ringwoodite),  $\beta$  phase (wadsleyite), and olivine: Implications for the electrical conductivity of the mantle. *J. Geophys. Res.* **105**, 513-529.
- Farver, J., and R. Yund (2000), Silicon diffusion in forsterite aggregates: Implications for diffusion accommodated creep. *Geophys. Res. Lett.* **27**, 2337-2340.
- Farver, J., and R. Yund (2000), Silicon diffusion in a natural quartz aggregate: constraints on solution-transfer diffusion creep. *Tectonophysics* **325**, 193-205.
- Farver, J. R., R. A. Yund, and D. C. Rubie (1994), Magnesium grain boundary diffusion in forsterite aggregates at 1000 - 1300 C and 0.1 MPa to 10 GPa. *J. Geophys. Res.* **99**, 19809-19819.
- Faul, U. H., and I. Jackson (2005), The seismological signature of temperature and grain size variations in the upper mantle. *Earth Planet. Sci. Lett.* **234**, 119-134.

- Faul, U. H., and I. Jackson (2007), Diffusion creep of dry, melt-free olivine. *J. Geophys. Res.* **112**, 4204. doi:10.1029/2006JB004586.
- Fei, H., C. Hegoda, D. Yamazaki, M. Wiedenbeck, H. Yurimoto, S. Shcheka, and T. Katsura (2012), High silicon self-diffusion coefficient in dry forsterite. *Earth Planet. Sci. Lett.* **345**, 95-103.
- Fei, H., M. Wiedenbeck, D. Yamazaki, and T. Katsura (2012), Small effect of water on the upper mantle rheology based on Si self-diffusion coefficient. *Nature* **498**, 213-215.
- Fischer, K. M., H. A. Ford, D. L. Abt, and C. A. Rychert (2010), The lithosphere-asthenosphere boundary. *Annu. Rev. Earth Planet. Sci.* **38**, 551-575.
- Frost, H. J., and M. F. Ashby (1982), *Deformation mechanism maps*. Pergamon, Oxford.
- Ganguly, J. (1988), Convolution effect in the determination of compositional profiles and diffusion coefficients by microprobe step scans. *Am. Min.* **73**, 901-909.
- Gérard, O., and O. Jaoul (1989), Oxygen diffusion in San Carlos olivine. *J. Geophys. Res.* **94**, 4119-4128.
- Giletti, B. J., and R. A. Yund (1984), Oxygen diffusion in quartz. *J. Geophys. Res.* **89**, 4039-4046.
- Girard, J., J. H. Chen, P. Raterron, and C. W. Holyoke III (2013). Hydrolytic weakening of olivine at mantle pressure: Evidence of [100](010) slip system softening from single-crystal deformation experiments. *Phys. Earth Planet. Int.* **216**, 12-20.
- Goetze, C., and D. Kohlstedt (1973), Laboratory Study of Dislocation Climb and Diffusion in Olivine. *J. Geophys. Res.* **78**, 5961-5971.
- Green, D. H., and A. E. Ringwood (1967), The genesis of basaltic magmas. *Contrib. Min. Petro.* **15**, 103.
- Gung, Y. C., M. Panning, and B. Romanowicz (2003), Global anisotropy and the thickness of continents. *Nature*, **422**, 707-711.
- Hansen, L. N., M. E. Zimmerman, and D. L. Kohlstedt (2011), Grain boundary sliding in San Carlos olivine: Flow law parameters and crystallographic-preferred orientation. *J. Geophys. Res.* **116**, 8201. doi:10.1029/2011JB008220.
- Harrison, L.G. (1961), Influence of dislocations on diffusion kinetics in solids with particular reference to alkali halides. *Trans. Faraday Soc.* **57**, 1191-1199.
- Hazen, R. M. (1976), Effects of temperature and pressure on the crystal structure of forsterite. *Am. Min.* **61**, 1280-1293.

- Herring, C. (1950), Diffusional viscosity of a polycrystalline solid, *J. Appl. Phys.* **21**, 437-445.
- Hier-Majumder, S., I. M. Anderson, and D. L. Kohlstedt (2005), Influence of protons on Fe-Mg interdiffusion in olivine. *J. Geophys. Res.*, **110**, B2202.
- Hiraga, T., and D. L. Kohlstedt (2007), Equilibrium interface segregation in the diopside–forsterite system I: Analytical techniques, thermodynamics, and segregation characteristics. *Geochim. Cosmochim. Acta.* **71**, 1266-1280.
- Hiraga, T., C. Tachibana, N. Ohashi, and S. Sano (2010), Grain growth systematics for forsterite ± enstatite aggregates: Effect of lithology on grain size in the upper mantle. *Earth Planet. Sci. Lett.* **291**, 10-20.
- Hirschmann, M. M., C. Aubaud, and A. C. Withers (2005), Storage capacity of H<sub>2</sub>O in nominally anhydrous minerals in the upper mantle. *Earth Planet. Sci. Lett.* **236**, 167-181.
- Hirschmann, M. M. (2006), Water, Melting, and the Deep Earth H<sub>2</sub>O Cycle. *Annu. Rev. Earth Planet. Sci.* **34**, 629-653.
- Hirschmann, M. M. (2010), Partial melt in the oceanic low velocity zone. *Phys. Earth Planet. Int.* **179**, 60-71.
- Hirth, G., and D. L. Kohlstedt (1995a), Experimental constraints on the dynamics of the partially molten upper mantle 2. Deformation in the dislocation creep regime. *J. Geophys. Res.* **100**, 15441-15450.
- Hirth, G., and D. L. Kohlstedt (1995b), Experimental constraints on the dynamics of the partially molten upper mantle 1: Deformation in the diffusion creep regime. *J. Geophys. Res.* **100**, 1981-2001.
- Hirth, G., and D. L. Kohlstedt (1996), Water in the oceanic upper mantle: implications for rheology, melt extraction and the evolution of the lithosphere. *Earth Planet. Sci. Lett.* **144**, 93-108.
- Hirth, G., and D. Kohlstedt (2003), Rheology of the upper mantle and the mantle wedge: A view from the experimentalists. *Geophys. Monograph. Am. Geophys. Union* **138**, 83-106.
- Hirth, J. P., and J. Lothe (1982), *Theory of dislocations*. John Wiley and Sons Press.
- Holzappel, C., D. C. Rubie, D. J. Frost, and F. Langenhorst (2005), Fe-Mg interdiffusion in (Mg,Fe)SiO<sub>3</sub> perovskite and lower mantle reequilibration. *Science* **309**, 1707-1710.
- Holzappel, C., S. Chakraborty, D. C. Rubie, and D. J. Frost (2007), Effect of pressure on Fe–Mg, Ni and Mn diffusion in (Fe<sub>x</sub>Mg<sub>1-x</sub>)<sub>2</sub>SiO<sub>4</sub> olivine. *Phys. Earth Planet. Int.* **162**, 186-198.

- Houlier, B., O. Jaoul, F. Abel, and R. C. Liebermann (1988), Oxygen and silicon self-diffusion in natural olivine at T= 1300 °C. *Phys. Earth Planet. Int.*, **50**, 240-250.
- Houlier, B., M. Cheraghmakani, and O. Jaoul (1990), Silicon diffusion in San-Carlos olivine. *Phys. Earth Planet. Int.* **62**, 329-340.
- Huang, R., and A. Audéat (2012), The titanium-in-quartz (TitaniQ) thermobarometer: A critical examination and re-calibration. *Geochim. Cosmochim. Acta* **84**, 75-89.
- Hull, D., and D. J. Bacon (2011), *Introduction to dislocations* (Fifth edition). Butterworth-Heinemann Press.
- Hunt, S. A., D. P. Dobson, I. G. Wood, J. P. Brodholt, J. Mecklenburgh, and E. C. Oliver (2009), Deformation of olivine at 5 GPa and 350–900 °C, *Phys. Earth Planet. Int.* **172**, 84-90.
- Inoue, T. (1994), Effect of water on melting phases-relations and melt composition in the system Mg<sub>2</sub>SiO<sub>4</sub>-MgSiO<sub>3</sub>-H<sub>2</sub>O up to 15 GPa. *Phys. Earth Planet. Int.* **85**, 237-263.
- Inoue, T., D. J. Weidner, P. A. Northrup, and J. B. Parise (1998), Elastic properties of hydrous ringwoodite (gamma-phase) in Mg<sub>2</sub>SiO<sub>4</sub>, *Earth Planet. Sci. Lett.* **160**, 107-113.
- Ito, G., Y. Shen, G. Hirth, and C. J. Wolfe (1999), Mantle flow, melting, and dehydration of the Iceland mantle plume. *Earth Planet. Sci. Lett.* **165**, 81-96.
- Iwamori, H., and T. Nakakuki (2013), Fluid processes in subduction zones and water transport to the deep mantle. *Phys. Chem. Deep Earth*, 10.1002/9781118529492.ch13.
- Jackson, I. (2000), *The Earth's mantle: composition, structure, and evolution*. Cambridge Univ. press.
- Jacobsen, S. D., F. Jiang, Z. Mao, T. S. Duffy, J. R. Smyth, C. M. Holl, and D. J. Frost (2008), Effects of hydration on the elastic properties of olivine. *J. Geophys. Res.* **35**, Doi: 10.1029/2008GL034398.
- Jaoul, O., C. Froidevaux, W. B. Durham, and M. Michaut (1980), Oxygen self-diffusion in forsterite: Implications for the high-temperature creep mechanism. *Earth Planet. Sci. Lett.* **47**, 391-397.
- Jaoul, O., M. Poumellec, C. Froidevaux, and A. Havette (1981), Silicon diffusion in forsterite: a new constraint for understanding mantle deformation. *AGU Anelasticity Earth Geodynamics* **4**, 95-100
- Jaoul, O. (1990), Multicomponent Diffusion and Creep in Olivine. *J. Geophys. Res.* **95**, 17631-17642.

- Jaoul, O., F. Bejina, F. Elie, and F. Abel (1995), Silicon Self-Diffusion in Quartz. *Phys. Rev. Lett.* **74**, 2038-2041.
- Jung, H., and S. Karato (2001), Water-induced fabric transitions in olivine. *Science* **293**, 1460-1463.
- Jung, H., and S. Karato (2001), Effects of water on dynamically recrystallized grain-size of olivine. *J. Struct. Geology* **23**, 1337-1344.
- Jung, H. (2011), Seismic anisotropy produced by serpentine in mantle wedge, *Earth Planet. Sci. Lett.* **307**, 535-543.
- Karato, S., and M. Ogawa (1982), High-pressure recovery of olivine: implications for creep mechanisms and creep activation volume. *Phys. Earth Planet. Int.* **28**, 102-117.
- Karato, S., and H. Sato (1982), Effect of oxygen partial pressure on the dislocation recovery in olivine: a new constraint on creep mechanisms. *Phys. Earth Planet. Int.* **28**, 312-319.
- Karato, S. (1984), Grain-size distribution and rheology of the upper mantle. *Tectonophysics* **104**, 155-176.
- Karato, S. I., M. S. Paterson, and J. D. Fitzgerald (1986), Rheology of synthetic olivine aggregates - Influence of grain size and water. *J. Geophys. Res.* **91**, 8151-8176.
- Karato, S. (1990), The role of hydrogen in the electrical conductivity of the upper mantle. *Nature* **347**, 272-273.
- Karato, S. (1992), On the Lehmann discontinuity. *Geophys. Res. Lett.* **19**, 2255-2258.
- Karato, S., D. C. Rubie, and H. Yan (1993), Dislocation recovery in olivine under deep upper mantle conditions - Implications for creep and diffusion. *J. Geophys. Res.* **98**, 9761-9768.
- Karato, S., and P. Wu (1993), Rheology of the upper mantle: A synthesis. *Science* **260**, 771-778.
- Karato, S., and D. C. Rubie (1997), Toward an experimental study of deep mantle rheology: A new multianvil sample assembly for deformation studies under high pressures and temperatures. *J. Geophys. Res.* **102**, 20111-20122.
- Karato, S., and H. Jung (1998), Water, partial melting and the origin of the seismic low velocity and high attenuation zone in the upper mantle. *Earth Planet. Sci. Lett.* **157**, 193-207.
- Karato, S. I., and H. Jung (2003), Effects of pressure on high-temperature dislocation creep in olivine. *Philosophical Magazine* **83**, 401-414.
- Karato, S. (2008), *Deformation of earth materials: an introduction to the rheology of solid earth*. Cambridge Univ. Press.

- Karato, S. I. (2010), Rheology of the deep upper mantle and its implications for the preservation of the continental roots: A review. *Tectonophysics* **481**, 82-98.
- Karato, S. (2010), Rheology of the Earth's mantle: A historical review. *Gondwana Res.*, **18**, 17-45.
- Karato, S. (2012), On the origin of the asthenosphere. *Earth Planet. Sci. Lett.* **321**, 95-103.
- Katayama, I., and S. Karato (2008), Effects of water and iron content on the rheological contrast between garnet and olivine. *Phys. Earth Planet. Int.* **166**, 57-66.
- Katsura, T., A. Yoneda, D. Yamazaki, T. Yoshino, and E. Ito (2010), Adiabatic temperature profile in the mantle. *Phys. Earth Planet. Int.* **183**, 212-218.
- Kawakatsu, H., P. Kumar, Y. Takei, M. Shinohara, T. Kanazawa, E. Araki, and K. Suyehiro (2009), Seismic evidence for sharp lithosphere-asthenosphere boundaries of oceanic plates. *Science* **324**, 499-502.
- Kawazoe, T., N. Nishiyama, Y. Nishihara, and T. Irifune (2010), Deformation experiment at P–T conditions of the mantle transition zone using D-DIA apparatus. *Phys. Earth. Planet. Int.* **183**, 190-195.
- Kawazoe, T., Y. Nishihara, T. Ohuchi, M. Nishi, N. Nishiyama, Y. Higo, K. Funakoshi, and T. Irifune (2011), In situ stress-strain measurements in a deformation-DIA apparatus at P-T conditions of the upper part of the mantle transition zone. *Am Min.* **96**, 1665-1672.
- Kelemen, P. B., J. L. Rilling, E. M. Parmentier, L. Mehl, and B. R. Hacker (2003), Thermal structure due to solid-state flow in the mantle wedge beneath arcs. *Geophys. Monograph. Series* **138**, 293-311.
- Kirchheim, R. (2001), Solubility and diffusivity of hydrogen in complex materials. *Physica Scripta.* **T94**, 58-67.
- Koch-Muller, M., and D. Rhede (2010), IR absorption coefficients for water in nominally anhydrous high-pressure minerals. *Am. Min.* **95**, 770-775.
- Koga, K., E. Hauri, M. Hirschmann, and D. Bell (2003), Hydrogen concentration analyses using SIMS and FTIR: Comparison and calibration for nominally anhydrous minerals. *Geochem. Geophys. Geosystems* **4**, doi:10.1029/2002GC000378.
- Kohlstedt, D. L., and C. Goetze (1974), Low-stress high-temperature creep in olivine single crystals. *J. Geophys. Res.* **79**, 2045-2051.
- Kohlstedt, D. L., H. P. K. Nichols, and P. Hornack (1980), The effect of pressure on the rate of dislocation recovery in olivine. *J. Geophys. Res.* **85**, 3122-3130.

- Kohlstedt, D. L., H. Keppler, and D. C. Rubie (1996), Solubility of water in the alpha, beta and gamma phases of  $(\text{Mg,Fe})_2\text{SiO}_4$ . *Contrib. Min. Petrol.* **123**, 345-357.
- Kohlstedt, D. L., and S. J. Mackwell (1998), Diffusion of hydrogen and intrinsic point defects in olivine. *Z. Phys. Chem.* **207**, 147-162.
- Kohlstedt, D. L. (2006), The role of water in high-temperature rock deformation. *Rev. Min. Geochem.* **62**, 377-396.
- Kohlstedt, D. L., Y. Li, and S. J. Mackwell (2012), O Water in olivine, Where art thou? *Am. Geophys. Union 2012*. Conference Abstract.
- Koizumi, S., T. Hiraga, C. Tachibana, M. Tasaka, T. Miyazaki, T. Kobayashi, A. Takamasa, N. Ohashi, and S. Sano (2010), Synthesis of highly dense and fine-grained aggregates of mantle composites by vacuum sintering of nano-sized mineral powders. *Phys. Chem. Min.* **37**, 505-518.
- Kröger, F. A., and H. J. Vink (1956), Relations between the concentrations of imperfections in crystalline solids. *Solid State Phys.* **3**, 307-435.
- Lehmann, L. (1959), Velocities of longitudinal waves in the upper part of the Earth's mantle. *Ann. Geophys.* **15**, 93-118.
- Lerchbaumer, L., and A. Audétat (2012), High Cu concentrations in vapor-type fluid inclusions: An artifact? *Geochim. Cosmochim. Acta* **88**, 255-274.
- Li, L., D. J. Weidner, J. Brodholt, D. Alfee, and G. D. Price (2006), Elasticity of  $\text{Mg}_2\text{SiO}_4$  ringwoodite at mantle conditions. *Phys. Earth Planet. Int.* **157**, 181-187.
- Li, L., D. Weidner, P. Raterron, J. H. Chen, M. Vaughan, S. H. Me, and B. Durham (2006), Deformation of olivine at mantle pressure using the D-DIA. *Eur. J. Min.* **18**, 7-19.
- Libowitzky, E., and G. R. Rossman (1997), An IR absorption calibration for water in minerals. *Am. Min.* **82**, 1111-1115.
- Long, M. D., and R. D. van der Hilst (2006), Shear wave splitting from local events beneath the Ryukyu arc: Trench-parallel anisotropy in the mantle wedge. *Phys. Earth Planet. Int.* **155**, 300-312.
- Mackwell, S. J., D. L. Kohlstedt, and M. S. Paterson (1985), The Role of Water in the Deformation of Olivine Single Crystals. *J. Geophys. Res.* **90**, 11319-11333.
- Mackwell, S. J., and D. L. Kohlstedt (1986), High-temperature deformation of forsterite single crystals doped with vanadium. *Phys. Chem. Min.* **13**, 351-356.

- Mackwell, S. J., D. Dimos, and D. L. Kohlstedt (1988), Transient creep of olivine: point-defect relaxation times. *Philosophical Magazine A*, **57**, 779-789.
- Mackwell, S. J. (1991), High-temperature rheology of enstatite: Implications for creep in the mantle. *Geophys. Res. Lett.* **18**, 2027-2030.
- Magee, C. W. (1981), Hydrogen depth profiling using SIMS—Problems and their solutions. *J. Vac. Sci. Technol.* **19**, 47-52.
- Manning, J. R. (1990), *Diffusion kinetics for atoms in crystals*. Princeton, New Jersey London. pp. 1-29.
- Manthilake, M., T. Matsuzaki, T. Yoshino, S. Yamashita, E. Ito, and T. Katsura (2009), Electrical conductivity of wadsleyite as a function of temperature and water content. *Phys. Earth Planet. Int.* **174**, 10-18.
- Mao, Z., S. D. Jacobsen, F. Jiang, J. R. Smyth, C. M. Holl, and T. S. Duffy (2008), Elasticity of hydrous wadsleyite to 12 GPa: Implications for Earth's transition zone. *Geophys. Res. Lett.* **35** (L2130521). doi:10.1029/2008GL035618.
- McKenzie, D. P. (1967), The viscosity of the mantle. *Geophys. J. Royal. Astro. Soc.* **14**, 297-305.
- Mei, S., and D. L. Kohlstedt (2000a), Influence of water on plastic deformation of olivine aggregates 2. Dislocation creep regime. *J. Geophys. Res.* **105**, 21471-21481.
- Mei, S., and D. L. Kohlstedt (2000b), Influence of water on plastic deformation of olivine aggregates 1. Diffusion creep regime. *J. Geophys. Res.* **105**, 21457-21469.
- Mei, S., W. Bai, T. Hiraga, and D. L. Kohlstedt (2002), Influence of melt on the creep behavior of olivine–basalt aggregates under hydrous conditions. *Earth Planet. Sci. Lett.* **201**, 491-507.
- Montagner, J. P., and L. Guillot (2000), Seismic anisotropy in the Earth's mantle, in *Problems in Geophysics for the New Millennium* (edited by E. Boschi, G. Ekstrom, and A. Morelli). Editrice Compositori press, 217-253.
- Mordehai, D., E. Clouet, M. Fivel, and M. Verdier (2008), Introducing dislocation climb by bulk diffusion in discrete dislocation dynamics. *Philosophical Magazine* **88**, 899-925.
- Nabarro, F. (1948), Deformation of crystals by the motion of single ions, in *Report of a conference on strength of solids*, edited by G. Nooky, pp. 75-90, *Phys. Soc.* London, 1948.
- Nakamura, H., and H. Iwamori (2009), Contribution of slab-fluid in arc magmas beneath the Japan arcs. *Gondwana Res.* **16**, 431-445.

- Nettles, M., and A. M. Dziewonski (2008), Radially anisotropic shear velocity structure of the upper mantle globally and beneath North America. *J. Geophys. Res.* **113**, B02303B2. Doi:10.1029/2006JB004819.
- Paterson, M. S. (1970), A high-pressure, high-temperature apparatus for rock deformation. *Int. J. Rock. Mech. Min.* **7**, 517-526.
- Paterson, M. S. (1982), The determination of hydroxyl by infrared absorption in quartz, silicate glasses and similar materials. *Bull. Min.* **105**, 20-29.
- Paterson, M. S. (1990), Rock deformation experimentation. *Geophys. Monograph.* **56**, 187-194.
- Peltier, W. R. (1998), Postglacial variations in the level of the sea: implications for climate dynamics and solid-earth geophysics. *Rev. Geophys.* **36**, 603-689.
- Presnall, D. C. (1995), Phase diagrams of Earth-forming minerals. *Min. Phys. Crystallography* **2**, 248-268.
- Putirka, K. D. (2005), Mantle potential temperatures at Hawaii, Iceland, and the mid-ocean ridge system, as inferred from olivine phenocrysts: Evidence for thermally driven mantle plumes. *Geochem. Geophys. Geosys.* **6**, Q05L08, doi:10.1029/2005GC000915.
- Raterron, P., Y. J. Wu, D. J. Weidner, and J. H. Chen (2004), Low-temperature olivine rheology at high pressure, *Phys. Earth Planet. Int.* **145**, 149-159.
- Raterron, P., J. Chen, L. Li, D. Weidner, and P. Cordier (2007), Pressure-induced slip-system transition in forsterite: Single-crystal rheological properties at mantle pressure and temperature. *Am. Min.* **92**, 1436-1445.
- Raterron, P., E. Amiguet, J. Chen, L. Li, and P. Cordier (2009), Experimental deformation of olivine single crystals at mantle pressures and temperatures. *Phys. Earth Planet. Int.* **172**, 74-83.
- Raterron, P., J. Chen, T. Geenen, and J. Girard (2011), Pressure effect on forsterite dislocation slip systems: Implications for upper-mantle LPO and low viscosity zone. *Phys. Earth Planet. Int.* **188**, 26-36.
- Reddy, K.P.R., S.M. Oh, L.D. Major Jr., and A. R. Cooper (1980), Oxygen diffusion in forsterite. *J. Geophys. Res.*, **85**, 322-326.
- Ricoult, D. L., and D. L. Kohlstedt (1983), Structural width of low-angle grain boundaries in olivine. *Phys. Chem. Min.* **9**, 133-138.
- Ricoult, D. L., and D. L. Kohlstedt (1985), Experimental evidence for the effect of chemical environment upon the creep rate of olivine. *AGU Geophys. Monograph* **31**, 171-184.

- Ricoult, D. L., and D. L. Kohlstedt (1986), Creep Behavior of Single Crystals of Vanadium doped Forsterite. *J. Am. Ceram. Soc.* **69**, 770-774.
- Ringwood, A. E. (1962), A Model for the upper mantle. *J. Geophys. Res.* **67**, 857-867.
- Ringwood, A. E. (1991), Phase-transformations and their bearing on the constitution and dynamics of the mantle. *Geochim. Cosmochim. Acta* **55**, 2083-2110.
- Ross, J. V., H. G. Avelallemant, and N. L. Carter (1979), Activation volume for creep in the upper mantle. *Science* **203**, 261-263.
- Ryerson, F. J., W. B. Durham, D. J. Cherniak, and W. A. Lanford (1989), Oxygen diffusion in olivine: Effect of oxygen fugacity and implications for creep. *J. Geophys. Res.* **94**, 4105-4118.
- Sano, S., N. Saito, S. Matsuda, N. Ohashi, H. Haneda, Y. Arita, and M. Takemoto (2006), Synthesis of high density and transparent forsterite ceramics using nano-sized precursors and their dielectric properties. *J. Am. Ceram. Soc.* **89**, 568-574.
- Savage, M. K. (1999), Seismic anisotropy and mantle deformation: What have we learned from shear wave splitting? *Rev. Geophys.* **37**, 65-106.
- Schmalzried, H. (1995), *Chemical kinetics of solids*. Wiley-VCH Press.
- Schmidt, P., B. Lund, T. Arnadóttir, and H. Schmeling (2012), Glacial isostatic adjustment constrains dehydration stiffening beneath Iceland, *Earth Planet. Sci. Lett.* **359**, 152-161.
- Schwenn, M. B., and C. Goetze (1978), Creep of olivine during hot-pressing. *Tectonophysics* **48**, 41-60.
- Sella, G. F., T. H. Dixon, and A. Mao (2002), REVEL: A model for recent plate velocities from space geodesy. *J. Geophys. Res.* **107**, 2081. Doi: 10.1029/2000JB000033.
- Shatskiy, A., H. Fukui, T. Matsuzaki, K. Shinoda, A. Yoneda, D. Yamazaki, E. Ito, and T. Katsura (2007), Growth of large (1 mm) MgSiO<sub>3</sub> perovskite single crystals: A thermal gradient method at ultrahigh pressure. *Am Min.* **92**, 1744-1749.
- Shatskiy, A., K. D. Litasov, T. Matsuzaki, K. Shinoda, D. Yamazaki, A. Yoneda, E. Ito, and T. Katsura (2009), Single crystal growth of wadsleyite. *Am. Min.* **94**, 1130-1136.
- Shatskiy, A., D. Yamazaki, Y. M. Borzdov, T. Matsuzaki, K. D. Litasov, T. Cooray, A. Ferot, E. Ito, and T. Katsura (2010), Stishovite single-crystal growth and application to silicon self-diffusion measurements. *Am Min.* **95**, 135-143.
- Shekhar, S. (2012), *The origins of olivine fabric transitions and their effects on seismic anisotropy in the upper mantle*. Ph.D thesis, University of Bayreuth.

- Shimojuku, A., T. Kubo, E. Ohtani, and H. Yurimoto (2004), Silicon self-diffusion in wadsleyite: Implications for rheology of the mantle transition zone and subducting plates. *Geophys. Res. Lett.*, **31**, L1360613.
- Shimojuku, A., T. Kubo, E. Ohtani, T. Nakamura, R. Okazaki, R. Dohmen, and S. Chakraborty (2009), Si and O diffusion in  $(\text{Mg,Fe})_2\text{SiO}_4$  wadsleyite and ringwoodite and its implications for the rheology of the mantle transition zone. *Earth Planet. Sci. Lett.* **284**, 103-112.
- Shimojuku, A., T. Kubo, E. Ohtani, T. Nakamura, and R. Okazaki (2010), Effects of hydrogen and iron on the silicon diffusivity of wadsleyite. *Phys. Earth Planet. Int.* **183**, 175-182.
- Smyth, D. M., and R. L. Stocker (1975), Point defects and non-stoichiometry in forsterite. *Phys. Earth Planet. Int.* **10**, 183-192.
- Smyth, J. R., D. J. Frost, F. Nestola, C. M. Holl, and G. Bromiley (2006), Olivine hydration in the deep upper mantle: Effects of temperature and silica activity. *Geophys. Res. Lett.* **33**, L15301.
- Snyder, D., and M. Bruneton (2007), Seismic anisotropy of the Slave craton, NW Canada, from joint interpretation of SKS and Rayleigh waves. *Geophys. J. Int.* **169**, 170-188.
- Song, T. A., and H. Kawakatsu (2012), Subduction of oceanic asthenosphere: Evidence from sub-slab seismic anisotropy. *Geophys. Res. Lett.* **39**, 17301. Doi: 10.1029/2012GL052639.
- Spandler, C., and H. S. O'Neill (2010), Diffusion and partition coefficients of minor and trace elements in San Carlos olivine at 1,300 degrees C with some geochemical implications. *Contrib. Min. Petrol.* **159**, 791-818.
- Stocker, R. L., and D. M. Smyth (1978), Effect of enstatite activity and oxygen partial pressure on the point-defect chemistry of olivine. *Phys. Earth Planet. Int.* **16**, 145-156.
- Sundberg, M., and R. F. Cooper (2008), Crystallographic preferred orientation produced by diffusional creep of harzburgite: Effects of chemical interactions among phases during plastic flow, *J. Geophys. Res.* **113**, B12208B12. Doi: 10.1029/2008JB005618.
- Tasaka, M., T. Hiraga, and M. E. Zimmerman (2013), Influence of mineral fraction on the rheological properties of forsterite + enstatite during grain – size – sensitive creep: 2. Deformation experiments. *J. Geophys. Res.* **118**, 1-22. Doi: 10.1002/jgrb.50284.
- Thomas, S., M. Koch-Müller, P. Reichart, D. Rhede, R. Thomas, R. Wirth, and S. Matsyuk (2009), IR calibrations for water determination in olivine,  $r\text{-GeO}_2$ , and  $\text{SiO}_2$  polymorphs. *Phys. Chem. Min.* **36**, 489-509.

- Thybo, H., and E. Perchuc (1997), The seismic 8 degrees discontinuity and partial melting in continental mantle, *Science* **275**, 1626-1629.
- Thybo, H. (2006), The heterogeneous upper mantle low velocity zone. *Tectonophysics* **416**, 53-79.
- Tomita, M., K. M., A. H., and T. S. (2012), Investigation of the factors determining the SIMS depth resolution in silicon-isotope multiple layers. *J. Vac. Sci. Technol.* **B30**, 1108031.
- Turcotte, D. L., and G. Schubert (2002), *Geodynamics*. Cambridge Univ. Press.
- Van Orman, J., T. Grove, N. Shimizu, and G. Layne (2002), Rare earth element diffusion in a natural pyrope single crystal at 2.8 GPa. *Contrib. Min. Petrol.* **142**, 416-424.
- Vauchez, A., F. Dineur, and R. Rudnick (2005), Microstructure, texture and seismic anisotropy of the lithospheric mantle above a mantle plume: Insights from the Labait volcano xenoliths (Tanzania). *Earth Planet. Sci. Lett.* **232**, 295-314.
- Wada, I., M. D. Behn, and J. He (2011), Grain-size distribution in the mantle wedge of subduction zones, *J. Geophys. Res.* **116**, 10203, Doi: 10.1029/2011JB008294.
- Walker, A. M., K. Wright, and B. Slater (2003), A computational study of oxygen diffusion in olivine. *Phys. Chem. Min.* **30**, 536-545.
- Walter, M. J., Y. Thibault, K. Wei, and R. W. Luth (1995), Characterizing experimental pressure and temperature conditions in multi-anvil apparatus. *Ca. J. Phys.* **73**, 273-286.
- Wanamaker, B. J. (1994), Point defect diffusivities in San Carlos olivine derived from reequilibration of electrical conductivity following changes in oxygen fugacity. *Geophys. Res. Lett.* **21**, 21-24.
- Wang, Y. B., W. B. Durham, I. C. Getting, and D. J. Weidner (2003), The deformation-DIA: a new apparatus for high temperature triaxial deformation to pressures up to 15 GPa. *Rev. Sci. Instr.* **74**, 3002-3011.
- Wang, Z., T. Hiraga, and D. L. Kohlstedt (2004), Effect of H<sup>+</sup> on Fe-Mg interdiffusion in olivine, (Fe, Mg)<sub>2</sub>SiO<sub>4</sub>. *Appl. Phys. Lett.* **85**, 209-211.
- Wang, D. J., M. Mookherjee, Y. S. Xu, and S. Karato (2006), The effect of water on the electrical conductivity of olivine. *Nature*, **443**, 977-980.
- Wang, D. J., H. P. Li, L. Yi, and B. P. Shi (2008), The electrical conductivity of upper-mantle rocks: water content in the upper mantle. *Phys. Chem. Min.* **35**, 157-162.
- Wang, J. Y., S. V. Sinogeikin, T. Inoue, and J. D. Bass (2006), Elastic properties of hydrous ringwoodite at high-pressure conditions. *Geophys. Res. Lett.* **33** (L1430814).

- Weertman, J. (1955), Theory of steady-state creep based on dislocation climb, *J. Appl. Phys.* **26**, 1213-1217.
- Weertman, J. (1999), *Mechanics and Materials: Fundamentals and Linkages*. ed. M. A., Meyers, R.W., Armstrong, and H. O. K., Kirchner, New York: John Wiley & Sons.
- Wheeler, J. (1992), Importance of pressure solution and Coble creep in deformation of polymineralic rocks. *J. Geophys. Res.* **97**, 4579-4586.
- Wolfe, C. J., and P. G. Silver (1998), Seismic anisotropy of oceanic upper mantle: Shear wave splitting methodologies and observations. *J. Geophys. Res.* **103**, 749-771.
- Wood, B. J., L. T. Bryndzia, and K. E. Johnson (1990), Mantle Oxidation State and Its Relationship to Tectonic Environment and Fluid Speciation. *Science* **248**, 337-345.
- Workman, R. K., and S. R. Hart (2005), Major and trace element composition of the depleted MORB mantle (DMM). *Earth Planet. Sci. Lett.* **231**, 53-72.
- Wu, P. (1995), Can observations of postglacial rebound tell whether the rheology of the mantle is linear or nonlinear? *Geophys. Res. Lett.* **22**, 1645-1648.
- Wu, P. (2001), Postglacial induced surface motion and gravity in Laurentia for uniform mantle with power-law rheology and ambient tectonic stress. *Earth Planet. Sci. Lett.* **186**, 427-435.
- Xu, J., D. Yamazaki, T. Katsura, X. Wu, P. Remmert, H. Yurimoto, and S. Chakraborty (2011), Silicon and magnesium diffusion in a single crystal of MgSiO<sub>3</sub> perovskite. *J. Geophys. Res.* **116**, 12205.
- Yamaoka, S., M. D. S. Kumar, M. Akaishi, and H. Kanda (2000), Reaction between carbon and water under diamond-stable high pressure and high temperature conditions. *Diam. Relat. Mater.* **9**, 1480-1486.
- Yamazaki, D., T. Kato, H. Yurimoto, E. Ohtani, and M. Toriumi (2000), Silicon self-diffusion in MgSiO<sub>3</sub> perovskite at 25 GPa. *Phys. Earth Planet. Int.* **119**, 299-309.
- Yoshino, T., T. Matsuzaki, S. Yamashita, and T. Katsura (2006), Hydrous olivine unable to account for conductivity anomaly at the top of the asthenosphere. *Nature* **443**, 973-976.
- Yoshino, T., G. Manthilake, T. Matsuzaki, and T. Katsura (2008), Dry mantle transition zone inferred from the conductivity of wadsleyite and ringwoodite. *Nature* **451**, 326-329.
- Yoshino, T., T. Matsuzaki, A. Shatskiy, and T. Katsura (2009), The effect of water on the electrical conductivity of olivine aggregates and its implications for the electrical structure of the upper mantle. *Earth Planet. Sci. Lett.* **288**, 291-300.

- Yurimoto, H., M. Kurosawa, and S. Sueno (1989), Hydrogen analysis in quartz crystals and quartz glasses by secondary ion mass spectrometry. *Geochim. Cosmochim. Acta* **53**, 751-755.
- Yurimoto, H., M. Morioka, and H. Nagasawa (1992), Oxygen self-diffusion along high diffusivity paths in forsterite. *Geochem. J.* **26**, 181-188.
- Zhang, B. H., X. P. Wu, and R. L. Zhou (2011), Calculation of oxygen self-diffusion coefficients in Mg<sub>2</sub>SiO<sub>4</sub> polymorphs and MgSiO<sub>3</sub> perovskite based on the compensation law. *Solid State Ionics* **186**, 20-28.
- Zhang, Y. (2008), *Chemical kinetics*, Princeton University press.
- Zhang, Y., and D. J. Cherniak (2010), Diffusion in Minerals and Melts: Theoretical Background, *Rev. Min. Geophys.* **72**, 5-59.
- Zhao, Y., S. B. Ginsberg, and D. L. Kohlstedt (2004), Solubility of hydrogen in olivine: dependence on temperature and iron content. *Contrib. Min. Petrol.* **147**, 155-161.

# PUBLICATIONS

---

## Publications related to this work

### (1) Articles

1. **H. Fei**, C. Hegoda, D. Yamazaki, M. Wiedenbeck, H. Yurimoto, S. Shcheka, T. Katsura (2012). High silicon self-diffusion coefficient in dry forsterite. *Earth and Planetary Science Letters* **345**, 95-103 (**Chapter 2**).
2. **H. Fei**, M. Wiedenbeck, D. Yamazaki, T. Katsura (2013). Small effect of water on upper-mantle rheology based on silicon self-diffusion coefficients. *Nature* **498**, 213-215 (**Chapter 3**).
3. **H. Fei**, M. Wiedenbeck, D. Yamazaki, T. Katsura (2013). Water has no significant effect on oxygen self-diffusion rate in forsterite. Manuscript submitted to *Physics of the Earth and Planetary Interiors*. (**Chapter 4**).
4. **H. Fei**, S. Koizumi, N. Sakamoto, M. Hashiguchi, H. Yurimoto, D. Yamazaki, T. Katsura, dominance of diffusion creep in cold mantles based on Si grain-boundary diffusion. Completed manuscript for submission (**Chapter 5**).

### (2) Abstracts and Reports

1. T. Katsura, **H.Z. Fei**, M. Wiedenbeck, D. Yamazaki (2013), Si and O self-diffusion coefficient of forsterite as a function of water content, *European Geosciences Union 2013*, Vienna, Austria.
2. T. Katsura, **H.-Z. Fei**, M. Wiedenbeck, D. Yamazaki (2013), Small effect of water on upper mantle rheology based on Si self-diffusion coefficient, *Global-COE international symposium on Deep Earth Mineralogy*, Ehime, Japan.
3. **H. Fei**, M. Wiedenbeck, D. Yamazaki, T. Katsura (2012), Small effect of water on upper mantle rheology based on Si self-diffusion coefficients, DI13D-2448. *AGU Fall Meeting*, San Francisco, United States.
4. T. Katsura, **H. Fei**, C. Hegoda, D. Yamazaki, M. Wiedenbeck, H. Yurimoto, S. Shcheka (2012). High silicon self-diffusion coefficient in dry forsterite. MR31A-02. *AGU Fall Meeting*, San Francisco, United States.

5. **H. Fei**, M. Wiedenbeck, D. Yamazaki, T. Katsura (2012), Small effect of water on upper mantle rheology based on Si self-diffusion coefficients, *Bayerisches Geoinstitut Annual Report 2012*. 151-153.
6. **H. Fei**, M. Wiedenbeck, D. Yamazaki, T. Katsura (2012), The effect of water on oxygen self-diffusion coefficients in forsterite, *Bayerisches Geoinstitut Annual Report 2012*. 153-155.
7. T. Katsura, **H.-Z. Fei**, D. Yamazaki, J.-S. Xu, A. Shatskiy, C. Hegoda, S. Chakraborty, R. Dohmen, H. Yurimoto, M. Wiedenbeck (2012), Self-diffusion of the mantle minerals, *HPMPS 8*, Lake Tahoe, CA, United States.
8. T. Katsura, D. Yamazaki, S. Chakraborty, R. Dohmen, A. Shatskiy, J.-S. Xu, **H.-Z. Fei**, C. Hegoda, H. Yurimoto, M. Wiedenbeck (2012), Self-diffusion coefficients of mantle minerals and its applications to mantle rheology, *Dynamics and Evolution of the Earth's Interior: special emphasis on the role of fluids*, Misasa, Tottori, Japan.
9. T. Katsura, D. Yamazaki, S. Chakraborty, R. Dohmen, A. Shatskiy, J.-S. Xu, **H.-Z. Fei**, C. Hegoda, H. Yurimoto, M. Wiedenbeck (2012), Si and Mg self-diffusion in stishovite, Mg-perovskite, and forsterite, *EMPG XIV*, Kiel, Germany.
10. **H. Fei**, C. Hegoda, D. Yamazaki, S. Chakraborty, R. Dohmen, M. Wiedenbeck, H. Yurimoto, S. Shcheka, T. Katsura (2012), High silicon self-diffusion coefficient in dry forsterite, *EMPG XIV*, Kiel, Germany.
11. **H. Fei**, C. Hegoda, D. Yamazaki, S. Chakraborty, R. Dohmen, M. Wiedenbeck, H. Yurimoto, S. Shcheka, T. Katsura (2011), High silicon self-diffusion coefficient in dry forsterite, *Bayerisches Geoinstitut Annual Report 2011*. 152-154.
12. **H. Fei**, T. Katsura, S. Chakraborty, R. Dohmen, C. Hegoda, D. Yamazaki, M. Wiedenbeck, H. Yurimoto, S. Shcheka, K. Pollok, A. Aud at (2011), Silicon self-diffusion in forsterite, revisited. *Goldschmidt Conference 2011*, Prague, Czech Republic, *Mineralogical Magazine*, **75** (3), 834.

# ACKNOWLEDGMENTS

---

## Acknowledgments

First of all, I would like to appreciate my supervisor, Prof. T. Katsura, who patiently and largely guides my work and life during the Ph.D period. I also thank D. Yamazaki, A. Yoneda, E. Ito, T. Yoshino, and C. Hegoda at Okayama University, Misasa (Japan), M. Wiedenbeck at Helmholtz Centre Potsdam (Germany), H. Yurimoto, N. Sakamoto, and M. Hashiguchi at Hokkaido University, Sapporo (Japan), S. Chakraborty and R. Dohmen at Ruhr-University of Bochum (Germany), S. Koizumi and T. Hiraga at Tokyo University (Japan), and H. Keppler, A. Audéat, T. Boffa-Ballaran, S. Shcheka, and F. Heidelbach at University of Bayreuth for their help in sample analyses and discussions in this project. Thank all the colleagues and technicians at Bayerisches Geoinstitut and at Misasa for the experimental performance and high pressure experimental cell-assembly preparation.



# Erklärung

---

## Erklärung

Hiermit erkläre ich, dass ich die Arbeit selbständig verfasst und keine anderen als die von mir angegebenen Quellen und Hilfsmittel benutzt habe.

Ferner erkläre ich, dass ich anderweitig mit oder ohne Erfolg nicht versucht habe, diese Dissertation einzureichen. Ich habe keine gleichartige Doktorprüfung an einer anderen Hochschule endgültig nicht bestanden.

Fei Hongzhan

费宏展

Bayreuth, 4th, Nov, 2013